Scale Effects in Testing of a Monopile Support Structure Submerged in Tidal Currents.

Oghenevwori Patricia Okorie.

A thesis submitted in partial fulfillment of the requirements of the Robert Gordon University for the degree of Doctor of Philosophy.
Aberdeen, UK.

November, 2011

Acknowledgement

I acknowledge my Supervisor Dr Alan Owen for giving me the opportunity to start this project and for all his help and support throughout this project. He provided me with opportunities to network with those with similar research interest which was very helpful.

I thank Prof. Pat Pollard for her encouragement, help and readiness to facilitate the completion of this project.

I thank Dr Mamdud Hossain for his supervision, constructive criticism and encouragement throughout this project.

I will not fail to thank the team from University of Aberdeen Dr. Beth, Evelyn her PhD student and the boat crew for their contribution in the ADCP experiment.

I cannot express my gratitude enough to my beloved husband Eze, for his patience and love that continued to sustain me throughout this period of toil. My heartfelt thanks go to my children, David, Faith, Stephanie and Daniel for their understanding throughout this time. My family members did more than their fair share of housework just to encourage me to succeed.

My thanks also goes to all my friends, extended family members, well wishers too numerous to mention for their care, prayers and support that has enabled me succeed.

Above all I thank God who gave life, strength and ability to me and everyone who in one way or the other who contributed to the success of this project.

Dedication

This thesis is dedicated to God, the Father of science.

Supervisory Team/Funding

Dr Alan Owen

Professor Pat Pollard

Dr Mamdud Hossain

The project is funded by Engineering and Physical Science Research Council (EPSRC) via SuperGen Marine.

Abstract

Climate change and energy security are key issues motivating the development of Tidal Current Energy (TCE) technology. Small scale model testing of TCE devices is a major challenge facing the technology due to turbulent flow in tidal currents environment and scaling is a fundamental engineering procedure for prototype development and optimisation for cost effectiveness. This thesis presents the outcome from investigating Dimensional Scale Effects (DSE) and Turbulence Scale Effects (TSE) of a monopile support structure using Computational Fluid Dynamics (CFD).

Scale models dimensioned according to the Froude scaling criterion was used for the DSE investigation whereas real time turbulent velocity profile sampled from the Firth of Forth, Scotland was used for the TSE investigation. The real time turbulent velocity profile is influenced by waves, channel sidewalls, seabed roughness and other natural, physical and biological processes occurring in the estuary.

The following observations were made:

1) For the DSE, the drag coefficient of scale models within the subcritical flow regime varies as a function of a non-dimensional length and velocity scale. Equations for estimating the scale effects are presented.

2) The TSE investigation demonstrates a novel application of Acoustic Doppler Current Profiler (ADCP) data from a real site to generate significant upstream turbulence structures suitable for testing tidal current energy devices. The results show that, significant increase in turbulence in terms of maximum vorticity magnitude, by a factor more than 4, can be achieved in an empty channel and seabed drag coefficient is significantly reduced when compared with simulations done by specifying theoretical velocity profiles in a Large Eddy Simulation (LES).

3) Ambient turbulent flow around a monopile support structure causes a significant reduction in drag coefficient compared with simulations done by specifying the uniform and the $1/7^{th}$ power law velocity profiles.

The simulation results further demonstrate the possibility of representing a large scale prototype with a small scale numerical simulation domain that captures ambient vortex structures in real sites and that, the use of uniform flow and 1/7th power law velocity profiles in numerical simulations would lead to overestimation of hydrodynamic forces acting on an energy device and underestimation of available energy for extraction due to lower seabed drag coefficient.

Further work is recommended to investigate effect of ambient turbulent structures on hydrodynamic loading and performance of a turbine undergoing sea trials using the methodology proposed in this study. The methodology has potential application to oil and gas subsea structures.

TABLE OF CONTENTS

LIST OF FIGURES

LIST OF TABLES

NOMENCLATURE

Description	Symbol
Turbulent kinetic energy	k
Turbulent dissipation rate	ε
Time	t
Density	ρ
Molecular viscosity	μ
Turbulent viscosity	μ_t
Kinematic viscosity	ν
Pressure	P
Scalar measure of deformation	S
Mean strain rate tensor	S_{ij}
Turbulent Prandtl number for k	σ_k
Turbulent Prandtl number for ε	σ_ε
Stress due to molecular viscosity	σ_{ij}
Subgrid scale stress	τ_{ij}
Subgrid length scale	L_s
Von karman constant	κ
Distance to the closest wall	d
Smagorinsky constant	C_s
Local grid scale	Δ

Frequency of sound waves	F_{sound}
Doppler shift	$F_{doppler}$
Velocity of water particles	$V_{particles}$
Speed of sound	C_{sound}
Drag coefficient	C_D
Lift coefficient	C_L
Pressure coefficient	C_p
Drag force	D
Lift Force	L
Pressure force	p
Static pressure	p_a
Frontal area	A
Diameter of model	D_m
Prototype diameter	D_p
Number of nodes on model	N_m
Number of nodes on prototype	N_p
Reynolds number	Re
Froude number	Fr
Strouhal number	St

Acceleration due to gravity	g
Length scale	l
Velocity of prototype	u_p
Velocity of model	u_m
Frequency of vortex shedding	f
Drag coefficient error	e_{C_D}
Drag force error	e_D
Dimensionless length scale	K_L
Dimensionless velocity scale	K_V
Inertia coefficient	C_m
Total force	F

Chapter 1.0

General Introduction

1.1 Background

In response to the growing need for sustainable energy and climate change, fundamentally driven by the Kyoto protocol (1) and the Renewable Obligation (RO) order (2), tidal current energy technology has been identified as a viable option among the energy mix portfolio. Tidal currents energy resource in the UK has been estimated by several sources (3) that include (4-6) but with differing estimates resulting from the analysis method. Also, the World Offshore Renewable Energy Report (7), released by the Department of Trade and Industry, suggests that 3000GW of tidal energy is estimated to be available.

A target has been set to generate 15% of electricity from renewable energy sources by 2015 (8). A recent publication by the Department of Trade and Industry (9) underpins the RO order with current target set to generate 20% of electricity from Renewable sources by 2020. Technological development of tidal currents energy is underway to facilitate achieving the set target.

1.2 Tides and energy extraction

Tide is caused by the effect of the gravitational pull between the sun and the moon acting on the oceans of the rotating earth. Tidal currents are the horizontal movement of water associated with the periodic change of the surface level of water (10). They are rotary currents in the open ocean because they are not restricted by any barrier. They become flood and ebb near the shore signified by oncoming and the receding tide respectively. Between the ebb and flood is a flow reversal period when there is no current called slack water. Tidal currents occur in rivers, estuaries as well as in the sea or ocean (11).

The energy in the tide had been tapped as far back as AD 1100, using *tide mills* driven by the rise and fall of the tides. These mills were disadvantaged because of tidal surge, expensive labour and workers reluctance to work during odd hours as dictated by the tides. Several tidal mills are spread across Europe (12). The tidal mills are the predecessors of modern *tidal barrages.* The later include the use of several sluice gates that allows the filling of a water reservoir and make use of low head water turbines to extract energy instead of water wheels as opposed to tidal mills however, they are disadvantaged due to high civil infrastructural cost and potential negative environmental impact. Despite the drawbacks, the la Rance (13) tidal barrage has been harvesting tidal energy since the 1960's and has the capacity to generate 240 MW of electricity. The challenges associated with tidal barrages stimulated interest in energy extraction directly from tidal current using the *tidal stream* or *Tidal Current Energy (TCE)* technology thus evading the need to constrain tidal flow by building barrages.

Several devices/technologies for harnessing the available resource are currently being developed and tested. The progress made so far is significant with some commercial test prototype currently connected to the grid for example, the Marine Current Turbines (12).

1.3 General description of a TCE system.

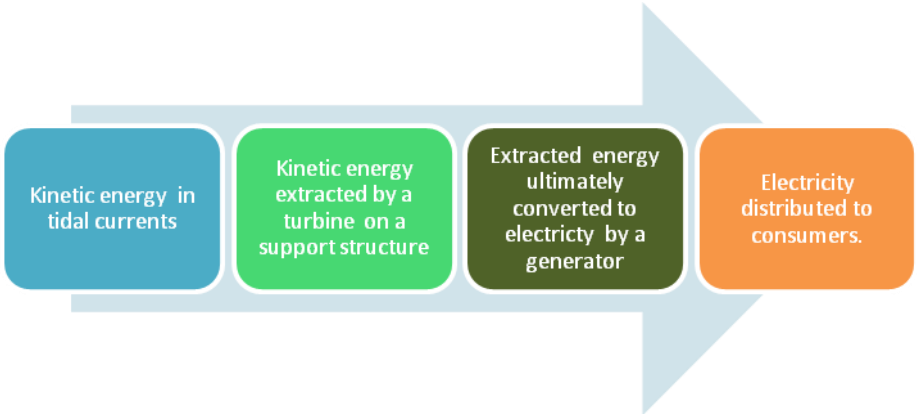

Figure 1.1: An illustration of a TCE conversion system.

TCE systems are designed to extract kinetic energy from fast flowing current constrained by the sides of a channel created by two land masses The block diagram in Figure 1.1 illustrates a TCE conversion process. A TCE installation generally includes a turbine on a fixed supporting or anchoring structure that is required to withstand turbulent loading in the environment. The turbine is positioned to extract kinetic energy from the flow of tidal currents and converts it to mechanical energy. The mechanical energy is further converted into electrical energy using a generator incorporated into the system. The power generated is transported and distributed for consumption. The energy extracted by a turbine submerged in a tidal current channel, is a function of the cube of the current velocity, water density and the cross sectional area swept by the turbine blades exposed to the incoming flow. A database of some known TCE technologies/devices can be found in (14). The devices are at different development stages. A few examples are illustrated in what follows.

1.4 Categories of TCE Devices

Tidal current energy devices can be categorised into four types namely;

- Horizontal axis turbine
- Vertical axis turbine
- Oscillating devices
- Venturi effect devices.

1.4.1 Horizontal axis turbine

A horizontal axis tidal turbine has its blades rotating about a horizontal axis parallel to the streamwise direction. An example of a horizontal axis tidal current turbine is the Seagen in Figure 1.2 (12). It is operated by the Marine Current Turbine (MCT) and has a power production capacity of 1.2

megawatts. It consists of two 16m diameter rotors mounted on a beam across a monopile support structure. The Seagen machine is currently

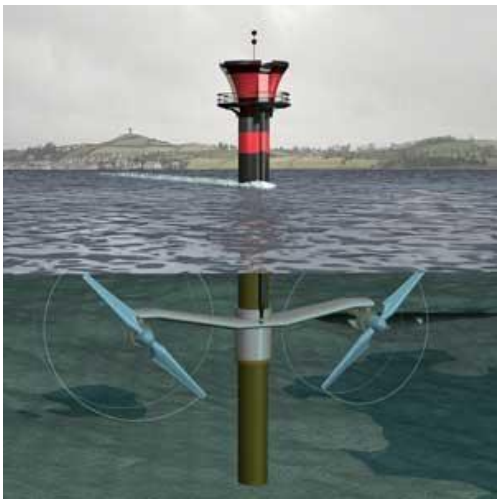

Figure 1.2: Seagen turbine

installed at Strangford Lough in Northern Island and is the first commercial scale tidal current turbine that can generate electricity for up to 1140 homes (12). The history of the development and testing of Seagen is published in (15).

The TidEl® turbine (12,16) shown in Figure 1.3 below is another example of

Figure 1.3: The TidEl® turbine

a horizontal axis turbine consisting of a 500 kW contra-rotating twin turbine with rotors of 15m diameter that freely changes direction with the tide. The twin turbine is mounted on a single cross beam and tethered to the seabedwith mooring chains. The SMD Hydrovision of Tyne and Wear based in the UK conceived and developed the TidEL® concepts. A 1:10 scale model has been tested in the laboratory.

1.4.2 Vertical axis devices

Vertical axis turbines have their axis perpendicular to the streamwise direction. An example is the Gorlov Helical Turbine (GHT) (17) shown in Figure 1.4.

Figure 1.4: Gorlov helical turbine

It is developed by GCK Technology Inc in USA based on the Darrieus Windmill concept. It consists of helical blades twisted about the axis to benefit from every possible angle of attack. It is at the proof of concept stage.

1.4.3 Oscillating devices

The oscillating hydrofoil (16,18) in Figure 1.5 below known as the Stingray is a tidal energy converter developed by the Engineering Business Limited in the UK. The stingray makes use of tidal stream over a hydroplane to produce an oscillating motion which operates hydraulic cylinders to drive a motor that drives a generator to produce electricity.

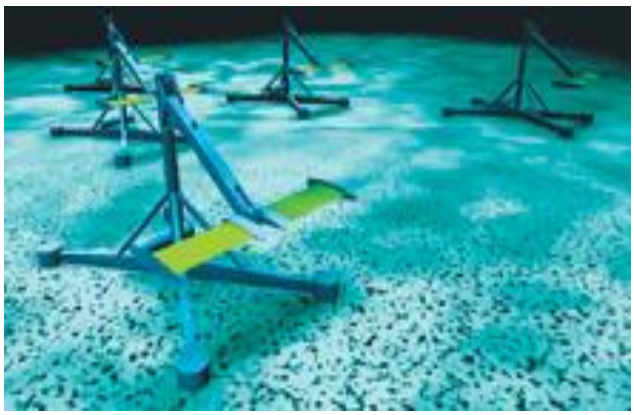

Figure 1.5: Reciprocating hydrofoil

A 150 kW prototype was tested in 2002 in the Yell Sound in UK, but the development was stalled (19) owing to poor cost competitiveness.

1.4.4 Venturi effect devices.

The Rotech Tidal Turbine (RTT) shown in Figure 1.6 (20) is an example of a device that uses the venturi effect. It is a horizontal axis ducted turbine operated by Lunar Energy Limited based in UK. It is 1MW directional turbine with a duct diameter of 15m, duct length of 19.2 m and rotor diameter of 11.5m. A venturi effect is caused when the flow is concentrated through a

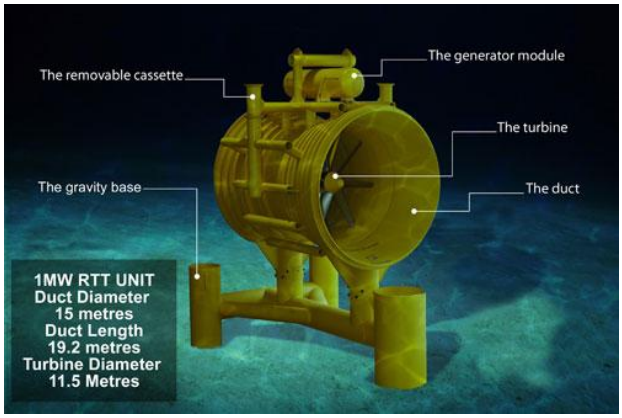

Figure 1.6: Rotech tidal turbine

funnel-like shape. The RTT is a bi-symmetric turbine housed in a venturi that has removable cassette for easy maintenance. The RTT is mounted on a gravity base support structure.

1.5 Classification of tidal current turbine support structures

Tidal current energy technology is rapidly developing and a variety of tidal turbine support structures are currently considered in the industry. They include, but not limited to;

- Monopile and multi-leg support structure.
- Sea snail support structure.
- Gravity based support structure.
- Flexible or fixed anchoring support structures.

1.5.1 Monopile and multi leg pile support structure

Monopile support structures are made of steel tubes which can be drilled, vibrated or hammered to a secured fit on the sea bed. The Seagen tidal turbine shown in Figure 1.2 is supported on a monopile. A multi leg pile structure consists of more than one pile.

1.5.2 Sea snail support structure

The Sea-snail shown in Figure 1.7, patented by (21) is a hydrofoil inducing

Figure 1.7: The sea snail support structure

force support structure. It consists of an array of symmetrical hydrofoil sections supported on pin jointed tubular steel structures. The Sea snail is required to generate sufficient down force to resist over turning moment generated by hydrodynamic forces acting on it and any turbine mounted on it.

1.5.3 Gravity base support structure

The Rotech Tidal Turbine unit shown in Figure 1.6 above is an example of a gravity base support structure. Gravity base support structures could be made of a huge mass of concrete or steel structures attached to its base to achieve and maintain stability.

1.5.4 Flexible or fixed anchoring support structures.

Fixed or flexible anchoring support structures are used for floating energy extraction devices, for example the TidEl turbine was supported by chains moored to the seabed.

A tidal current turbine and its support structure submerged within flow in tidal currents channel are subject to fluctuating loads. The current generating the loads is influenced by waves, channel walls, bottom wall bathymetry and other physical, natural and biological processes occurring in tidal flow environment. The flow within tidal currents is generally described as turbulent. A turbulent flow is random and consists of coherent structures.

1.6 Statements of the challenges facing the TCE industry.

There is a growing need to maximise the use of kinetic energy resources in tidal current channels within the reasonable extractable limit suggested in (22) and (6). This will reflect a favourable reduction in the unit cost of energy while providing opportunity to meet the 20% target to produce electricity from renewable energy sources by 2020. In view of this, energy

devices are undergoing numerous testing required to move forward, but effect of ambient turbulence inherent in tidal current channel environment needs to be tackled and incorporated in the development and optimisation of energy devices.

1.6.1 Tidal current energy device testing methods and their implications.

There are generally accepted methods for testing tidal current energy devices: small scale laboratory testing, numerical modelling and field testing.

a) Laboratory testing facilities

Small scale laboratory testing methods involves the use of a tow tank or a water circulating channel where the device to be tested is towed or fixed respectively. A laboratory tow tank consists of a facility that contains a large volume of still water with an overhead carriage for transporting the device to be tested. It is not possible to reproduce a real tidal current velocity profile in a tow tank because the water is not in motion. Ambient turbulence level in tow tanks has been assumed to be zero (23). Since local turbulence is generated in the vicinity of a towed device during testing, tow tanks can be assumed to have negligible turbulence which is unrepresentative of that encountered in real tidal current flows.

A water circulating tank consists of a testing facility with moving water. The flow of water is predominantly one directional with evidence of a sheared velocity profile from previous experiments conducted at Chilworth research laboratory (24) and Ifremer (23) water circulating tanks. In terms of turbulence, it is an improvement over a tow tank facility because turbulence involves movement of fluid associated with shear stresses (25). However reproducing turbulent velocity profiles resembling those in tidal current is still difficult.

Team members of SuperGen Marine work package eleven (26), in establishing and assessing a suitable laboratory testing procedures for tidal current energy devices, set out to identify guidelines and to establish the limits to laboratory scale model testing. The output from the work stream demonstrated that there are differences between measured forces when device are towed in water and when devices are fixed in flowing water resulting from turbulence and flow shear. Despite the laboratory testing limitations, these testing facilities are widely used for energy device studies (27-31).

b) Relationship between the testing methods

Laboratory testing, sea trials and numerical simulation are viewed as complementary methods for dealing with a complex flow regime such as flow around any device submerged in a stream of tidal currents. Field measurements or sea trials provide the best data but it is the most expensive. Also, natural turbulence conditions make data interpretation more difficult. Small scale laboratory testing and numerical modelling are relatively cheaper than sea trials because their input conditions are more easily controlled and can be varied systematically to study their effects. Laboratory physical modelling in turn is more expensive than numerical modelling. According to Versteeg (32), the investment cost of Computational Fluid Dynamics (CFD) is high but the total expense is not normally as great as the cost of a high quality experimental facility. Furthermore, the cost associated with new designs and parametric studies are avoided in numerical modelling. The advantages of numerical modelling however, do not prevent the use of physical models, instead progress has been made with them. In some cases results from a physical model are used as input conditions to a numerical model and vice–versa. Also, physical models provide calibration and verification data for numerical data/results.

c) Challenges with numerical modelling of tidal current energy devices.

In computational fluid dynamics of TCE devices, theoretical velocity profiles are commonly specified as inlet boundary conditions. For example, Doherty (27) specified the uniform flow boundary condition; in (33) and (34) the $1/7^{th}$ power law velocity profile was specified at the inlet of a simulation domain for modelling tidal current turbines. Although, the $1/7^{th}$ power law profile is a good approximation to turbulent velocity profiles (35), theoretical profiles do not contain evidence of turbulent fluctuations inherent in natural flows due to the averaging process used in generating theoretical profiles. The popular use of theoretical profiles for turbulence modelling is largely attributed to the scarcity of real tidal current velocity profiles or perhaps the logistics and the associated cost of acquiring real current profiles.

Furthermore, it is customary to compare numerical simulation results with laboratory experimental results. Reasonable accuracy and agreement can be achieved on the premise that the already known flow parameters of the laboratory test facility are specified as boundary conditions in the numerical domain. For example, O'Doherty (27) replicated the known and well defined uniform velocity profile of 1m/s velocity and turbulent intensity of 5% typical of the laboratory test facility into a numerical simulation model. Results showed good correlation in torque and power curve. The agreement between the numerical model results and the laboratory results underpin the importance of specifying real sea conditions in a numerical model to achieve credible results for satisfactory prediction of behaviour of prototypes. McCann (36) highlighted the criticality of using site data in the prediction of loading and performance of a tidal stream device. Williams (37) demonstrated the significance of using data measured at site to develop CFD models for tidal stream devices. Also, the common use of the averaged Navier Stokes equation in CFD modelling undermines the

contribution of the large scale turbulent eddies to numerical simulation results.

In this present study, numerical modelling techniques were used to investigate scale effects in tidal current energy device testing. The word scale or scaling is generic so it is necessary to clarify the meaning in the context of this research. Scale has a dual meaning: dimensional scale or turbulence scale. Dimensional scale refers to geometric dimensions of a physical model or prototype while turbulent scale refers to sizes of eddies or vortices contained in a turbulent flow. Dimensional and turbulent scales have implications during device testing.

1.6.2 Dimensional scale effect.

In physical model testing of TCE devices, relationship between prototype and scale model are traditionally achieved using the Froude scaling criterion. This practice is known to result to scale effects and it is therefore important to understand scale effects in device testing. Norvak (38) underpin the importance of investigating scale effects in physical model testing, by stating that "…*If we cannot quantify the error, at least we must be aware in which direction it acts and be able to answer the question - does it contribute to safety or does it diminish the safety factor? Only then can we modify the saying "models are to be used but not believed into models are to be used, sometimes believed but always understood*".

Numerical modelling techniques have been employed in this study to investigate similitude between different sizes of a generic support structure within the critical flow regime. This investigation is based on the premise that devices occupying the same flow regime should have the same dimensionless force coefficients and that maintaining the same mesh density for every scale model within the same flow regime should produce equivalent force coefficients. The results from this investigation illustrated the significance of representing a prototype by a particular scale model size.

1.6.3 Turbulence scale effect

Turbulent flow is generally regarded as a challenge facing the energy industry. Turbulence is a three dimensional, unsteady, unpredictable flow with strong vorticity and has a range of scale that increases with Reynolds number. Three identifiable turbulent scales have been used to characterise the turbulent energy spectrum: The integral length scale, the Taylor length scale and the Kolmogorov scale. The present study is concerned with the energetic, integral length scale of turbulence where the anisotropy of turbulence resides in the energy containing coherent structures. More information on coherent structures is presented in chapter 5.

Large scale turbulence is known to play a key role in hydrodynamic loading of structures and may result to premature structural fatigue and subsequent failure of devices due to its fluctuating nature. TCE technology draws analogy from the wind energy technology and it is known in wind energy generation that, significant departures from steady operating loads conditions occur in gusty conditions according to Harrison (39). One method used to simulate turbulence effects in wind energy systems is the Von Karman Spectra (VKS). However, it is known that the Von Karman spectra do not represent turbulence near the bottom topography adequately enough. An investigation of the suitability of the Von Karman spectrum on a complex terrain (40) confirms that intense topography effect cannot be model adequately by the Von Karman formulation. Nevertheless, the Von Karman spectrum is still commonly used because of consistency with the analytical expression for the correlations (41). To avoid or mitigate turbulence generated by the bottom topography in wind systems, wind turbine towers are built sufficiently high enough, amongst all other design considerations (39).

Conversely, in real operation, a tidal current energy conversion system is bounded by a free water surface which does not allow the freedom of space possible with wind energy systems also, the channel side walls and bottom bathymetry will induce unavoidable turbulence in the environment. It is

anticipated that the energetic large scale eddies associated with turbulence may have structural implication for a tidal current energy device when they interact. Therefore it is important to account or discount for the effect of large scale turbulent structures in device dynamic loading and performance during testing. Figure 1.8 illustrates an eddy interacting with a generic tidal turbine supporting monopile structure.

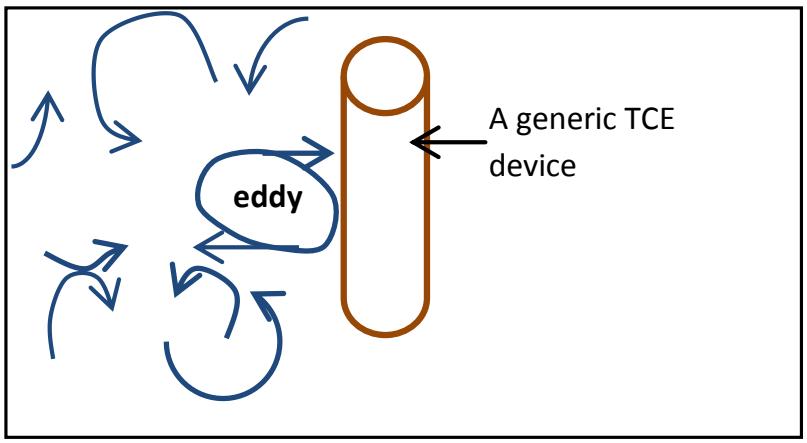

Figure 1.8: Eddy interacting with a structure

The need to understand the effect of ambient turbulence during model testing was highlighted by Bearman, (42) in wind tunnel experiments. He emphasised that turbulence should be accounted for before satisfactory scale model results are extrapolated and applied to prototypes. During the development of tidal current energy device performance protocol (43) the effect of turbulence on device performance and survivability was highlighted as a knowledge gap that could become a major issue with device performance and survivability. It is widely accepted that turbulence be accounted for in model testing of TCE device so that its effect can be incorporated in design and optimisation of energy device because it has the potential to progressively reduce the strength of material which could lead to device failure.

1.7 Relationship between dimensional and turbulence scale effects

The scale effect is related to basic engineering theories as illustrated in the Venn diagram in Figure 1.9 below.

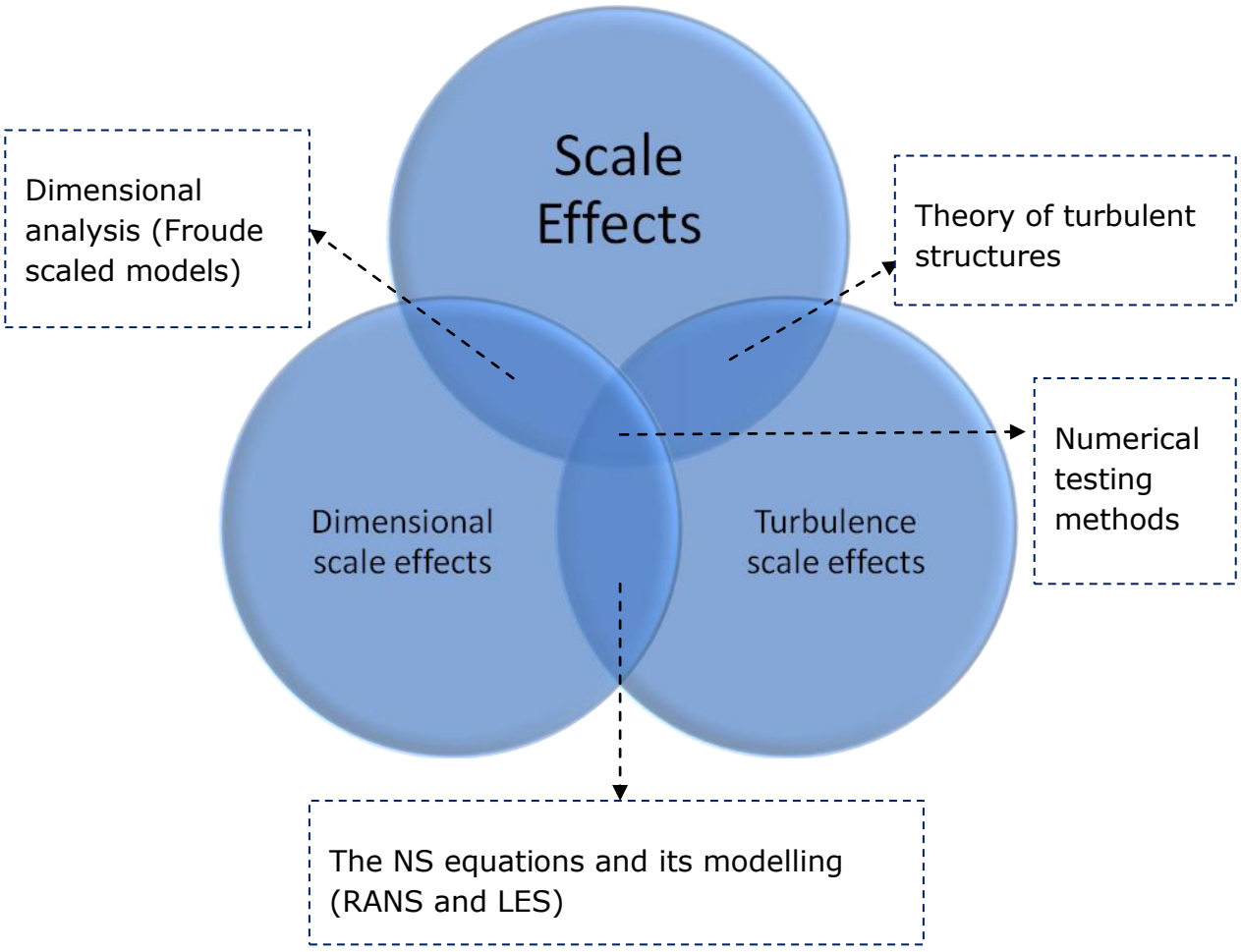

Figure 1.9:Venn diagram illustrating Scale effects.

Dimensional and turbulent scale effects are linked by the Navier-Stokes (NS) equations. The dimensional scale effects was investigated based on Froude scaled virtual models by solving the Reynolds Averaged Navier-Stokes (RANS) equations while the turbulence scale effect was investigated based on simulating the large scale turbulent eddies using the Large Eddy Simulation (LES) with real turbulent velocity profiles specified at domain inlet by solving the filtered NS equations.

1.8 Previous studies in the use of RANS and LES modelling technique.

Turbulence modelling using RANS approach had been the object of numerous studies. The k–epsilon ($k-\varepsilon$) turbulence model is a very popular and widely used turbulence model largely because, it is computationally economical with ability to obtain reasonable and accurate solutions with the available computer power in limited class of flows (44).

A majority of turbulence research has been a case by case examination and validation of existing turbulence models for specific problems. The $k-\varepsilon$ model has been used by Sangsan (45) in predicting aerodynamic force on a square cylinder when investigating the performance of conventional $k-\varepsilon$ models. The findings suggest that the $k-\varepsilon$ model successfully reproduced unsteady force coefficients without piling up turbulent kinetic energy near the forward stagnation.

In a validation study Doherty (27), used different RANS turbulence closure models to predict the torque and power generated by a turbine. The results showed that good correlation was achieved between the measured data and the CFD results in terms of trend. One of the models employed in the comparative studies was the Reynolds Stress Models (RSM) with anisotropic abilities. It was observed that RSM and the realisable $k-\varepsilon$ turbulence models compared best globally with flume experiment results.

In a comparative study between LES and RANS models of turbulent air flow past a surface mounted cube by Rodi (46), it was evident that, the turbulent fluctuations were severely under predicted in all RANS calculations, the low values were attributed to the low frequency variations of the shedding motion due to 3D effect. LES picked up motions from the 3D effect, and in general gave a better simulation of the flow details with a higher computational cost in terms of time.

Turbulence is a three dimensional phenomenon that cannot be credibly accounted for in RANS calculation (47).The ability of LES to pick up 3D effect suggests a reason for its use in investigating the effect of turbulent coherent structures in this present study. The lower cost RANS methodology was used to determine mean force coefficients in investigating dimensional scale effect because it is suitable to predict some mean flow quantities.

1.9 Research Aims and Objectives

As a consequence of the challenges expressed in section 1.6, the research aim to investigate scale effects resulting from testing a monopile support structure using CFD and ADCP instrument for site data acquisition based on the following enumerated objectives.

Objectives

Specifically, five objectives are logically outlined to achieve the overall aim of the project.

1 Investigate dimensional scale effect based on four virtual Froude scaled models using RANS numerical simulation.

2. Deploy an Acoustic Doppler Current Profile (ADCP) instrument at the Firth of Forth, Scotland UK to acquire tidal current velocity profiles required for input to numerical simulation domain.

3. Analyse the data acquired with the ADCP from the Firth of Forth Scotland, UK.

4. Simulate and study turbulent structures in an empty open channel with the aid of the acquired ADCP data using LES.

5. Investigate the effect of large scale turbulent structures on a monopile rigidly fixed to the bottom of an open channel with a flat bed.

1.10 Thesis overview

Chapter 1.0

Chapter 1 contains an overview of the fundamental drivers of renewable energy, set targets to produce electricity from renewable energy sources, examples of currently considered tidal current energy devices, support structures and testing methods with their inherent challenges. Justification for the method employed in the present study and the project objectives are also included.

Chapter 2.0

The general methodology for investigating the listed objectives in chapter 1 is presented. It begins with a flow chart describing the process used to achieve the project objectives. It includes a summary of numerical modelling techniques and the experimental set up for acquiring turbulent velocity profiles from the Firth of Forth using the ADCP.

Chapter 3.0

This chapter reports the results from investigating similarity between Froude scaled models occupying the subcritical flow regime. It explains the significance of dimensional scale effect and the justification for numerically investigating scale effect in tidal current energy devices. It presents the scaling strategy used to evaluate the model dimensions with a description of the computational domain. The meshing strategies, including the size functions are explicit. Description of the boundary conditions and solution method are included. Empirical equations derived from investigating dimensional scale effects are presented. The use of the equations is limited to flows within the subcritical flow regime. A technical paper published from this study is attached as appendix B.

Chapter 4.0

This chapter reports the analysis of the ADCP data acquired from the Firth of Forth. The ADCP data were quality checked before analysis. Mean velocity

profiles and single realisations velocity profiles representing the flow at the Forth estuary were compared with theoretical velocity profiles. Some of the analysed ADCP data is included in the publications in appendix C and D.

Chapter 5.0

Results from simulating large scale turbulent structures suitable for testing energy devices are presented in chapter 5. Three simulation cases namely; the ADCP data simulation case, the uniform velocity and the $1/7^{th}$ power law simulation cases were compared against each other. The simulated flow fields were also compared with the qualitative description observed in flow in a natural environment. The resulting seabed drag coefficients were also compared with measurements carried out in some tidal current sites. Some results from this study have been published and presented in appendix C.

Chapter 6.0

The effect of the large scale turbulent structures simulated in the previous chapter on the drag coefficient of a monopile support structure, fixed and submerged in a tidal current is presented in chapter 6. The chapter discusses flow over structures and some wind tunnel test results previously carried out. The simulation results were benchmarked with simulation cases using theoretical velocity profiles and were also compared with published experimental results. The output from this chapter won a gold award in a poster competition at the SuperGen annual symposium in November 2010. Poster is appended as appendix D.

Chapter 7.0

Chapter seven contains the overall summary, conclusion and recommendation for further work followed by reference pages and appendixes.

Chapter 2.0

Approach and Methodology

2.1 Introduction

This chapter presents an overview of the methodology and approach taken to investigate dimensional and turbulence scale effects. The process basically consists of a combination of physical experiment for site data acquisition and numerical simulation of a generic tidal current turbine support structure represented as a monopile. The block diagram in Figure 2.1 below illustrates the process.

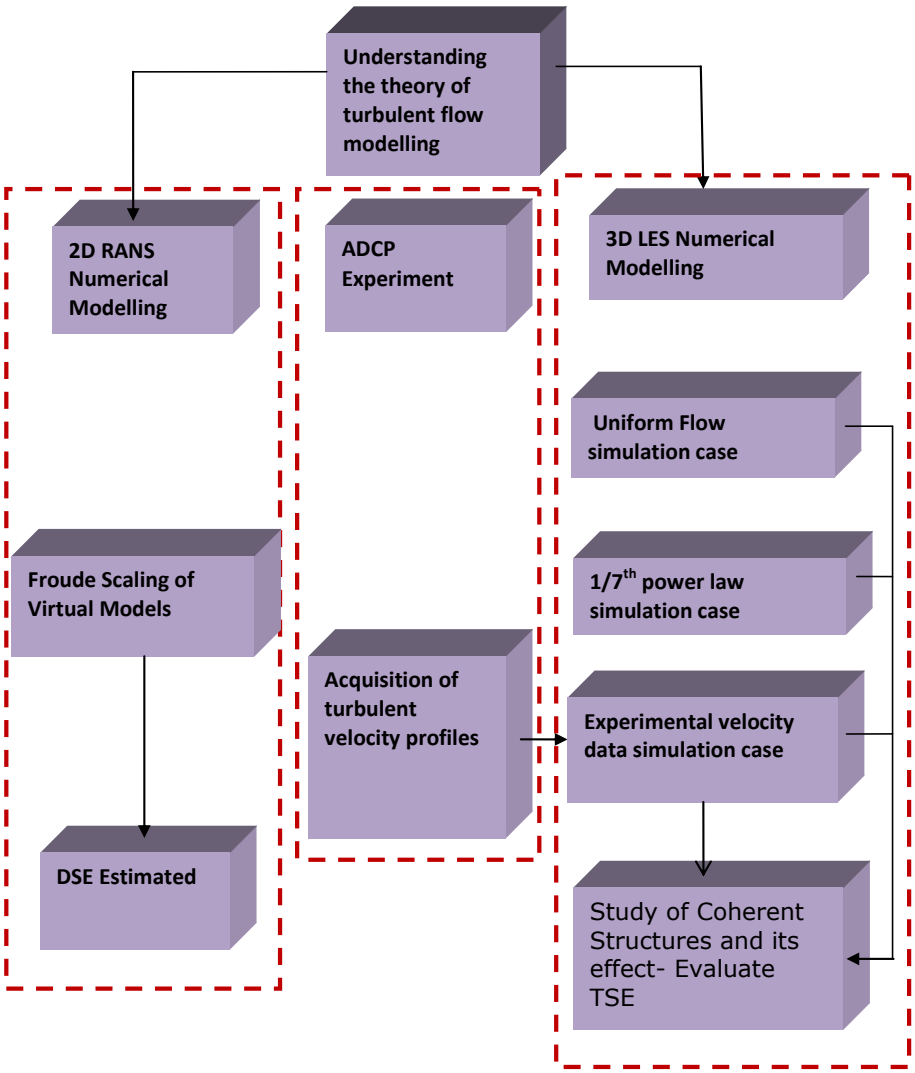

Figure 2.1:Sketch showing research components involved in the methodology.

A 2-dimensional numerical modelling approach was taken to investigate dimensional scale effects, because it is adequate to resolve mean values of the device force coefficients. The method is based on the Reynolds Averaged Navier - Stokes (RANS) modelling technique built on the turbulent viscosity concept introduced by Boussinesq (48).

A 3-dimensional numerical modelling technique was employed to investigate the effect of large scale turbulent structures on device hydrodynamic loading using LES. Turbulence is a multidimensional phenomenon and LES provides a platform for resolving the large scale energy containing eddies and it requires a 3-dimensional geometry to function in the commercial ANSYS software used for the simulation.

The physical experiment involves the use of ADCP instrument to acquire real turbulent velocity profiles from the Firth of Forth. The experimental velocity profile was used as input data into the 3-dimensional LES.

The 2-dimensional and 3-dimensional numerical modelling techniques were based on solving the NS equations expressed below in equation 2.1.

$$\frac{\partial u_i}{\partial t} + \frac{\partial u_i u_j}{\partial x_j} = -\frac{1}{\rho}\frac{\partial P}{\partial x_i} + \nu\frac{\partial^2 u_i}{\partial x_j \partial x_j} \qquad (2.1)$$

The background to the RANS and the LES modelling techniques lies in the computationally expense relating to solving the NS on complex flows such as those encountered in a tidal current channel using the Direct Numerical Simulation (DNS). Although the DNS technique is able to obtain tractable solution for turbulent flow processes, it is limited to simple flows with relatively small Reynolds number of say 10^3. The challenge in obtaining a tractable solution for higher Reynolds number flow gave rise to averaging the NS equations with a consequence of appearance of correlation terms called the Reynolds stresses (49). These stresses need additional equations known as turbulence models to close the averaged equations. Solving the additional equations together with the RANS equations, it became possible

to find approximate solution to turbulence flow problems. One of these equations, known as the k-epsilon turbulence model, integrated into the commercial ANSYS software has been used for the 2-dimensional numerical studies. The basics leading to the formulation of the k-epsilon turbulence model is summarily explained in what follows.

It has been previously mentioned that the RANS equations are based on the turbulent viscosity concept introduced by Boussinesq. The Boussinesq approach relates the Reynolds stresses to the mean velocity gradient.

$$-\rho\overline{u_i' u_j'} = \mu_t\left(\frac{\partial u_i}{\partial x_j}+\frac{\partial u_j}{\partial x_i}\right)-\frac{2}{3}\left(\rho k+\mu_t\frac{\partial u_k}{\partial x_k}\right)\delta_{ij} \tag{2.2}$$

ρ is the fluid density, $u_i' u_j'$ are the Reynolds stresses. $\frac{\partial u_i}{\partial x_j}+\frac{\partial u_j}{\partial x_i}$ is the mean velocity gradient. δ_{ij} is the kronecker delta defined as: $\delta_{ij}=1$ if $i=j$ and $\delta_{ij}=0$ if $i\neq j$ i and j takes the value 1, 2 or 3.

The turbulent viscosity μ_t is calculated from equation 2.2 below;

$$\mu_t = \rho C_\mu \frac{k^2}{\varepsilon} \tag{2.3}$$

k is the turbulent kinetic energy while ε is the turbulent dissipation rate. C_μ is a variable and methods for computing it can be found in (54).

The k – epsilon $(\boldsymbol{k-\varepsilon})$ turbulence model requires solving two transport differential equations: one for the turbulent kinetic energy and the other for the turbulence energy dissipation rate, $\boldsymbol{\varepsilon}$. The main reason for adopting the two equation model was that, it allows for calculating the length scale from a transport equation instead of prescribing it algebraically. This eliminates the difficulties encountered with complex geometries when using the earlier zero and one equation turbulence models. The two equations model solves

the problem of incompleteness of the one equation model and can produce reasonable results for complex flows (50). More detailed information of the RANS turbulence models based on the Boussinesq hypothesis can be found in (51-52).

2.2 Numerical methodology for 2D RANS modelling of a generic tidal current turbine support structure.

The k-epsilon $(k-\varepsilon)$ turbulence model has several variations which includes standard $k-\varepsilon$ turbulence model, the RNG turbulence model based on the Renormalisation Group theory and the realisable formulation. The realisable, non-equilibrium $(k-\varepsilon)$ turbulence numerical model was used to investigate dimensional scale effect presented in chapter 3. The realisable model is based on a new formulation of eddy viscosity and dissipation rate equation that ensures that, a mathematic constraint consistent with the physics of turbulent flow, allows the normal stresses to remain positive (53).

The transport equation for the realizable $k-\varepsilon$ turbulence model which solves for the Reynolds stresses are given by turbulent kinetic energy, k and the turbulent dissipation, ε as:

$$\frac{\partial}{\partial t}(\rho k)+\frac{\partial}{\partial x_j}(\rho k u_j)=\frac{\partial}{\partial x_j}\left[\left(\mu+\frac{\mu_t}{\sigma_k}\right)\frac{\partial k}{\partial x_j}\right]+G_{k+}G_b-\rho\varepsilon+S_k \qquad (2.4)$$

$$\frac{\partial}{\partial t}(\rho \varepsilon)+\frac{\partial}{\partial x_j}(\rho \varepsilon u_j)=\frac{\partial}{\partial x_j}\left[\left(\mu+\frac{\mu_t}{\sigma_\epsilon}\right)\frac{\partial \epsilon}{\partial x_j}\right]+\rho C_1 S\varepsilon-\rho C_2\frac{\varepsilon^2}{k+\sqrt{\nu\varepsilon}}+C_{1\varepsilon}\frac{\varepsilon}{k}C_{3\varepsilon}G_b \qquad (2.5)$$

respectively where;

$$C_1=max\left[0.43,\frac{\eta}{\eta+5}\right],\qquad \eta=S\frac{k}{\varepsilon},\qquad S=\sqrt{2S_{ij}S_{ij}}$$

G_k is turbulence kinetic energy generation term, G_b is the generation of turbulence due to buoyancy S_k and S_ε are source terms. S is a scalar measure of deformation and S_{ij} is the mean strain rate tensor. The model constants: $C_{1\varepsilon}$, C_2, σ_k and σ_ε are 1.44, 1.9, 1.0 and 1.2 respectively. The constant have been established to perform well for certain canonical flows (54). The flow in this study is assumed incompressible without buoyancy effects. The model transport equation for *k* is derived from the exact NS equation and the model equation for ε is based on the dynamic equation of the mean square vorticity fluctuation.

The kinetic energy, the dissipation rate as well as the Reynolds averaged equation were solved to simulate the flow past a Froude scaled models. Details of the dimensioning strategy using the Froude scaling criterion (55), meshing strategy and problem/physics set up are presented in chapter 3. The RANS methodology was applied to simulate a generic tidal current turbine support structure represented as a monopile in a 2-dimensional horizontal plane of a tidal current channel.

2.3 Numerical methodology for LES

Although successes have been attained with the RANS modelling techniques, a major drawback in all RANS turbulence models lie in the fact that the models average out the effect of the large scale coherent structures existing in a turbulent flow. This is significant because the small scale eddies behave differently from the large scale eddies. The small scale eddies are nearly isotropic and have a universal behaviour while the large scale eddies behaviour depends on the problem geometry, body forces and boundary conditions. The energy and anisotropy of turbulence are contained in the large scale eddies which dominates the transfer of momentum. The LES is a numerical approach that separates the large scale from the small scale eddies using a filtering time dependent NS equations. It consists of eliminating scales of turbulence smaller than the mesh size by using a low pass filter on the time dependent NS equations so that, what is left of the

filtering operation governs the evolution of the large scales of turbulence. The basic concept of LES was laid in the work of Smagorinsky (56) in the early 1960's. The LES technique allows the prediction of instantaneous and mean turbulence quantities of higher Reynolds number flows. LES has the advantage that a resolution of the large scale is possible while the small scales are modelled (57) by a cheaper subgrid scale model. The Fourier cut off filter was used in the ANSYS software employed for this study. The filtered continuity and Navier-Stokes equations for an incompressible flow are expressed in equations 2.6 and 2.7 below;

Continuity equation

$$\frac{\partial \bar{u}_i}{\partial x_i} = 0 \tag{2.6}$$

Momentum equation

$$\frac{\partial \bar{u}_i}{\partial t} + \frac{\partial \bar{u}_i \bar{u}_j}{\partial x_j} = \frac{\partial \sigma_{ij}}{\partial x_j} - \frac{1}{\rho}\frac{\partial \bar{p}}{\partial x_i} - \frac{\partial \tau_{ij}}{\partial x_j} \tag{2.7}$$

σ_{ij} is the stress due to molecular viscosity defined by;

$$\sigma_{ij} \equiv \left[\mu\left(\frac{\partial \bar{u}_i}{\partial x_j} + \frac{\partial \bar{u}_j}{\partial x_i}\right)\right] - \frac{2}{3}\mu\frac{\partial \bar{u}_i}{\partial x_i}\delta_{ij} \tag{2.8}$$

where *i* and *j* in tensor notation takes the values *1, 2* or *3* and δ_{ij} is a unit tensor and τ_{ij} is the subgrid scale stress defined by;

$$\tau_{ij} \equiv \rho\overline{u_i u_j} - \rho\bar{u}_i\bar{u}_j \tag{2.9}$$

The small scale eddies were modelled by dynamic Smagorinsky–Lily subgrid scale model (58). The subgrid scale model is also built on the turbulent viscosity concept based on the Boussinesq hypothesis used for RANS turbulence models.

The model equation for the turbulent viscosity is given by;

$$\mu_t = \rho L_S^2 |\bar{S}| \tag{2.10}$$

Where the sub grid length scale L_s, is given by;

$$L_s = min(\kappa d, C_s \Delta) \tag{2.11}$$

$$|\bar{S}| \equiv \sqrt{2\bar{S}_{ij}\bar{S}_{ij}} \tag{2.12}$$

$$\bar{S}_{ij} \equiv \frac{1}{2}\left(\frac{\partial \bar{u}_i}{\partial x_j} + \frac{\partial \bar{u}_j}{\partial x_i}\right) \tag{2.13}$$

$\bar{S}_{ij}$ is the rate of strain tensor, κ is the von karman constant, d is the distance to the closest wall, C_s is the Smagorinsky constant and Δ is the local grid scale computed according to the volume of the computational cell using;

$$\Delta = V^{1/3} \tag{2.14}$$

The dynamic model constant C_s is not universal, but dynamically computed taking up values based on the information provided by the resolved scales of motions (58-59). The concept of evaluating the model constant is based on applying a second (test filter) whose filter width is twice the grid filter

width to the governing equations. The information based on the difference between the flow fields resolved in both filter cases is used to compute the model constant. The computed model constant varies in space and time. To avoid numerical instability, the model constant is clipped at zero and 0.23 (54).

The LES methodology was applied to three simulation cases, each distinguished by its characteristic inlet velocity profile. Two of the simulation cases are benchmark studies. The third simulation case involved integrating ADCP acquired velocity profile from a real tidal site to the simulation domain inlet. LES was first carried out on an empty channel to investigate the behaviour of the resulting flow fields and to demonstrate the differences existing between flow fields generated using theoretical velocity profiles and experimental velocity profiles as input conditions. Secondly, to simulate flow past a monopile support structure fixed to the channel bed to investigate the effect of the resulting ambient flow on the monopile drag coefficient. The meshing strategy including the use of size function, and the problem set up in ANSYS are reported in chapters 5 and 6.

2.4 ADCP experiment methodology

The SonTek/YSI ADP was employed to measure tidal current velocity profiles at the Firth of Forth near the Isles of May. The ADCP was deployed on the seabed on the 20th of July 2010 at 12.00pm and was retrieved on the 11th of August at 14:40 pm. The ADCP was deployed at location 56^{o} 10.642'N, 2^{o} 32.359'W in a 53 meter depth of water.

2.4.1 ADCP hardware and principle of operation

A physical view of ADCP instrument set up with its supporting frame before deployment is shown in Figure 2.2 below. *The ADCP sensor* is supported on a gimbal. It consists of three acoustic transducers for three dimensional profiling and receiver electronics. The transducers are spaced with equal azimuthal radial spacing of 120^{o} which point at 25^{o} from the instrument's

vertical axis. The ADCP processor sends and receives signal from the ADCP sensor and perform calculations to compute velocity profiles based on the Doppler Effect principle. The Doppler Effect is described as a change in the observed frequency or wave length of sound waves transmitted from the transducer relative to the suspended moving water particles.

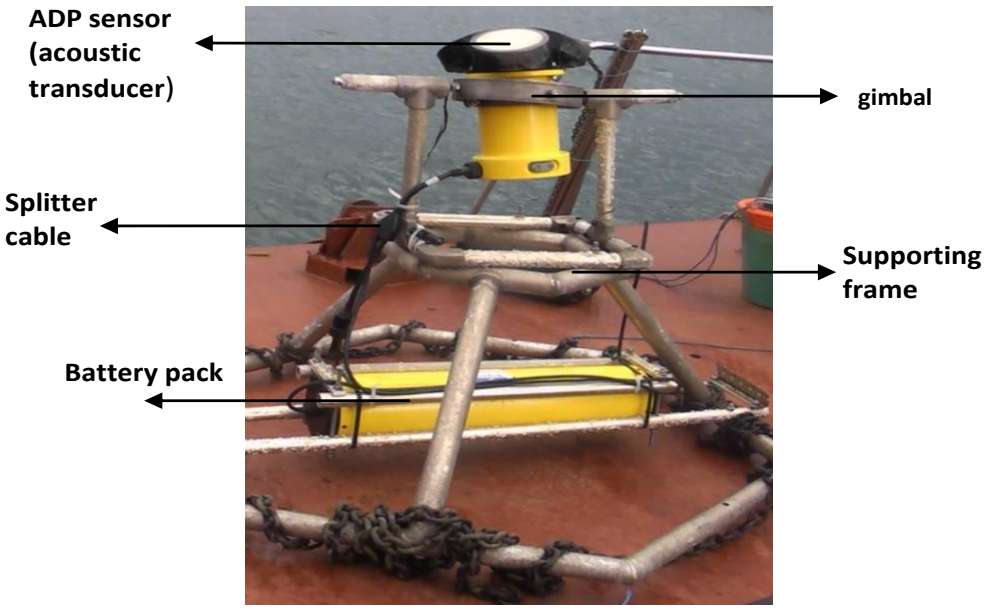

Figure 2.2: A three beam SonTek/ YSI ADP.

The change in frequency $F_{doppler}$ known as the Doppler shift is calculated by using;

$$F_{doppler} = -2F_{sound}\frac{V}{C_{sound}} \tag{2.15}$$

Where F_{sound} is the frequency of sound waves, $V_{particles}$ is the relative velocity of the suspended water particles and C_{sound} is the speed of sound in m/s. The suspended water particles are form of planktons also known as scatterers. The scatterers reflects sound back to the transducer after being hit by an acoustic beam transmitted from the ADCP. The water particles are assumed to move with the same velocity as the water velocity on the average. It is desirable to have sufficient particles in the water which is mostly the case in tidal currents sites due to sedimentation processes.

The ADCP measures the velocity component parallel to the acoustic beams and one beam is required for one velocity component so that a three beam instrument have the ability to measure three velocity components. The velocity along each respective beam is converted to the east, north and up velocity components using trigonometric relations. A limitation that lies with the use of trigonometry relation to evaluate the east, north and up velocity components is that, the beams take measurements at different location which implies that the current velocity have been assumed to be the same at these locations. Water currents homogeneity has been a reasonable assumption in flow in rivers, oceans and estuaries etc.

The computed water currents velocity profiles and associated information is recorded by a circuit board within the processor. *A splitter cable* connects the ADCP to the battery pack for autonomous deployment. *A power and communication cable* (not shown) connects the ADCP to a computer used for instrument configuration before deployment, and downloading of data after instrument retrieval.

2.4.2 ADCP configuration and set up

The sketch, Figure 2.3 (not drawn to scale), illustrates the terminologies used in describing the ADCP set up configuration. The vertical water column above the seabed beginning from the ADCP transducer head was divided

equally into 50 depth cells or bins excluding the blanking distance. The third beam is excluded from the sketch for clearer illustration. The top of the transducers was approximately 1 meter above the seabed. No measurement is possible from the seabed up to bin 1. This presents one limitation of the ADCP. From this set up, the distance between seafloor and the start of the first bin is approximately 2m because the blanking distance was set for 1m. A bin size (cell size) of 1m was specified because it is a reasonable value that ensures insignificant noise in the recorded data. The blanking distance was required for effective recovery of instrument electronic and transducers from transmit pulse, during the alternate sending out and receiving signals before data for the next profile is acquired. With

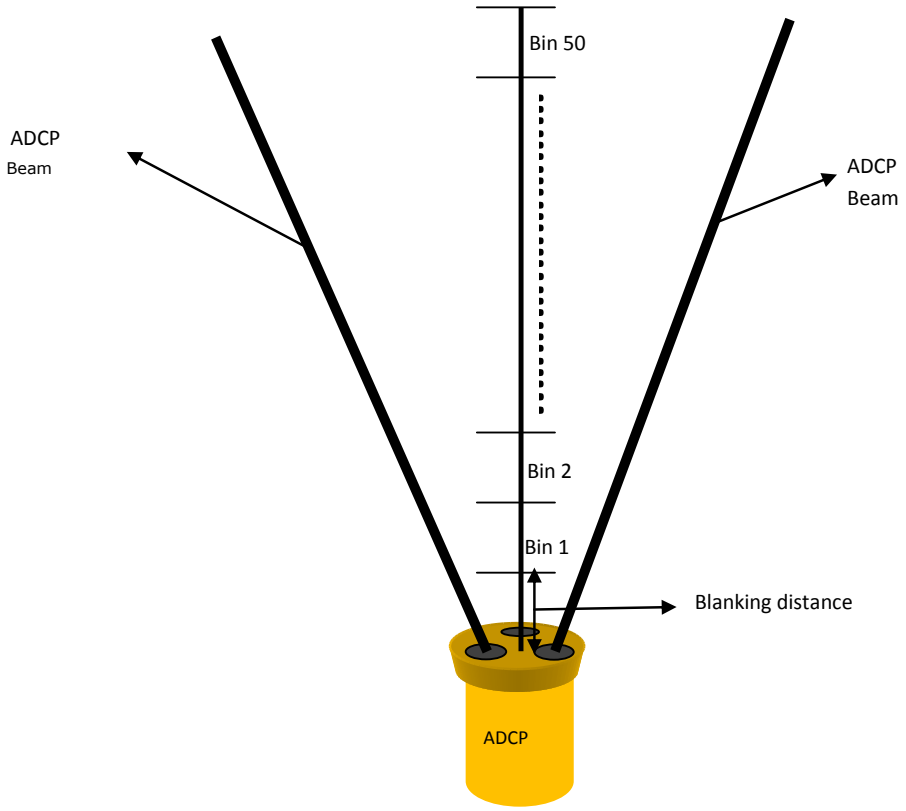

Figure 2.3:Illustration of ADCP set up configuration.

this set up and configuration, velocity profile samples were acquired for 23 days with an autonomous sampling setting, averaging one sample over 1

minute every 10 minutes for every one profile. A total of 3185 turbulent velocity profiles were acquired.

No instrument calibration except compass calibration was required. The data were recorded by the ADCP internal recorder. The recorded data was downloaded for quality checks and analysed. All data were sampled over the water column above the ADCP. Results are reported in chapter 4. The ADCP user set up and configuration output from the ADCP recorder is shown in Table 2.1 below;

Table 2.1: ADCP user set up and configuration information

Default Temperature	20.00 deg C
Default Salinity	34.50 ppt
Default Speed of Sound	1520.90 m/s
No. of Cells	50
Cell Size	1.00 m
Blank Distance	1.00 m
Sensor Depth	0.00 m
Temperature Mode	MEASURED
Averaging Interval	60 s
Profile Interval	600 s
Ping Interval	0.00 s
Burst Mode	DISABLED
Coordinate System	ENU
Magnetic Declination	0.00
Out Mode	AUTO
Out Format	ASCII
Recorder Enabled	ENABLED
Recorder Mode	NORMAL
Deployment Mode	ON
Deployment Name	JULY
Deployment Start Date/Time	2010/07/20 12:00:00

2.4.3 ADCP deployment location

The Forth estuary is 93km long and extends from Stirling to join the North Sea, with the Isles of May lying at its entrance. Figure 2.4 show the map of the Forth estuary and Figure 2.5 show the precise location where the ADCP was deployed.

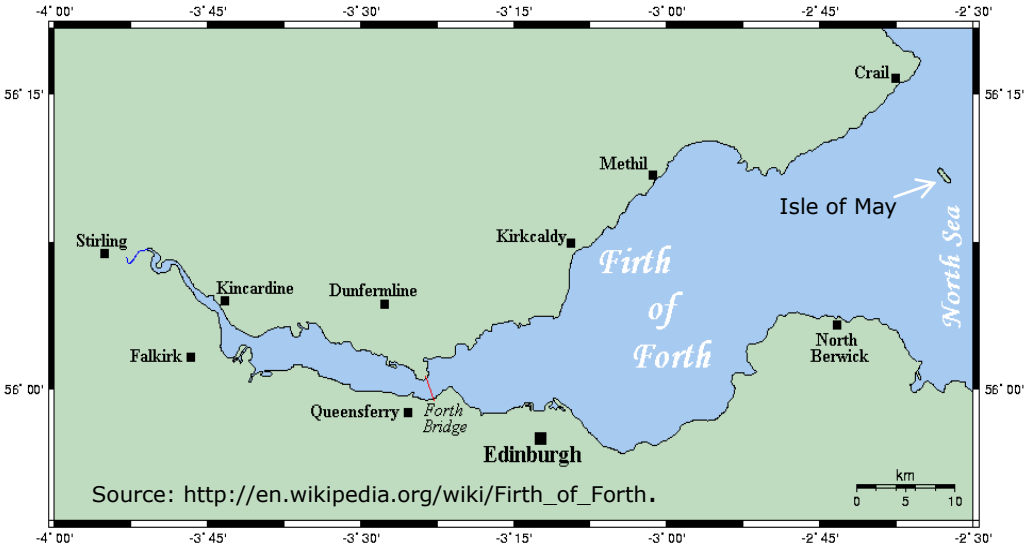

Figure 2.4:Map of the Firth of Forth.

Figure 2.5:ADCP deployment location.

It is reported that the bathymetry of the upper Forth varies and changes with time. These changes occur naturally and continuously giving an indication of high degree sedimentation processes caused by the flow of tidal currents. Further downstream, the estuary increases in width and the bathymetry is more stable. This could be a potential site to install a tidal current turbine because of its nearness to community.

Chapter 3.0

Numerical Investigation of Dimensional Scale Effects of a Monopile.

3.1 Introduction

This chapter investigates dimensional scale effects in numerical modelling of Froude scaled monopiles of different magnitude and a fixed scale monopile with varying fluid velocity occupying the subcritical flow regime. Predicting the behaviour of any engineering prototype requires similarity between scale model and prototype is established. This occurs when certain scale laws and conditions are met. The scale laws can be derived by non-dimensionalising the continuity and the Reynolds Averaged Navier-Stokes (RANS) equations that governs fluid flow. The procedure for non-dimensionalising the RANS equations with associated assumptions are explained in (55). Results from non-dimensionalising the equations suggest that complete similarity is established when the Froude, Reynolds, Euler and the Struohal numbers have the same value in model and prototype. In practice, it is difficult to maintain similarity of the Reynolds number in a free surface flow. Therefore it is customary to assume the Froude similarity criterion as the most important parameter. Scaling based on this assumption introduces the Reynolds scale effect even though viscosity becomes important near the wall of any device. From the foregoing, it implies that scale effects in testing of devices are a phenomenon we must live with.

Scaling is a known challenge from the testing of hydraulic structures and ship building where scale effect has been used as a term that indicates the implications of representing a prototype with a scale model. The scale effect phenomenon is responsible for the occurrence of the drag crises in flow over a cylinder because of the difficulties in scaling the developing boundary layer due to flow transition (60).

As tidal current devices grow in size and following the enormous numerical simulations that tidal current turbines and support structures undergo and the custom of scaling based on the Froude scaling criterion for free surface flow, it has become necessary to understand dimensional scale effect associated with numerical simulation and to quantify them where possible.

Dimensional scale effect investigation in this study is based on the premise that, different sizes of scaled monopiles occupying the same flow regime would have the same force coefficients irrespective of their Reynolds number, Re and that geometries having the same mesh density with same meshing size functions should produce the same results. The analysis of the scale model results will demonstrate the extent of similitude of numerically simulated models.

In physical modelling of hydraulic structures, scale effects have been widely researched, (38) and (60). In numerical modelling, attempts have been made to investigate dimensional scale effect for example, Young and Byeong (61) carried out a numerical analysis of wind turbine scale effects, on several virtual scale model wind turbines, by solving the three dimensional Navier - Stokes equations with RANS realizable turbulence model. The results were validated by comparing with the performance of an existing wind turbine. A correction method was proposed by Young and Byeong (61) which showed reasonable agreement between scaled model and full scale wind turbine only in the linear torque region. In another study by Starke (62) the scale effects on ship wave systems was carried out using RANS method for a steady, incompressible flow. Although, these studies have no direct application for a fully submerged tidal current energy device they do however, indicate that scale effect can be and have been estimated in numerical modelling.

A monopile submerged in tidal currents and fixed to the seabed is subject to both steady and unsteady time dependent forces. An unsteady incident flow acting on a monopile exerts an unsteady drag force parallel to the incident

flow direction and a lift force transverse to the incident current direction. A monopile can be modelled as a fixed vertical circular cylinder. A cylinder is known as a bluff body with usually a high drag coefficient compared with the lift force coefficient. Flow around a smooth circular cylinder has been extensively studied mainly in wind tunnel experiments with low stream turbulence level for force measurements with results published in literatures (63) and (64).

Flow around a cylinder has been categorised into regimes characterised by the Reynolds number; beginning with the creeping flow with Reynolds number, Re less than 5 to the transcritical flow with $Re > 4 \times 10^6$ which represent flows of practical engineering interest. Between these extremes lies the subcritical flow regime with Re range $300 < Re < 3x10^5$. Amongst the numerous studies on flow over cylinders, the physical experimental results of Schewe (65) were used to validate the numerical simulation result in this present study. The flow induced forces on the monopile can be non-dimensionalised to yield the drag coefficient C_D, the lift coefficient C_L, and the pressure coefficient C_p given as;

$$C_D = \frac{D}{\frac{1}{2}\rho u^2 A} \qquad (3.1)$$

$$C_L = \frac{L}{\frac{1}{2}\rho u^2 A} \qquad (3.2)$$

$$C_p = \frac{p - p_a}{\frac{1}{2}\rho u^2} \qquad (3.3)$$

Where D, L, and p are the drag, lift and pressure force respectively. ρ is the density of water, u is the mean current velocity, A is the frontal area of monopile facing the incident flow direction and p_a is the static pressure.

3.2 Froude scaling of virtual models

The Froude scaling criterion is used to evaluate the dimensions of four virtual scale models expressed in scale ratios as; 1:90, 1:70, 1:50 and 1:30 based on a virtual monopile prototype of 5m diameter submerged in a stream of tidal current flowing at 1m/s. The Froude transfer relation is given in equation (3.4) below as;

$$\frac{u_p}{u_m} = \sqrt{\frac{l_p}{l_m}} \tag{3.4}$$

The Froude transfer relation states that the velocity ratio of prototype to model equals the square root of their length scale ratio. The subscripts p and m stands for prototype and model respectively. Based on this relation, the Froude number of the four models and the prototype should be equal to ensure similitude between the scale models and prototype. The equation used to evaluate the Froude number is given in equation 3.5 below as;

$$\mathrm{Fr} = \frac{u}{\sqrt{gl}} \tag{3.5}$$

Where u is the velocity of fluid, g is the acceleration due to gravity and l is based on the height of each domain. The Reynolds number Re is expected to vary and is calculated from the formula given in equation 3.6 below;

$$Re = \frac{uD_m}{\nu} \tag{3.6}$$

Where $\boldsymbol{\nu}$ is the kinematic viscosity with value of 1.004 x 10^{-6} m^2/s at sea water temperature of 20°C. Based on the fluid viscosity and acceleration due to gravity of 9.8m/s, the length and velocity scales of the virtual models and prototype were evaluated. The associates Reynolds and Froude numbers for each scale model were also calculated based on the device diameters and the domain height respectively. The results are presented in Table 3.1 below;

Table 3.1: Froude scaled models dimensions

Length scale ratio	1:1	1:30	1:50	1:70	1:90
Domain Size	120 x 80	4 x 2.66	2.4 x 1.6	1.7 x 1.14	1.33 x 0.88
Velocity scale (m/s)	1	0.18	0.14	0.12	0.11
Monopile diameter (m)	5	0.17	0.10	0.07	0.056
Froude number	0.04	0.04	0.04	0.04	0.04
Reynolds Number	$5x10^6$	$3X10^4$	$1.4x10^4$	$8.4x10^3$	$6x10^3$

3.3 The Physical Model

The physical model is illustrated in Figure 3.1. It represents the simulation domain for each Froude scaled model. Each physical model consists of a monopile fixed to the channel bed and viewed in a 2 dimensional horizontal

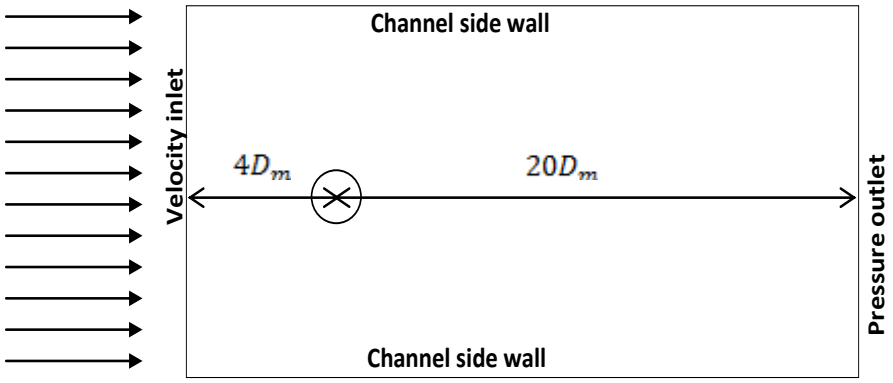

Figure 3.1: A sketch of a virtual physical model.

plane. It has a velocity inlet located at 4 monopile diameters from the center of the monopile and a pressure outlet located at 20 monopile diameters downstream the centre of the monopile. The side channel walls are each located 8 cylinder diameters from the channel centre.

3.3.1 Physical model behaviour.

The result from investigating flow over a cylinder by Schewe (65) in a wind tunnel experiment adequately describes the behaviour of the scale models. The experiment was carried out in a pressurized wind tunnel that could reach a maximum velocity of 38m/s on a cylinder of diameter 0.06m. He varied the Reynolds number by varying the velocity of air in the wind tunnel. The minimum Reynolds number obtained for Schewe's experiment was 10^4. The behaviour of the model was described in terms of drag coefficient, lift coefficient and the Strouhal number therefore, the wind tunnel experimental results provides data against which the numerical simulation results were validated.

Although, the physical properties of water are different from those of air, the flow over a monopile or cylinder in a wind tunnel is comparable to that in the water channel when considering dimensionless number such as Reynolds number. This justifies the reason for validating the numerical results in this study with wind tunnel experiments. Details of the numerical

simulation results and validation with experimental data are presented in section 3.4.

3.3.2 Meshing strategy and problem set-up

The first goal in the meshing procedure was to build a mesh that produces the best results comparable to the known drag coefficient of a cylinder using the 1:50 scale model. Following from satisfactory numerical results of the 1:50 scale model, the meshing strategy used for the 1:50 scale was then applied to the remaining scale models.

Firstly, the equivalent number of nodes around the prototype diameter was evaluated to be 4000 based on 80 nodes used for the 1:50 scale model using the simple proportion formula expressed in equation 3.7.

$$\frac{D_p}{D_m} = \frac{N_p}{N_m} \tag{3.7}$$

D_p is the prototype diameter, D_m is the model diameter, N_p is the number of nodes on the prototype and N_m is the number of nodes on the scale model.

Based on the evaluated value of 4000 nodes on the prototype, the number of nodes around the remaining scale models was computed and tabulated in Table 3.2 below.

Table 3.2: number of nodes specified for each monopile scale.

Length scale ratio	1:1	1:30	1:50	1:70	1:90
Monopile diameter (m)	5	0.17	0.10	0.07	0.056
No. of nodes on monopile	4000	136	80	56	45

Each monopile was meshed according to the number of nodes calculated for each diameter. Figure 3.2 show a mesh section around the monopile.

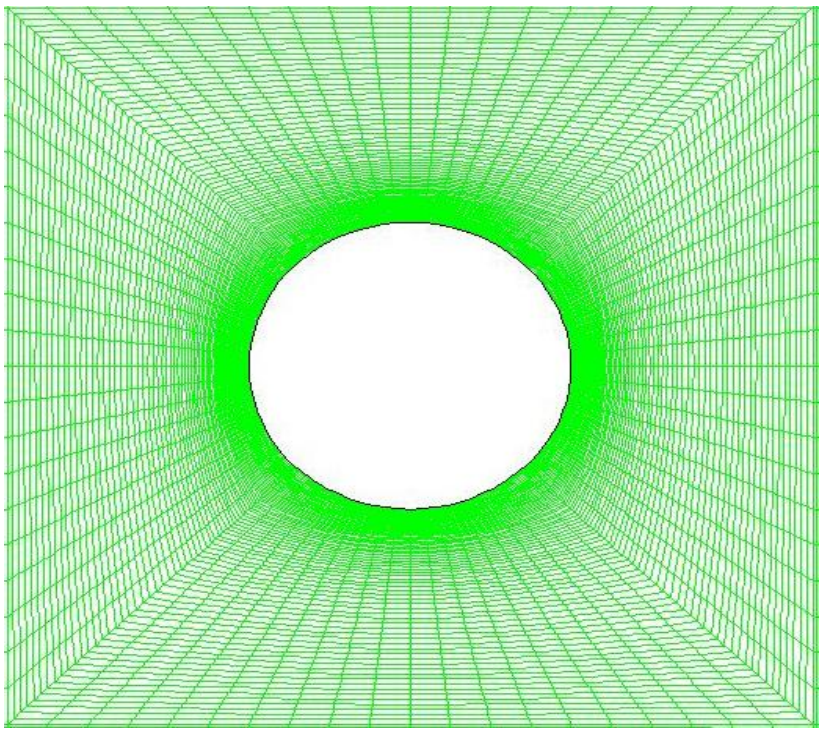

Figure 3.2: 2-D mesh structure around a monopile in a horizontal plane.

A fixed size function of 0.0001 with a growth rate of 1.05, was applied on the monopile. A structured mesh, made of quad elements was constructed using the Gambit software available in the commercial ANSYS simulation package. The applied size function and the meshing strategy ensures that the developing boundary layer that grows in thickness in real flow, as the fluid enters the boundary and leaves at the exit is not only achieved but also similar in shape for all four models. Also, a stretched grid immediately following the monopile will catch more of the essentials of the actual boundary layer in comparison to a uniform mesh (66).

The pressure-based time dependent Navier-Stokes equation was discretisized using the finite volume method and the viscous two equation realisable k-epsilon $(k-\varepsilon)$ turbulence model discussed in chapter two. A non-equilibrium wall function in conjunction with the turbulence model was employed for the simulation. The non-equilibrium wall function is recommended (67) for flow with pressure gradients involving flow separation and it is able to calculate the cell averaged turbulence kinetic

energy production and dissipation in wall neighbouring cells in the flow. Thus it is suitable for flows that depart from the local equilibrium theory of turbulence.

The solution method was based on a second order implicit transient formulation with the pressure-velocity coupled scheme. The second order transient formulation offers better accuracy compared with the first order formulation.

3.3.3 Boundary specification

Wall boundaries – The monopile and the channel side walls are modelled as stationary walls. A no slip boundary shear condition and a roughness constant of 0.5 are applied at the monopile and the channel side walls where $u = v = 0$ for each scale model. The no slip boundary condition ensures that there is friction due to the presence of the walls.

Inlet conditions – A velocity inlet varying as each scale model as presented in Table 3.1 was specified for each respective scale model. A turbulent intensity, I of 0.01 % (a value lower than the acceptable value in wind tunnel testing) as recommended in (49) is specified for the four scale models to ensure that the ambient turbulent intensity is the same.

$$k_{inlet} = \frac{3}{2}(u_{inlet} I)^2 \tag{3.7}$$

$$\varepsilon_{inlet} = C_{\mu}^{\frac{3}{4}} \frac{k^{\frac{3}{2}}}{l} \tag{3.8}$$

The turbulent kinetic energy, k_{inlet} and dissipation rate, ε_{inlet} expressed in equations 3.7 and 3.8 above are calculated based on the specified turbulent

intensity. l represents the domain size and C_μ is a variable and methods for computing it can be found in (54).

Outlet boundary condition -A gauge pressure of zero Pascal was specified at the outlet boundary.

3.4 Results and Discussion.

Critical flow parameters resulting from the numerical simulations were compared with Schewe's (65) experiment and presented in Table 3.3 below;

Table 3.3: Numerical results compared with Schewe's experimental result.

Parameters	Schewe's results	Length scale ratio			
		1:30	1:50	1:70	1:90
Re	300 < Re < 3 x 10^5	3x10^4	1.4x10^4	8.4x10^3	6x10^3
Mean C_D	1.2	0.99	1.06	1.12	1.18
r.m.s value of C_L	0.38	0.25	0.37	0.47	0.48
St	0.2	0.25	0.25	0.23	0.20
		Present study (numerical simulation results)			

The four models investigated in this study are within the sub critical flow regime which has Reynolds numbers in the range 300 < *Re* < 3 x 10^5. Specifically, the range of Reynold number simulated in this study is 6x10^3 < *Re* < 3x10^4. Flow within this regime is characterized by a completely turbulent wake and a laminar boundary layer separation.

From Schewe's experimental data, the calculated mean drag coefficient C_D has an approximate value of 1.2; the root mean square of the lift coefficient C_L has a maximum value of 0.38 in the sub-critical regime while the Strouhal number, *St* was around 0.2 with very minimal scatter. In the

present study, the mean drag, the lift coefficient and the Strouhal number were extracted from the steady state values of the drag and lift convergence monitors. Globally, the results are satisfactory and comparable to Schewe's experimental result, with the 1:90 scale model results having the best agreement with Schewe's experimental value of 1.2 and 0.2 for the drag coefficient and Strouhal number respectively. The lift coefficient of the 1:50 scale model, agrees best with the work of Schewe. It could naturally be expected that the lift coefficient for the 1:90th scale model results should agree best with Schewe's data since both the Strouhal numbers and the drag coefficient fits better however, it was not so from the simulation results. The reason for this is not immediately clear but could be attributed to numerical errors. The behaviour of the lift coefficient may require further investigation.

The simulated Strouhal number, St was evaluated using equation (3.9) below;

$$St = \frac{fD_m}{u} \tag{3.9}$$

Where f is the frequency of vortex shedding. D_m and u are the monopile diameter and velocity scale for each model respectively. The frequency of vortex shedding f is the inverse of the time interval between two troughs or two crests of the lift coefficient monitor plot after iteration have reached a steady state. It is expected from physical experiment that the four models would have the same value of force coefficients since they are within the same flow regime that have the same boundary layer separation and wake behaviour.

However, the numerical simulation results clearly show a deviation from the wind tunnel results as the model scale increases. The drag coefficient values

for the wind tunnel test results were reported as having a constant of about 1.2 but the numerically simulated drag coefficient varies the scale of the model. The values of the Strouhal number show an increasing trend.

From the numerical simulation results, it can be stated that the sensitivity of the k-epsilon turbulence model to changes in boundary layer separation and wake behaviour in relation to model size is different from physical experiments. Further work is needed to investigate the reasons why numerical model are unable to reproduce wind tunnel experimental data for all scale model sizes within the subcritical flow regime.

To underpin the variance of drag coefficient in each scale model in the present study, the simulation results were checked against numerical simulation studies carried out by Tutar (68) on flow around a cylinder based on a Reynolds number of 1.4×10^5. This Reynolds number value falls within the sub critical flow regime, and represents 1:10 scale model in this present study. Tutar (68) found the drag coefficient of the cylinder to be 0.82 which agrees with the trend demonstrated in this present study.

In what follows, empirical equations that can be used to estimate scale effects resulting from numerical simulation of scale models of different magnitude including mean pressure coefficient analysis are presented.

3.4.1 Estimation of dimensional scale effect on Froude scaled models

The simulated monopile drag force coefficient in Figure 3.3 has shown that it deviates from the experimental value as the model size increases. The differences between the experimental and the simulated drag coefficient e_{C_D} are shown in Table 3.4 as scale errors. The drag coefficient errors are expressed as a function of dimensionless length K_L scale normalised by the scale of the prototype. $K_L = D_m/D_p$ where D_m is the diameter of the model and D_p is the diameter of the prototype. A plot showing how the drag

coefficient errors, e_{C_D} varies with the length scale, K_L is shown in Figure 3.3. The function describing the dimensional scale effect varies logarithmically according to equation 3.10 below;

Table 3.4: Scale error resulting from differences in drag coefficient

	Scale model ratios			
	1:30	1:50	1:70	1:90
Experimental C_D	1.2	1.2	1.2	1.2
Simulated C_D	0.99	1.06	1.12	1.18
Error, e_{C_D}	0.21	0.14	0.08	0.02
Percentage error, %.	17.5	11.7	6.7	1.7

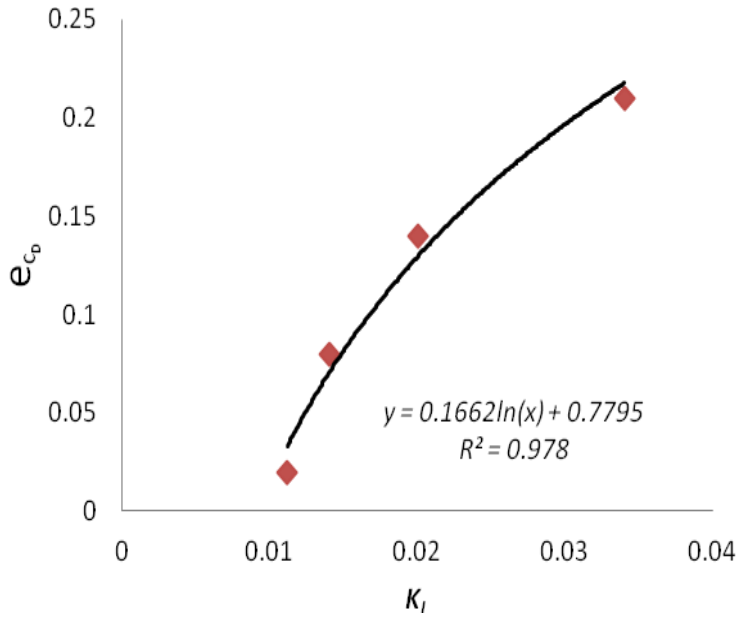

Figure 3.3: Error, versus normalized length scale.

$$e_{C_D} = 0.1662 In(K_L) + 0.779 \quad (3.10)$$

The equation has a coefficient of determination of 0.978 which gives a measure of how well the mathematical model will likely predict the scale errors in model. The equation show that the drag coefficient error increases as the normalised length scale.

Also, the drag force *D*, acting on all monopile models were analytically calculated based on the generally accepted drag coefficient, C_D value of 1.2 observed from Schewe's (65) experiment using equation 3.11 expressed below with units in Newton (N);

$$D = \frac{1}{2} C_D \rho A U^2 \qquad (3.11)$$

ρ, the fluid density was taken as 998.2kg/m^3. A is the respective monopiles diameter and U is the respective fluid velocity for each scale model. The simulated drag forces were extracted from the simulation database results. The difference between the analytical drag force and the simulated drag force e_D are presented in Table 3.5 below as scale errors.

Table 3.5: Scale error resulting from drag force calculations

Drag force	Scale ratios			
	1:30	**1:50**	**1:70**	**1:90**
Analytical (N)	3.298	1.174	0.604	0.400
Simulated (N)	2.762	1.060	0.580	0.390
scale errors, e_D	0.540	0.114	0.024	0.01

Similarly, a plot of the drag force error e_D versus a dimensionless length scale ratio is presented in Figure 3.4 below;

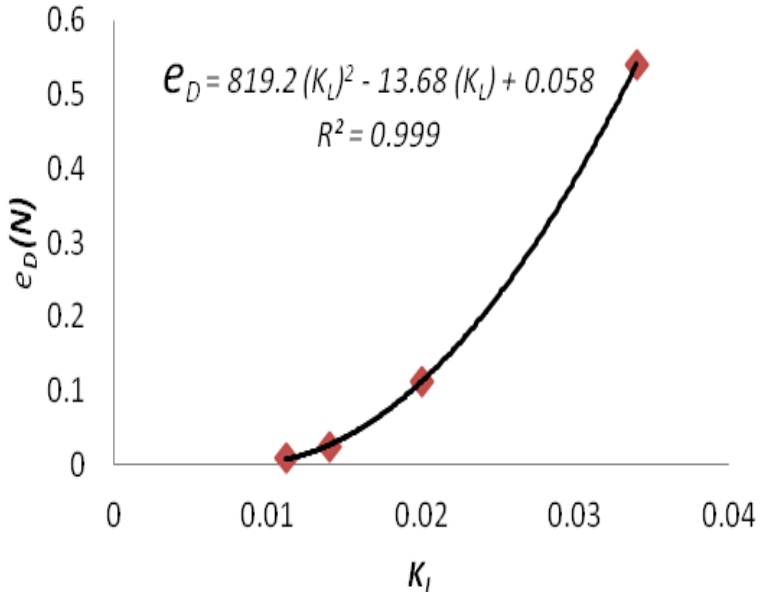

Figure 3.4: Error, versus normalized length scale.

The scale effects or drag force error can be approximated by a polynomial function described by equation 3.12 below;

$$e_D = 819.2K_L^2 - 13.68K_L + 0.058 \qquad (3.12)$$

It is seen that the drag force error increases as the normalised length scale. The coefficient of determination resulting from the curve fitting equation was 0.99.

3.4.2 Scale effects resulting from a change in velocity scale for the 1:50 scaled monopile.

In modelling, it is cheaper to increase the Reynolds number of a fluid system by changing the velocity scale while keeping the length scale constant. For example in a laboratory physical experiment, Schewe (65)

varied the speed of air in a wind tunnel experiment to achieve various Reynolds number for a device with a fixed length scale of 0.06m diameter. In numerically modelling it is also cheaper to use a particular meshed domain for parametric studies to reduce overall modelling time. An investigation was carried out on the 1:50 scale model with various inlet velocities ranging from 0.05m/s to 0.7m/s.

Table 3.6 shows the values of critical parameters and Reynolds number associated with each velocity scale from the RANS simulation result database.

Table 3.6: Critical parameter measured from numerical simulation.

Velocity of model, m/s	Reynolds number	Simulated mean drag coefficient.	Simulated r.m.s lift coefficient.	Strouhal number.
0.05	5×10^3	1.08	0.35	0.20
0.10	1.0×10^4	1.07	0.36	0.21
0.15	1.5×10^4	1.05	0.37	0.21
0.20	2.0×10^4	1.03	0.38	0.22
0.25	2.5×10^4	1.01	0.38	0.23
0.30	3.0×10^4	0.99	0.38	0.22
0.35	3.5×10^4	0.97	0.37	0.23
0.40	4.0×10^4	0.95	0.37	0.23
0.45	4.5×10^4	0.94	0.36	0.23
0.50	5.0×10^4	0.91	0.36	0.22
0.55	5.5×10^4	0.89	0.35	0.23
0.60	6.0×10^4	0.87	0.34	0.23
0.65	6.5×10^4	0.85	0.34	0.23
0.70	7×10^4	0.83	0.34	0.23

The 1:50 scale model domain is sized 2.4m x 1.6m, with a monopile diameter of 0.10m. Drag coefficient errors, e_{C_D} and the drag force error, e_D have also been calculated with results presented in Table 3.7 below.

The drag coefficient error was measured as the difference between the experimental drag coefficient of 1.2 and the simulated drag coefficient. The drag force error was measured by the difference between the analytical drag force calculated using equation 3.11 and the simulated drag force values extracted from the RANS database results.

Table 3.7: Table showing error estimates

Velocity of model, m/s	e_{C_D}	Analytical drag force (N)	Simulated drag force (N)	e_D
0.05	0.12	0.14973	0.135	0.01473
0.10	0.13	0.59892	0.5	0.09892
0.15	0.15	1.34757	1.2	0.14757
0.20	0.17	2.39568	2.1	0.29568
0.25	0.19	3.74325	3.1	0.64325
0.30	0.21	5.39028	4.6	0.79028
0.35	0.23	7.33677	5.93	1.40677
0.40	0.25	9.58272	7.4	2.18272
0.45	0.26	12.12813	9.79	2.33813
0.50	0.29	14.973	11.2	3.773
0.55	0.31	18.11733	13.5	4.61733
0.60	0.33	21.56112	16.1	5.46112
0.65	0.35	25.30437	17.66	7.64437
0.70	0.37	29.34708	20.43	8.91708

A function that can estimate the scale effects resulting from a change in velocity scale is derived from curve fitting the drag coefficient and the drag force error data. Figure 3.5 shows how the drag coefficient error varies with

a normalised velocity scale, $K_V = u_m/u_p$ where u_m is the fluid velocity of the model and V_p is the fluid velocity of the prototype.

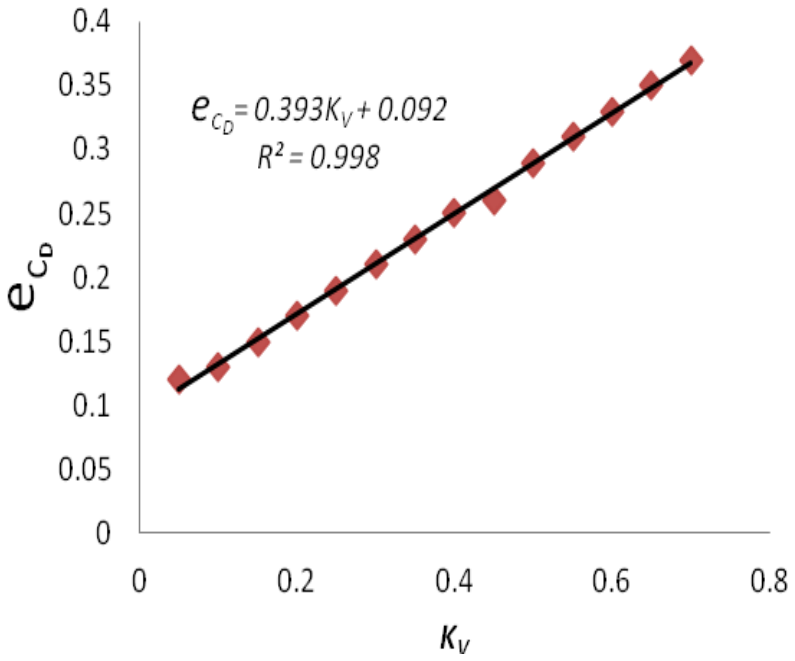

Figure 3.5: Drag coefficient errors from change in velocity scale.

The graph describing the relationship is a linear function described by the equation;

$$e_{C_D} = 0.393K_V + 0.092 \qquad (3.13)$$

with an R-square value of 0.998. It is evident from the plot that the deviation from experimental drag coefficient values is significant as the velocity scale was increased. From the trend, it is anticipated that models with Reynolds number occupying the higher range of the subcritical flow regime will produce higher errors in numerical testing using the RANS methodology. The drag force errors were also plotted against a normalised velocity scale shown in Figures 3.6 and 3.7. A power or a polynomial

function is suitable to describe the equations that can be used to predict the scale effect resulting from a change in velocity scale.

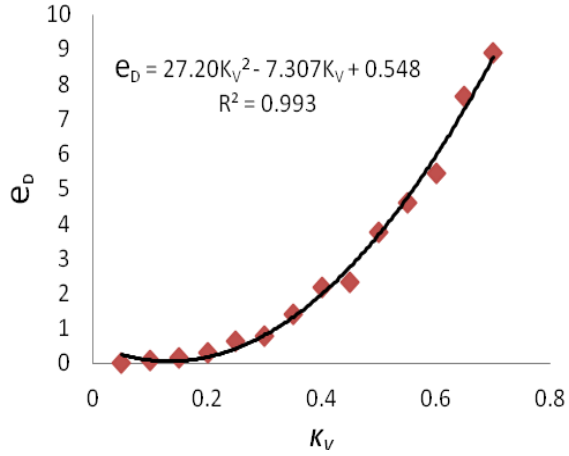

Figure 3.6: Drag force error from change in velocity scale described by a polynomial function.

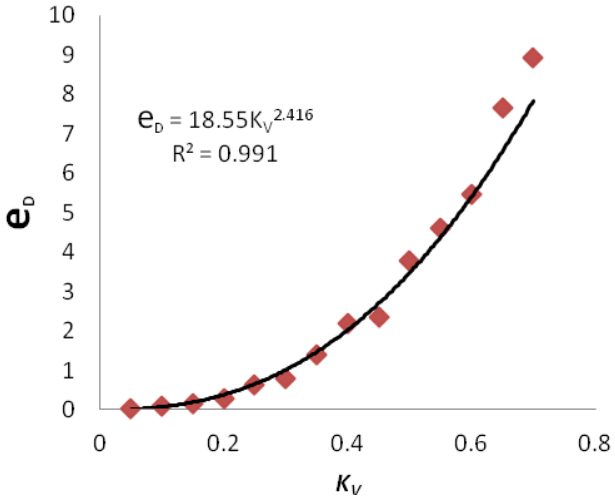

Figure 3.7: Drag force error from change in velocity scale described by a power function.

The power function is described by equation 3.14 given below as;

$$e_D = 18.55K_V^{2.416} \tag{3.14}$$

With an R-square value of 0.991. The polynomial function is described by equation 3.15 given below as;

$$e_D = 27.20{K_V}^2 - 7.307K_V + 0.548 \qquad (3.15)$$

and has an R square value of 0.993.

3.4.3 Analysis of Mean Pressure Coefficient

The drag force acting on the monopile is a sum of the inline force due to pressure and friction. Although, for Reynolds number greater than 10^4, the friction drag only contribute about 2% to 3% to the total drag force and is therefore neglected in most cases (63). Equation 3.16 expresses the contributions from the pressure and friction force to the mean drag force.

$$D = \int_0^{2\pi} \left(\overline{p}\cos(\phi) + \overline{\tau_0}\sin(\phi)\right) r_0 d\phi \qquad (3.16)$$

$\overline{p}$ is the mean pressure, $\overline{\tau_0}$ is the mean shear stress, r_0 is the radius of the monopile and ϕ is the separation angle. The parameters in the equation are illustrated in the sketch in Figure 3.8 below.

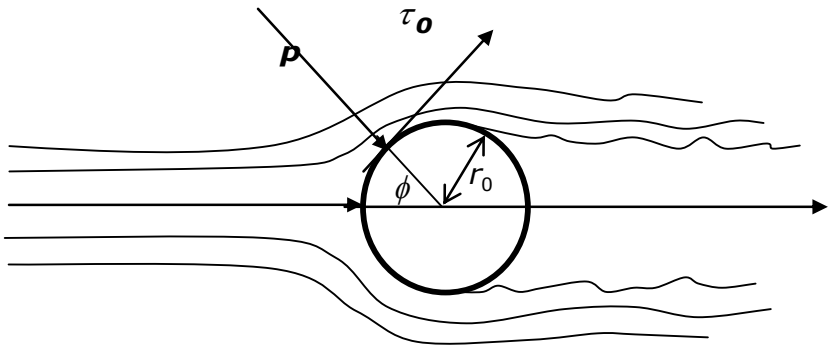

Figure 3.8: A Sketch defining the terms in equation 3.15

Equation 3.16 can also be written in a form that expresses its relation to the pressure coefficient, C_p as follows in equation 3.17 below;

$$D = \int_0^{2\pi} \left(\left(\frac{\overline{p} - p_a}{\rho U^2} \right) \cos(\phi) + \left(\frac{\overline{\tau_0}}{\rho U^2} \right) \sin(\phi) \right) d\phi \tag{3.17}$$

The equation above indicates that drag force and subsequently the drag coefficient is a function of the Reynolds number of the flow. In a real flow involving vortex shedding, the pressure on the lee side of the model is negative. The mean pressure coefficient around the monopile is plotted for the various input velocities used to investigate the 1:50 scale model and shown in Figure 3.9 below.

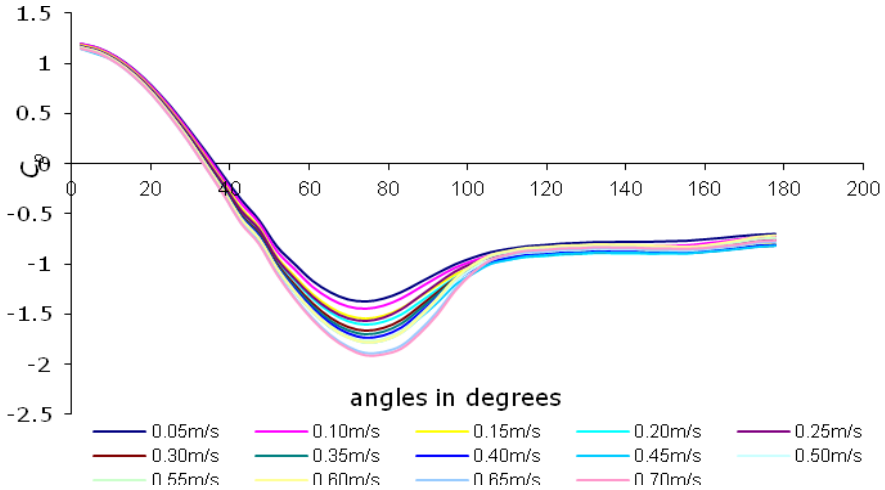

Figure 3.9: Graph of mean pressure coefficient.

It is accepted that flow separation takes place at an angle of about 78^0 for flows within the sub-critical flow regime (63). The numerical simulations have boundary layer separation angles ranging from 74.24^0 to 78.8^0. The base pressure decreases significantly from -1.37 to -1.9 as the velocity scale increases from 0.05m/s to 0.70m/s. The pressure coefficient at the lee end of the monopile for each simulation case remains fairly constant and it shows a lesser disparity between each simulation case than the base pressure coefficient values as seen in Figure 3.9.

All simulation cases occupies the same flow regime that exhibits similar boundary layer separation and wake behaviour so that, they are expected

to produce the same drag coefficient. The differences in drag coefficient exhibited in the simulation cases can be attributed to the differences in separation angles, base pressure and the pressure at the lee side of each simulation case. The base pressure show more significant differences compared to pressure at the lee side for the simulation cases.

Flow separation is caused by an adverse pressure gradient created due to the geometry resulting to a stream of shed vortices behind the monopile. The shed vortices can be visualized in the instantaneous velocity magnitude (m/s) contour plots in Figures 3.10 - 3.13 below. The flow time for all plot are approximately 100s of flow time.

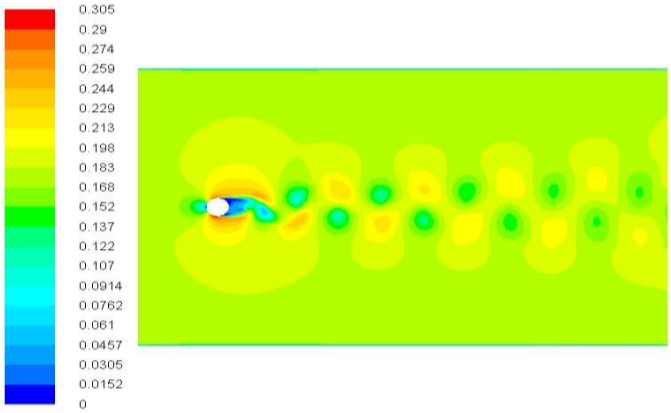

Figure 3.10: Vortices behind 1:30th scale device.

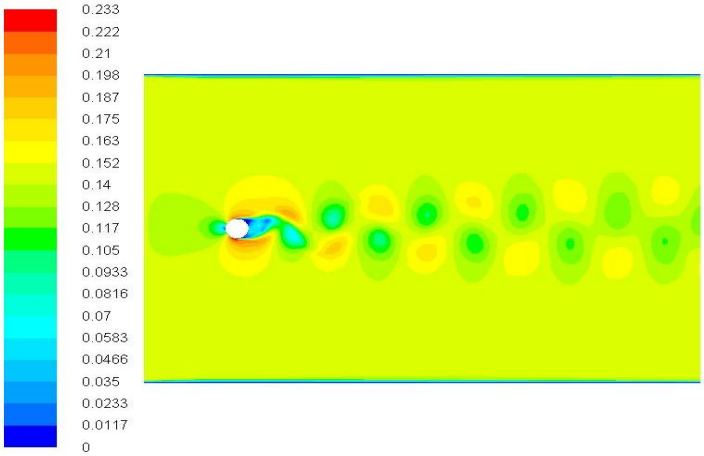

Figure 3.11: Vortices behind 1:50th scale device.

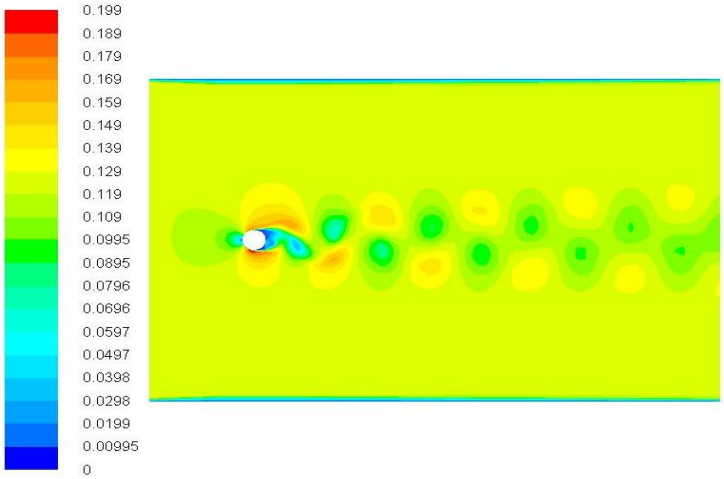

Figure 3.12: Vortices behind 1:70th scale device.

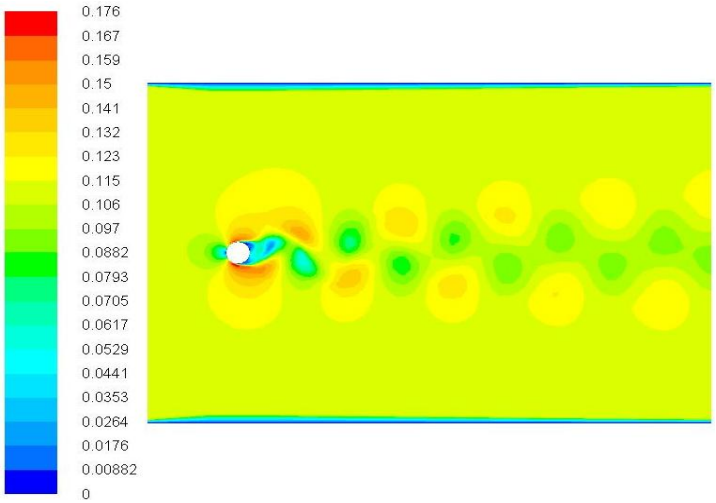

Figure 3.13: Vortices behind 1:90th scale device.

From the figures above, it is clear that the k-epsilon turbulence model has the ability to capture the vortex shedding phenomenon reasonably. In design of structures, the vortex shedding frequency is a critical parameter. There is a potential hazard if vortex shedding frequency equals the natural frequency of the structure.

3.5 Chapter Summary and Conclusion

The flow around a monopile is a classical problem of fluid mechanics that has potential application to tidal current energy technology. The force

coefficient of a circular cylinder varies as a function of Reynolds number as established from past experimental studies.

Force coefficients and non-dimensional vortex shedding frequency have been calculated on four Froude scaled models from numerical simulation using the k-epsilon ($k-\varepsilon$) realisable turbulence frequently used in engineering applications in this era of 'hybrid' modelling.

The numerical simulation results have been compared with physical experimental results. A key conclusion is that, the forces acting on the monopile can be simulated with the best accuracy depending on the choice of a length and a velocity scale associated with the model. Specifically, the smaller the physical model dimensions, the more accurate simulation results compares with experimental results. This behaviour was regarded as insensitivity of mathematical model formulation to changes in Reynolds numbers of a physical model. As a result, empirical equations that predict the scale effect resulting from a choice of a particular scale model size have been formulated. The equations are valid for flow systems with Reynolds within the subcritical flow regime. Further investigations are recommended to understand the lack of agreement between the RANS modelling technique and wind tunnel test results.

Chapter 4.0

Analysis of ADCP Experimental Data

4.1 Introduction

In recent times, the Acoustic Current Doppler Profiler (ADCP) has become the standard instrument for estimating the mean flow and turbulence quantities in a tidal current channel (69). Although the ADCP is limited in the sense that, it cannot be used to measure the smallest scale of turbulence and there are zones in the water column where measurements are not possible because of the inaccessibility of the acoustic beams. Nevertheless, the ADCP data is still popularly in use for example as in (70-77). The ADCP is primarily used to estimate mean flow and turbulent quantities in tidal currents channels. ADCP data are also useful for several other purposes which include but not limited to:

- Numerical model correlation (large scale)
- Site selection for tidal current or wave energy project
- Energy production forecast
- Power speed curve
- Kinetic energy resource characterisation
- Device optimisation for device developers
- Environment impact assessment and monitoring.
- Harmonic analysis of tidal currents.

In this present study, ADCP data has been integrated into a Large Eddy Simulation of an open channel to aid simulation of ambient turbulent structures resembling those in real sites. In this current chapter, tidal currents data sampled from Firth of Forth has been analysed and presented.

The methodology for the ADCP experiment was reported in chapter 2 of this thesis.

The ADCP data analysis results are presented in form of velocity-time series plots, velocity-depth profiles plots, horizontal velocity scatter plot, mean water level plot and tidal harmonic analysis plot. A plot comparing the ADCP data with theoretical velocity profiles is also presented.

Although the main goal of the ADCP experiment was to acquire turbulent velocity profiles from a real site, that would aid generation of coherent structures suitable for numerical testing of tidal current energy devices, it was necessary to analyse the ADCP data to reasonable details in order to appreciate the strength and nature of the flow at the Firth of Forth and also to provide a data base that could be used for other types of analysis such as enumerated section in 4.1.

4.2 ADCP data quality checks.

The ADCP sampled from the Forth Estuary was subject to quality checks before further analysis. Several factors which include the speed of sound, the beam geometry and noise can affect the accuracy of the ADCP data. Significant sound speed error is uncommon but if any, it can be corrected during post processing by specifying values for the temperature and salinity of the environment since the speed of sound depends on these two parameters.

The default temperature and salinity values of 20 degree centigrade and 34.5 respectively were specified at the beginning of the experiment. A temperature sensor integrated into the ADCP instrument automatically corrects the sound speed during measurement. No further sound speed correction was done on ADCP data before analysis. The beam geometry is factory fixed and does not require re-calibration.

Doppler noise is inherent in all ADCP's. The noise level is affected by ADCP system configuration, acoustic frequency, averaging interval and the bin

size. For example, less noise is associated with a high averaging interval. In this analysis it is assumed that the noise level is insignificant because of the averaging interval used.

Other physical factors that can affect the quality of velocity samples include incorrect positioning of the ADCP on the seabed during deployment as was experienced from a previous ADCP deployment in the course of this research, ADCP acoustic beam hitting the end of a profiling range and data recorded during ADCP deployment and retrieval operations.

4.2.1 Standard Deviation of the ADCP data.

The standard deviation is a direct measure of the quality of the velocity data. Plots showing the standard deviation also known as standard error for the east, north and vertical velocity are shown in Figures 4.1, 4.2, and 4.3.

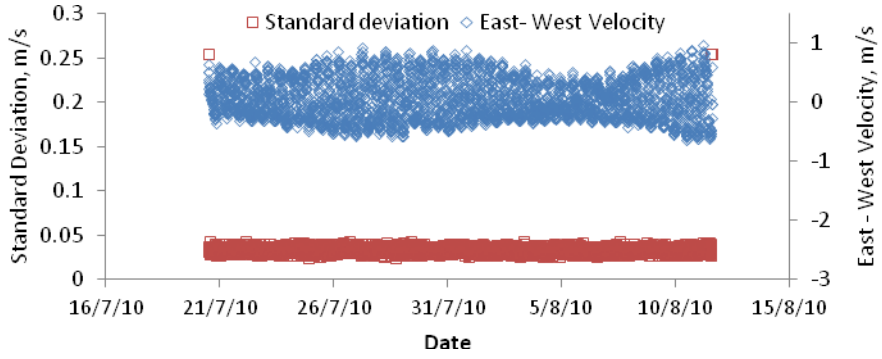

Figure 4.1: Standard deviation of the east-west velocity.

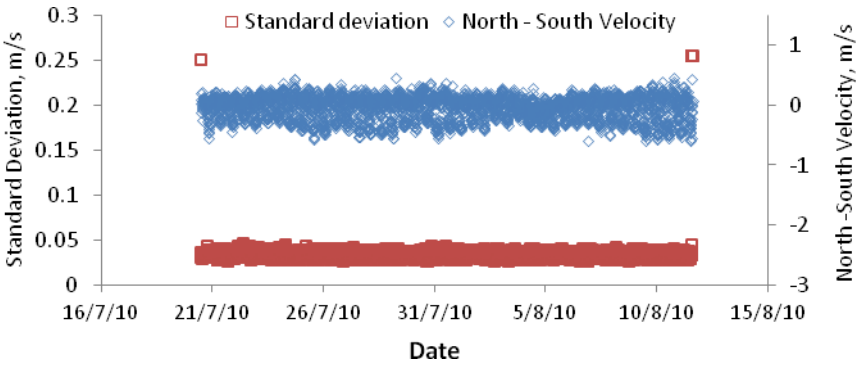

Figure 4.2: Standard deviation of the North-South velocity.

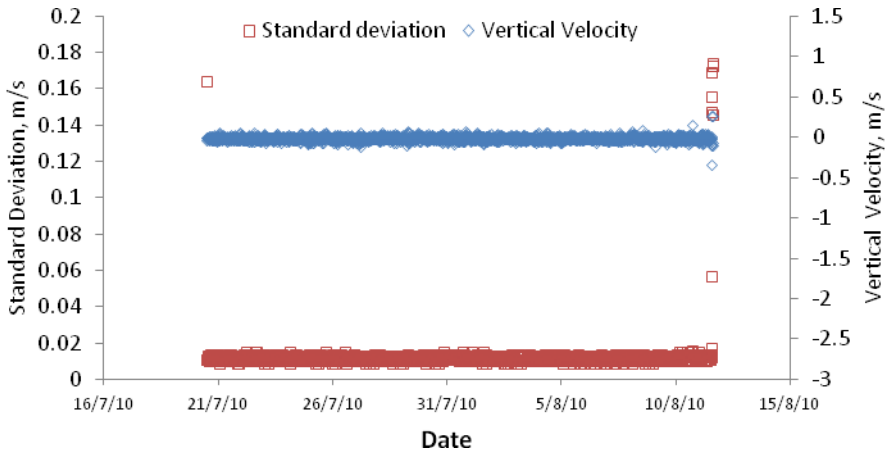

Figure 4.3: Standard deviation of the vertical velocity.

The velocity data is good if the standard deviation remains fairly constant. If the standard deviation increases significantly, it suggests that the acoustic beam may have hit the end of a profiling range for example, the water surface for an upward facing ADCP or the seabed for a downward facing ADCP.

The observed trend in standard deviation values shown in Figures 4.1, 4.2 and 4.3 are similar showing a significant increase in standard deviation in the first 10 minutes and the last 60 minutes of the data acquisition period. The maximum standard deviation for the east –west velocity component is 0.255m/s and the minimum is 0.025m/s. The maximum standard deviation for the north-south velocity component is 0.255 m/s and the minimum is 0.026m/s. The maximum standard deviation for the vertical velocity component is 0.174 m/s and the minimum is 0.009m/s. The reason for the rapid increase in standard deviation is because the ADCP was configured to start data collection at 12.00pm on 20th of July, 2010 however, the ADCP was satisfactorily positioned on the seabed, 10 minutes later than the specified time. At the end of the deployment period, it was only possible to stop the ADCP from recording data after successful retrieval of the ADCP from the sea and when it was placed on the boat. The long duration of the retrieval operation was influenced by rough weather conditions.

Velocity data acquired during these periods contain errors and do not represent flow at the Firth of Forth and were therefore discarded. Data from 34 meters above bottom were used as a representative sample for the quality plots in Figures 4.1. 4.2 and 4.3.

4.3 Mean Water Level at the Forth Estuary

The Firth of Forth is a funnel like estuary with tides occurring twice a day with two high water levels (Spring tides) and two low water levels (neap tides) occurring in a month. Figure 4.4 show the time series plot of the mean water level during the 23 days period of the ADCP deployment.

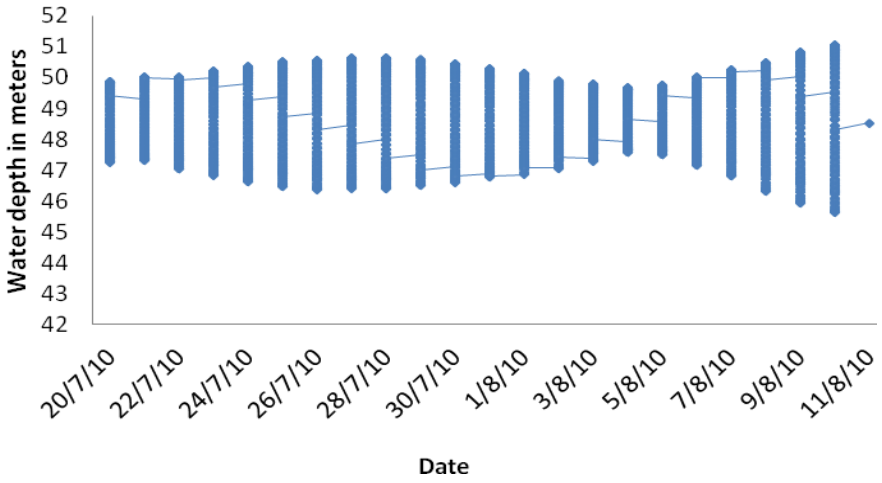

Figure 4.4: Plot of mean water level at the Forth of Forth.

The water level was sensed by a strain gauge pressure sensor mounted on the ADCP sensor head between the acoustic transducers. The pressure is recorded in dbar. This essentially represents the water depth in meters with a reference pressure of 0 dbar at the water surface.

The shape of the plot confirms that the tides are semi-diurnal as expected. It can be estimated from the plot that, the lowest tidal range was about 1.84m during the neap tides occurring at around the 4th of August 2010 and the highest range was over 5m in the spring tide, occurring 10th of August 2010.

4.4 Analysis of tidal current velocity at the Forth estuary.

The along beam velocity measured by the ADCP can be converted to the x, y, z coordinates relative to the instrument's axis or the ENU coordinates system relative to the earth axis. The ENU coordinate system illustrated in Figure 4.5 allows the ADCP to always report the true water velocity each time. This is possible because of the updated compass/tilt information made available during the averaging of the velocity vectors for each time profile so that, the data reported in the ENU coordinate system are not affected by the orientation of the ADCP.

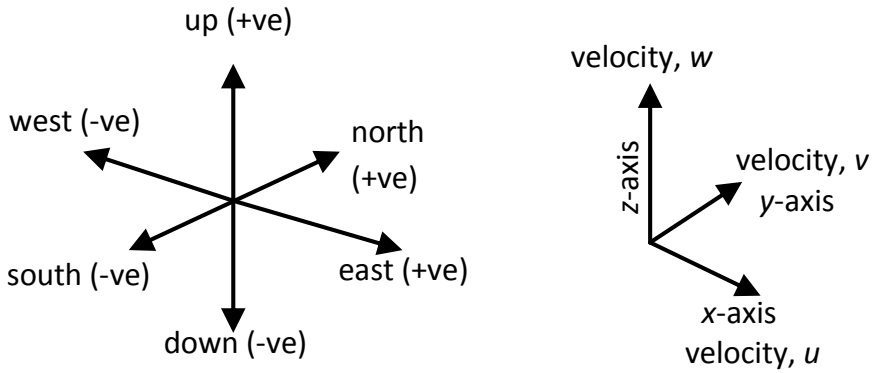

Figure 4.5: Frame of reference illustrating the coordinate system

The acronym ENU stands for East, North and Up respectively. The east-west velocity components is the along channel velocity and flows along the x-axis. The north-south components is the across channel velocity component and it flows along the y-axis. Both represent the horizontal velocity components of tidal current. The up velocity component represents the vertical velocity component. The east –west, the north- south and the up-down velocity are analogous to the u, v and w components in the Cartesian coordinate system respectively. Using vector arithmetic, the time averaged current velocity magnitude, $\bar{u}$ or the resultant vector in the net flow was calculated using equation 4.1 below;

$$\bar{u} = \sqrt{u^2 + v^2 + w^2} \tag{4.1}$$

The angle that the averaged current velocity vector makes with the three directions can be evaluated using equations 4.2- 4.4 expressed below;

$$\cos(\propto) = \frac{u}{\bar{u}} \tag{4.2}$$

$$\cos(\beta) = \frac{v}{\bar{u}} \tag{4.3}$$

$$\cos(\gamma) = \frac{w}{\bar{u}} \tag{4.4}$$

Where $\propto$, β and γ are the angles, the resultant velocity vector makes with the positive directions of x, z and y axis respectively.

4.4.1 Horizontal velocity scatter plot.

The horizontal velocity scatter plot showing the east - west (e-w) and the north – south (n-s) components is presented in Figure 4.6.

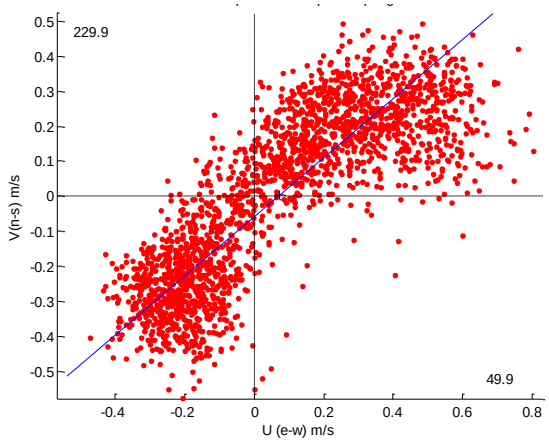

Figure 4.6: Horizontal velocity scatter plot during a neap and spring tide.

The data used for the horizontal velocity scatter plot was sampled at 12m water depth corresponding to bin10 data set. The horizontal velocity scatter

plot gives a strong visual clue to the tendency of the current vectors to align along a particular directional axis (marked in blue colour), where the flood and the ebb direction are 229.9 and 49.9 degrees respectively along the axis. Coriolis forces contribute to the direction the water particles tend to take in a natural flow. Peak ebb and flood tidal currents are not equal because of interactions between tidal constituents of different period, the shape of the coastline as well as local weather conditions. It is evident from Figure 4.6 that, the along channel (e-w) velocity component is stronger than the lateral (n-s) velocity component.

4.4.2 Velocity-time series analysis.

Velocity of natural flows like those in tidal current is three dimensional. Therefore a complete analysis of the three velocity components at the Firth of Forth is required for an adequate understanding of the flow in the estuary. The analysis of each velocity component also provides a global view of the strength of each velocity vectors in relation to each other. Figure 4.7 is the time series plots for the along channel velocity component.

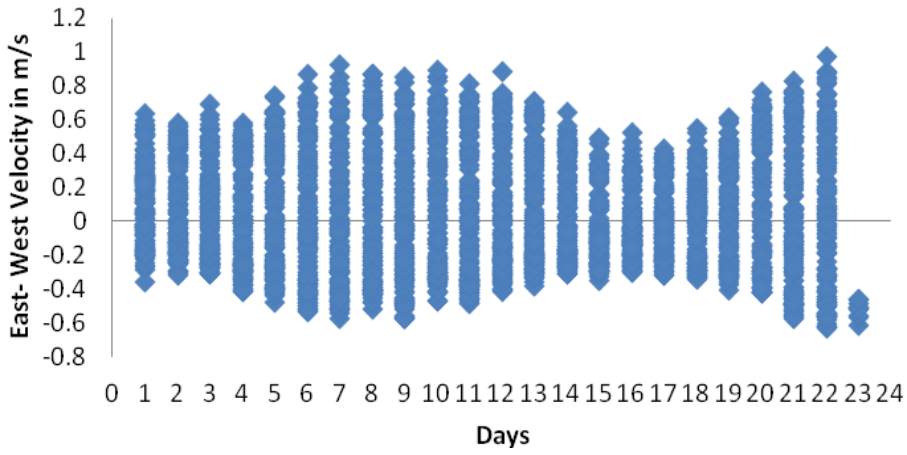

Figure 4.7: Along channel velocity time profile plot.

The along channel velocity-time profile plot also confirm that the tides are semi-diurnal. A maximum velocity magnitude, slightly more than 1m/s was recorded for the along channel velocity component during the ADCP

deployment period. When tide changes direction, the current speed became relatively slower scarcely reaching a maximum magnitude of 0.6m/s as evident in the plot. The variation in velocity magnitude during the ebb and flood flow will have implications for energy extraction purposes.

The lateral velocity component plot in Figure 4.8 is also significant although not as strong as the along channel flow.

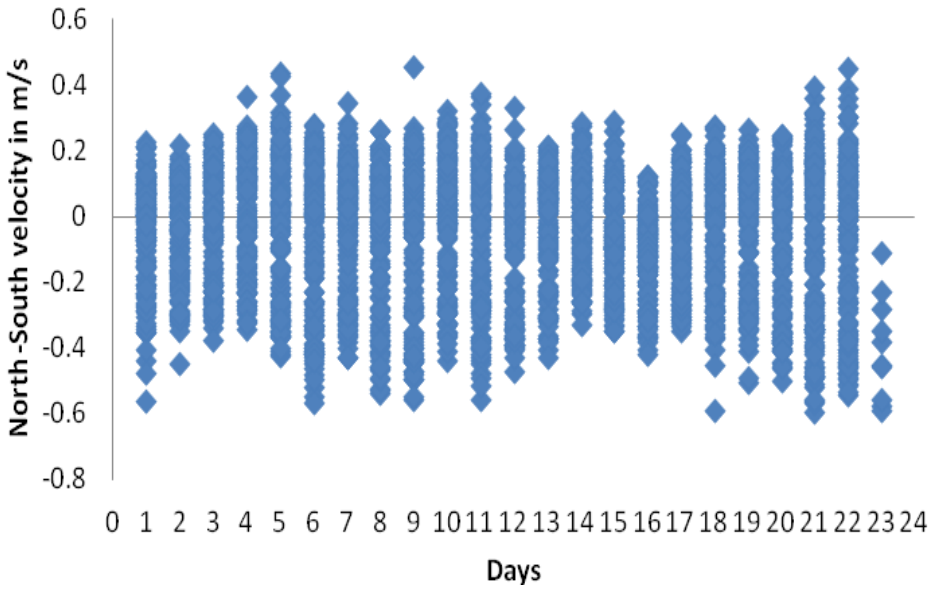

Figure 4.8: Across channel velocity time profile plot.

The maximum current speed recorded was 0.6m/s. The strenght of the lateral velocity component will have a profound effect on the resultant velocity magnitude. Although, flow in tidal current may appear predominantly one directional, an assumption of one directionality will underestimate the effect of the lateral velocity component on the resultant velocity vector and subsequently an underestimation of the the critical parameters derived from it. The pattern of the plot also show semidiurnal tides although not as noticeable as in the east-west velocity component plot. The semidiurnal pattern is not evident in the vertical velocity component plot shown in Figure 4.9 below.

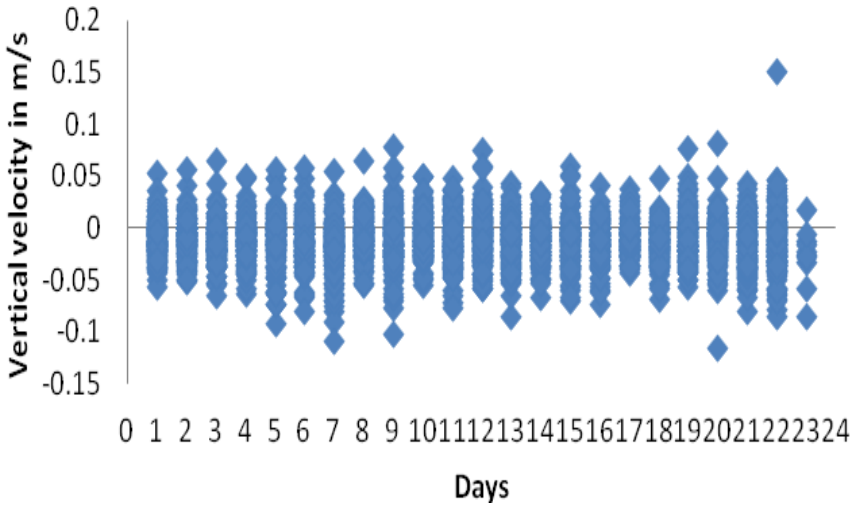

Figure 4.9: Vertical velocity time profile plot.

The magnitude of the vertical velocity component is significantly weaker than the horizontal velocity components. This suggest a reason why 2 dimensional turbulence has been assumed in geophysical flows. However, because direction is an integral part of turbulence, the effect of the vertical velocity component when considering direction can be significant.

4.4.3 Single realisations of turbulent velocity profiles

Tidal flows occur at a period of approximately 12 hours with a high and a low tide occurring twice a day. However, turbulent fluctuations in tidal currents are reflected in a single realisation of ADCP experimental data. These fluctuations vary rapidly as a function of time and space. Due to difficulties associated with the mathematical handling of the complex details of turbulent flow. Attention is normally focused on the averaging the fluctuating properties.

In this study, three samples of single realisations of turbulent flow profiles acquired at different times from the estuary are analysed to visualise their behaviour based on the shape of the profiles and with intent to apply one of

the profiles as a boundary condition in a numerical simulation to aid generation of coherent structures in a LES.

One of the samples acquired during a high tide is designated the 309th profile. Another profile designated as the 441st profile, was also acquired during another high tide. A third sample acquired during a low tide in the spring is designated the 1187th profile. These single realisations samples were arbitrarily chosen and they represent other turbulent profiles because their fluctuations are comparable.

Examination of each realisation sample was also aimed to investigate the effect that the number of velocity component has on the shape and magnitude of the turbulent velocity profile. This was achieved by using a one, two and three velocity component equation to generate data for each plot: A one dimensional profile was plotted with one component of the velocity data, a two dimensional profile was generated using two velocity component data and the three dimensional profile was plotted using three velocity components. The ADCP data used for the one-dimensional velocity profile plot was computed using;

$$\sqrt{u^2} \tag{4.6}$$

It represents the along channel velocity component only. Similarly, data used for the two-dimensional and the three-dimensional velocity profile plots were computed using;

$$\sqrt{u^2 + v^2} \tag{4.7}$$

and $$\sqrt{u^2 + v^2 + w^2} \tag{4.8}$$

The vertical axis for all the profile plots are designated meters above bottom (mab) while the horizontal axis is the velocity magnitude scale.

Comparison plots for the 309th profile are shown in Figures 4.10.

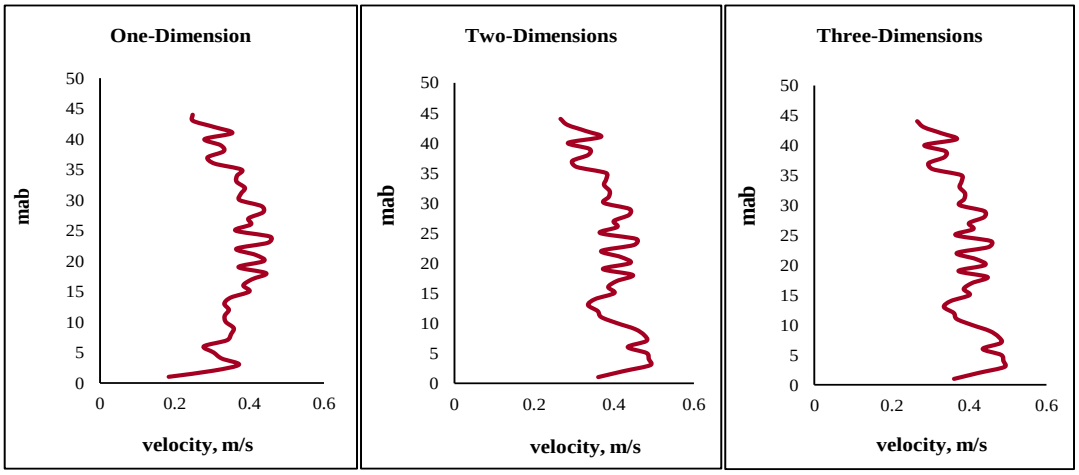

Figure 4.10: Turbulent velocity plot using the 309th profile data.

The 309th velocity profile had a peak velocity magnitude of about 0.49m/s not occurring at the water surface and a mean velocity of 0.37m/s using three velocity components to calculate the resultant velocity magnitude. The difference between the one dimensional and the (two or three) dimensional plot are obvious but it is difficult to notice any difference between the two and three dimensional plots. Figure 4.11 show the profile plots using the 441st profile data. The 441st had a peak velocity magnitude

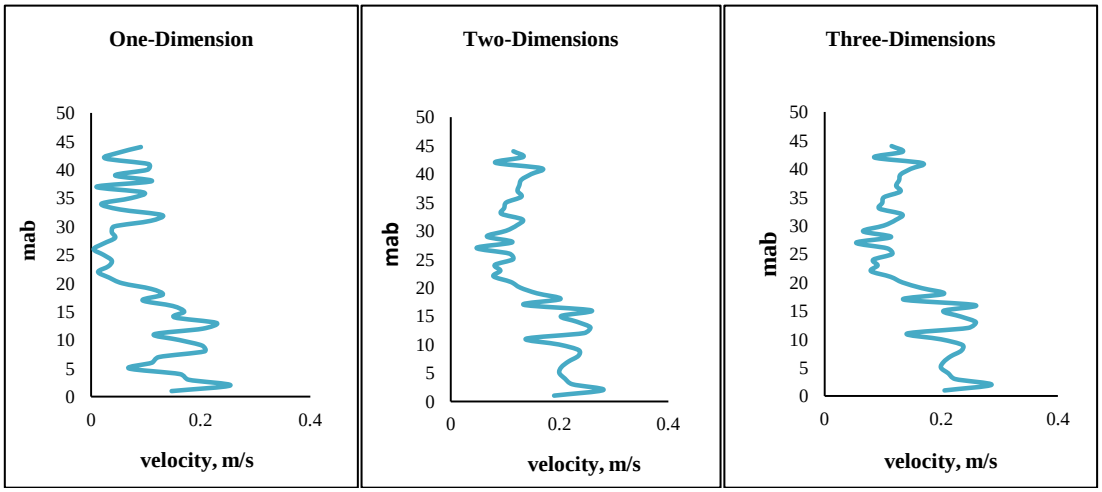

Figure 4.11: Turbulent velocity plot using the 441st profile data.

of 0.284m/s and a mean velocity of 0.17m/s. The resulting shapes show some dissimilarity, more significantly between the one dimensional and the (two or three) dimensional plots. Figure 4.12 below show the 1187th profile

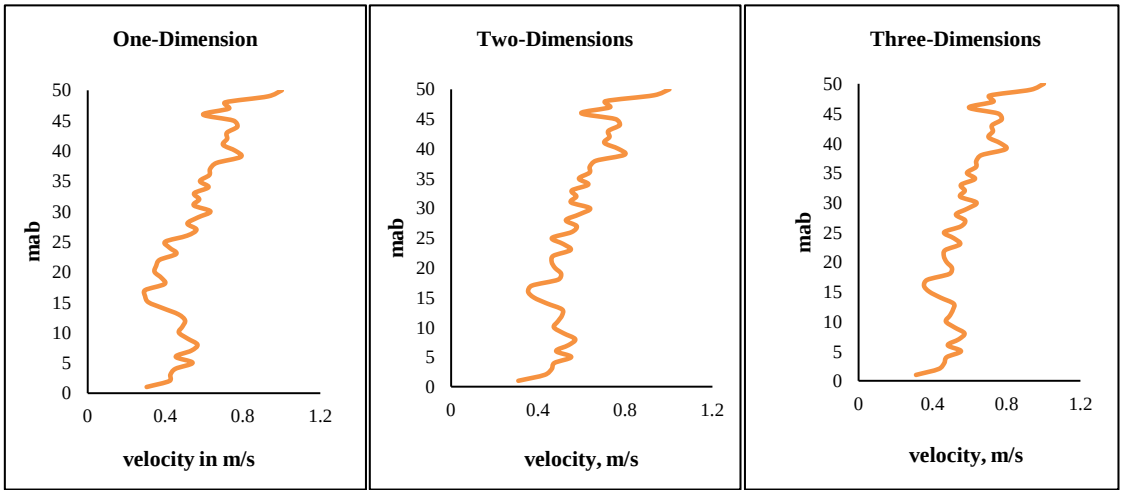

Figure 4.12: Turbulent velocity plot using the 1187th profile data.

plots with a peak velocity magnitude of about 1m/s and a mean velocity of 0.56m/s. Differences are hardly noticeable between the three plots because the lateral velocity and the vertical velocity component are much lower in value than the along channel velocity component.

Differences between the two and three dimensional plots are more obvious in the 309th and the 441st turbulent profiles implying that the vertical velocity magnitude is insignificant compared to the magnitude of the horizontal components. This suggests the reason for the usual assumption of a two dimensional turbulent flow in natural environment. However, it is believed that, when the direction of the velocity components are considered, the effect of the vertical velocity component on the simulated flow field will be substantial.

The 309th, the 441st and the 1187th profile data were sampled from the same vertical water column where the ADCP was located at the Firth of Forth.

4.4.4 Twenty three days averaged ADCP velocity profiles.

Twenty-three days ADCP data were time-averaged and plotted to investigate the nature of the velocity profile. The three plots shown in Figure 4.13 below are based on the three velocity components.

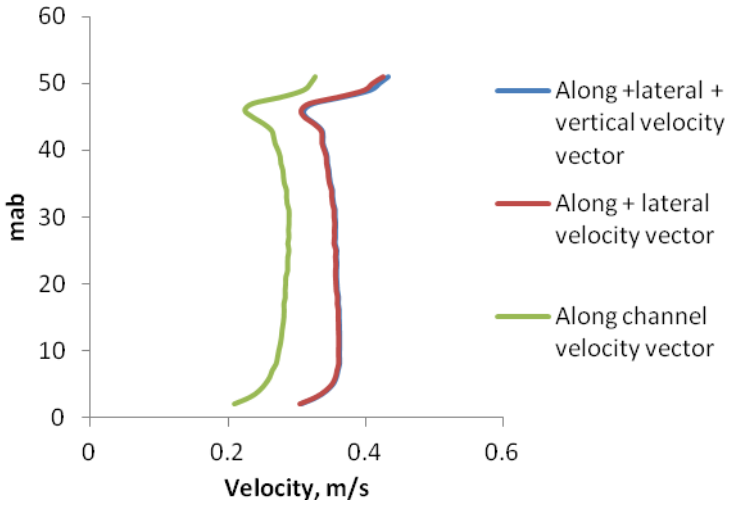

Figure 4.13: Mean velocity profiles averaged over 23 days.

The data used for the line plots were generated using equations 4.6, 4.7 and 4.8 to evaluate the along channel velocity data, along + lateral velocity data and all three components respectively. The green coloured graph corresponds to the along channel or *u* only. The red line plot corresponds to the resultant of the *u* and *v* velocity components and the blue line plot lying underneath the red line plot is the resultant velocity profile for all three velocity components. It is very clear that the vertical velocity component, *w* has little or no effect on the overall magnitude and shape of the velocity profile because of its relatively small magnitude. The lateral velocity component significantly enhances the resultant velocity magnitude as observed from the comparatively large difference in magnitude between the green and the red line plot.

Data from all the bins was used to plot Figure 4.13. The velocity profile show evidence of current shear toward the bottom of the channel as well as

velocity inflection points in the water surface region. The strength of the velocity vector is greatly enhanced near the water surface. The rapid increase in current speed and the presence of inflections are attributed to the influence of wind, waves and other physical processes such as boat movements and rough weather conditions on the water surface. The behaviour of the mean profile also agree with the 'double drag' effect described and observed by Fan (78) from analysis of ADCP data sampled from a coastal raft-culture area. The plot also shows a nearly uniform flow profile at the mid portion of the channel. The first data point (bin 1) was acquired at 2 meters above bottom (mab) which the ADCP assume to be 0m from the configuration set up. The overall mean velocity during the 23 days ADCP deployment was 0.36m/s with a peak mean speed of 0.43m/s occurring near the water surface.

4.4.5 Comparing real site velocity data with theoretical velocity profiles.

It is common to use the 1/7th power law or the uniform flow profile for numerical simulation of tidal current energy devices. In order to compare the theoretical velocity profiles with the data sampled from the Firth of Forth, theoretical velocity profiles data were evaluated based on a mean value of 0.37m/s and a peak velocity magnitude of 0.49m/s resulting from the 309th profile data. The $1/7^{th}$ power law profile can be approximated by equation 4.9 below;

$$\frac{u_x}{u_{max}} = \left(\frac{y}{z}\right)^{\frac{1}{7}} \qquad (4.9)$$

where y is any distance measured from the seabed. z is the channel depth.

u_x is the mean velocity and u_{max} is the max velocity close to the channel

surface. The mean velocity, u_x acts to average out the turbulent fluctuations in the *x* direction measured at any particular value of *y*. Theoretically, it is known that the 1/7th power law approximation is valid for flow with Reynolds number of $10^{5.}$ The exponent value falls below $\frac{1}{7}$ for higher Reynolds number flow having values of $\frac{1}{8}, \frac{1}{9}$ *and* $\frac{1}{10}$ at extreme values of Re.

The 1/7th power law approximation is normally used to describe mean turbulent velocity profile as discussed in (79) and has been a successful modelling strategy within the defined limit of usage. Recently, De Chant et. al (35) related the success of the 1/7th power law approximation to a more fundamental understanding of turbulent flow, its modelling closures and their connection to stochastic processes. Although, the 1/7th power law approximation was first developed for turbulent pipe flow, it is applicable to open channel flows. The only difference is that, for a pile flow the velocity is maximum at the pipe centre while the maximum velocity for an open channel flow occurs at the water surface. The theoretical time averaged velocity profile is described as a fairly flat profile in the vicinity of the free surface except near the seabed where the no slip boundary conditions becomes valid due to shear.

The 1/10th power law profile has a steeper velocity gradient than the 1/7th power law profile at the bottom region of the channel. This implies that the steeper the velocity shear, the higher the Reynolds number and a more turbulent flow. The presence of shear in both profiles implies that it will act to sustain turbulence although the turbulent fluctuations have been averaged out from the profiles thus producing a smooth profile. The theoretical profiles also assumed that flow is streamwise in one direction.The approximate Reynolds number of the flow at the Forth estuary calculated based on the flow depth of 53m is 1.9 x 10^7. This value represents undoubtedly a transcritical flow of engineering interest.

Figure 4.14 is a plot comparing the theoretical velocity profiles with real site velocity profiles. A 60s averaged profile in the Forth of Forth is not smooth like the theoretical profiles. It contains evidence of turbulence fluctuations on the current profile influenced by waves, physical and natural processes inherent in the flow of tidal currents. However, the 23 days averaged experimental velocity profiles lacks evidence of such fluctuations on the velocity profile.

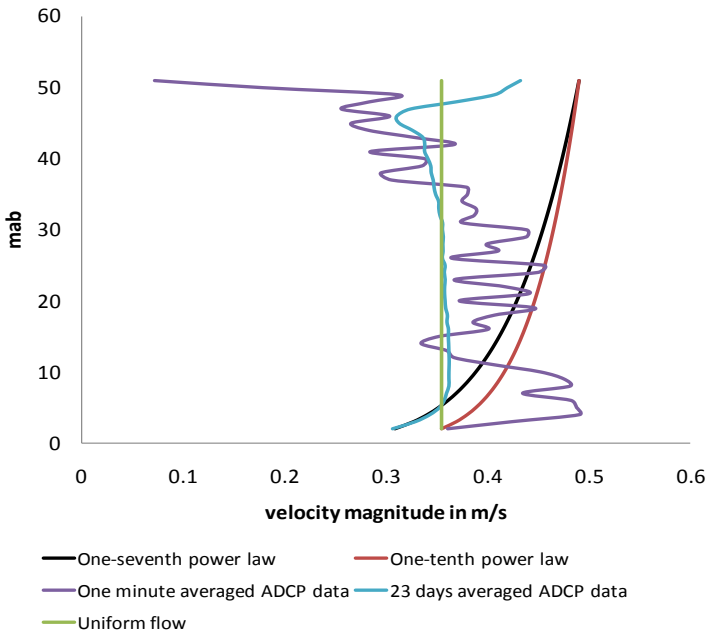

Figure 4.14: Comparison plot for ADCP data profile with theoretical velocity profiles.

An interesting feature to note is the clean overlay between the $1/7^{th}$ power law and the 23 days averaged velocity data in the first few bins from the seabed and for the most part, the middle section of the plot approximates a uniform flow profile for the ADCP data plot.

The observed shape of a single realisation of the velocity profiles is not in qualitative agreement with theoretical velocity profiles although the velocity values are equal. It is clear from the above analysis that averaging of velocity profiles has a profound effect on turbulent velocity profiles. It dampens the effect of turbulent fluctuations inherent in the profiles.

Averaging a 23 days turbulent velocity data sampled with an autonomous sampling strategy has enough dampening effect to create a smooth profile, while a one minute averaged data adequately reflect the turbulent fluctuations present in the velocity profile.

4.4.6 Tidal and non-tidal velocity analysis.

Tidal harmonic analysis allows one to have a perception of the magnitude of residual currents in the experimental velocity profile. Residual currents are produced by other processes other than the relative motion between the sun, moon and earth. These currents can be significant in sediments processes although have speed of a few cm/s (10). The resulting plot from the tidal harmonic analysis is shown in Figure 4.15.

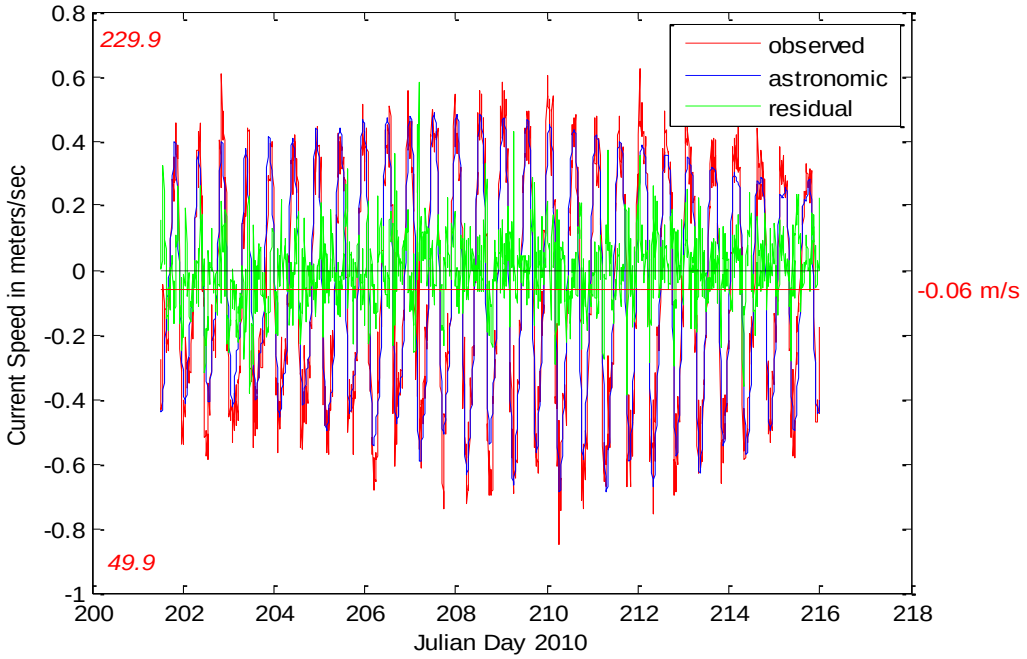

Figure 4.15: Astronomical versus observed tidal currents.

The aim of this analysis is to distinguish between the current velocity that oscillate at both tidal and non-tidal frequencies using the horizontal velocity component data for a full spring period. The astronomical current results from the gravitational interactions between the earth, moon and the sun. The difference between the observed and the astronomical prediction gives

the residual currents. Residual currents are attributed the effect of weather conditions, coriolis forces, geometry of the coastline, physical and biological processes on the water. The residual currents have a mean speed of 0.06m/s. The tidal constituents used for the harmonic analysis are presented in Table 4.1. The tidal harmonic analysis result is limited by the number of days the ADCP data was acquired. Using more ADCP data points for the analysis, would allow more tidal constituents into the analysis with an effect of further reduction of the residual current.

Table 4.1: Phase and Amplitude of Tidal harmonic constants

Tidal Constituent	Amplitude	Phase
O1	0.020	332.53
K1	0.035	142.86
N2	0.113	201.16
M2	0.484	287.49
S2	0.167	37.77
M4	0.075	303.72
2MS6	0.040	122.73

4.5 Mean shear evaluation for the Firth of Forth.

Current shear results from the retardation of the flow near the seabed and movement of adjacent fluid particles as they slide past each other due to frictional forces. The flow in a tidal current is associated with a total shear stress τ, which relates the viscosity of water and the velocity gradient as;

$$\tau = \frac{(\mu+\eta)(d\bar{u})}{dz} \qquad (4.5)$$

$\frac{d\bar{u}}{dz}$ is the time averaged velocity gradient above the channel bed, with units in per sec. μ is the molecular viscosity and η is the turbulent viscosity.

The molecular viscosity is constant and is property of the fluid but the turbulent viscosity varies as a function of flow. The shear is the vertical

gradient of the ambient horizontal current. Plots showing the shear rate for the horizontal velocity components for bin 10 are show in Figures 4.16 and 4.17 below.

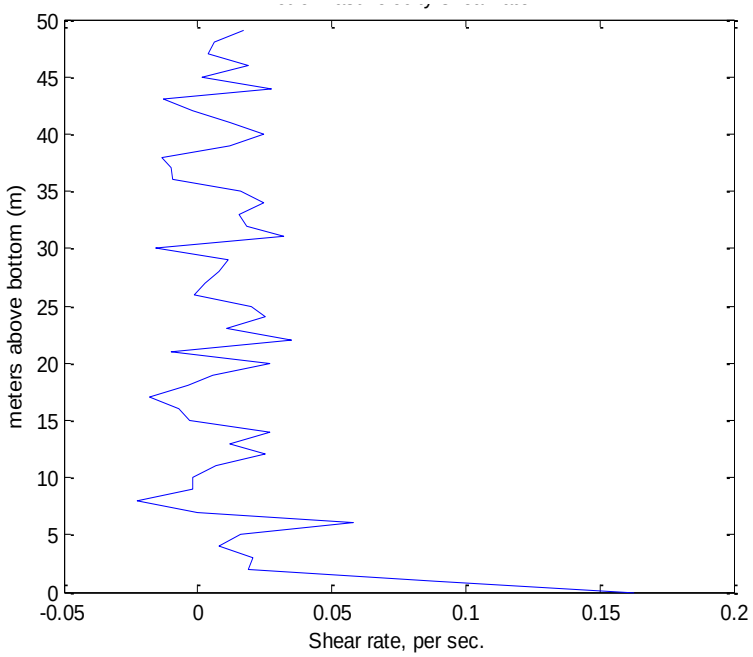

Figure 4.16: East-west velocity shear rate in s^{-1}

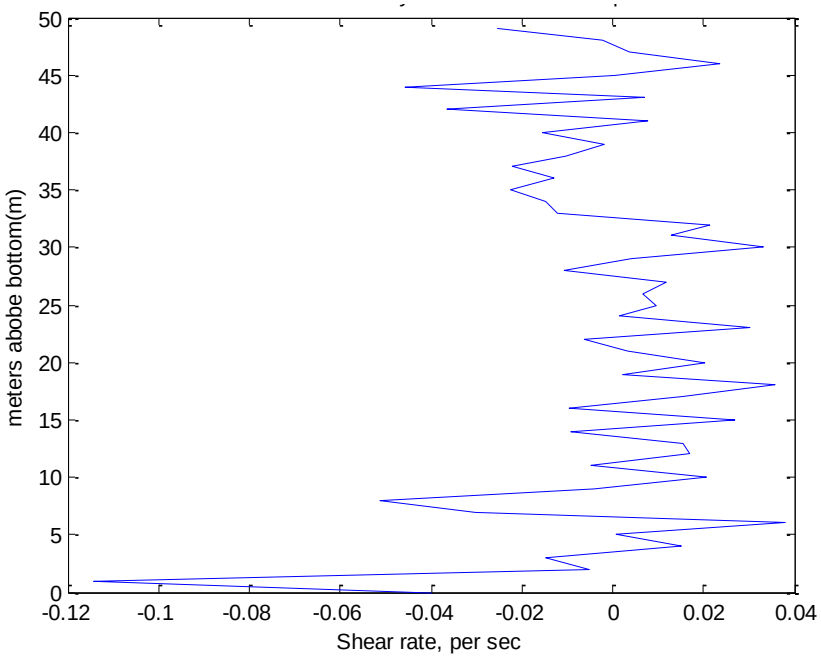

Figure 4.17: North-south velocity shear rate in s^{-1}

Due to the presence of shear, the flow departs from ideal homogeneous and isotropic assumptions because shear modifies the homogeneity and isotropy by deforming the turbulent eddies which exchange energy with the background shear through the mechanism of Reynolds stresses, which represents the transport of momentum by turbulence.

The shear vary continuously because of the presence of eddies that occurs on all scale from centimetres to metres. Theoretically, the total shear stress can be evaluated from equation 4.5 when the turbulent stresses are known. Laminar shear stresses dominate near the wall region while turbulent shear stresses are dominant in the outer region of the flow.

4.6 Chapter Summary and Conclusion.

The ADCP experiment was intended to acquire turbulent velocity profiles from a typical tidal current site that would be integrated into a LES to aid generation of coherent structures suitable for numerical testing of tidal current energy devices. Based on the ADCP experimental data, a first-hand investigation of the turbulent velocity profiles at the Firth of Forth was carried out to gain in-depth understanding of the flow behaviour. Rough and variable weather conditions influences the recorded ADCP data. However, the data presented represents the typical flow profile at the estuary. The resulting velocity from the estuary have been analysed and compared with approximated theoretical velocity profiles.

Following the ADCP data analysis results, the following conclusion can be reached.

1. The flow at the Firth of Forth have relatively weak currents that could reach 1m/s with an overall mean of 0.36m/s

2. Turbulent velocity profiles averaged within seconds show evidence of velocity fluctuations on the profile which are not visible on the 23 days averaged profile. The 23 days averaged turbulent velocity profiles produces a smooth, relatively uniform profile at the middle

region of the channel and a relatively high shear rate near the lower region of the channel.

3. The shapes of the velocity profiles at the Forth estuary deviate from the theoretical velocity profile especially in the upper region of the channel. These deviations are attributed to interactions of tidal current with surface frictional forces due to wind stress, waves, and other physical and natural processes occurring on the water surface. The theoretical $1/7^{th}$ power law closely approximates the 23 days averaged current profile in the lower region of the channel where velocity shear is significant.

4. There is evidence of constantly varying shear that acts to deform turbulent eddies in the flow, causing natural flow of tidal currents to deviate from the assumption of isotropy and homogeneity.

5. Investigation of single realisations of the turbulent velocity profiles sampled from the estuary confirms the variability of turbulent flow velocity in time and space. Also, the influence of the vertical velocity on the resultant velocity profile in terms of magnitude was in significant. This suggests a reason for a two- dimensional turbulence assumption. However, it is anticipated that the direction of the vertical velocity component will significantly affect the behaviour of the turbulent velocity field.

6. The tidal harmonic analysis result show the presence of residual currents resulting from other processes than the effect of the gravitational pull between the sun, moon and the earth. These processes include the shape of the coastline, the roughness of the seabed and other physical and natural process.

In general, the measured current at the Firth of Forth is influence by waves, coriolis forces, biological processes, physical processes and the shape of the coastline. Real operating devices will be subject to current

modified by these processes. It is anticipated that, specifying the raw turbulent velocity profile averaged within seconds in a numerical simulation as boundary condition, would facilitate understanding the effect of these processes at least qualitatively.

Chapter 5.0

Study of Coherent Structures Suitable for Numerical Testing of Tidal Current Energy Devices.

5.1 Introduction

Tidal currents energy technology is developing and several energy devices are currently considered. In spite of the progress made, turbulent flow inherent in tidal channel flows presents a challenge for scale model testing of energy devices. Testing of small scale tidal current energy devices are usually carried out in water circulating channels or tow tanks. Differences have been shown to occur between measured forces when device are towed in water and when fixed in flowing water from studies reported in (26). Furthermore, turbulence generated in these test facilities does not represent those inherent in natural flows (24) and (23).

In Computational Fluid Dynamics (CFD) simulations of marine devices, it is a common practice to specify the 1/7th power law or the uniform flow velocity profiles as boundary conditions. These theoretical profiles cannot reproduce ambient turbulent structures comparable to real flows. The theoretical power law profiles often appear as organised well patterned flow lines upstream of the structure being simulated.

Ambient turbulence within tidal currents has a wide range of scales which have been summarised in a review paper (80) attached as appendix 1. Matthes was the first to give a qualitative description of turbulent structures in natural flows which were referred to as macroturbulence in (81).

The need to understand the effect of turbulence during model testing has long been highlighted by Bearman, (42) in wind tunnel experiments. He emphasised that turbulence should be accounted for before satisfactory scale model results are extrapolated and applied to prototypes. During the development of tidal current energy device performance protocol (43), the

effect of turbulence on device performance and survivability was highlighted as a knowledge gap that needed investigation.

5.1.1 Description of turbulent structures, its identification and implications

Turbulence within tidal current is a random and appears in form of coherent structures ranging from small scale to large scales eddies. The interaction between the small and large scale structures is described by the energy cascade process (82) illustrated in Figure 5.1. Kinetic energy extracted from the mean flow enters turbulence at large scale of motion in form of eddies.

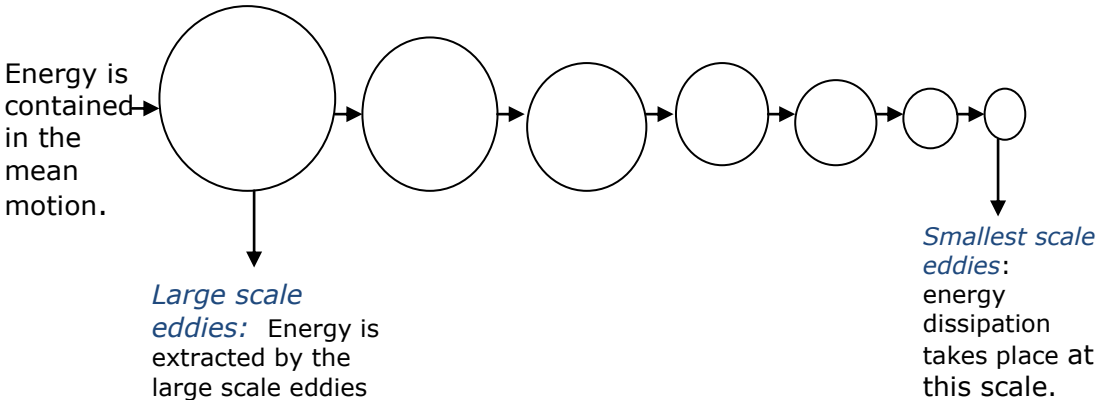

Figure 5.1: An illustration of the energy cascade process.

Due to the instability of the large scale eddies, they break up while transferring their energy to smaller eddies. The breaking up and transferring process continues until the eddy motion becomes stable enough for kinetic energy dissipation to heat takes place in the smallest eddies. In mixing processes, there is possibility for eddies coalescing to form larger eddies.

Turbulence is also described from the energy spectrum view point illustrated in Figure 5.2. The spectrum explains the contribution of different sizes of eddies to turbulence kinetic energy. Large scale coherent structures contain most of the turbulent kinetic energy. Turbulence phenomenon has been mathematically explained by the Kolmogorov spectrum (83) in the high

frequency range where the smaller scale eddies occupy, while the large scale structures fall into the lower frequency range of the energy spectrum.

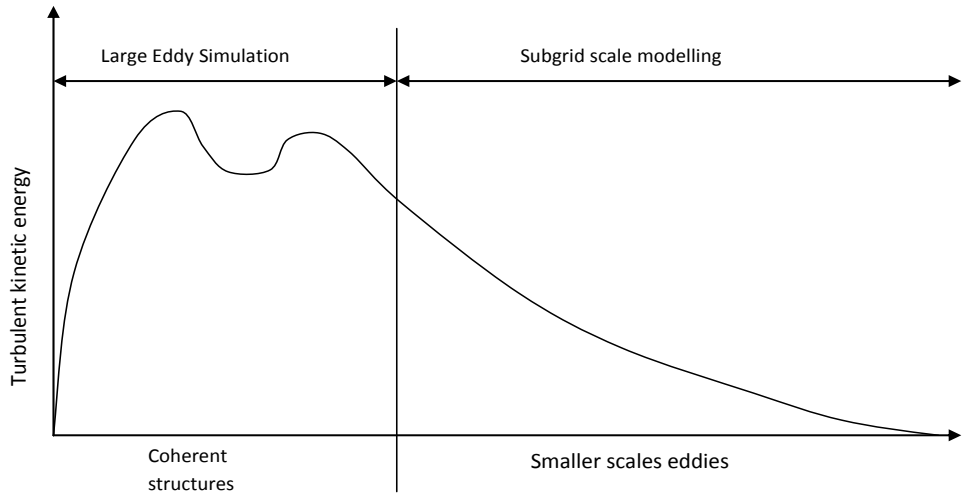

Figure 5.2: Turbulent kinetic energy spectrum.

The behaviour of the small scale eddies are random and are nearly isotropic and can be described using statistical techniques. On the other hand, the large scale coherent structures falls into the energy production range of the spectrum and LES has been known to be an appropriate tool for describing their evolution (47) while the associated smaller scale eddies can be modelled by a subgrid scale model. The coherent structures behave in an organised fashion and have the ability to retain their nature as they are convected within the flow for a considerable distance. Deardorff (84) was the first to carry out a numerical study of three dimensional turbulent flow at large Reynolds number using LES to predict several features of turbulent flow with a fair level of success using only 6720 grid point for the domain. It was concluded that, with a modest increase of numerical resolution, increased accuracy is expected. This pioneering work significantly demonstrated the potentials of LES in turbulence modelling of high Reynolds number flows however, the computations that produced a fair agreement with experimental data was from regions away from the walls. The study reported by Moin and Kim in (85) on numerical investigation of turbulent channel flow was focused on the flow structures near the wall region. The mean velocity profiles and turbulence statistics showed good agreement

with experimental data. Other studies on turbulent flow reported in (49) suggest that, the largest scales of turbulent motion do not necessarily contain most of the turbulent kinetic energy. The description of turbulent flow in natural environment by Matthes (81) also contained in (47) categorised the anisotropic large scale turbulent structures into the bursting phenomenon and large scale vortical motion.

a) The bursting phenomenon

The bursting phenomenon is a quasi-cyclic process of sweeps and ejections motion that generates Reynolds stresses and produces the turbulent energy that acts to maintain turbulence in shear flows. The ejection process consists of a lifting away of a low speed parcel of fluid from the wall region into the outer region of the flow. The sweeping process consists of a higher speed parcel of fluid rushing into the wall region to sweep away the left over low speed fluid parcel from the wall region. These structure appears streaky and randomly in space and time. The bursting phenomenon has been observed in previous studies to occur both in rough and smooth bed as reported in (86).

b) Large scale vortical motion

Based on the classification of coherent structures, not all large scale vortical motion constitutes turbulence. Large scale motion that constitutes turbulence consists of a strong upward vortex called kolk. The kolk vortices are generated intermittently near the channel bed. Kolk vortices with high enough turbulence have the potential to ascend to the water surface to become a boil. Large scale vortical motion observed in natural flow that does not constitutes turbulence are regarded as a pulsation of the mean flow and it is a much lower frequency motion containing fine turbulence.

The large scale coherent structures are potential hazard when they interact with an energy device. Vortex structures interacting with a generic tidal current energy device is illustrated in Figure 5.3 below;

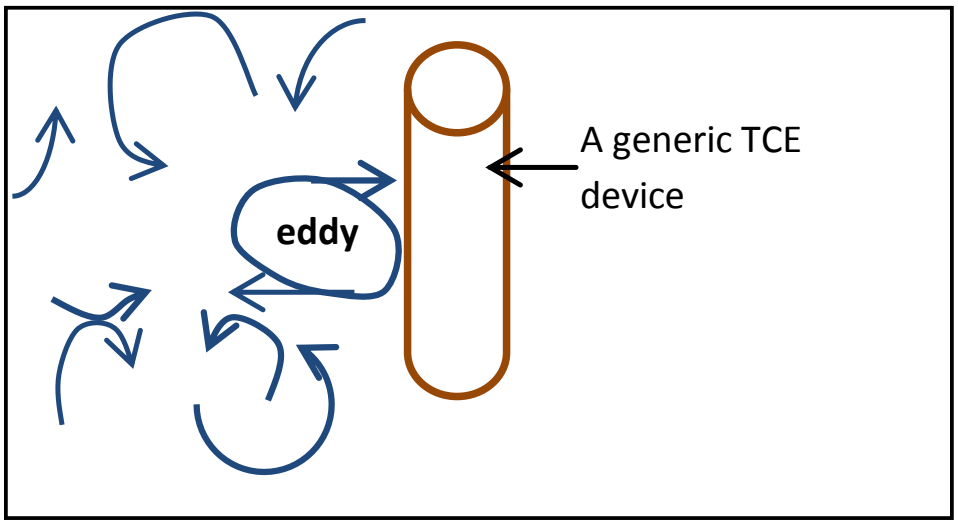

Figure 5.3: An eddy interacting with a generic TCE device.

In wind energy generation, significant departures from steady operating loads conditions can occur in gusty conditions as reported in (39). Correspondingly, it is anticipated that the large scale structures will have some structural implication for the device. Consequently, the testing of tidal current energy devices in an ambient field of vortices is necessary to avoid over or under design of structures.

The primary goal in this chapter is to demonstrate the possibility of simulating a flow field of ambient coherent structures suitable for numerical testing of a tidal current energy device, with the aid of real time turbulent velocity profile measured by an ADCP and integrated into a Large Eddy Simulation (LES) of an empty channel. The study thus presents a preliminary step for accounting for large scale turbulent structures during numerical simulation of tidal current energy devices.

5.1.2 Identification of coherent vortices in LES

In numerical simulation of turbulent flow using LES, coherent vortices can be recognised as regions of high concentration of vorticity. They are defined in (87) as regions of flow satisfying a high concentration of vorticity, enough to enable a local roll up of the surrounding fluid. Therefore, vorticity relates

to a measure of rotation of a fluid element as it moves in a flow field. Turbulent flows contain regions of strong coherent vorticity and also regions with little vorticity. The fluctuation of the vorticity field is critical and has structural implications on energy devices. Vorticity, $\boldsymbol{\omega}$, is formally defined as the curl of the velocity vector expressed in equation 5.1 below:

$$\omega = \nabla x \hat{u} = \left(\frac{\partial w}{\partial y} - \frac{\partial v}{\partial z}, \frac{\partial u}{\partial z} - \frac{\partial w}{\partial x}, \frac{\partial v}{\partial x} - \frac{\partial u}{\partial y}\right) \quad (5.1)$$

where $\boldsymbol{u}$, $\boldsymbol{v}$ and $\boldsymbol{w}$ are the velocity components in the $\boldsymbol{x}, \boldsymbol{y}$ and $\boldsymbol{z}$ directions respectively. The vorticity magnitude is evaluated from equation 5.2 below;

$$|\omega| = \sqrt{\omega_x^2 + \omega_y^2 + \omega_z^2} \quad (5.2)$$

The vorticity field is calculated based on the velocity fields. Coherent structures or eddies can be easily identified as recirculating vectors regions. Although there are other methods for identifying vortices, the vorticity approach is preferred in this study because, the kinematic and the dynamic evolution of an incompressible fluid can equivalently be expressed in terms of velocity and vorticity so that no information about the numerical simulated flow field is lost (88).

5.2 Methodology

The methodology is based on simulating coherent structures using a tidal current velocity profile influenced by the action of waves, seabed roughness, shape of the coastline, physical, natural and biological processes that affects natural flow. The numerical solver is based on filtering the Navier-Stokes equations using the LES methodology in the commercial Fluent code. More details of the numerical methodology and the governing equations have been presented in section 2.3.

5.2.1 Creation of the geometry

A 3-dimensional open channel domain with dimensions 10m x 5m x 3m illustrated in Figure 5.4 was design using Gambit. Tidal flow enters the domain at the left boundary and exits at the right boundary.

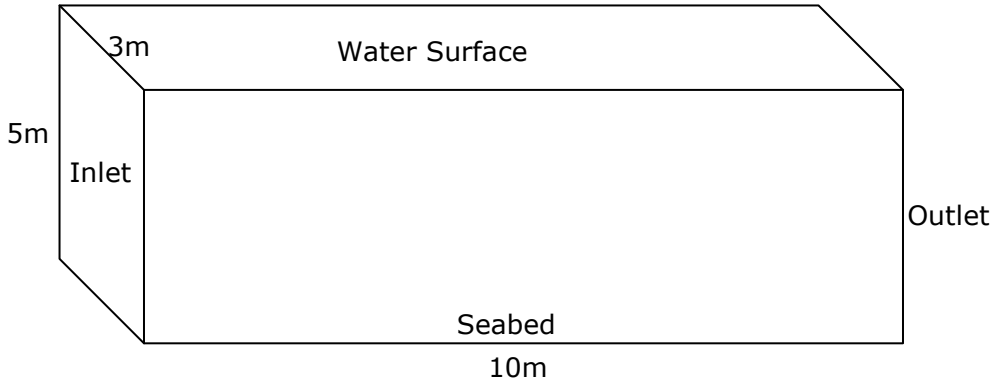

Figure 5.4: Computational domain geometry for an open channel flow.

5.2.2 Meshing strategy

The accuracy of simulation results depends on the number of cells or control volume in the mesh. A mesh sensitivity test was carried out based on three different meshes shown in Table 5.1 by monitoring the seabed drag coefficient.

Table 5.1: Mesh sensitivity test result

	Mesh 1	Mesh 2	Mesh 3	Mesh 4
Number of nodes	118,496	159,681	373,592	1,238,361
Bottom drag coefficient	.0028	0.0025	0.0025	0.0026

The results show that the drag coefficients for all meshes do not change significantly with number of nodes, having mean values of approximately 0.003. Since the sensitivity test results also suggest that a finer mesh will not add no significant value to channel bed drag coefficient, mesh 2 was selected for further analysis. Mesh 2 is a structured mesh consisting of a total of 150000 hexahedrons. The mesh constitute of 100(L) x 50(H) X

30(W) with 1500 inlet faces. Figure 5.5 is the three dimensional mesh showing the sides and the bottom wall of the channel and Figure 5.6 is a 2D vertical plane view (not to scale) of the same mesh.

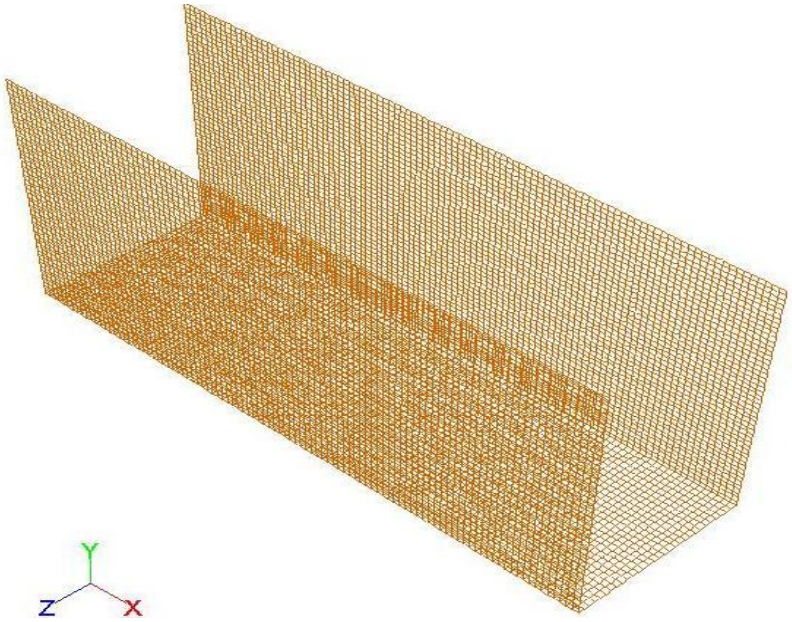

Figure 5.5: A 3-dimensional mesh showing the sides and the bottom wall.

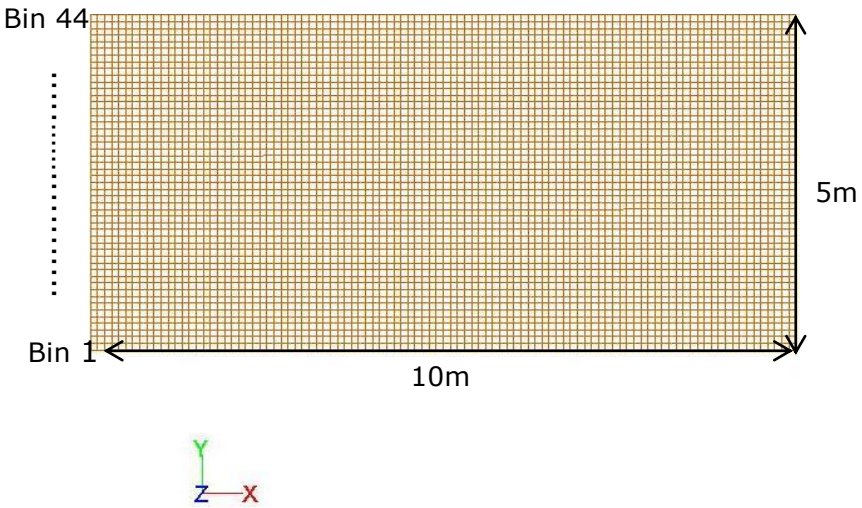

Figure 5.6: A-2 dimensional vertical plane mesh.

The vertical plane of the mesh is approximately 1:10 scale of the water depth at the Forth estuary while the horizontal scale is approximately 1:90,000. The boundary conditions are described in what follows.

5.2.3 Boundary Conditions:

Wall region: The flow is impermeable at the rigid walls so that, a no slip wall condition is specified for the channel sides and bottom. In three dimensions

that means velocity at the wall is; $u = v = w = 0$

Flow outlet: Gauge pressure of zero Pascal was specified at the outlet boundary.

Water surface: A zero shear was specified at the channel surface because it was assumed as a frictionless surface.

Flow inlet: Three different simulation velocity inlets were considered:

The uniform flow inlet: An inlet velocity of 0.37m/s was assigned to cell faces at the inlet by specifying a uniform profile file. The inlet velocity value was calculated averaging the value of the turbulent velocity profile measured by the ADCP at the Forth estuary.

The $1/7^{th}$ power law velocity profile inlet: The $1/7^{th}$ power law velocity profile data was evaluated based on the mean value of 0.37m/s and a maximum velocity of 0.49m/s of the turbulent velocity profile measure by the ADCP at the Forth estuary.

ADCP experimental velocity profile inlet: This profile is based on the data sampled using the ADCP at the estuary. There are evidences of turbulent fluctuations due to waves, bottom bathymetry, shape of the coastline and other physical and natural processes on this particular velocity profile.

The uniform and the $1/7^{th}$ power law velocity profiles are used as base case studies to benchmark the numerical simulation resulting from the ADCP

data simulation case. All inlet velocity profiles were specified as point profile files. The profiles were extrapolated using the zeroth order extrapolation technique. A turbulent scale of one meter length, a 10% turbulent intensity and the spectrum synthesizer based on the work of Smirnov (89), was specified as the random flow generator in LES of the open channel. The technique is based on synthesising a divergence free velocity vector that generates a non-homogenous and anisotropic flow field that represents turbulent velocity fluctuations and also satisfies the continuity equations. The flow problem was solved for an unsteady viscous incompressible flow using water at 20 degrees centigrade with density 998.2kg/m3 and viscosity 0.001003 kg/m-s as constant values.

5.2.4 Solution Methods

The governing equation presented in section 2.3 was discretisized using the finite volume method with a second order implicit transient formulation. A simple scheme algorithm was used to guarantee the conservation of the continuity equations. The numerical procedures and settings were repeated for three different simulation cases based on the uniform flow velocity inlet, the $1/7^{th}$ power law velocity inlet and the experimental turbulent velocity profiles measured by the ADCP from the Forth estuary.

The continuity, the x-velocity, y-velocity and z-velocity residuals were monitored for convergence. The absolute criteria value set for each parameter was 0.001. The steady state solution converged at approximately 5 iterations per convergence which is an ideal number recommended in the Ansys fluent manual (54).

The ability to visualise flow fields in a CFD calculation gives powerful insight into understanding the differences in the flow fields generated by specifying the ADCP measured velocity profile and the theoretical velocity profiles as boundary conditions. Visualisation plots for the evolved flow fields are shown for velocity magnitude pathlines, velocity vector plots and vorticity

magnitude contours plots. Investigation of the variation in velocity in space and time of the turbulent flow field are also presented.

5.2.5 Examining pathlines for uniform flow simulation case.

A pathline describes the path a massless fluid particle takes over time. Pathlines undergo natural changes as the flow progresses for transient flow calculations. The pathlines presented here are coloured by the velocity magnitude in order to visualise the velocity changes with time. The velocity magnitude is one of the critical parameters that determines dynamic loading and performance of a tidal current energy converter.

The changes in the pathlines over time are presented as instantaneous plots at 7.8s, 80.6s, 147.3s, 158.5s, 202.5s, 218.5s in Figures 5.7, 5.8, 5.10, 5.12, 5.13 and 5.14 respectively. The results are discussed in terms of velocity variation in time and space based on a vertical plane slice of the flow field extracted from the middle of the channel.

The input velocity of 0.37m/s for the uniform flow simulation case increased to a local maximum of 0.53m/s somewhere close to the top left corner of the plane in Figure 5.7 after 7.8 sec of simulation time.

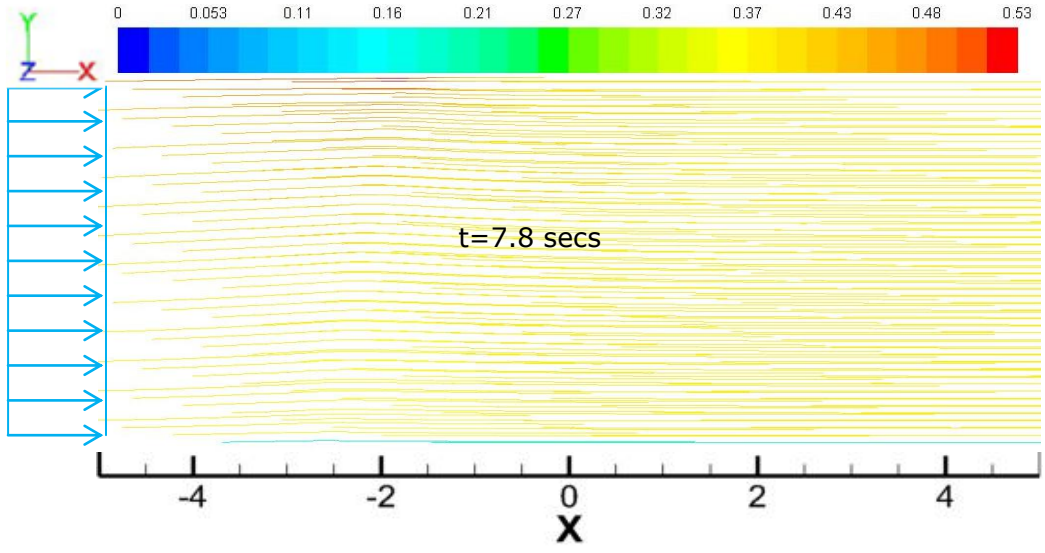

Figure 5.7: Pathlines at t = 7.8s

The pathlines at t = 80.6s in Figure 5.8 below evidently show some changes

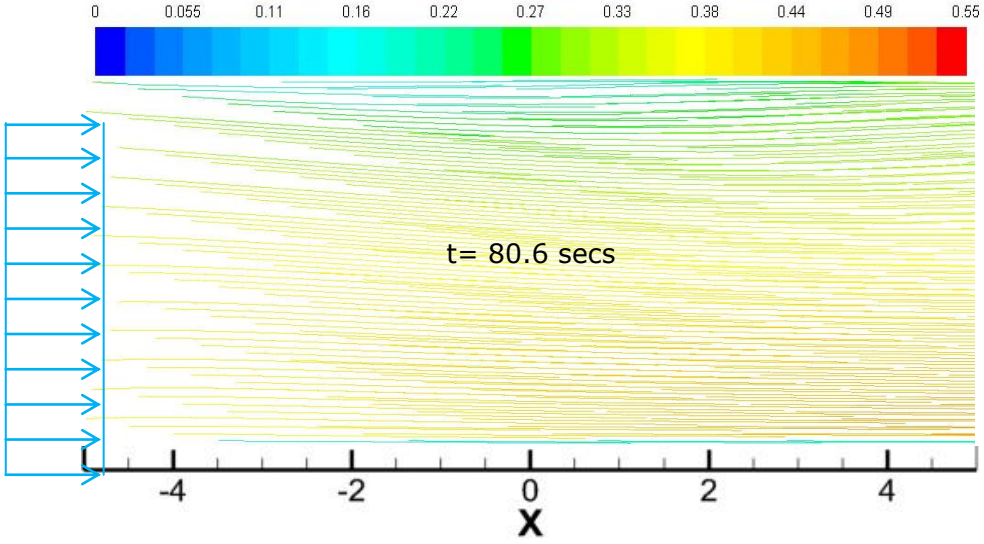

Figure 5.8: Pathlines at t = 80.6s

that has taken place from a uniform profile at inlet. The velocity of the fluid at the water surface is seen to have lower values than values at the middle of the plane. Line plots shown in Figure 5.9 taken at five different locations elucidate the instantaneous velocity magnitude profiles in the domain at t =80.6s.

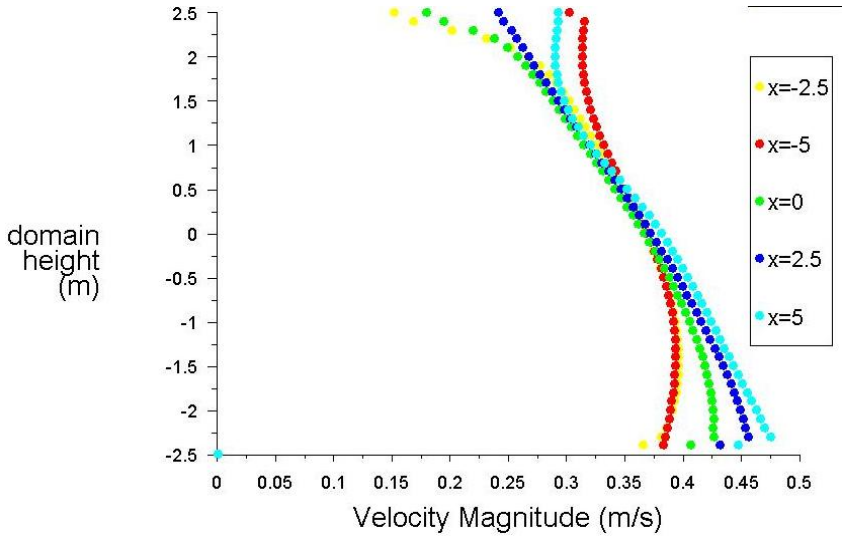

Figure 5.9: Velocity profiles at t= 80.6s.

The locations were chosen at equal intervals beginning at the inlet where x =-5m to the outlet where x=5m. The zero location lies at the centre of the simulation domain.

The velocity profiles at each spatial location in Figure 5.9 generally show a reduced velocity towards the top of the channel, more significantly at locations where x = -2.5 and 0 (mid channel). This is because the plots represent the instantaneous turbulent velocity profiles which changes from instant to instant. The averaged profile will be comparable to the $1/7^{th}$ power law profile for a fully developed flow. Although there is some evidence of invertion of velocity profiles associated with turbulence, the profiles generally lacks significant turbulent fluctuations comparable with a turbulent velocity profile measured from a real site. The level of turbulence fluctuation simulated is determined by the fluctuating velocity algorithm integrated into the LES code and the wall boundary effects.

Further investigation of the evolution of the velocity pathlines at 147.3s is carried out by observing the instantaneous plot in Figure 5.10. The velocity magnitude pathlines depict an open channel flow with velocity magnitude increasing from a minimum close to zero at the seabed to a maximum of 0.58m/s towards the water surface.

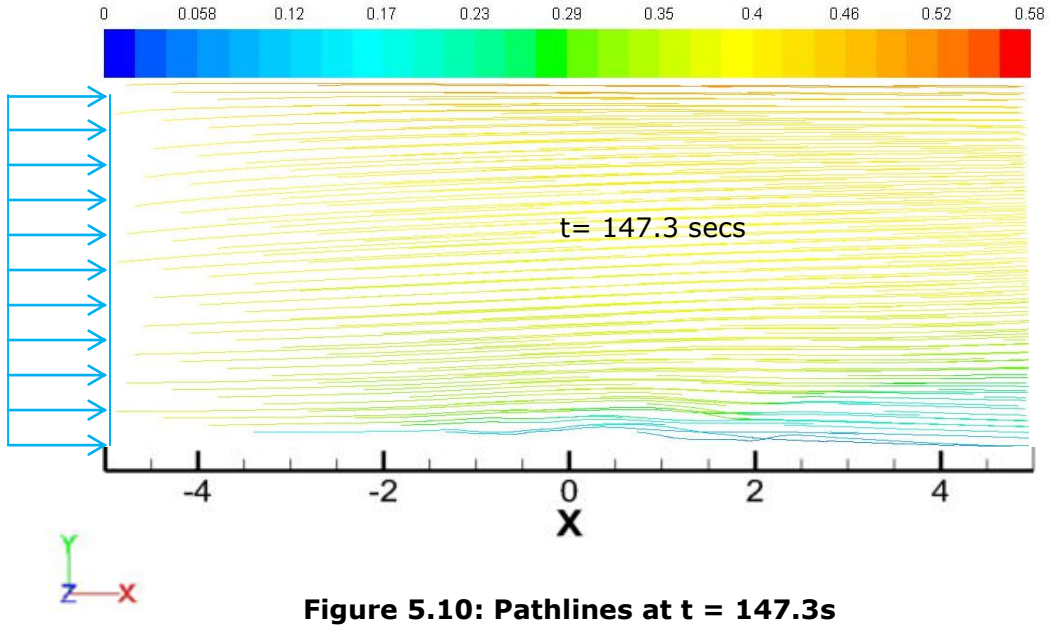

Figure 5.10: Pathlines at t = 147.3s

The shapes of the velocity profile associated with this flow field are presented in Figure 5.11 below.

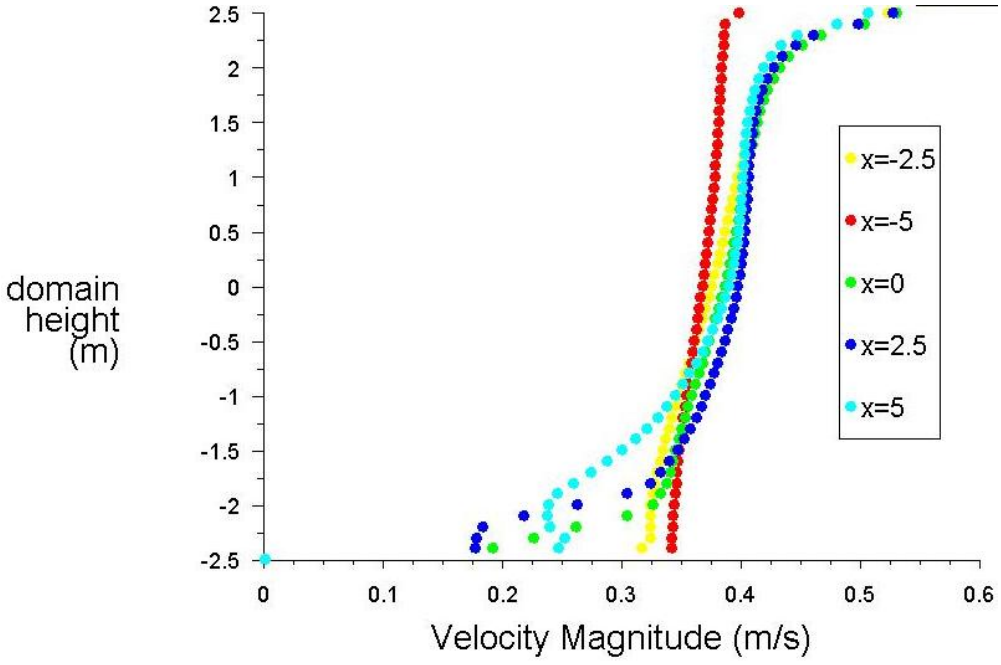

Figure 5.11: Velocity profiles at t= 147.3s

Figure 5.11 show the velocity profiles sampled at 5 different spatial locations ranging from x=-5m to x=5m. The line plots majorly show increase in velocity magnitude from a minimum near the bed to a maximum near the water surface. The shapes of the profiles except that at the inlet appears to agree with the assumption and description of a fully developed channel flow: A relatively uniform flow is exhibited by the profile at x = -5 (red plot) at the inlet. Velocity shear in the streamwise direction is apparent in the other four velocity profiles. Although the plot portrays changes in flow profile in time and space, there is however no evidence of fluctuation on the velocity profile as depicted by a single realisation of the experimental velocity profile presented in chapter 4 in Figure 4.14. The evolution of the velocity magnitude path lines were further investigated at instantaneous times t= 158.5s, 202.5s, and 218.5s by observing the behaviour of the pathlines plots in Figures 5.12, 5.13 and 5.14 respectively.

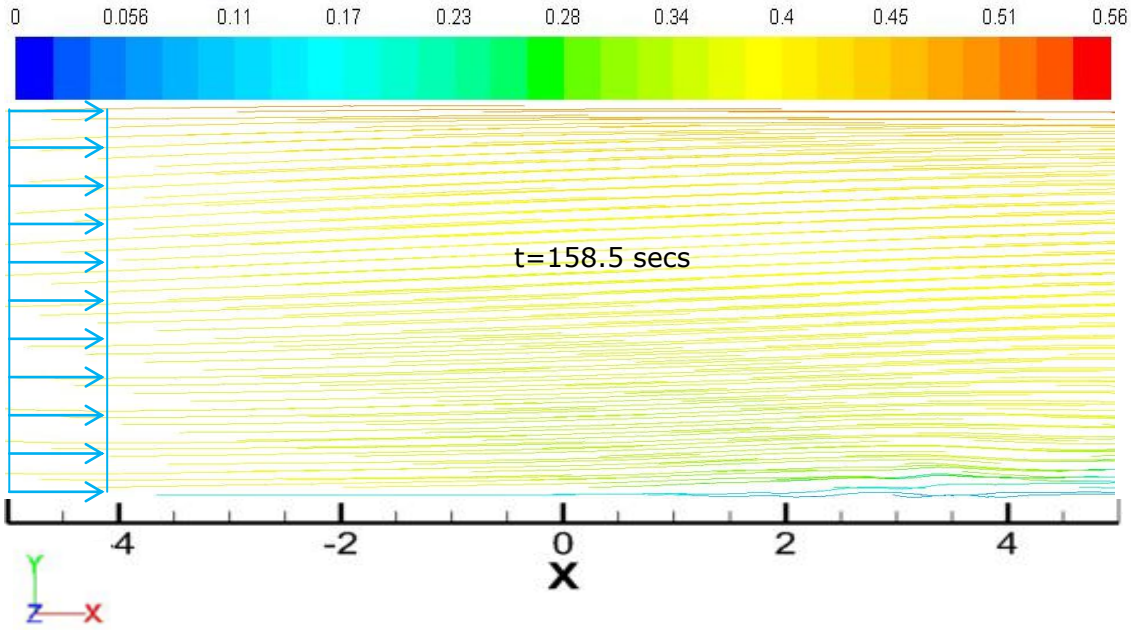

Figure 5.12: Pathlines at t = 158.5s

The appearance of flow field at t= 158.5s is not significantly different from the one at t= 147.3s. It appears to have similar pathlines behaviour showing a minimum velocity close to the seabed and a maximum velocity magnitude now reduced to 0.56m/s at the water surface.

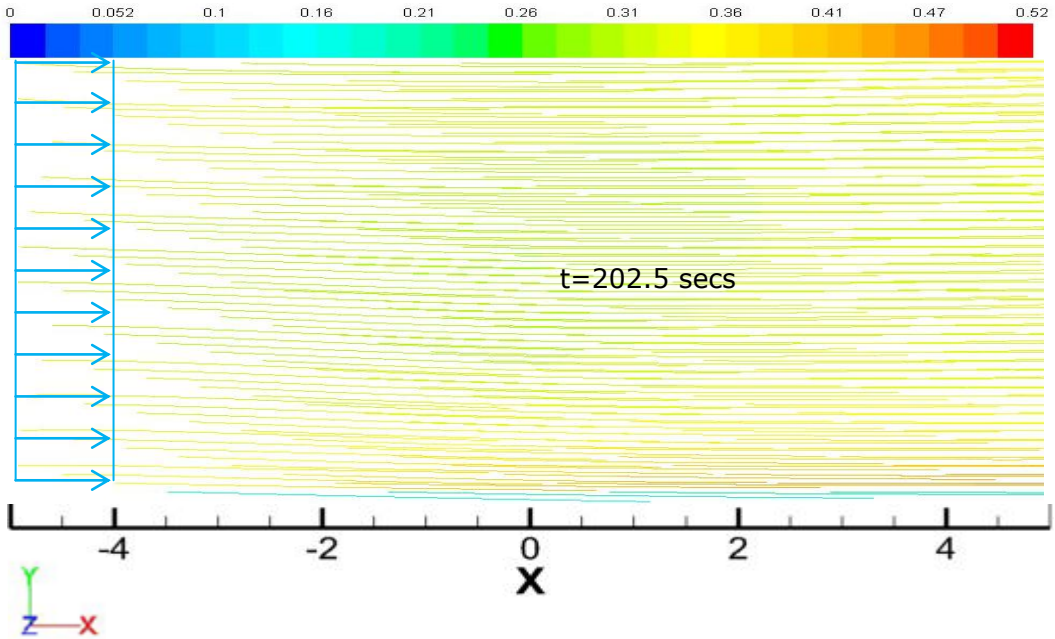

Figure 5.13: Pathlines at t = 202.5s

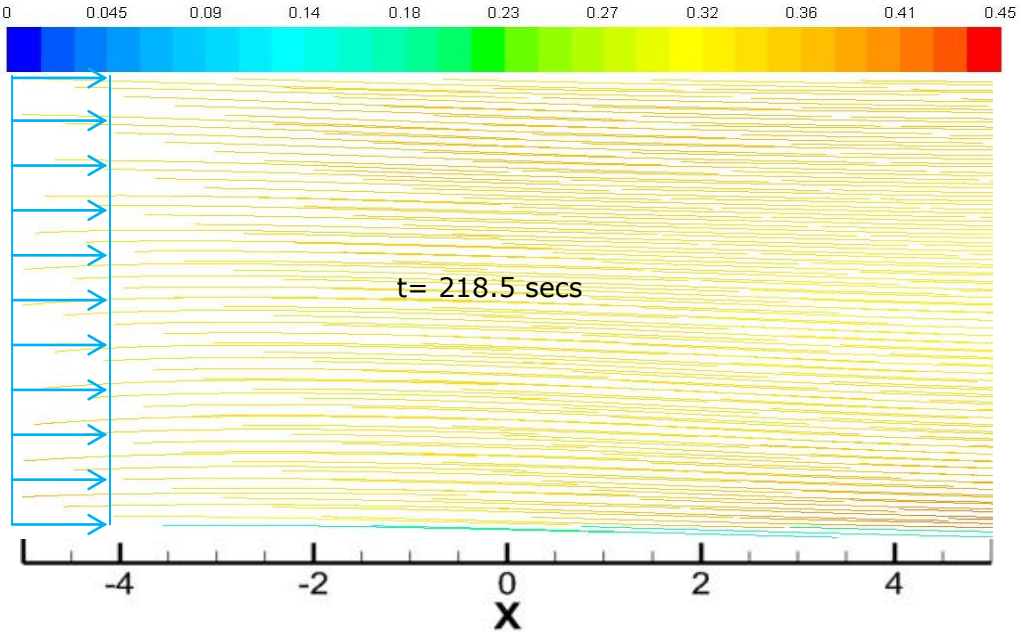

Figure 5.14: Pathlines at t = 218.5s

The double drag feature appear to be replicated in the flow field at t= 202.5s recognised by the colour coding in Figure 5.13. The maximum velocity magnitude at this time is further reduced to a value of 0.52m/s as seen from the instantaneous plot. Lastly, the instantaneous flow field at t= 218.5s in Figure 5.14, show a reduction of the maximum velocity with value of 0.45m/s. In general, although there is evidence of velocity fluctuations in space and time from all instantaneous plots, it is not significant. The uniform flow velocity profile is modified by specification of the non-slip boundary condition at the channel bottom.

In CFD calculations with uniform flow specified at inlet, it is anticipated that the flow will develop to assume the $1/7^{th}$ power law velocity profile shape at some distance downstream of the channel. Therefore a flow field initialised with a $1/7^{th}$ is expected to evolve faster comparatively. In what follows, the implications of specifying the $1/7^{th}$ power law at the inlet will be investigated to understand the flow field behaviour.

5.2.6 Examining pathlines for 1/7th power law flow simulation case.

The data used for the 1/7th power law simulation case is based on the maximum velocity of 0.49m/s attained during sampling the 309th experimental velocity profile at the Forth estuary. The values defining the profile data points were evaluated using equation 4.9. The profile data was specified as a profile file at the inlet of a LES of an empty channel. The influence of the 1/7th power law velocity profile on the evolution of the flow field are visualised as velocity magnitude pathlines, velocity vector plots and vorticity contour plots. Figure 5.15 shows the pathlines plot at t= 9.0s. At 9.0s of simulation flow time, the maximum velocity input of 0.49m/s of the 1/7th power law profile remained relatively the same. Appreciable changes were yet to occur because the simulation is at an early stage.

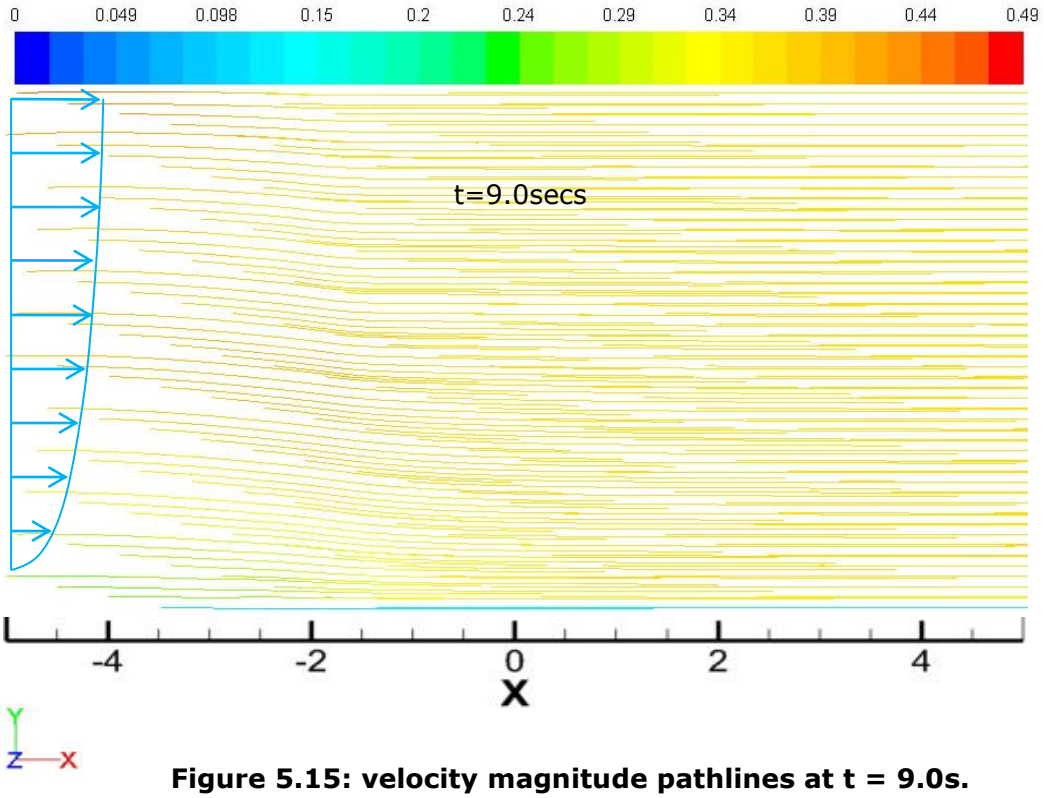

Figure 5.15: velocity magnitude pathlines at t = 9.0s.

However at 27.7s of simulation time, significant changes became obvious with some fluid particle velocity reaching a maximum of 0.53m/s, a value

higher than the input maximum as seen in Figure 5.16 below.

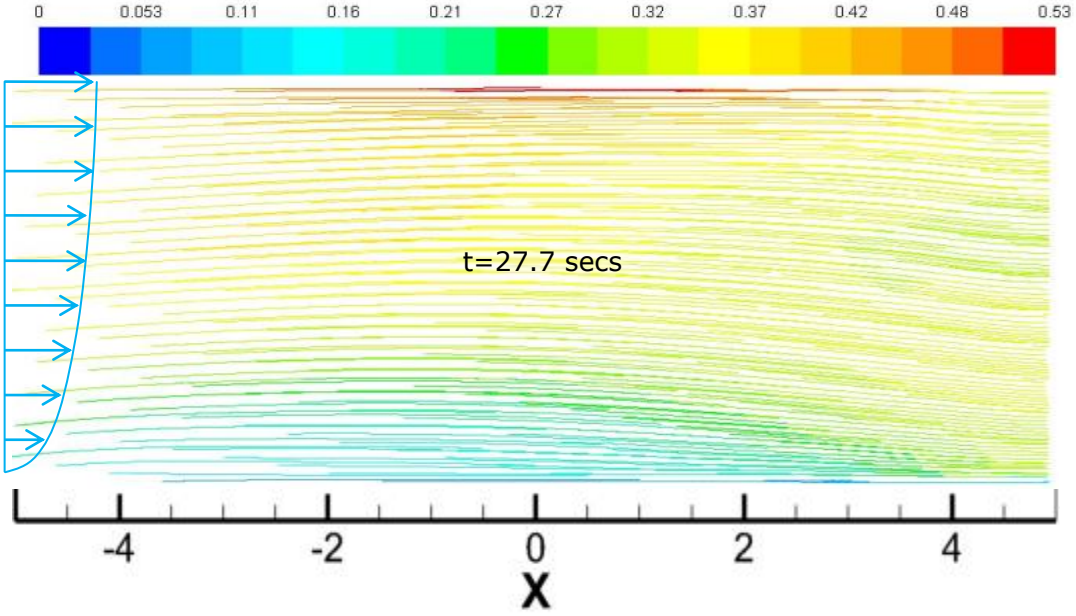

Figure 5.16: velocity magnitude pathlines at t = 27.7s

Figure 5.17 below illustrates the spatial variation in velocity magnitude

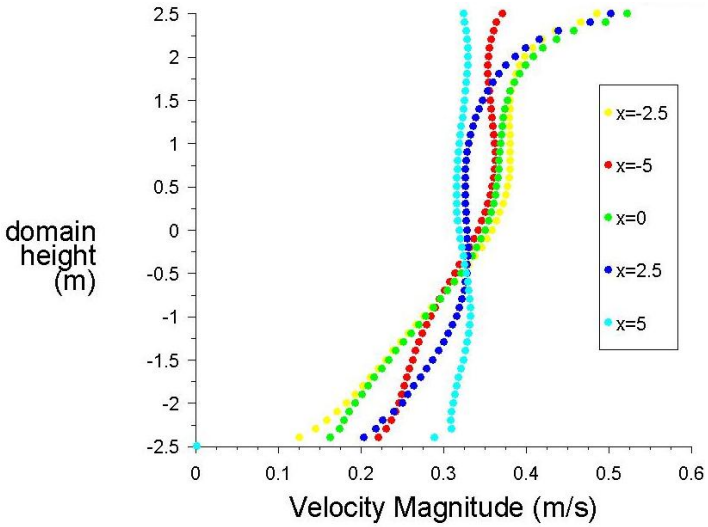

Figure 5.17: Velocity profiles at t=27.7s

profile along the channel at different spatial locations. The plot in Figure 5.17 generally show increase in velocity magnitude towards the water surface in agreement with behaviour of the power law profiles but with

differing shapes. The velocity magnitude plot in Figure 5.17 corresponds to vertical spatial locations at x =-5m, x= -2.5m, x = 0m (mid channel), x = 2.5m and x = 5m. Further investigation of the flow field evolution was carried out by examining the pathlines plot at t = 58.5s in Figure 5.18 below.

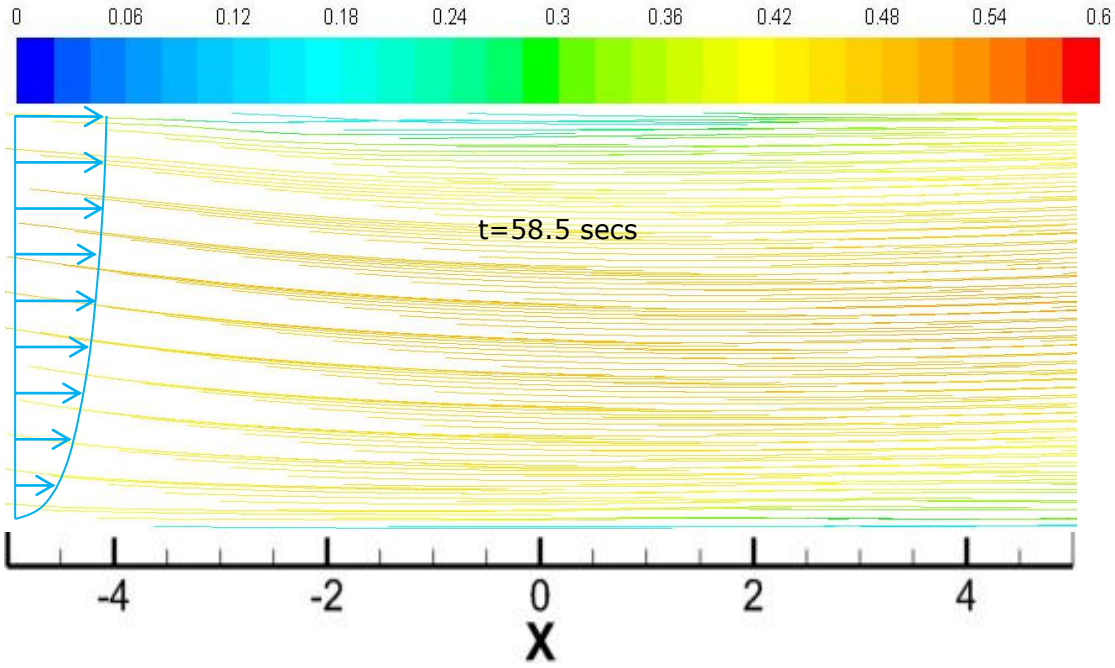

Figure 5.18: velocity magnitude pathlines at t = 58.5s.

The plot shows a reduction in the velocity of the water particles at the water surface. This flow behaviour signifies the evidence of shear near the water surface. Similar observations have been made in natural flows by Fan (78) in a costal raft-culture area where it was referred to as a 'double drag' effect. The double drag effect could also be caused by wind, surface waves and other natural processes on the water surface. However, in numerical simulation, it is attributed to the effect of the random velocity generating technique integrated into the LES solver and the boundaries. The maximum velocity attained at this instant was 0.6m/s confirming the fluctuating nature of the flow field. The velocity magnitude profiles plot in Figure 5.19 below corresponding to the pathline plot in Figure 5.18 above clearly illustrates the shapes of the velocity profiles associated with the pathlines

plot. The velocity profiles were sampled from five spatial locations x= -5, x=-2.5, x=0, x=2.5, x=5 along the x-axis of the channel. The 'double drag' effect is obvious from the line plots.

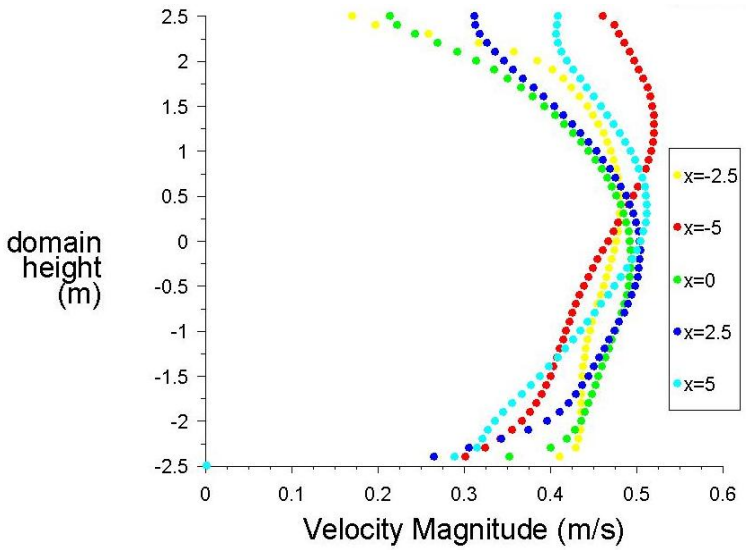

Figure 5.19: Velocity profiles at t=58.5s.

The flow field is further examined at t = 108.5s, 158.5s, 208.5s by observing the pathlines plots in Figures 5.20, 5.22 and 5.23 below.

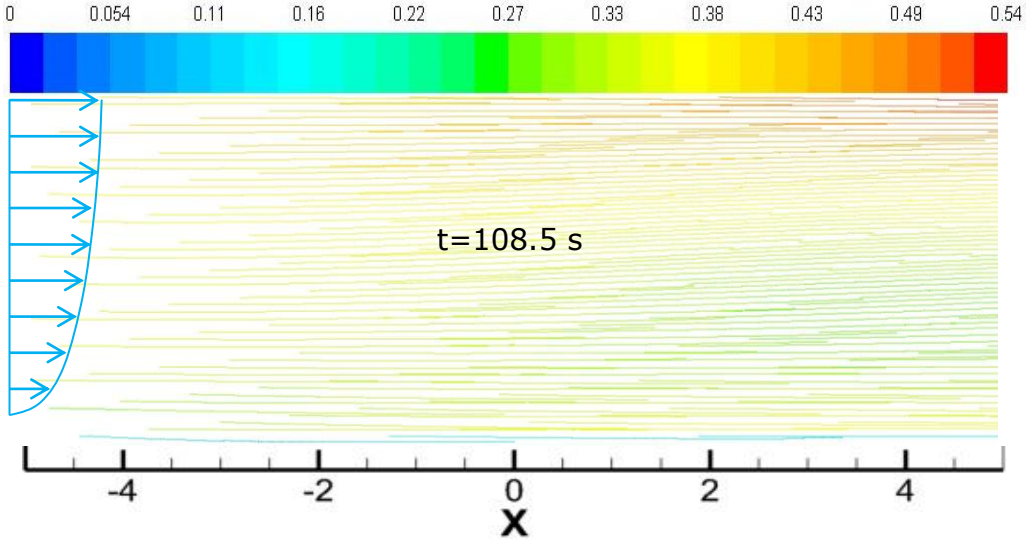

Figure 5.20: velocity magnitude pathlines at t = 108.5s.

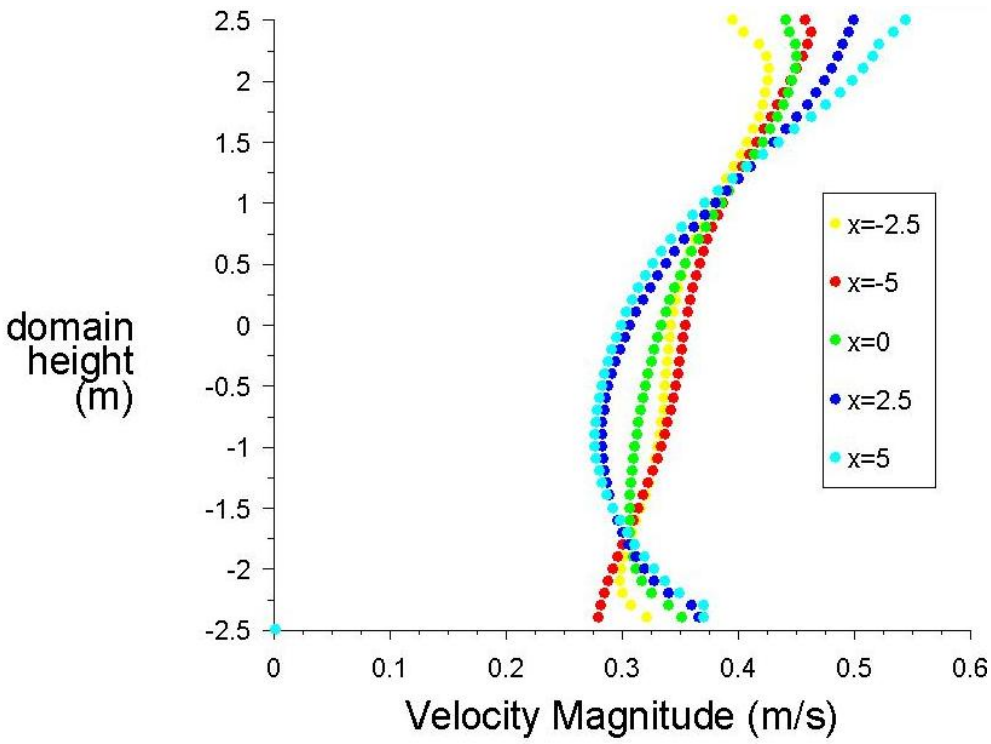

Figure 5.21: Velocity profiles at t=108.5s.

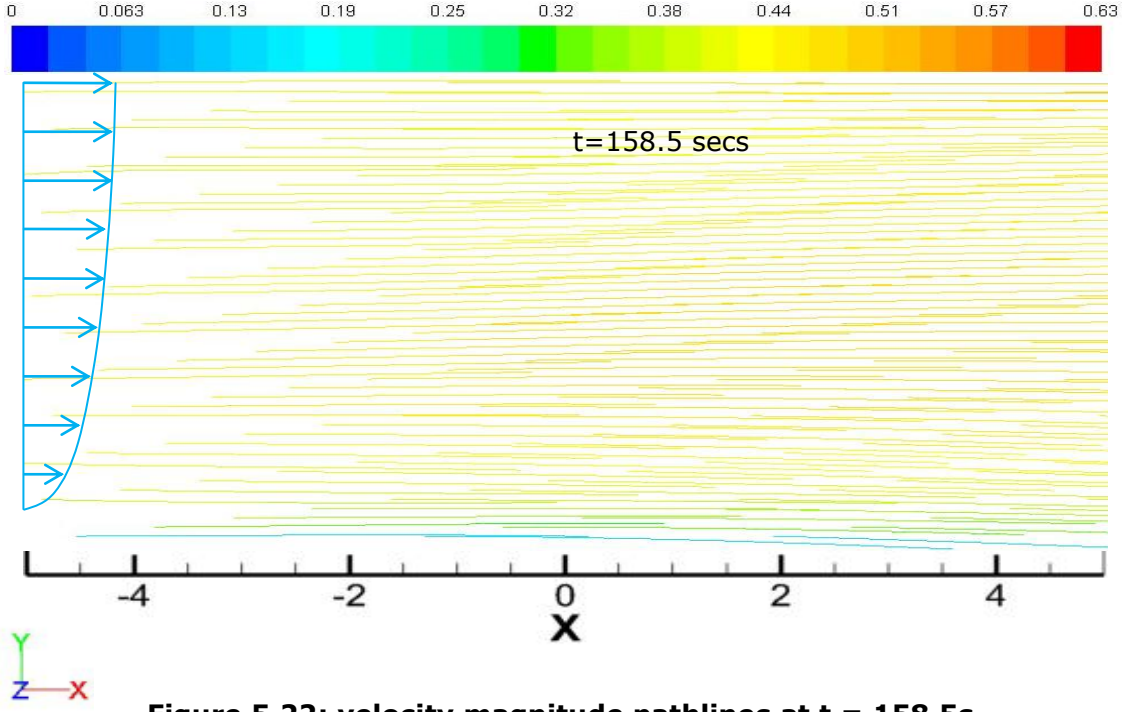

Figure 5.22: velocity magnitude pathlines at t = 158.5s.

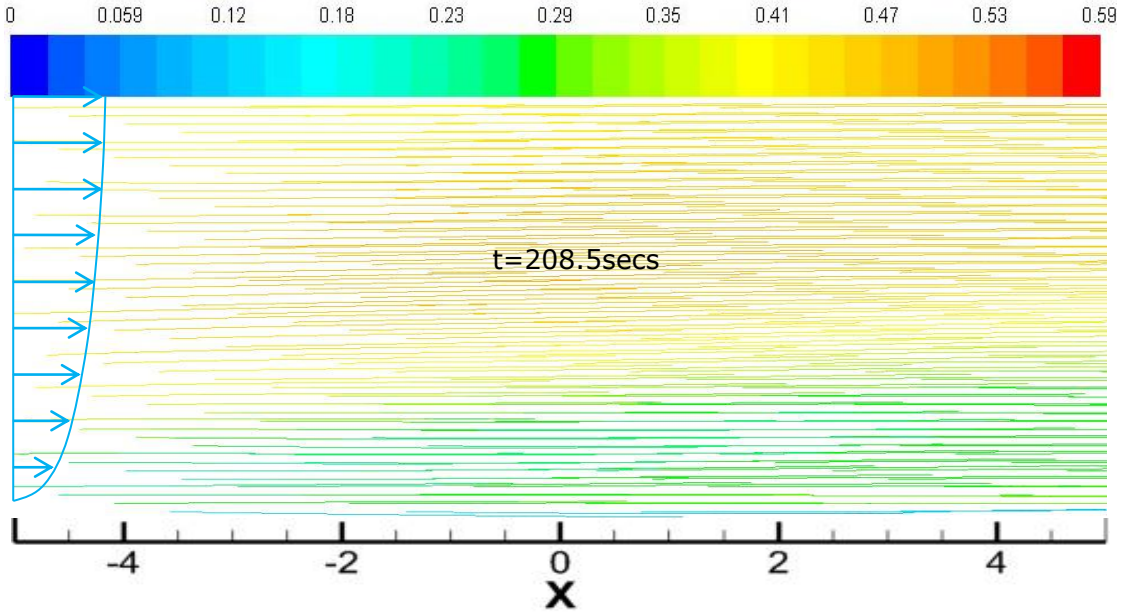

Figure 5.23: velocity magnitude pathlines at t = 208.5s.

Examination of the flow fields at t= 108.5s, 158.5s and 208.5s show a replication of the behaviour already observed and described in previous plots. Basically showing evidence of a fluctuating velocity profile over time and space modified by the boundary conditions. Figure 5.21 show evidence of velocity inflection of the profiles indicating some form of turbulence at t=108.5.

From the foregoing plots, it can be stated that, the pathlines and the velocity magnitude plots for the uniform flow and the $1/7^{th}$ power law simulation cases display similar characteristic. Their similarity is judged on the fact they are both mean and one dimensional approximation of the experimental velocity profile.

Comparison of the velocity profiles sampled at different instantaneous times for the uniform and the $1/7^{th}$ power law simulation cases show relatively smooth with the occurrence of double drag behaviour or inversion of the velocity profile at some time and point in the flow. The simulated turbulence in both cases using LES can summarily be described as a pulsation of the mean flow having some form of turbulence enhanced by the random flow

generation procedure integrated in the LES code and the wall boundaries. The behaviour of the pathlines for the uniform flow and the $1/7^{th}$ law velocity profile can be described as well patterned or organised. However, the flow in real sea state is chaotic. In what follows, investigation carried out on flow field simulated with real current profiles are presented and compared with the theoretical velocity profile simulation cases.

5.2.7 Examining pathlines generated by the experimental velocity profile.

The experimental velocity profile used for the third simulation case represents a single realisation of a turbulent velocity profile sampled at the Firth of Forth within 60s. This turbulent velocity profile has been analysed and reported in section 4.4.3. The maximum velocity for the profile was 0.49m/s and it did not occur at the water surface as predicted by the theoretical power law profiles for an open channel flow. For the numerical simulation specification, the 3-components of the turbulent velocity profile were used at the inlet boundary of a LES.

The evolution of the flow field is presented in form of velocity magnitude pathlines, velocity magnitude vector and vorticity contour plots. Figure 5.24 is the instantaneous pathlines plot at t = 31.4s.

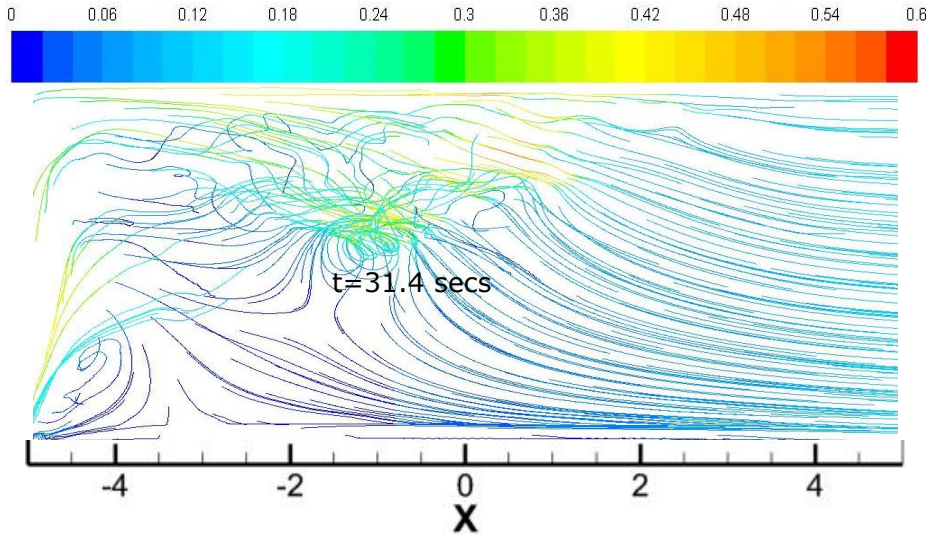

Figure 5.24: Experimental velocity pathlines at t = 31.4s.

The velocity magnitude pathlines are noticeable tangled in the upstream region of the domain. The chaotic and tangled flows lines are indication of high level of shear in the flow. The downstream region appear to have uniform flow lines due to the stage of the simulation because the effect of the inlet conditions are yet to be felt in the downstream region.

The pathlines appear to curl upward at the channel bottom close to the inlet region due to adverse pressure conditions resulting to flow reversal. The effect of the experimental velocity profile specified at the inlet, turbulence generated at the bottom channel wall in addition to the fluctuating velocity algorithm in LES has enough potential to cause turbulence that spread up to the water surface. Figure 5.25 below is a plot of the turbulent velocity profiles associated with the instantaneous pathlines plot in Figure 5.24 above. The velocity profiles were sampled at different spatial location along the x-axis of the simulation domain.

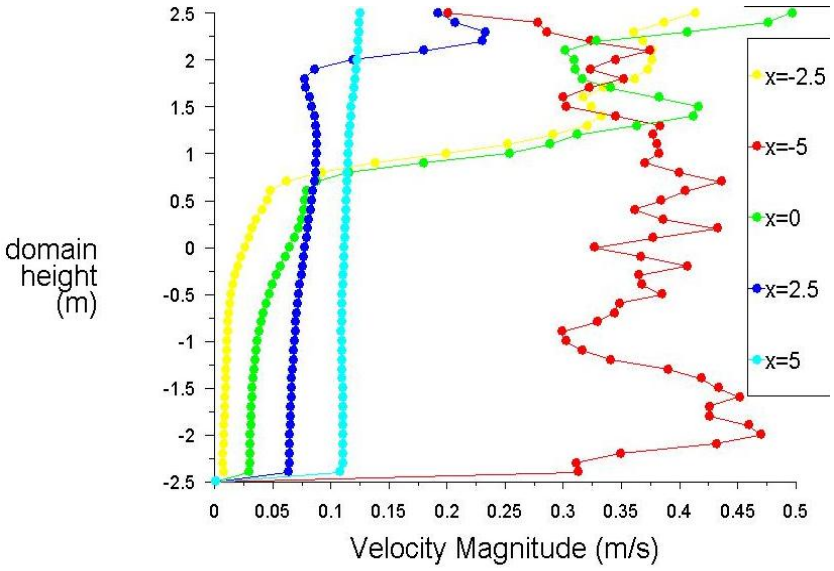

Figure 5.25: Turbulent velocity profiles at t=31.4s.

Investigation of the turbulent velocity profiles deduced from the pathline plot show relatively higher velocity magnitude towards the water surface and lower velocity magnitude at the lower region. The reduced velocity at the lower region of the channel is due to the resistance offered by the no

slip wall boundary condition at the channel bottom on the fluid. The lower velocity was offset by relatively higher velocity magnitude at the upper region to satisfy a divergence free velocity field.

The velocity profile at x=-5 (the red line plot) resembles the shape of the raw experimental velocity profile except at y = - 2.5 now modified by the no slip condition. Due to the simulation stage, the velocity profiles at the other spatial location remain mostly unaffected by the flow except towards the water surface, believed to be the effect of high level of turbulence reaching up to the water surface.

A further survey of the flow field generated by the experimental velocity profile at t = 90.9s, t = 146.9s and t = 227.4 continues to show a chaotic behaviour of the flow field exhibiting irregular unidentifiable patterned flow lines. Some of the pathline have been removed to give a clearer illustration. It is very obvious that turbulence has saturated the entire flow field. Related to the pathlines plot at t = 90.0s in Figure 5.26 is a plot of turbulent velocity profiles sampled at five different spatial location in Figure 5.27 shown below.

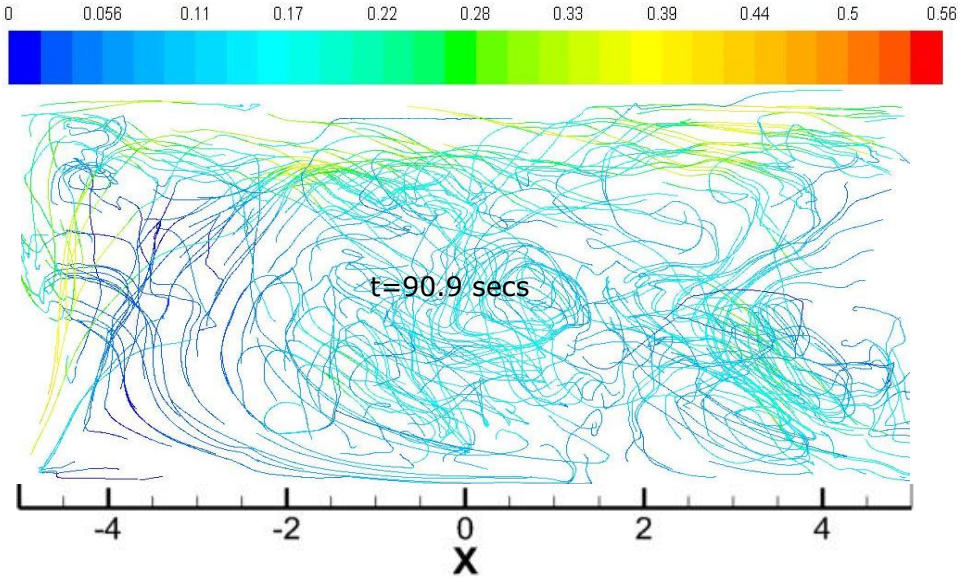

Figure 5.26: Experimental velocity magnitude pathlines at t = 90.9s.

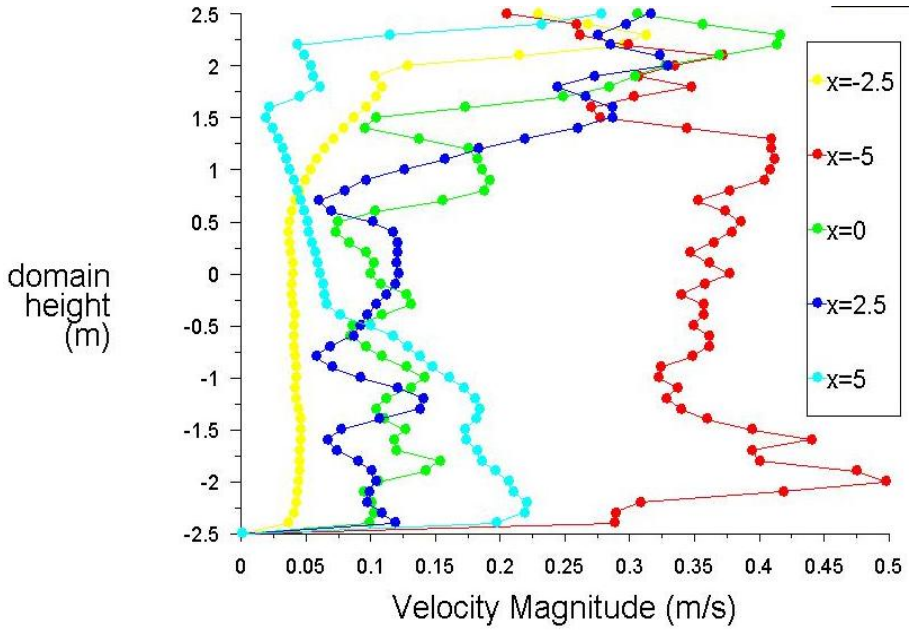

Figure 5.27: Turbulent velocity profiles at t=90.9s

The pathlines plot in Figure 5.26 shows that a maximum value of turbulent velocity of nearly 0.56m/s was attained by the fluid. A close examination of all the turbulent velocity profiles in Figure 5.27 again shows that, all the profiles apart from the one at x =-5 (inlet) generally have lower velocity magnitude than the input values especially at about the lower half of the channel. The significant reduction in velocity magnitude is attributed to the effect of flow reversal caused by the adverse pressure condition created by turbulence. The relatively lower values of velocity magnitude are then offset by the higher values velocity values towards the water surface to satisfy the divergence free velocity vector (continuity equation).

The pathlines plots at t = 146.9s in Figure 5.28 and the corresponding turbulent velocity profile plot in Figure 5.29 below are used to further examine the flow evolution. The flow lines in the pathline plot exhibit turbulence with the maximum velocity in the flow field reaching 0.67m/s a value, relatively higher than the input maximum value of 0.49m/s. The increase in velocity is required to offset the lower velocity in local regions of the fluid caused by the attempt of the fluid to reverse direction.

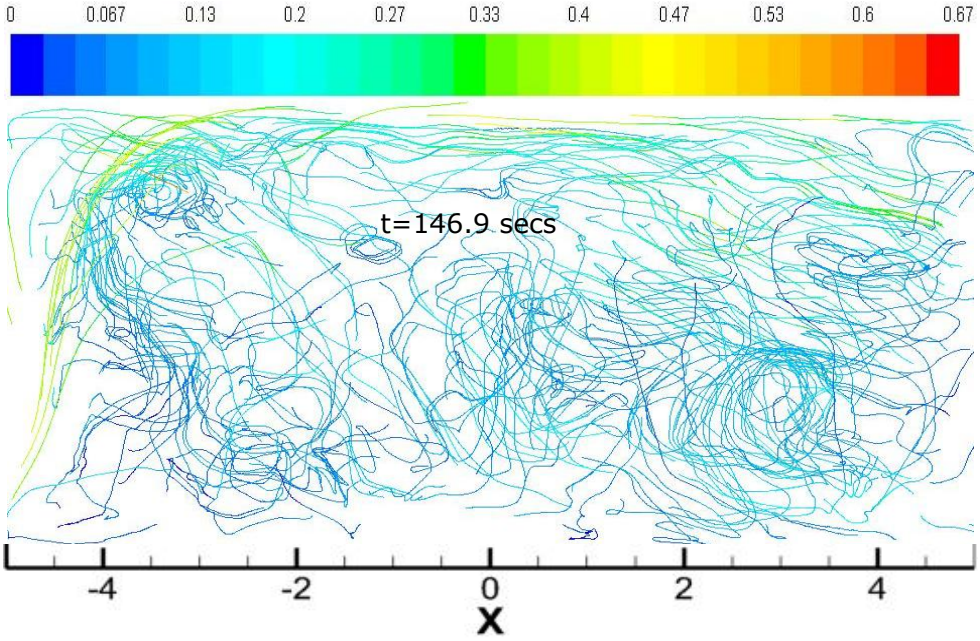

Figure 5.28: velocity magnitude pathlines at t = 146.9s.

The turbulent fluctuations are now evident on all velocity profiles which suggest that the chaotic motion has now saturated the entire water column.

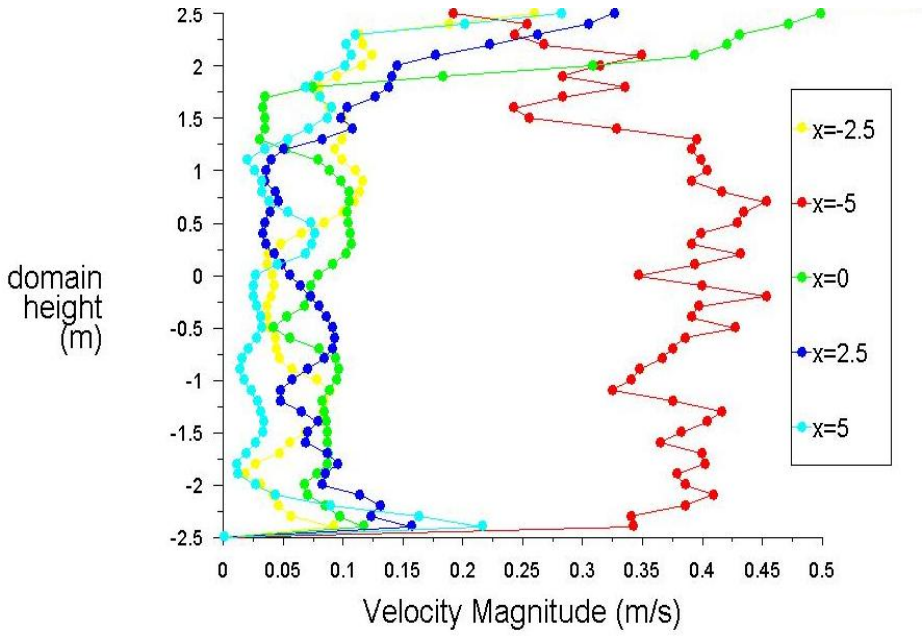

Figure 5.29: Turbulent velocity profiles for at t=146.9s.

The flow field at t = 227.4s shown as a pathlines plot in Figure 5.30 and velocity profile plot at 5 spatial locations in Figure 5.31 below are further used to investigate how the flow field has developed with time.

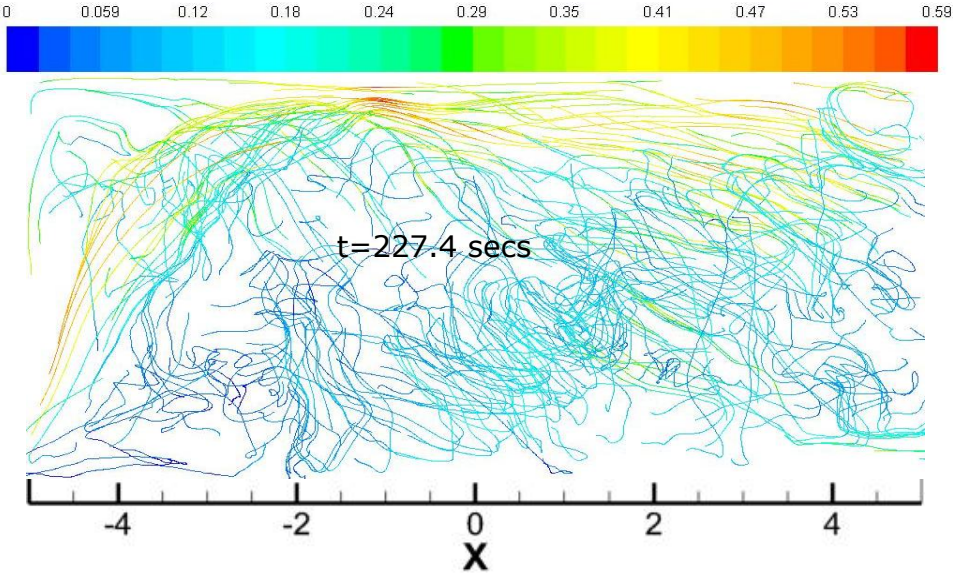

Figure 5.30: velocity magnitude pathlines at t = 227.4s.

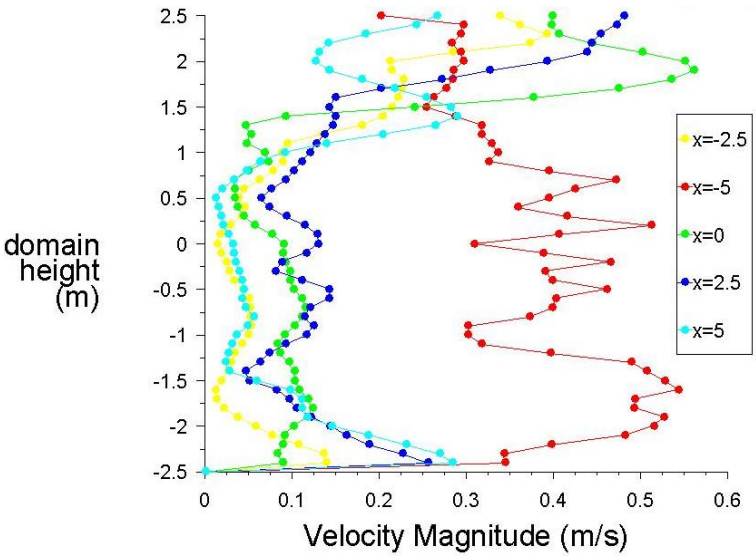

Figure 5.31:Turbulent velocity profiles at t=227.4s

The flow field plots at t = 227.4s exhibit similar trend of tangled and disorganised flow lines with associated turbulent velocity profile with significant fluctuations.

The behaviour of the flow fields simulated using the theoretical and the experimental velocity profiles described above are generally unsteady, fluctuating in space and time. The level of fluctuation is more significant in the experimental velocity profile simulation case because the specified profile at inlet is influenced by waves, estuary boundaries, seabed roughness and other physical and natural processes occurring at the Forth estuary. It is desirable to install a turbine for energy extraction in a good quality environment in terms of sufficient velocity magnitude and a smooth velocity profile. In reality, it is difficult to achieve that due to ambient turbulence generated by the aforementioned factors in any natural environment.

The occurrence of flow reversal due to adverse pressure gradient has significant consequences for submerged energy devices due to flow separation and vortex shedding. The adverse pressure gradient modifies the pressure distribution and subsequently affects the hydrodynamic forces acting on the devices.

Flow in natural environment is chaotic and also contain vortices. The vortex field associated with the three simulation cases are investigated in what follows.

5.2.8 Visualisation of vortices generated in flow field with a uniform flow inlet condition.

It has been mentioned that the curl of the velocity vector yields the vorticity magnitude. The parameter describes the tendency of the fluid to rotate with units in per second. It is important for characterising turbulence and has been utilised in this study to visualise turbulent structures generated in the three simulation cases. In what follows an evolution of the turbulent flow

field in terms of vorticity magnitude with a uniform flow inlet boundary condition is investigated and reported. The flow features for all simulation plots are examined using instantaneous slice of the flow field in the x – y or vertical plane where z = 0 (mid channel). Figure 5.32 is the instantaneous vorticity contour plot at 7.8s showing what appear like a parcel of fluid with a relatively strong vorticity around 0.6s-1 near the channel bed where x = -2.5m and having

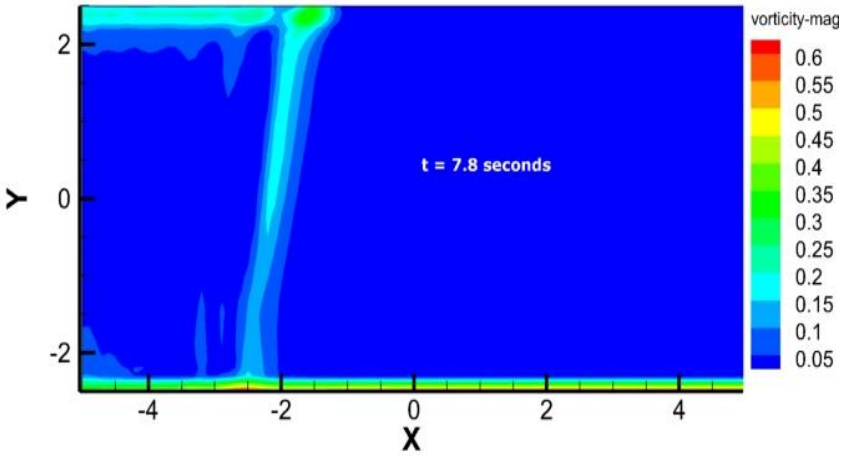

Figure 5.32: vorticity magnitude plot at t=7.8s

interactions with the water surface. The fluid parcel at the water surface appears to have diminished vorticity magnitude of around 0.3/s. This observed flow field behaviour seems to resemble the evolution of Kolk – boil vortices as observed by Matthes (81) in the study of macroturbulence in natural stream flows which was also reported in (47). A further investigation of the flow field t = 80.6s in Figure 5.33 below show evidence of dissipation. The evidence of dissipating structures at 80.6s undermine the possibility of kolk – boil vortices appearing earlier at t = 7.8s in a uniform flow inlet condition. The structure at t=7.8s is a possible effect of numerical variability occurring at early stage of simulations. In reality, kolk-boil vortices are sustained in flow in natural environment (81).

The local maximum vorticity magnitude increased from a maximum value of $0.6s^{-1}$ at t = 7.8s to a maximum of $0.9s^{-1}$ at 80.6s confined to the channel

bottom. The boundary layers exhibits significant values of background vorticity or turbulence not necessarily associated with large scale coherent structures (90). Turbulence is generated near walls and can also be dissipated near walls but not all generated turbulence is dissipated. Some turbulence exists in form of large coherent structures within the flow field. These structures oscillate and cascade their energy to smaller structures

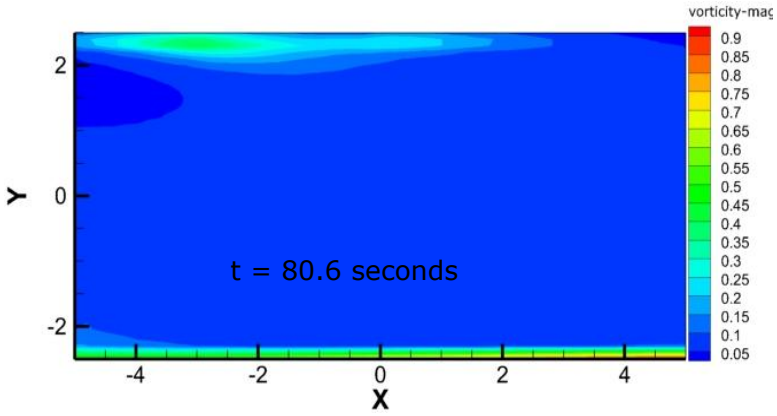

Figure 5.33: vorticity magnitude plot at t=80.6s

through which brings about possibility of maintaining ambient turbulence within a flow. The lack of turbulent structure therefore indicates significant turbulent dissipation. The instantaneous plots at t= 147.3s, in Figure 5.34 below also show evidence of turbulent dissipation although the vorticity magnitude has increased to a value of 1.1s-1 confined to the channel bed.

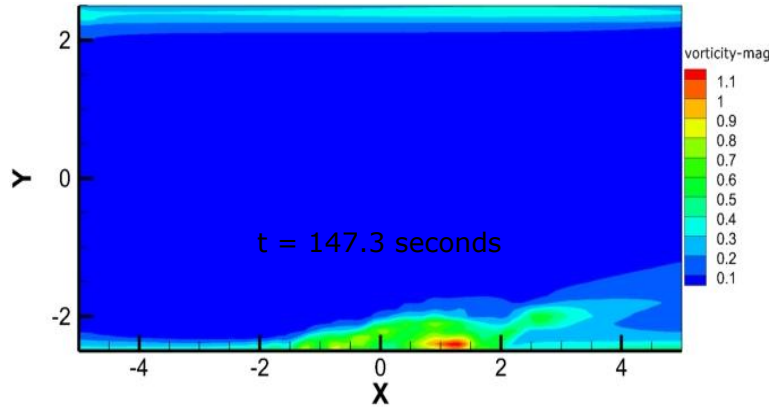

Figure 5.34: vorticity magnitude plot at t=147.3s

There are no significant turbulent structures in the outer flow away from the wall. There had been no further evidence of structures resembling kolk- boil vortices as noticed at the early stage of the simulation. So that the flow structure observed at t =7.8s at the early stages can only be attributed to the instability of the flow field due to initialisation. The turbulence in terms of vorticity generated near the channel bottom results from instabilities from very high shear generated due to the resistance encountered by the fluid as it flow over the channel wall surface. Since there are evidences of turbulence dissipation due to lack of significant coherent structures, it can be stated that the shear resulting from the instability with a uniform flow inlet condition is insufficient to sustain ambient turbulence in the outer flow. A further investigation of vortices generated at t = 158.5s is shown in the vorticity magnitude contour plot in Figure 5.35 below. Some interesting features that seem like low speed and high speed streaks of fluid can be faintly visualised in Figure 5.35 close the region of maximum vorticity magnitude at the channel wall. The streaks of fluid also show evidence of vortices due to turbulence flow. It is known that turbulence shear stress near wall is negligible and can easily be damped by the viscous forces. Thus turbulence fluctuation near the walls, scales according to the viscosity and

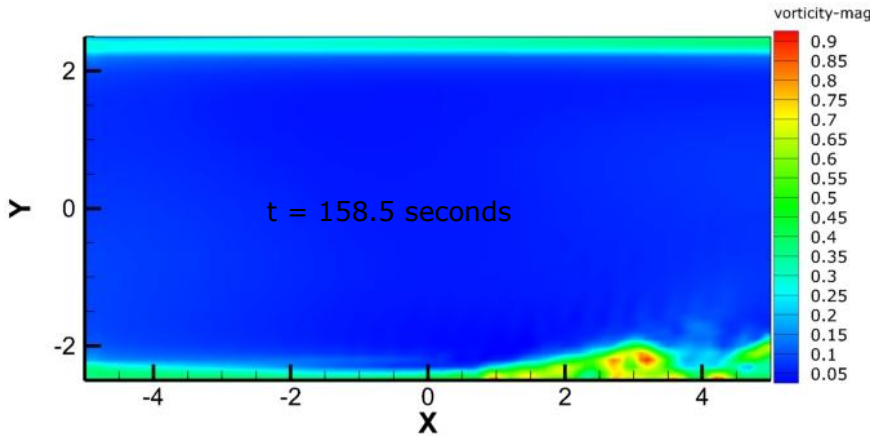

Figure 5.35: vorticity magnitude plot at t=158.5s

is felt at a very short distance away from the wall. Turbulent shear stresses dominate away from the wall and are responsible for most of the transport

of momentum in the flow. If a flow is highly turbulent, the low speed streaks can gradually lift away from the wall, ejected and burst while the high speed streaks of fluid rushes wall ward to sweep away the retarded fluid. This phenomenon known as the bursting phenomenon has been described in section 5.1.1 and is responsible for inflections of turbulent velocity profiles.

Further investigation of the flow field in Figures 5.36 and 5.37 at 202.5s and 218.5s respectively, show further evidence of turbulent dissipation with the maximum vorticity magnitude values now reduced to 0.65s^{-1} and 0.7s^{-1} respectively still confined to the channel beds.

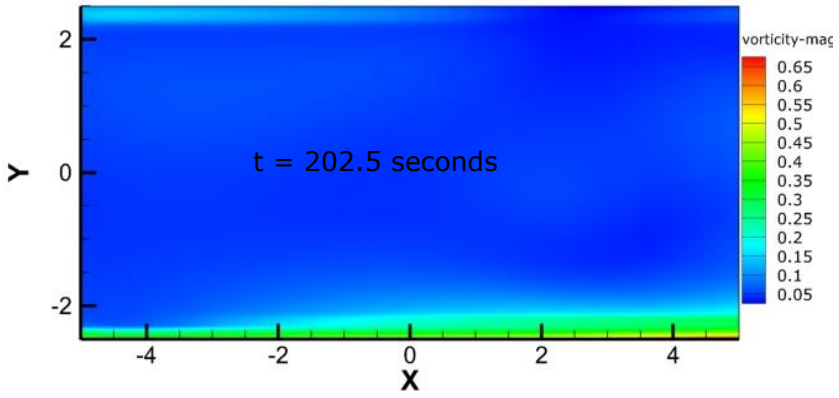

Figure 5.36: vorticity magnitude plot at t=202.5s.

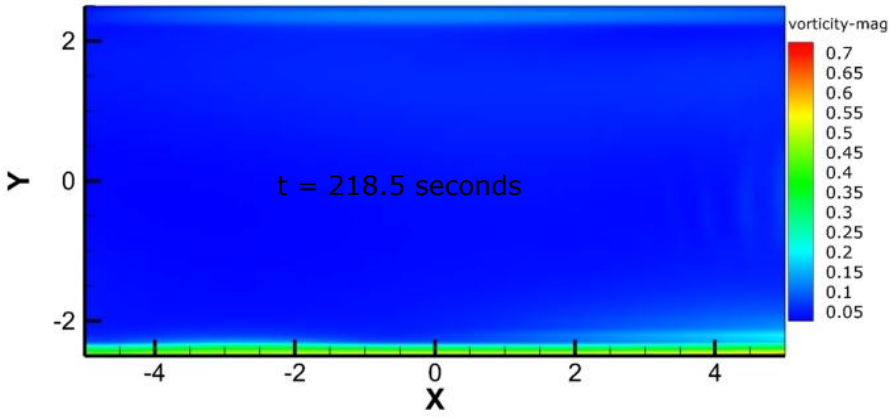

Figure 5.37: vorticity magnitude plot at t=218.5s.

The behaviour observed by investigating the instantaneous vorticity contour plots for the uniform flow simulation case can be summarised by stating that significant ambient turbulence resembling large scale flow processes cannot be generated intermittently and sustained in a LES using a uniform flow velocity inlet. Although a structure that looks like a kolk, formed at the channel bed at the early stage of the simulation, t = 7.8s seems to surge up to the water surface to become a boil. It was attributed to numerical instabilities due to initialisation process. There was no further evidence of another 'kolk' formation but turbulent dissipation. Kolk vortices are generated intermittently in a real turbulent flow near the bed and boils due to turbulence are associated with the development of bursting phenomenon that consists of streaky fluid structures that were found barely indistinguishable in the instantaneous vorticity plot at 158.5s. The scanty structures found in the uniform form simulation case could be seen as large scale structures because of the simulation methodology but can be better described as a pulsation of the mean flow containing fine turbulence.

5.2.9 Visualisation of vortices generated in flow Field with a 1/7th Power Law velocity profile at inlet boundary.

The development of the vorticty field for the 1/7th power law simulation case is investigated in this section. Figure 5.38 is a vorticity magnitude plot showing the evolved flow structures at 9.0s of the simulation time.

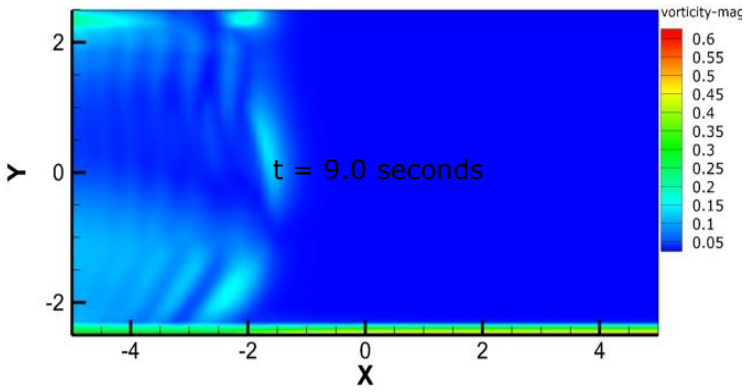

Figure 5.38: vorticity magnitude plot at t=9.0s

The 1/7th power law profile specified at the inlet boundary of a LES implies that the flow field exhibits a sheared velocity profile beginning at the inlet thereby reducing the simulation time necessary for flow transition. The 1/7th power law profile is generally accepted as a suitable approximation to a wall bounded developed open channel flow. The plot already indicates the presence of streaky fluid structures predominantly at the domain inlet region. The faster development of the streaky looking fluid structures in the 1/7th power law simulation case compared with the uniform flow case is due to the shear velocity profile specified as inlet condition. Another plot at t = 27.7s in Figure 5.39 shows the entire domain saturated with streaky looking

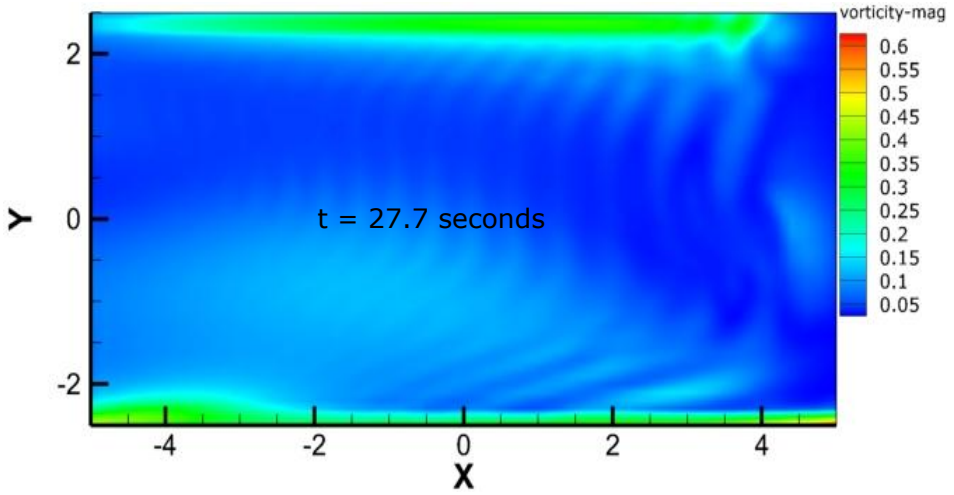

Figure 5.39: vorticity magnitude plot at t=27.7s.

fluid structures. The maximum vorticity value at t = 27.7s was about 0.6/s near the channel bed region. Also, the assumption of a frictionless wall at the water surface and a no slip wall at the channel bed can also be responsible for this development: in addition to the fluctuating velocity algorithm specified in LES, the no slip bottom boundary condition causes a further reduction of fluid velocity at the bed region while the velocity of fluid at other regions of the domain act to offset the lower velocity magnitude at the bed region to satisfy the continuity equation. A further vorticity magnitude plot at t=58.8s in Figure 5.40 shows no evidence of the streaky

structures as was observed in the previous instantaneous plot however, a free surface vorticity and channel wall vorticity with maximum magnitude

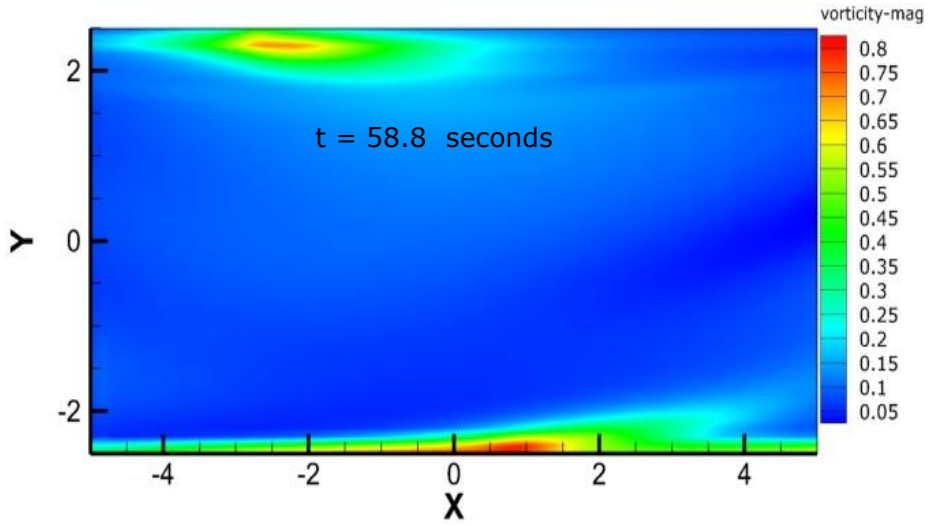

Figure 5.40: vorticity magnitude plot at t=58.8s

reaching up to 0.8 s^{-1} can be seen visible. The next instantaneous plot at t= 108.5s in Figure 5.41 show strong evidence of dissipating or diffusing flow structures with a slight decrease in the maximum vorticity magnitude to a

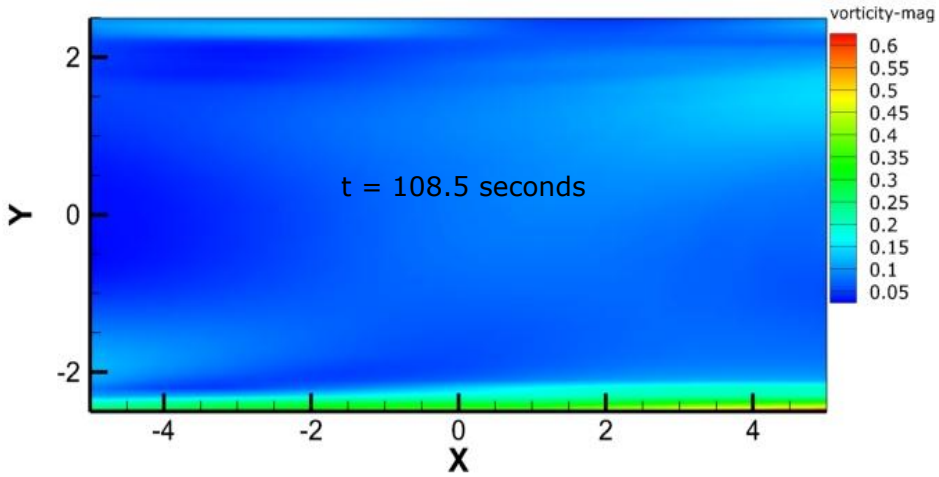

Figure 5.41: vorticity magnitude plot at t=108.5s

value of 0.6s^{-1}. Further investigation of the flow field at t = 158.5s in Figure 5.42 below shows an increase in the vorticity magnitude with a value

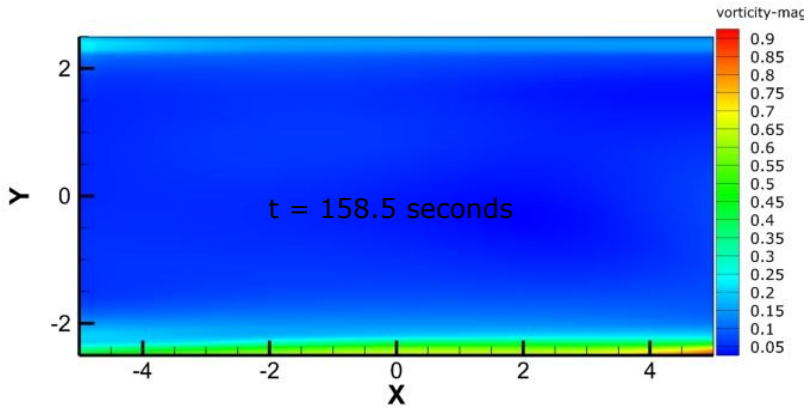

Figure 5.42: vorticity magnitude plot at t=158.5s.

of up to $0.9s^{-1}$. Yet no significant flow structures were observed and maximum vorticity is still confined to the channel bottom wall. This behaviour also confirms that a large amount of vorticity does not necessarily mean the presence of energy containing coherent structures. The temporal evolution of the flow field at 208.5s shown in Figure 5.43 also shows a dissipating or diffused turbulence field. No clear flow structures were identified.

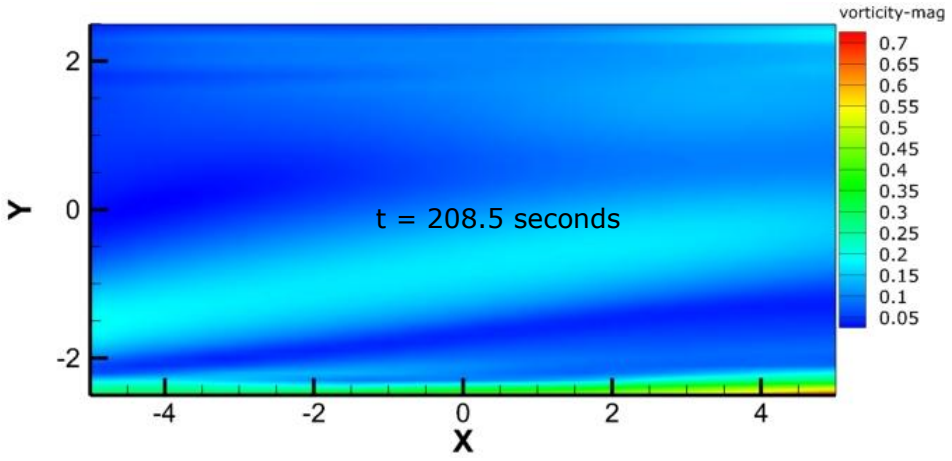

Figure 5.43: vorticity magnitude plot at t=208.5s.

It can be stated for the $1/7^{th}$ power law simulation case that, the temporal evolution of the flow field is dynamic with flow structures appearing early in the simulation. The later disappearance of these structures suggests that they may be due to numerical instabilities. Based on this observation, it is

anticipated that the 1/7th law velocity profile is unable to produce significant coherent structures resembling those within tidal current. This is majorly because the theoretical profiles assume flow in one direction but turbulence in real flow is at least two dimensional.

Although there were inflections on the velocity profiles associated with the flow fields simulated by specifying theoretical velocity profiles, the evolved structures are attributed to a pulsation of the mean flow. The theoretical velocity profile simulation cases were used to benchmark results from experimental velocity profile simulation case reported below.

5.2.10 Visualisation of vortices generated in a flow field with experimental velocity profile from the Firth of Forth.

This section discusses the temporal evolution of a turbulent flow field generated by specifying experimental velocity profile as boundary condition. Figure 5.44 is the vorticity magnitude contour plot at t= 31.4s.

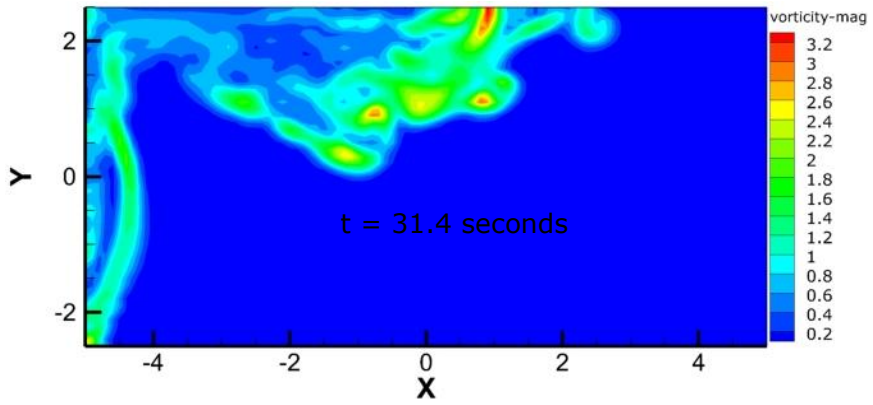

Figure 5.44: vorticity magnitude plot at t=31.4s.

All exploratory instantaneous plots were chosen arbitrarily. It is informative to state that the flow field development was comparatively faster with the experimental velocity profile as inlet condition. The temporal evolution of the flow field was monitored throughout the simulation period.

The plot in Figure 5.44 above shows a strong upward vortex near the inlet of the channel. The strength of this vortex seems so high that its effect could be felt some appreciable distance away from the inlet and at the water surface. The strong upward movement of the vortex clearly mimic the behaviour of the kolk-boil vortices described by Matthes (81) in natural flows. The maximum vorticity magnitude attained during at this time was $3.2s^{-1}$. This represents an increase in turbulence in terms of vorticity magnitude of about 30% more than the maximum of $1.1s^{-1}$ generated in the theoretical velocity profiles simulation cases.

Further plots representing the turbulent flow fields at instantaneous times 90.9s, 31.4s, 146.9s, 227.4s, 288.4s, are shown in Figures 5.45 - 5.49 respectively. Generally, the five plots evidently show considerable presence of vortices or flow structures that confirms the behaviour of turbulent flow in a natural environment. Based on the instantaneous vorticity contour plots, the maximum vorticity magnitude fluctuates between $2.8s^{-1}$ and $3.6s^{-1}$. Thus the ADCP experimental velocity profile in conjunction with a LES produced a comparatively higher vorticity magnitude at all times.

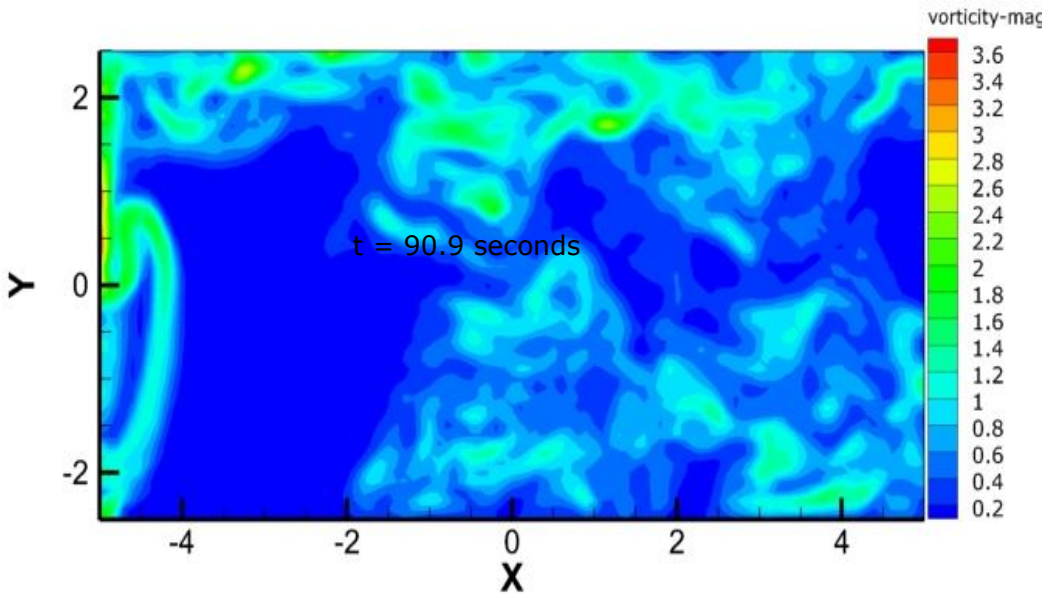

Figure 5.45: vorticity magnitude plot at t=90.9s.

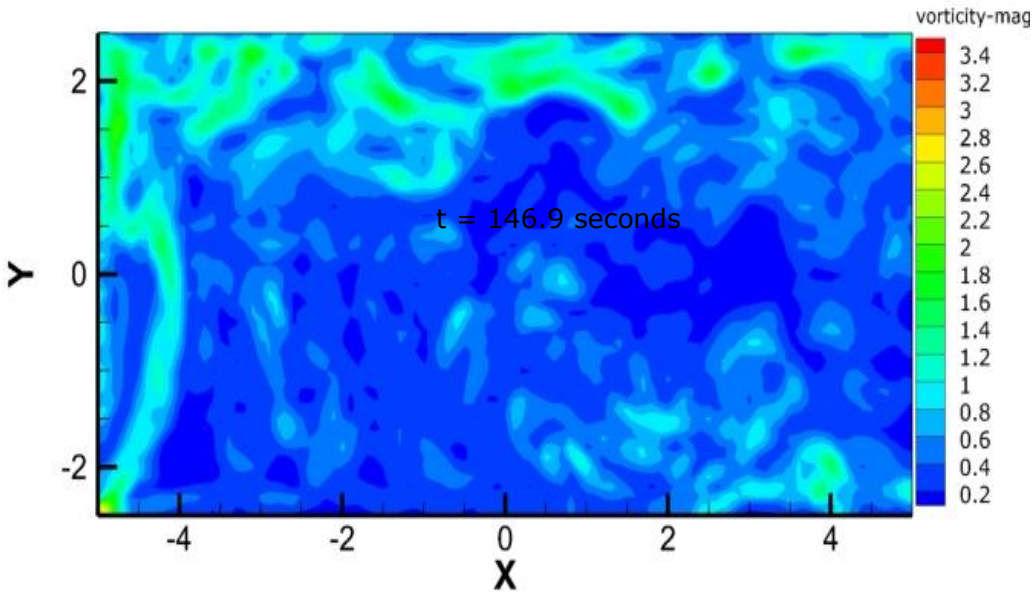

Figure 5.46: vorticity magnitude plot at t=146.9s.

At t = 146.9s, the vortices can be visualised everywhere in the flow field. The flow field represents natural typical behaviour in steady state. This behaviour is quite distinct from the behaviour of the flow field with the theoretical velocity profiles which lacked visible structures in the outer flow. The next three plots in Figures 5.47-5.49 show the evidence of sustained turbulent flow structures.

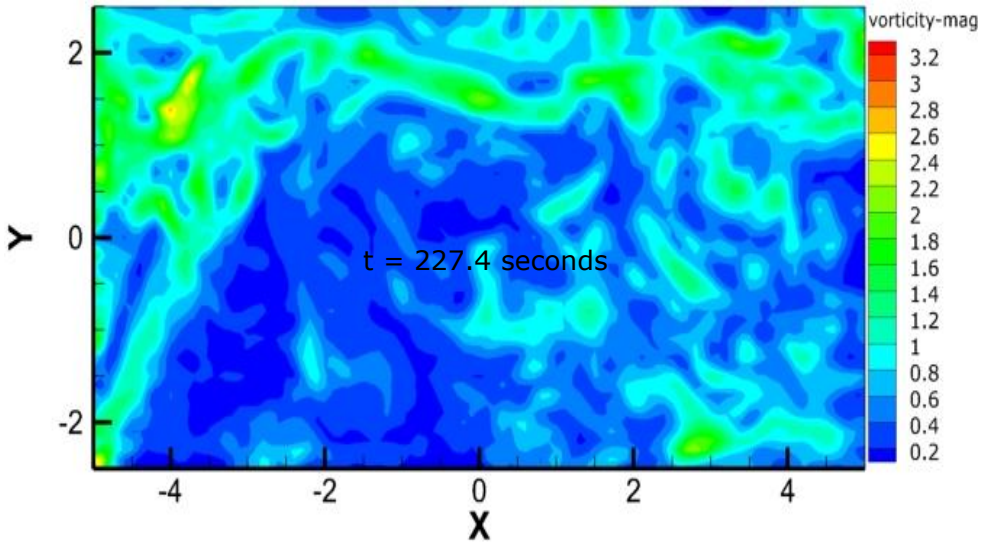

Figure 5.47: vorticity magnitude plot at t=227.4s.

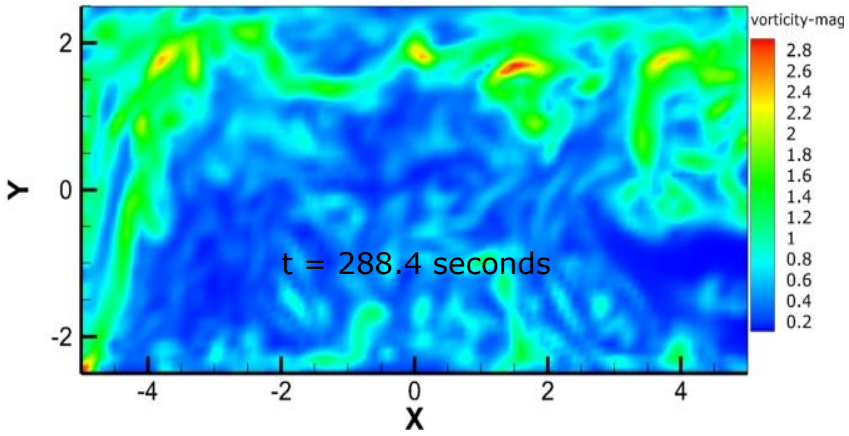

Figure 5.48: vorticity magnitude plot at t=288.4s.

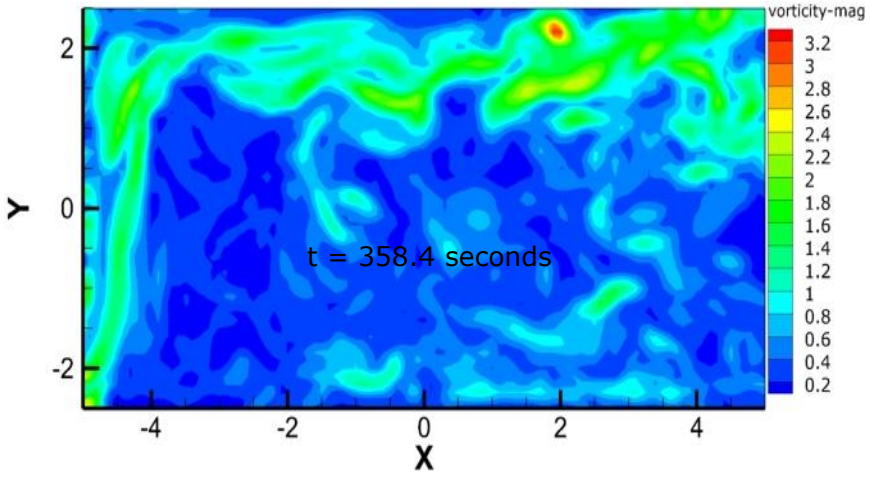

Figure 5.49: vorticity magnitude contour plot at t=358.4s.

The global vorticity magnitudes for the uniform flow and $1/7^{th}$ power law simulation cases are not significantly different from each other, with maximum values of $1.1s^{-1}$ and $0.9s^{-1}$ respectively. The slightly higher value of vorticity magnitude for the uniform flow simulation case is thought to result from a higher velocity shear rate resulting from the flow field development due to interactions between the fluid and the channel walls.

Although the $1/7^{th}$ power law and the uniform flow velocity profile data were evaluated from the experimental velocity profile, the turbulent flow structures generated by the experimental velocity simulation case were distinct from those generated by the theoretical velocity profiles. This is

because the 1/7th power law and the uniform flow profiles cannot pick up ambient turbulent structures resembling those in natural turbulent flow.

To underpin the sustainability of turbulence with simulation time, the flow was monitored up to instantaneous time t = 2458.4s. Two slice of the flow field at t = 518.4s and 2458.4s presented in Figure 5.50 and 5.51 has been selected to display the vortex flow field. Turbulence in terms of vorticity magnitude does not show any sign of dissipation but rather fluctuating

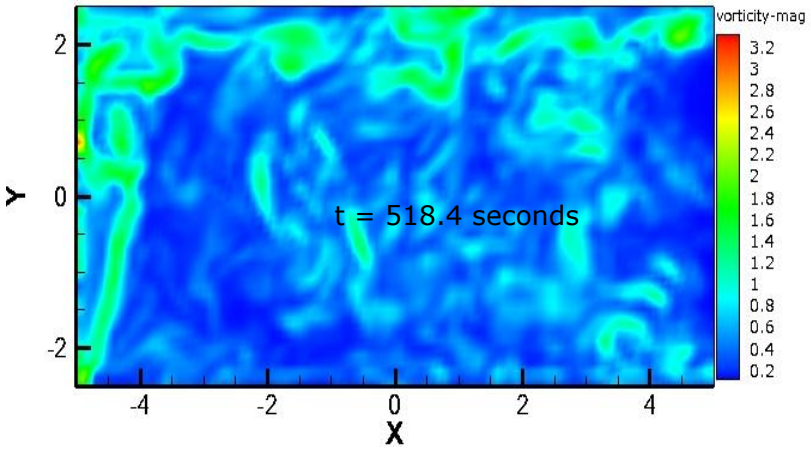

Figure 5.50: vorticity magnitude plot at t=518.4s.

and reaching a maximum value of 4.2/s at t = 2458.4s as observed in Figure 5.51 below.

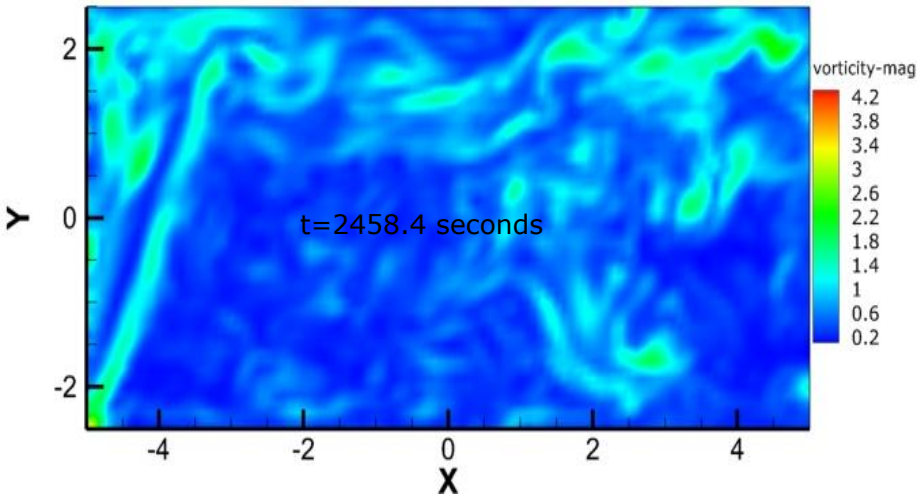

Figure 5.51: vorticity magnitude plot at t=2458.4s.

The vortex flow field in all instantaneous plots approximates the nature of the vorticity at the Firth of Forth except that, it has been reproduce in a 1:10 vertical scale ratio in a numerical domain. This demonstrates that large scale flow processes can be represented in a small scale numerical simulation domain.

Based on the way vorticty is calculated, higher velocity magnitudes would result to higher values of vorticity. The initial velocity inlet condition for the experimental velocity profile is realistic and peculiar to the velocity profile at the Firth of Forth therefore the resulting flow features can appropriately be compared qualitatively with flows in natural environment. A case by case study is required for practical application because turbulence is site specific.

5.2.11 Lateral view of the vorticity flow field.

The following instantaneous plot at 288.4s in Figure 5.52 below represents and demonstrates the lateral view of the vorticity flow field. The slices are extracted from locations where x= -2.5m, 0m, 2.5m and 5m where location zero is the channel centre. The lateral view vorticity plots show significant vortex activities similar to the horizontal plane view plots.

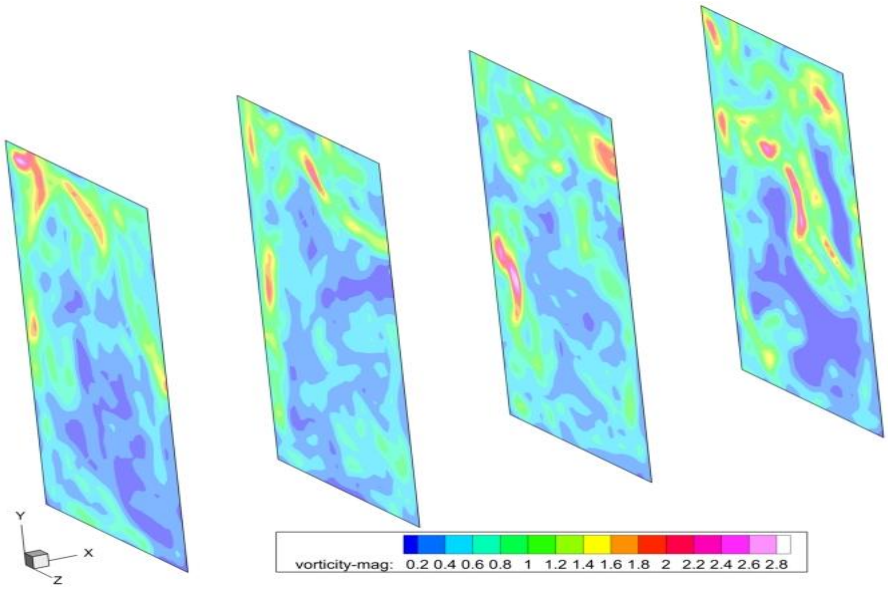

Figure 5.52: Illustration of the lateral view of the vorticity field

The maximum vorticity values was about $2.8s^{-1}$ and is not confined to channel walls but could be observed in the outer region of the domain.

5.2.12 Visualisation of velocity vector plots for uniform flow velocity profile.

Velocity magnitude vector plots are useful to show the length and the orientation of each vector in the flow field. All exploratory vector plots are sliced at z =0 (mid channel). The length and orientation of each vector indicates its magnitude and direction respectively. Vector plots representing the uniform flow simulation case at three instantaneous times are selected to visualise the behaviour of the velocity vectors.

The vector plots shown in Figures 5.53, 5.54 and 5.55 corresponds to the vorticity magnitude plots at times t = 7.8s, 147.3s, and 202.5s respectively. The vectors are one directional and appears well patterned although, the pathlines and the vorticity magnitude plots did show evidences of varying and fluctuating flow fields in time and space. A conscientious inspection of the vector plots in Figures 5.53, 5.54 and 5.55 demonstrate that the vectors vary in (length) magnitude in one direction only.

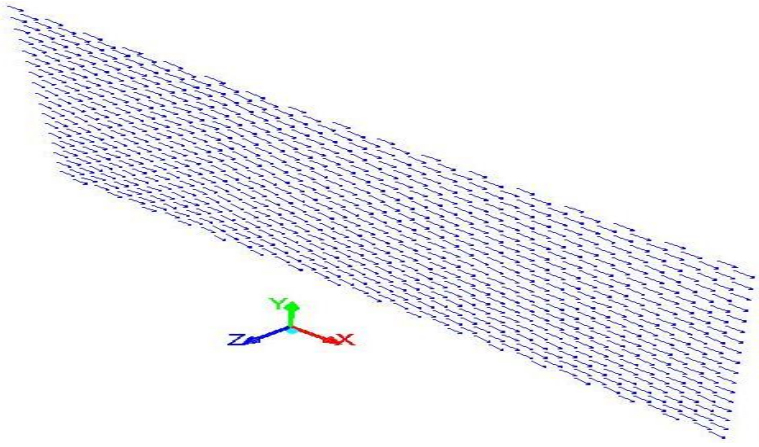

Figure 5.53: Uniform flow simulation case vector plot at 7.8s

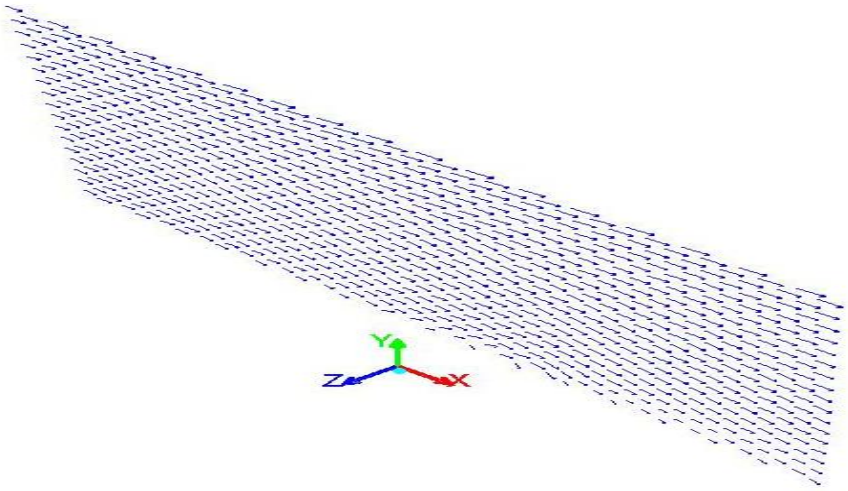

Figure 5.54: Uniform flow simulation case vector plot at 147.3s.

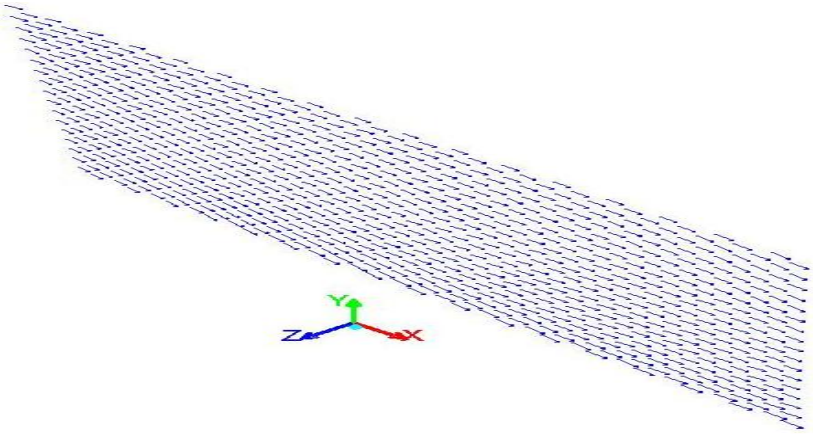

Figure 5.55: Uniform flow simulation case vector plot at 202.3s.

5.2.13 Visualisation of velocity vector plots for the 1/7th power velocity profile.

Vector field plots for the $1/7^{th}$ power law velocity profile simulation case can be visualised in Figures 5.56, 5.57 and 5.58 for instantaneous times, t = 27.7 s, 108.5 s, and 208.5s respectively. The behaviour of the vectors is similar to the uniform flow vector field. The vectors appear relatively regular and nearly organised as well as one directional. The colour density of the plots gives a quick assessment of the velocity magnitudes with the denser colour region having higher velocity magnitude. It is quite evident

in Figure 5.56 below that velocity magnitudes of the vectors closer to the channel bed are smaller than those near the channel surface.

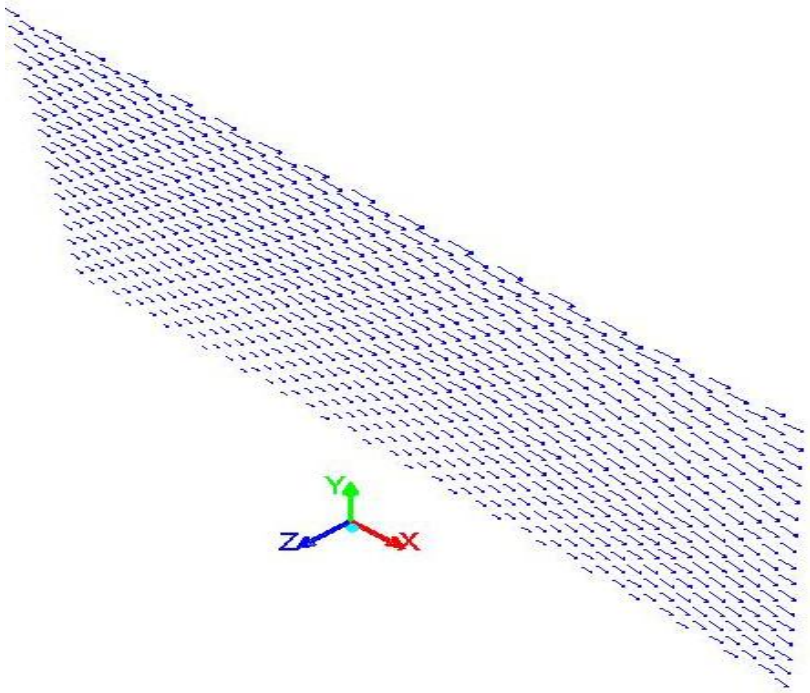

Figure 5.56: 1/7th power law simulation case vector plot at 27.7s.

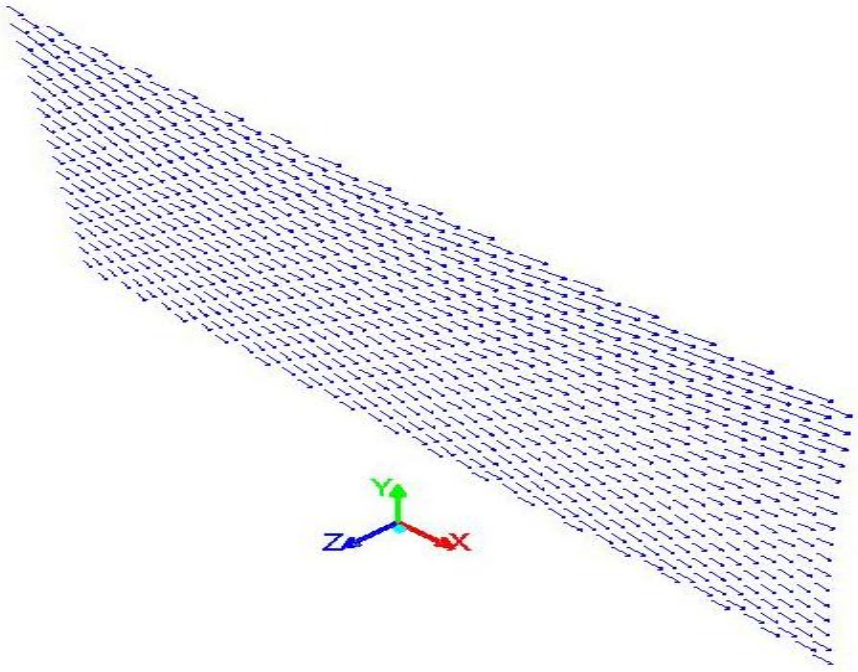

Figure 5.57: 1/7th power law simulation case vector plot at 108.5s

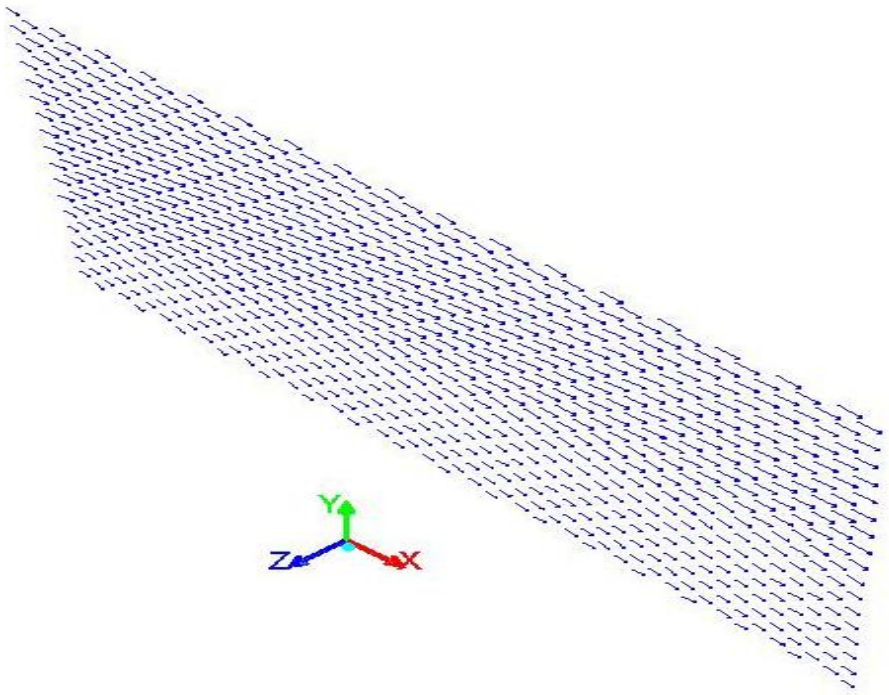

Figure 5.58: 1/7th power law simulation case vector plot at 208.5s.

Summarily, it can be stated that eddies and recirculation associated with turbulence in real flow cannot be picked up by the uniform flow or the $1/7^{th}$ power law velocity profile. It is however known that flow recirculation or eddies not related to turbulence can occur in simulations obtained by specifying theoretical velocity profiles in the presence of a bend or when there is a sudden change in flow geometry. In what follows eddies related to turbulence can be visualised.

5.2.14 Visualisation of velocity vector plots for the experimental velocity profile.

The vector field resulting from the experimental velocity profile specified at the inlet of the LES demonstrate significant presence of recirculating eddies comparable with those typical of a natural environment. Vectors in a turbulent flow show evidence of fluid rotation due to varying velocity magnitude in space and time. Although in theory, it is possible to have only translational motion in a fluid where the velocity magnitude vary from point

to point or a constant vorticity where the amount of fluid rotation is the same everywhere. In what follows, instantaneous x-y vector plots sliced from the centre of the channel are used to investigate the evolution of the velocity vectors with time. Figure 5.59 corresponds to the instantaneous time, t = 31.46s.

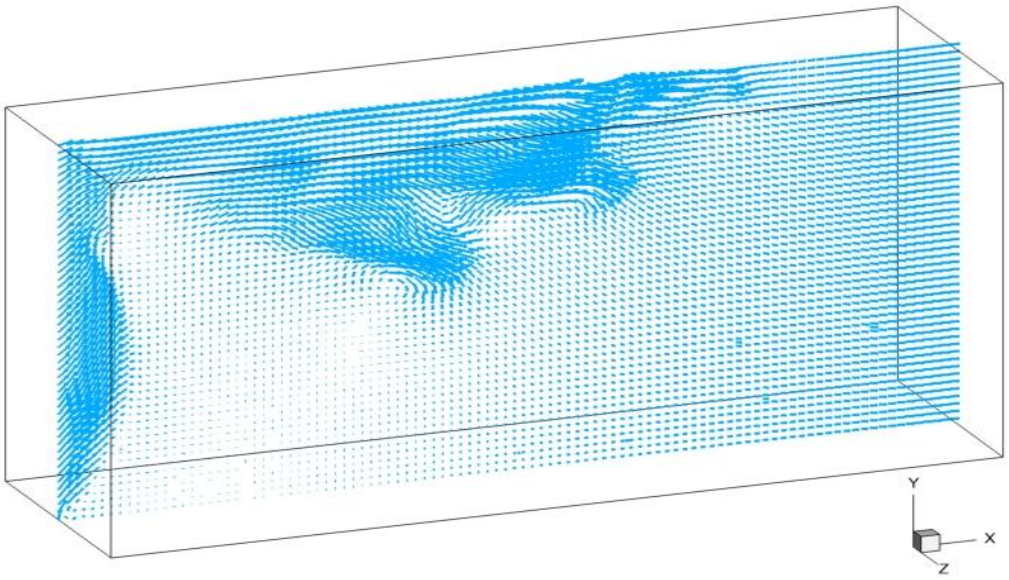

Figure 5.59: Experimental velocity simulation case vector plot at 31.46s

The relative magnitude of the velocity vectors can be appreciated by observing the colour density of the flow field. The darker shade represents a region of relatively higher velocity magnitude. About the second half of the domain downstream appears to have well patterned velocity vectors. This is because the simulation is at the early stage. A comparison of the vector field plot in Figure 5.59 with the pathlines plot represented in Figure 5.60 below indicates the path traced by the water particle as they move downstream. Evidence of fluid rotation is markedly seen at the inlet of the simulation domain near the channel bed in the encircled region. The fluid rotation was initiated at the domain bottom boundary and is associated with a reduction in velocity magnitude due to adverse pressure gradient and a relatively higher velocity zone to maintain a divergence free velocity field that satisfies the continuity equation.

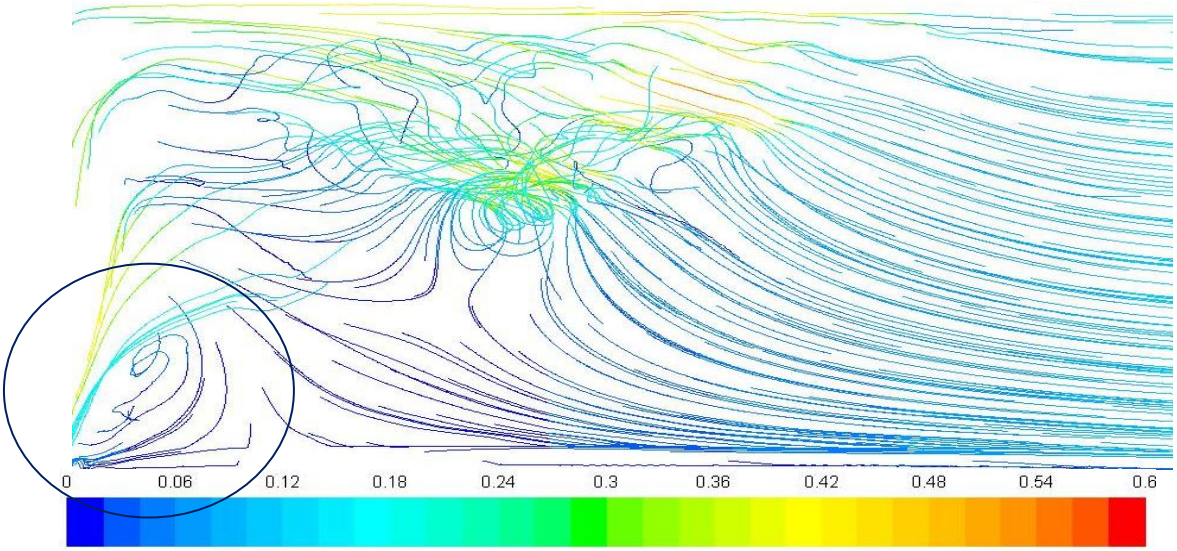

Figure 5.60: pathline plot corresponding to the vector plot at t=31.46s

Further evolution of the vector field at t = 76.9s is shown in Figure 5.61. The vector plot at t = 76.9s also show evidence of rotation of fluid parcels at different region of the flow domain. The evolution of the flow field is further investigated using the vector plot at t = 90.9s in Figure 5.62 with a corresponding pathline plot in Figure 5.63.

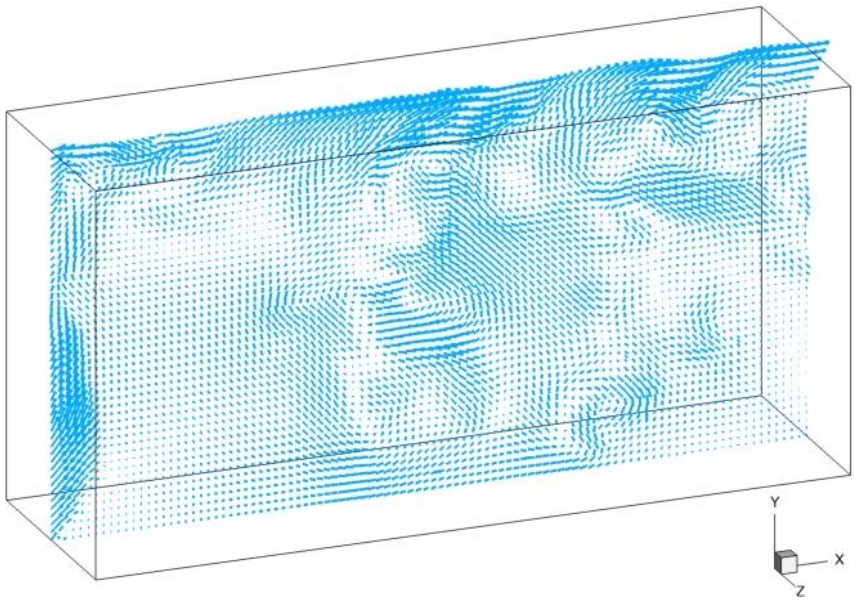

Figure: 5.61 Experimental velocity simulation case vector plot at 76.9s.

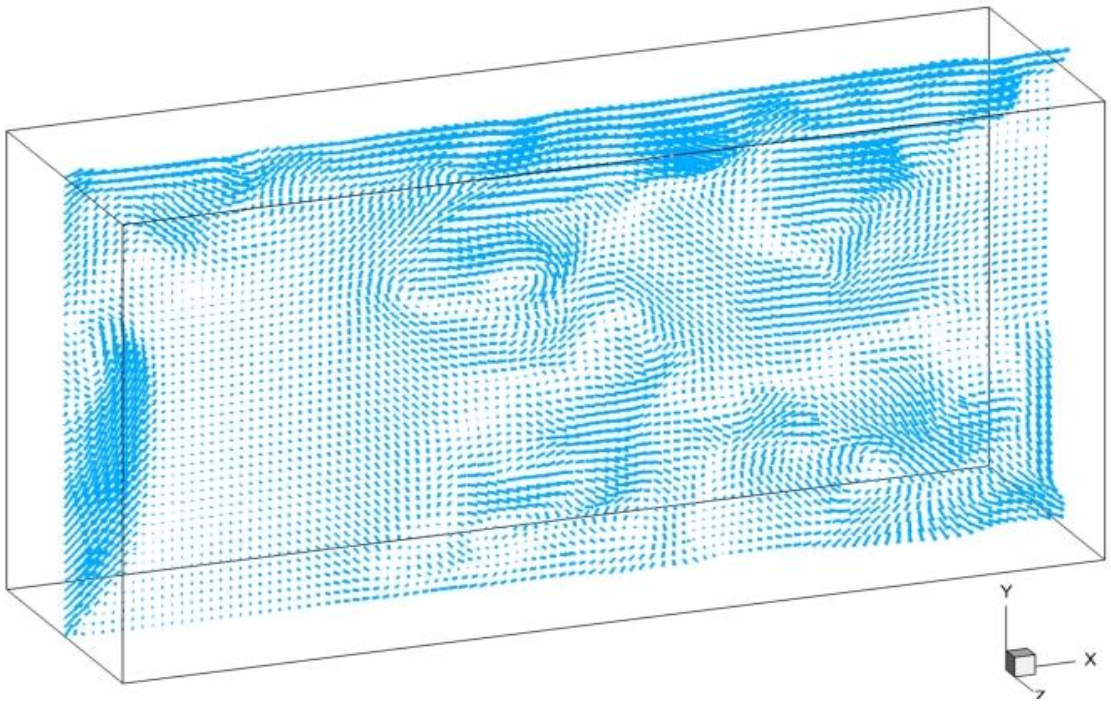

Figure 5.62: Experimental velocity simulation case vector plot at 90.9s.

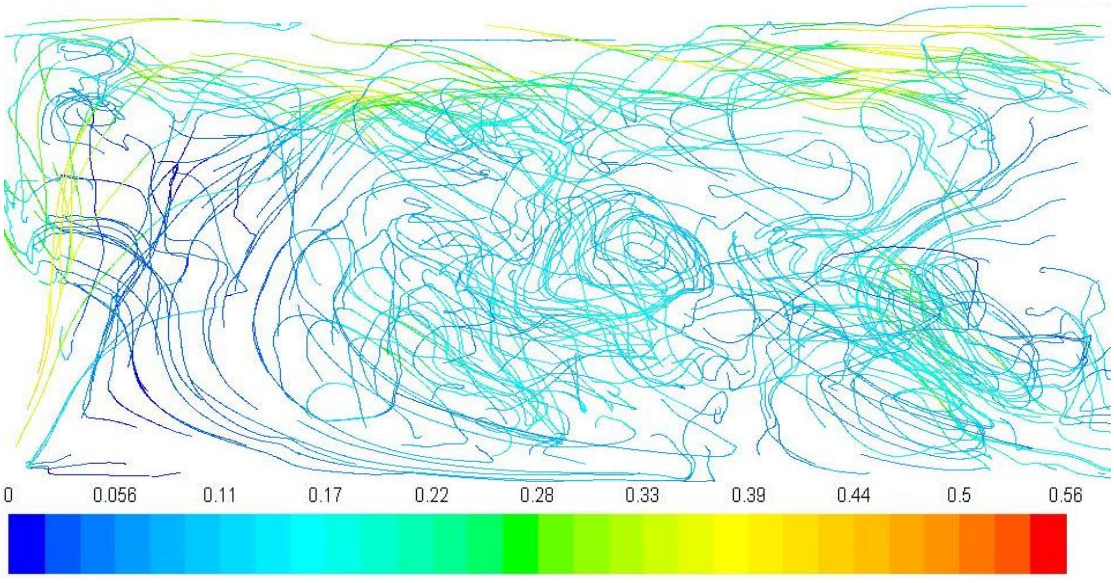

Figure 5.63: pathlines plot corresponding to the vector plot at t=90.9s

There is evidence of a continuously changing field temporally and spatially with pockets of rotating fluid parcel. The pathlines plot show regions of high and low velocity magnitude in a disorganised fashion that affects the quality of the velocity profile. The behaviour of the vector plots already discussed

and those presented in Figures 5.64, 5.65, 5.66 at instantaneous times, t = 146.9s, 227.4s, and 258.4s respectively, underpin that they represent a qualitative description of a turbulent vector field with the chaotic and tangled flow lines typical of flow in natural environment.

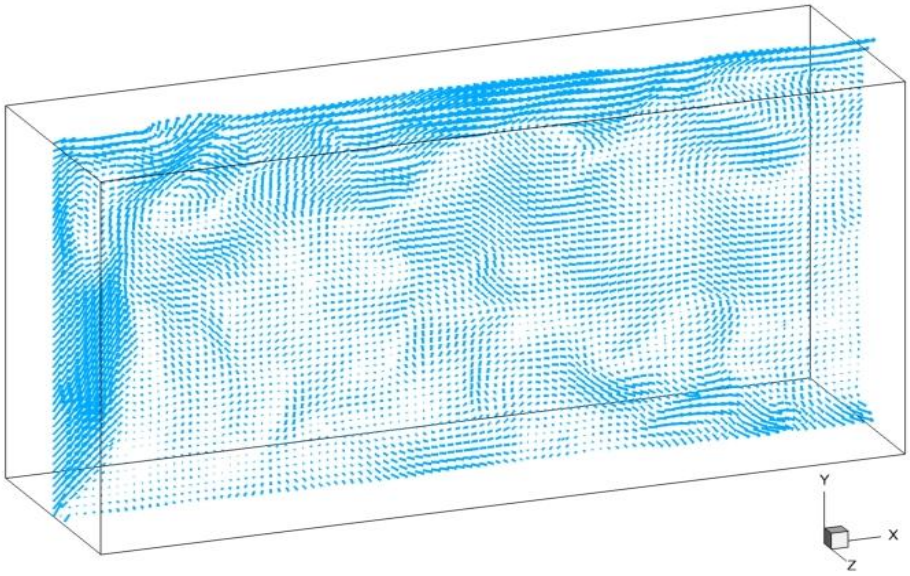

Figure 5.64: Experimental velocity simulation case vector plot at 146.9s

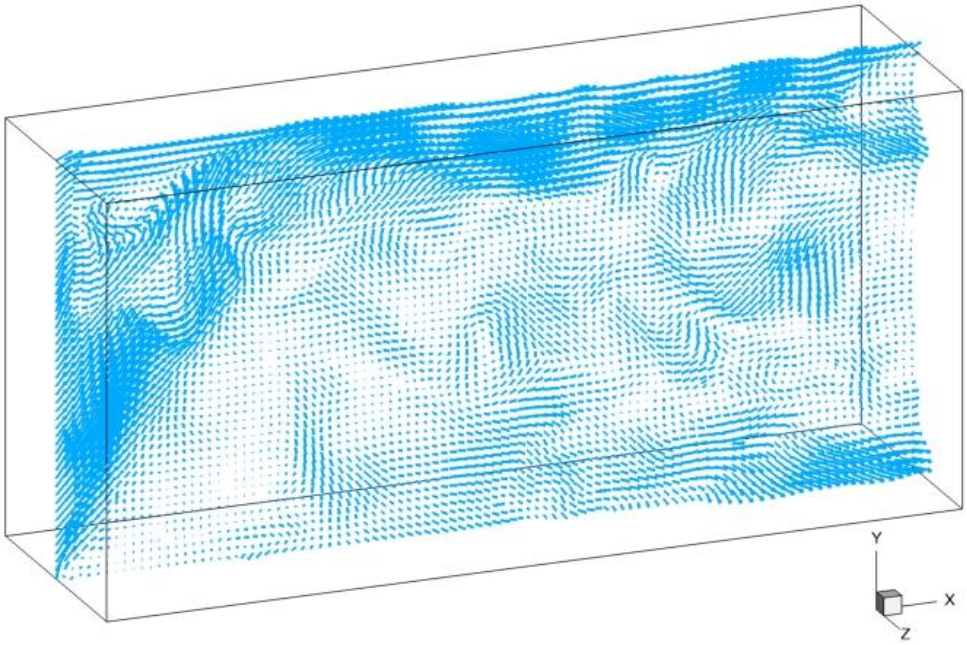

Figure:5.65 Experimental velocity simulation case vector plot at 227.4s.

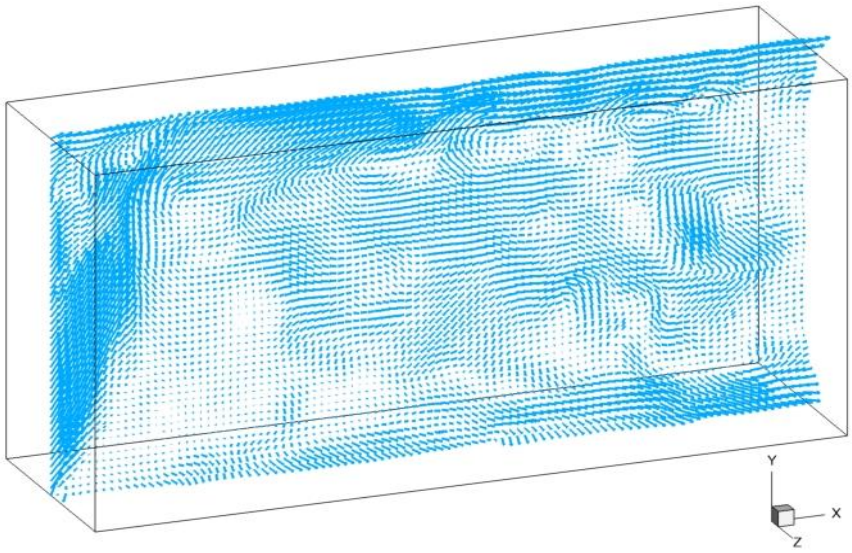

Figure 5.66: Experimental velocity simulation case vector plot at 258.4s.

Based on the simulation result, it is obvious that the experimental velocity profile contains fluctuations influenced by physical and a natural process in tidal current environment that enables the reproduction of ambient turbulent eddies in a numerical simulation. The plots show regions of sandwiched high and low velocity magnitude which imply that the energy available for extraction will not be smooth. This suggests the need for an energy storage facility to be integrated in a tidal current energy extraction system. Also important, is the turbulent fluctuations of the flow field that could potentially create undesirable effects for energy device performance and structural integrity.

5.2.15 Investigating turbulent velocity profiles and kinetic energy of flow field simulated with ADCP data.

The turbulent velocity profiles are investigated based on space and time variation. Firstly, instantaneous plots are used to visualise the relative magnitude of velocity components and the horizontal variation in velocity profile of the flow field. Secondly, a more detailed investigated was done by considering individual velocity components with associated velocity magnitude at four instantaneous times. Thirdly, times series plots of x, y and z velocity including their magnitude are also presented. Fourthly, an

instantaneous plot showing the kinetic energy of the flow field is also presented because it is of interest for energy extraction purposes.

a) Vertical and horizontal spatial variation of simulated velocity profiles.

The magnitude of velocity components along the vertical axis was investigated at t= 308s using the plot in Figure 5.67. The data used for the plot has been sampled from the channel centre where x, y, z = (0, -2.5 to 2.5, 0).

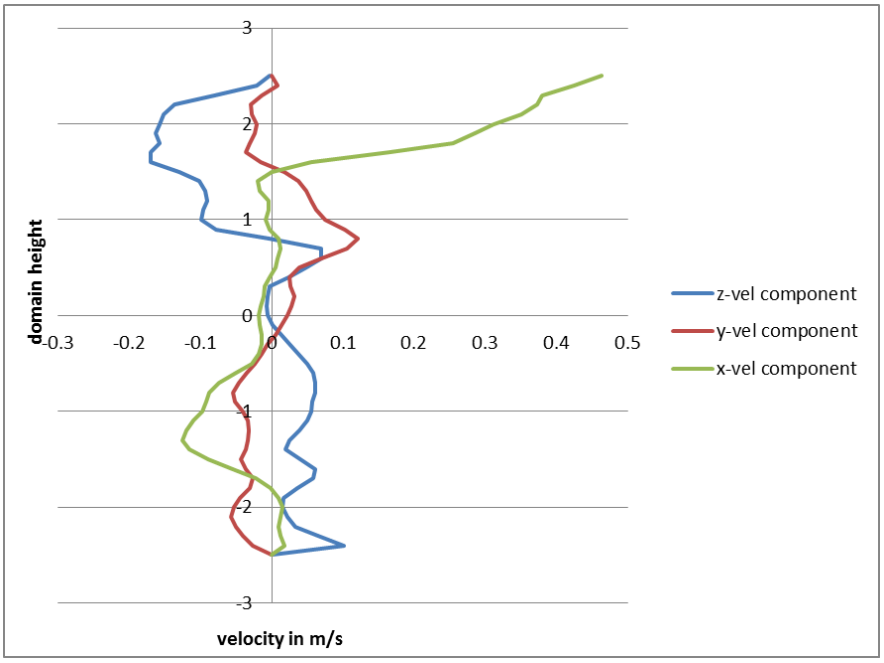

Figure 5.67: instantaneous turbulent velocity profiles

A turbulent flow field is associated with a 3 velocity components interacting within the flow that changes with the channel depth. At this instant, it is observed that the x velocity component is significantly higher in magnitude in the top 25% of the domain but weaker comparable to the lateral and the vertical velocity components at the lower region of the domain. The vertical and the lateral velocity components are comparable in magnitude over the vertical profile. The negative values indicate the presence of reverse flow due to turbulence.

Figure 5.68 below show the horizontal spatial variation of velocity profiles at various depth(y) locations where y=-2, very close to the channel bottom, y=2, upper region of the channel and y=2.4 very close to the water surface (2.5m).

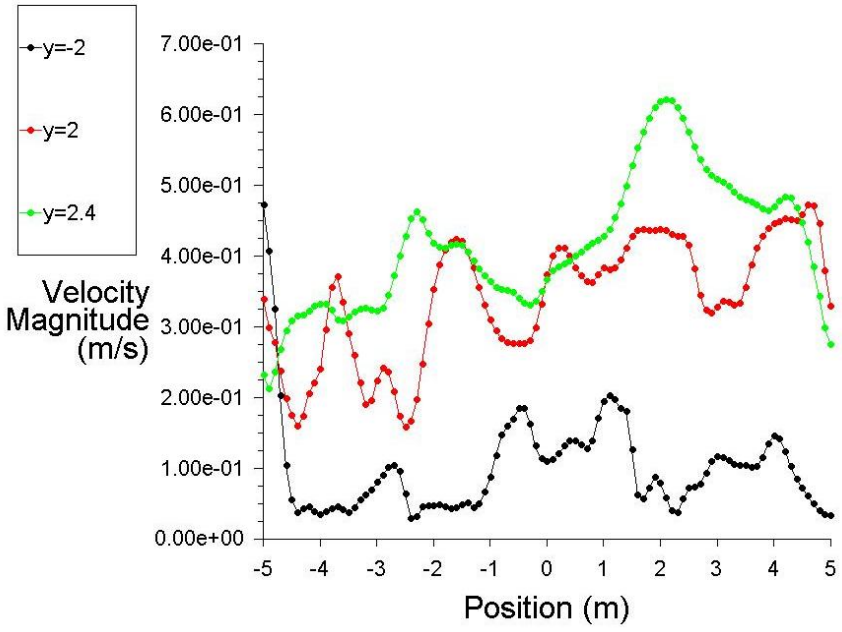

Figure 5.68: velocity magnitude at various depths.

The behaviour of the profiles agrees with the velocity-depth variation of open channel flow. It is seen that the green line plot (y = 2.4) has the highest velocity magnitude because, it is closest to the water surface (y =2.5). The black line plot (y = -2) has the smallest values of velocity magnitude because it is closest to the channel bottom (y =-2.5). The domain height is 5m while the domain length is 10m.

b) Temporal variation of turbulent velocity profiles at different instantaneous times.

The turbulent velocity profile was systematically investigated based on their individual components and magnitudes at four different instantaneous times t =90.8s, 188.4s, 278.4s and 368.4s. The data used to generate the plots were extracted from the channel centre where x, y, z = (0, -2.5 to 2.5, 0).

The velocity components and magnitude profiles at t =90.8s, is shown in Figure 5.69 below.

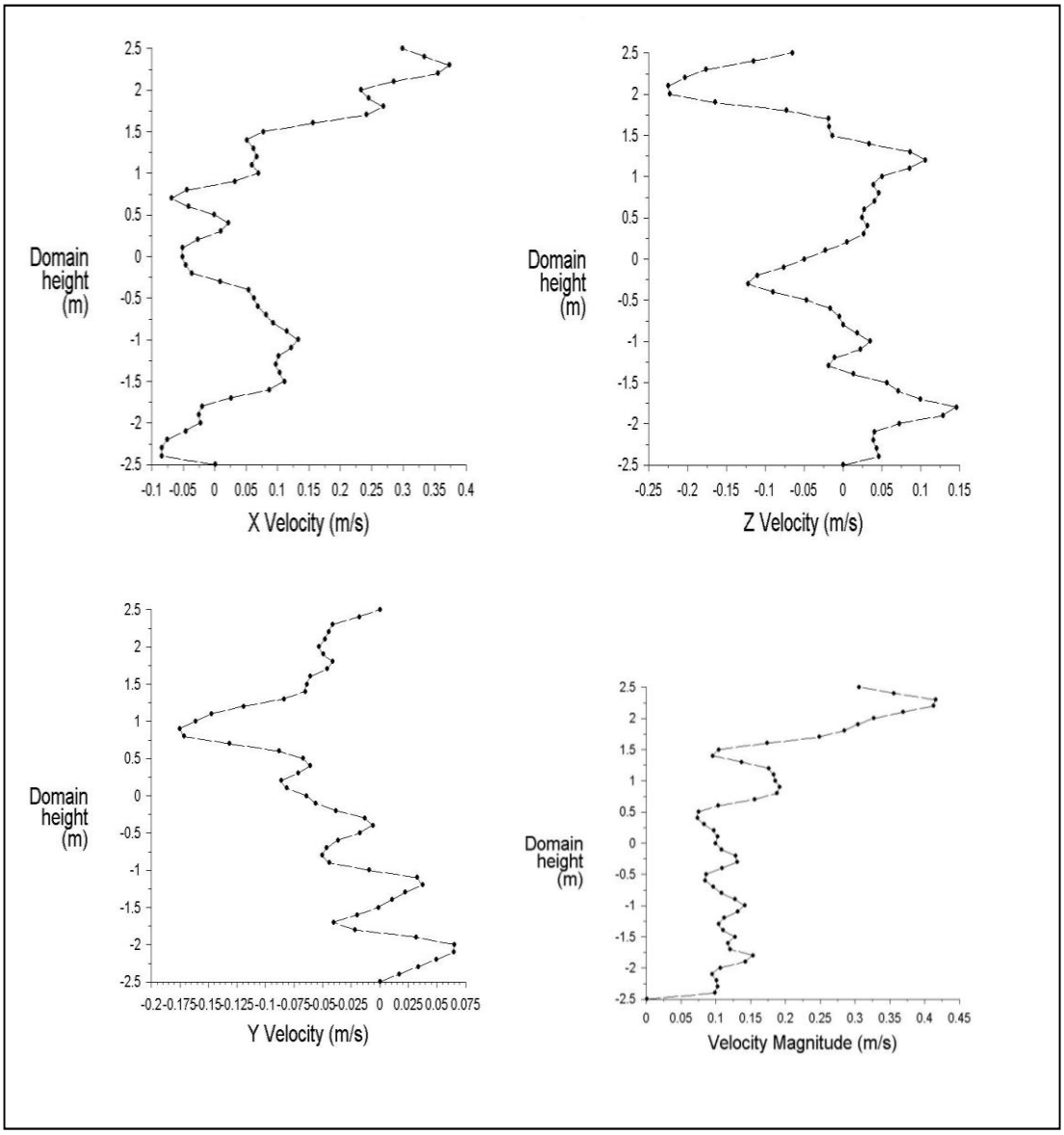

Figure 5.69: Turbulent velocity profiles at t = 90.8s

At this instant, the x velocity component is the strongest reaching a maximum of about 0.4m/s in the streamwise direction and the lateral velocity component had a maximum of about 0.25m/s in the upper region of the channel in the reverse direction. The vertical velocity component was

the weakest with less than 0.2m/s in the downward direction. The velocity magnitude vector reached a maximum of about 0.45m/s. The plot below show the how the turbulent velocity profiles have changed at t = 188.4s.

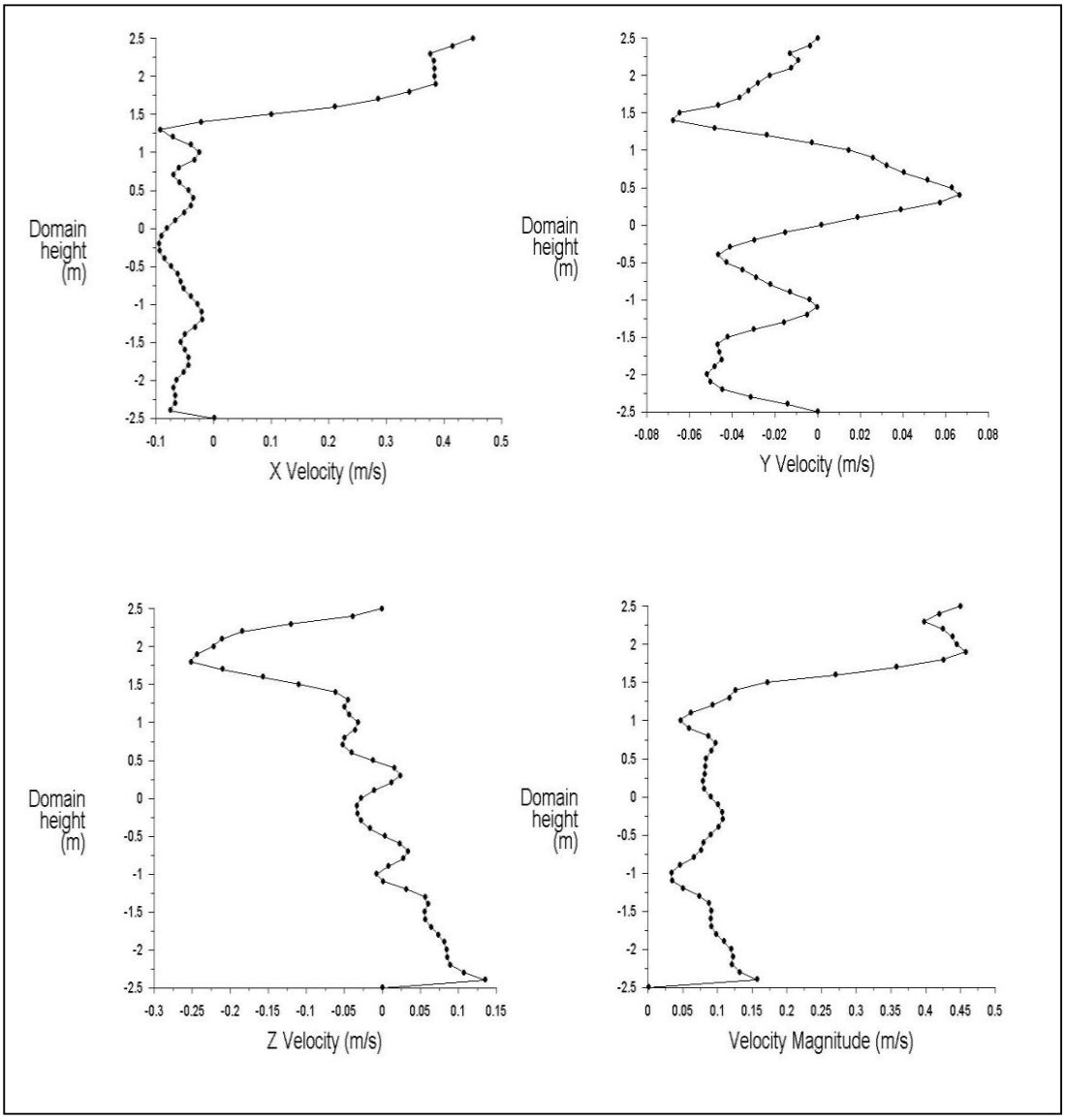

Figure 5.70: Turbulent velocity profiles at t = 188.4s

The x velocity component is still relatively stronger nearing about 0.5m/s at the water surface along the streamwise direction. The lateral velocity component is half as strong as the longitudinal velocity component and a

relatively weak vertical velocity current, an order of magnitude lower. The velocity magnitude profile shows a rapid increase at the top 25% of the domain. The flow profiles at t =278.4 are shown in Figure 5.71 below.

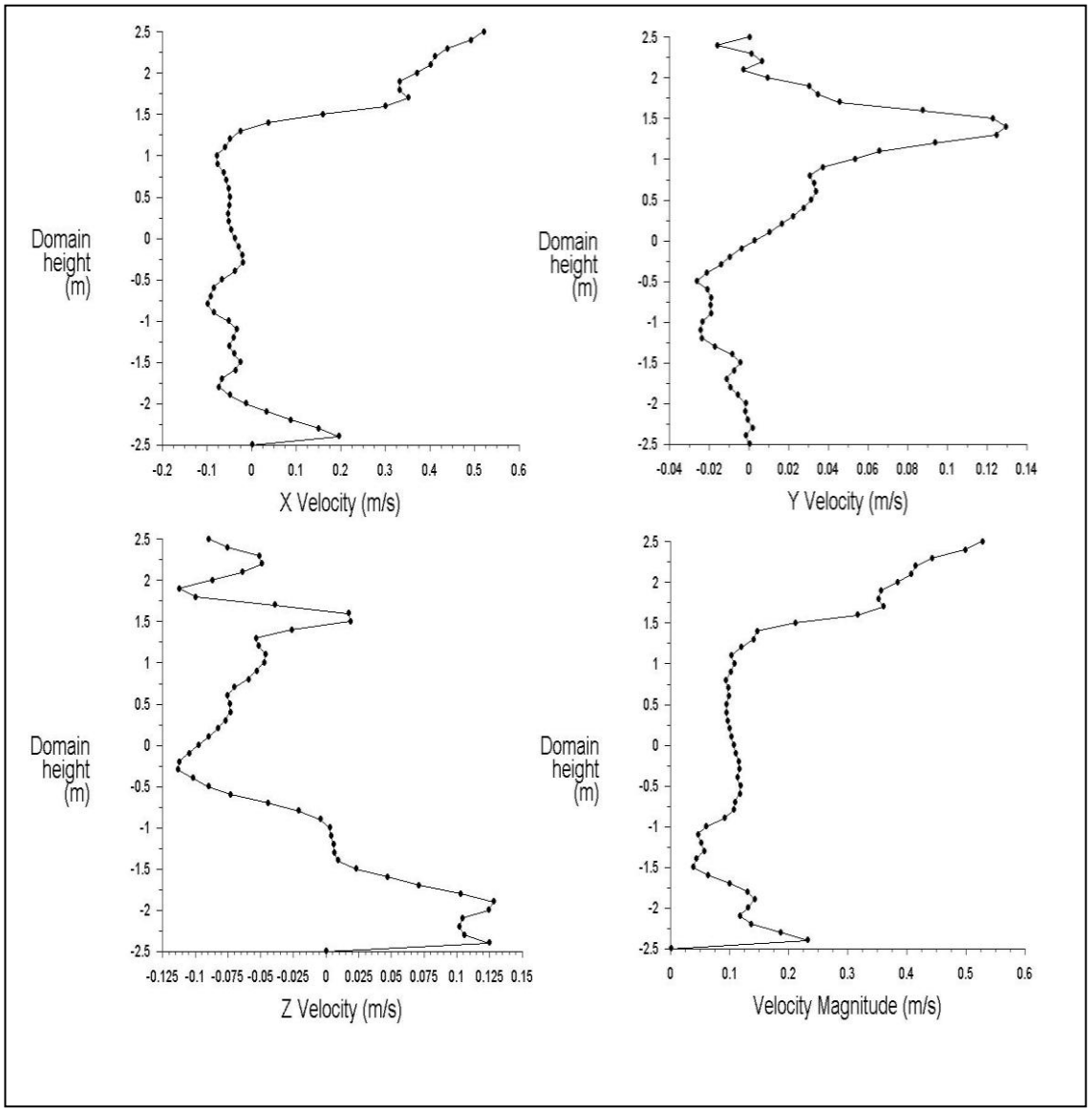

Figure 5.71: Turbulent velocity profiles at t = 278.4s

The x velocity component has been consistently strongest now reaching a maximum of 0.6m/s. This increase in strength of the x velocity component is in order to satisfy the continuity equation: The z velocity component which previously attained a maximum velocity of about 0.25 at t= 188.4, is now reduced to a values of less than 0.15m/s in the positive flow direction

at t =278.4s. The vertical velocity profile is comparable to the lateral velocity profile at this instant.

The turbulent profiles at t = 368.4s are shown in Figure 5.72

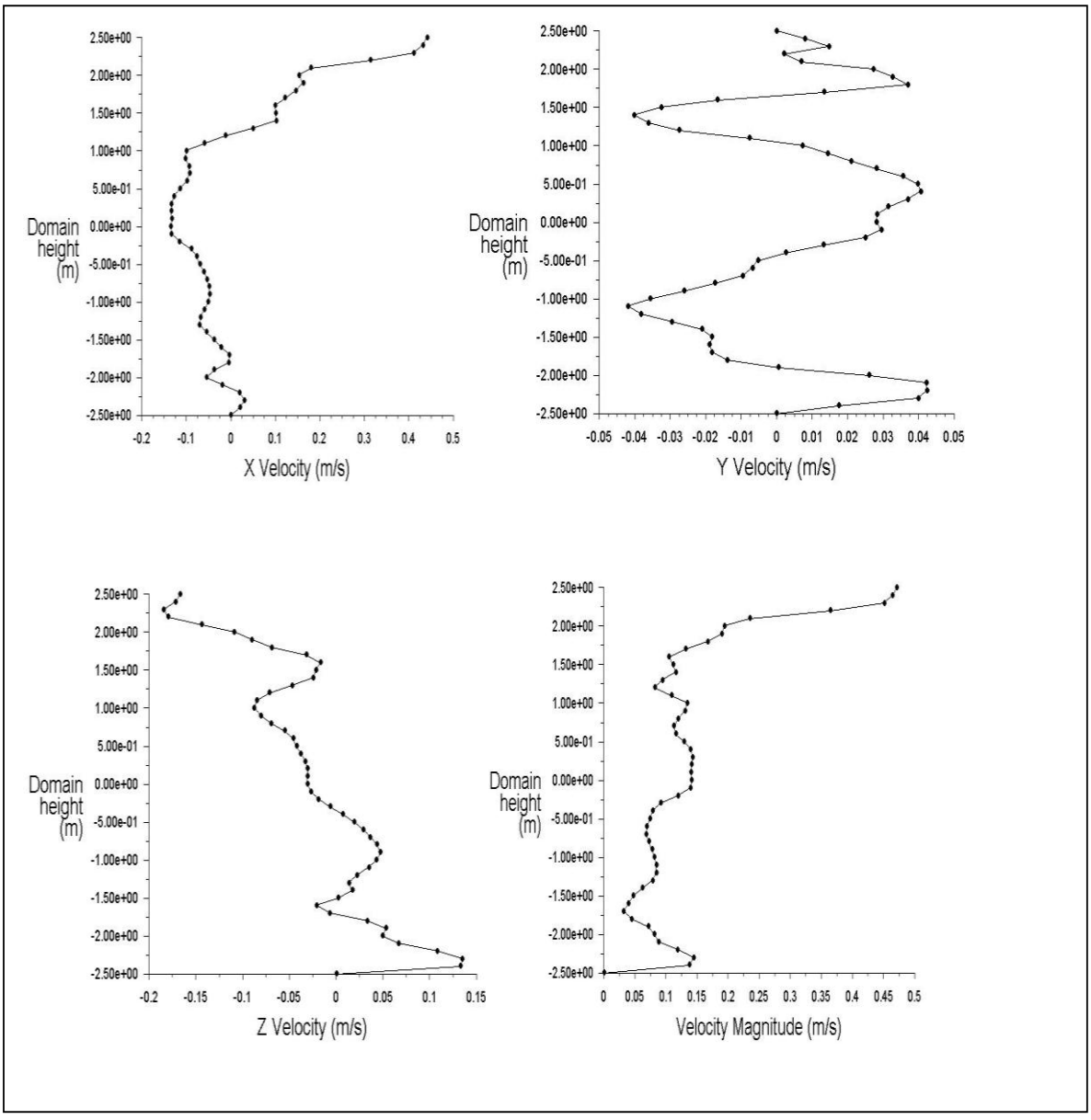

Figure 5.72: Turbulent velocity profiles at t = 368.4s

At this instant, the x velocity component is seen to have reduced from a maximum of 0.6m/s to 0.5m/s. The vertical velocity component has further reduced from a maximum of about 0.14m/s at t= 278.4s to about 0.04m/s

at t = 368.4s. It appears the reduction in the flow strength is common to all the velocity profiles. This is reflected in the overall velocity magnitude reduction of 0.6m/s at t = 278.4s to about 0.5m/s at t = 368.4s. This underpins the temporal variation of turbulent flow from instant to instant.

c) Time history of velocity profiles

A time history plot of the velocity components and magnitude measured at three different points of the flow field is presented in this section. Figure 5.73 show the fluctuations in the velocity at point (2, 2.4, 0.5).

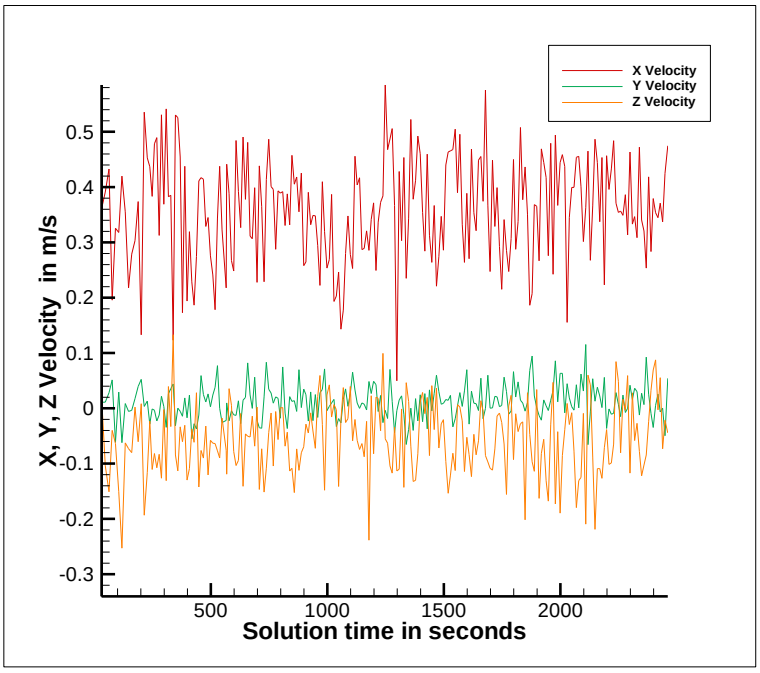

Figure 5.73: A time history plot for x, y, z velocity components (2, 2.4, 0.5)

The x velocity component is apparently strongest with an instantaneous maximum of over 0.5m/s. Most of the reverse flow appears to be caused by the influence of the lateral and the vertical velocity component at this point. The vertical velocity component is also observed to the weakest with magnitude fluctuating about zero m/s. A plot of the resultant velocity magnitude is shown in Figure 5.74. The overall magnitude shows an overall

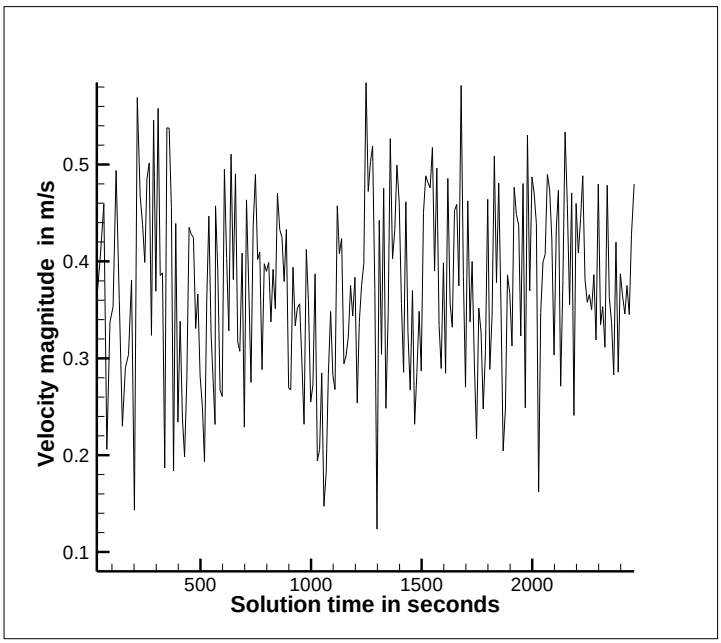

Figure 5.74: A time history plot for velocity magnitude (2, 2.4, 0.5)

instantaneous maximum value of less the 0.6m/s. This fluctuation is responsible for the generation of the turbulent structures observed in the flow fields. Time history variation of the velocity at two other points is further shown in Figures 5.75- 5.78.

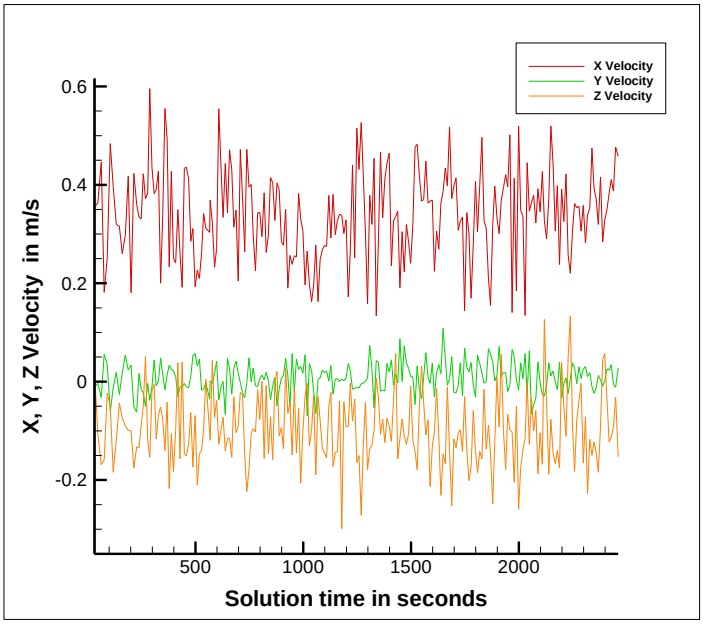

Figure 5.75: A time history plot for x, y, z velocity components at (2,2.4, 0)

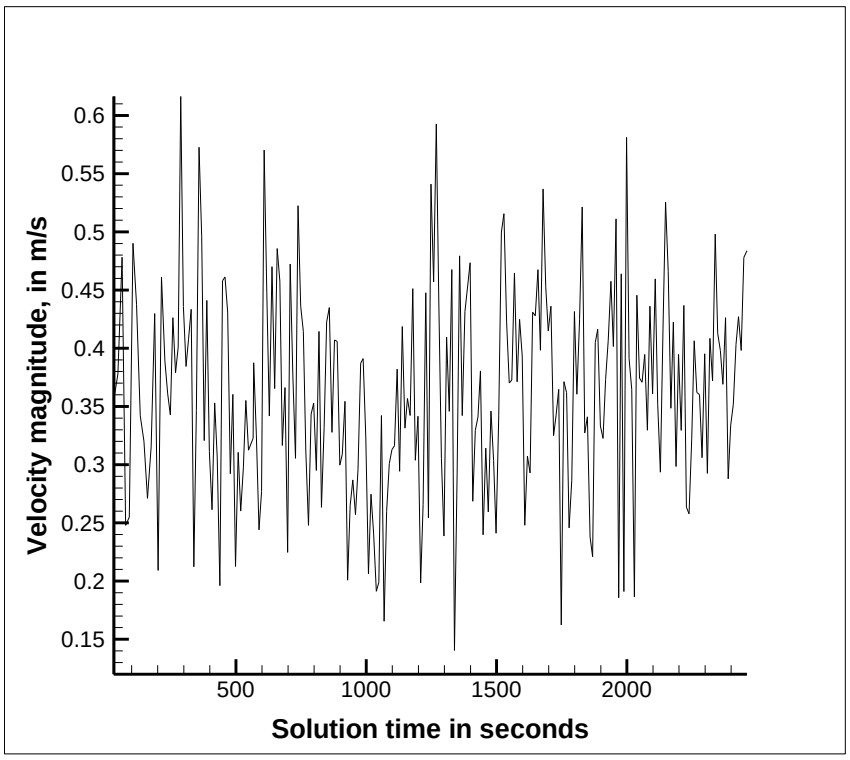

Figure 5.76: A time history plot for velocity magnitude at (2, 2.4, 0)

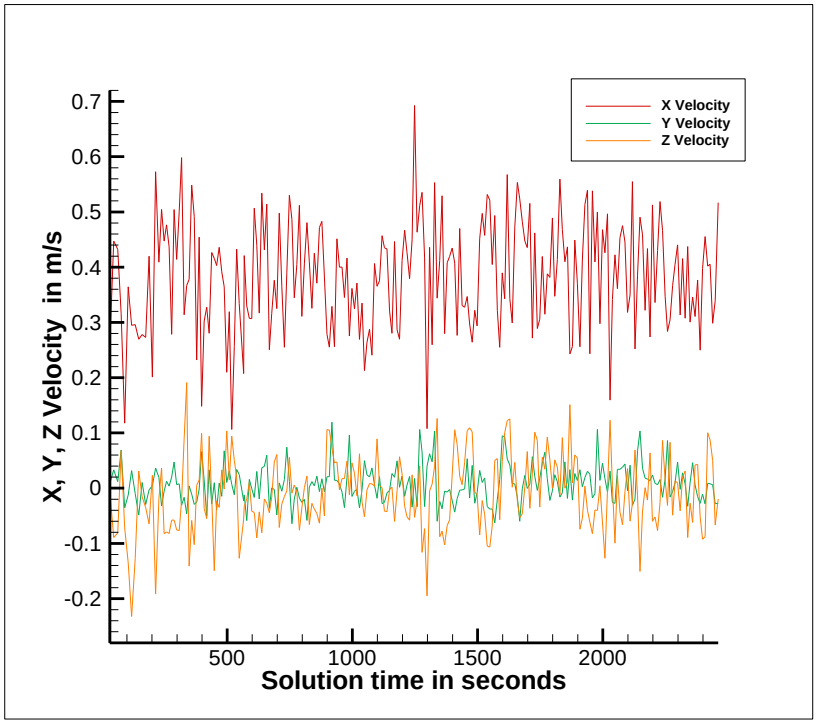

Figure 5.77: A time history plot for x, y, z velocity components at (2,2.4, 1)

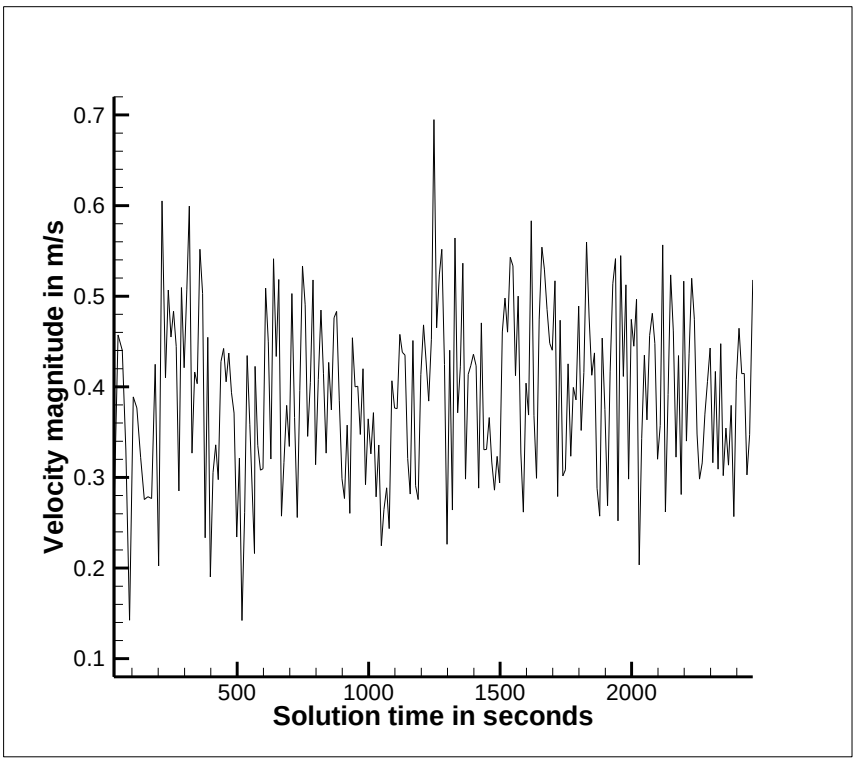

Figure 5.78: A time history plot for velocity magnitude at (2, 2.4, 1)

Observing Figures 5.75 -5.78 shows that the x velocity component contributes most to the velocity magnitude because it is persistently the strongest. The time history plots represent velocity values close to the surface where the maximum velocity is known to occur.

The lateral velocity is also consistently relatively stronger than the vertical velocity profile. These observations qualitatively agree with the behaviour of open channel flow.

d) Kinetic energy investigated of the flow field.

Turbulence kinetic energy derived from fluctuating velocity quantities is show in Figure 5.79 in y - z plane slices of contour plot at instantaneous time of 288s. The planes are located at z= -5m, -2.5m. 0m. 2.5m, and 5m marks of the computational domain. The plot shows that kinetic energy has higher values close to the water surface. This implies that velocity fluctuation is significant at the water surface.

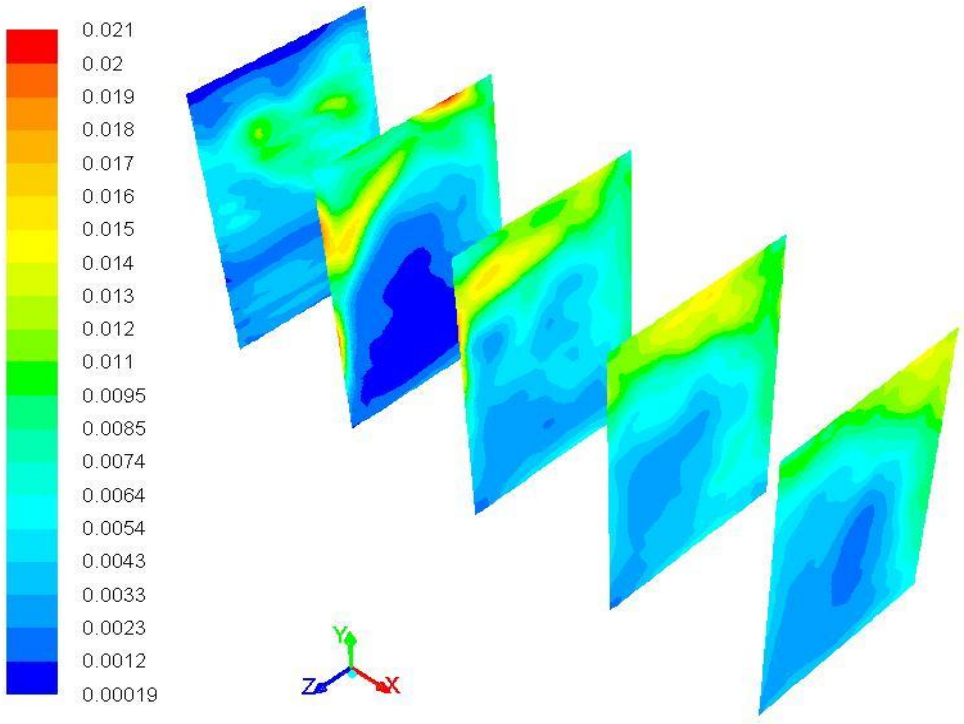

Figure 5.79: Contour plot of turbulent kinetic energy

Regions of high velocity fluctuations will not produce smooth power with regards to electricity generation. It is believed that most of the kinetic energy available in tidal currents occupies the top 25% of the channel which agrees with power estimation using the approximate power law function. However, if considerable fluctuations mingle with smooth velocity profile close to water surface, the effect of the fluctuation on power generation should be accounted for.

5.2.16 Comparing vorticity fields simulated with velocity profiles sampled at different times of tidal flow.

This section compares vorticity field generated using three different turbulent velocity profiles sampled at different times during the ADCP deployment period. Two velocity profiles designated as the 309th and 441st profile sampled during a high tide on different days and the 1187th profile sampled during a low tide has been used for the investigation. The simulation results are presented in Figure 5.80.

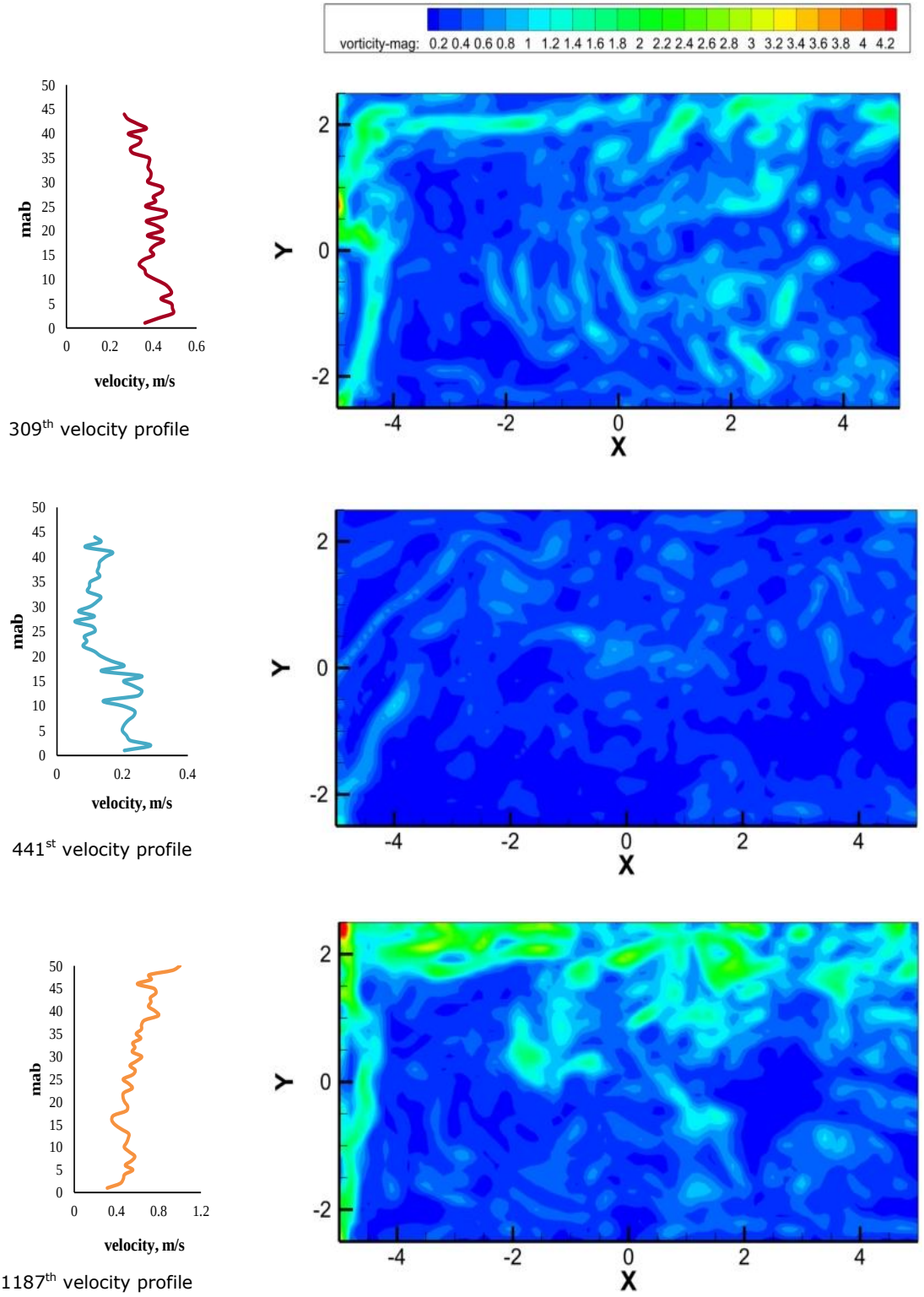

Figure 5.80:Comparing vorticity plot for different inlet profiles

The results show that all real profiles produces ambient turbulent structures but with varying levels of vorticity. This is because the vorticity is derived from velocity. The velocity profiles in tidal currents changes with time. It is also possible to have a slack water period when the tides changes direction and there is little or no horizontal flow of currents. It is observed that the vorticity magnitude is higher for profiles with higher velocity magnitude. This behaviour implies that the amount of energy extracted from tidal current will vary from instant to instant. Also hydrodynamic loading on submerged energy devices will fluctuate accordingly. Generally, the simulated vorticity field are similar and comparable. This is because all the experimental velocity profiles are evidently influenced by waves, seabed roughness and other physical and natural processes in the estuary necessary to generate turbulence.

5.3 Effect of ambient turbulent structures on seabed drag coefficient.

The effect of no slip condition implies that there will be a sea bed drag in numerical simulation. The seabed drag coefficient in real flows is not constant but can vary with time and can also be affected by several factors including changes in seabed roughness and weather conditions. The seabed drag is an important parameter for characterising the amount of energy available for extraction by a tidal current turbine. The seabed drag coefficient is used to estimate the amount of energy loss due to dissipation (91). Attempts has been made to measure seabed drag coefficient in several tidal currents sites which include the eastern Irish sea by Malcolm (92) where measurement was carried out at a 26m depth of water over two month period produced a mean drag coefficient estimate of 0.0025. Bricker (93) evaluated the variation of seabed drag coefficients in different sea states and currents in a shallow site in San Francisco bay where it was concluded that wind waves, surface and bottom boundary layers have a significant effect on seabed drag coefficient. A compilation of seabed drag coefficients for various sites can be found in (91). Table 5.2 show seabed

drag coefficient values for different sites including values measured by Campbell (94) and Rippeth (74) in Menai Strait.

Table 5.2: Estimate of seabed drag coefficient from various locations.

Site	Drag coefficient
Menai Strait by Rippeth	0.0024 -0.0026
San Francisco bay	0.08 – 0.004
Menai Strait by Campbell	0.017
Various point at Menai Strait	0.02 – 0.006
Eastern Irish sea by Malcolm	0.0025

There is no reported seabed drag coefficient for the Firth of Forth. In this study, seabed drag coefficient has been simulated using experimental velocity profiles sampled from the estuary. The results were benchmarked with simulation done by specifying theoretical velocity profiles, because theoretical velocity profiles are commonly used in tidal resource estimation in the absence of site data. The simulated drag coefficient using three different velocity profiles from the Forth estuary are presented and compared with measurement results presented in Table 5.2.

5.3.1 Comparing seabed drag coefficient simulated using experimental and theoretical velocity profiles

The time history plot of the drag coefficient for the uniform flow simulation case is presented in Figure 5.81. It was monitored for a period of 300s of simulation time. During this period, the drag coefficient was observed to fluctuate between the values of 0.04 to 0.22 with a mean value of 0.13. The plot displays a wavy kind of function. This shape of the drag history plot is attributed to the modification of flow profile specified at the inlet by the random velocity generating technique integrated into the LES.

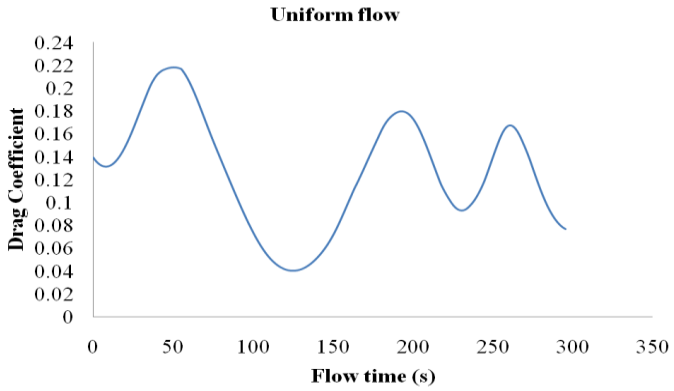

Figure 5.81: Drag coefficient history for uniform flow boundary condition.

Figure 5.82 is the drag coefficient history plot for the 1/7th power law simulation case. The values of the seabed drag coefficient fluctuate between

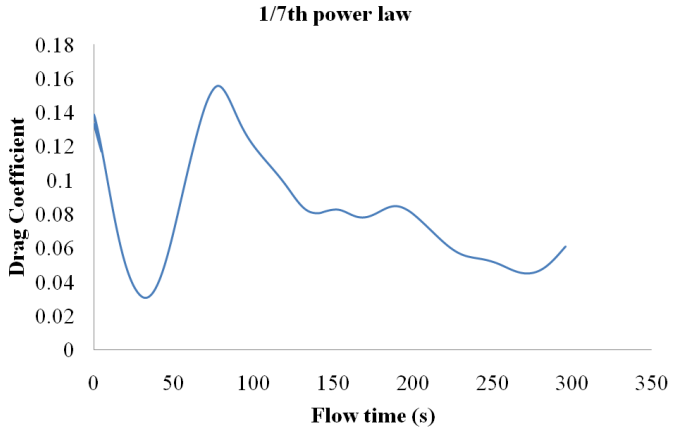

Figure 5.82: Drag coefficient history for 1/7th power law boundary condition.

0.03 and 0.16 with a mean value of 0.08 for the period of about 300s simulation flow time. The drag coefficient resulting from the uniform and the 1/7th power law velocity profiles are comparable having values between 0.03 - 0.22.

Figure 5.83 below shows the drag coefficient history plot for the experimental velocity profile. The drag coefficient resulting from the experimental velocity profile has relatively lower values with a maximum

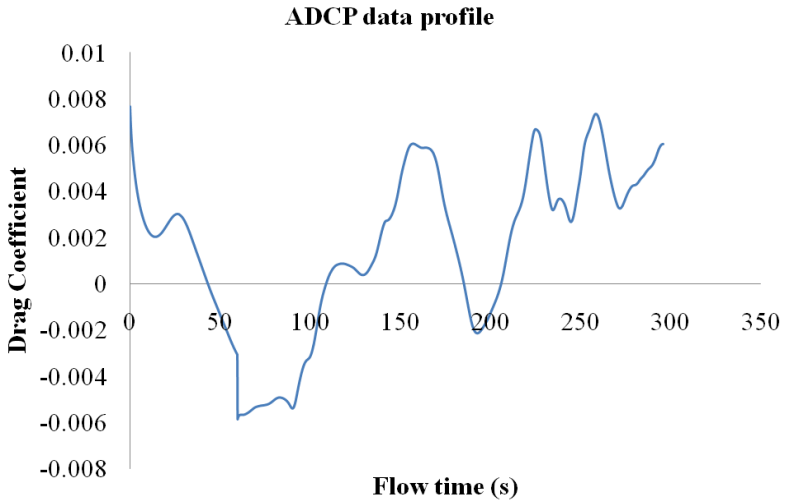

Figure 5.83: Drag coefficient history for the experimental data boundary condition.

of about 0.007 and a mean value of about 0.0035 with possible negative drag coefficient due the effect of reverse flow naturally encountered in a turbulent flow. The reduced drag coefficient is then attributed to the way drag force is normally calculated. Drag is known to be positive in the streamwise direction (95), in the event that velocity vectors reverses direction, the drag force component acting in the opposite acts to detracts from the positive values of drag force and its coefficients.

The observed behaviour agrees with the known Reynolds number drag relationship (79,96) where the drag coefficient of a structure submerged in a fluid generally decreases as the Reynolds number increases. The Reynolds number is a measure of turbulence. The results thus confirm that the flow field evolving from the ADCP data simulation case is more turbulent. It can then be stated that large scale structures in the ambient flow can lead to a significant reduction in channel bed drag coefficient when results are compared with the theoretical velocity profiles simulation cases. In the context of energy extraction it implies that less energy is required to overcome the resistance offered by the seabed. Implying more energy is available for extraction based on the simulation results.

5.3.2 Comparison of seabed drag coefficient using different velocity profile samples.

Turbulent velocity profiles sampled at different times during the deployment period, from the Firth of Forth were also used to investigate the seabed drag coefficient. Each one was monitored for about 500s of simulation flow time. The drag coefficient history based on the 309th velocity profile is shown in Figure 5.84.

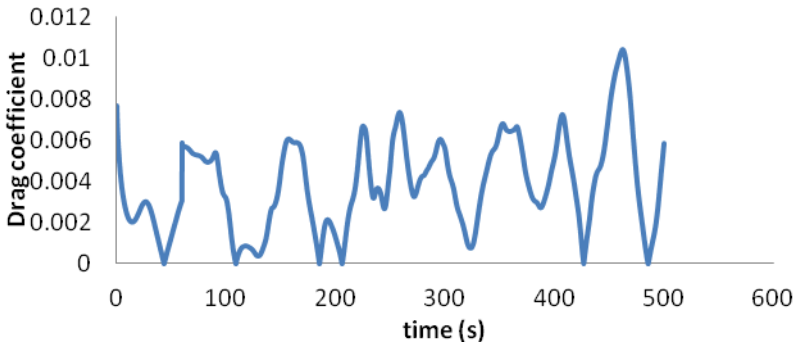

Figure 5.84: 309th velocity profile drag coefficient history

The mean drag coefficient generally fluctuates reaching a maximum of about 0.01 and have a mean value of 0.0039. This mean value generally agrees with the physical measurement results presented in Table 5.2. The drag coefficient history plot for the 441st velocity profile is shown in Figure 5.85.

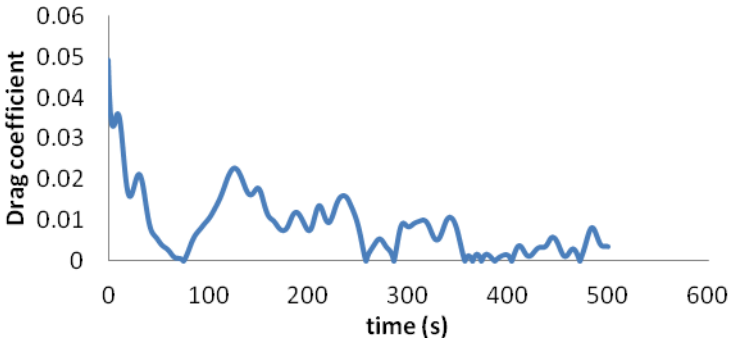

Figure 5.85: 441st velocity profile drag coefficient history

The drag coefficient for the 441st profile simulation case has a mean value of 0.0075 about double the mean value of the 309th profile drag coefficients. Drag coefficient history using the 1187th profile as boundary condition is shown in Figure 5.86.

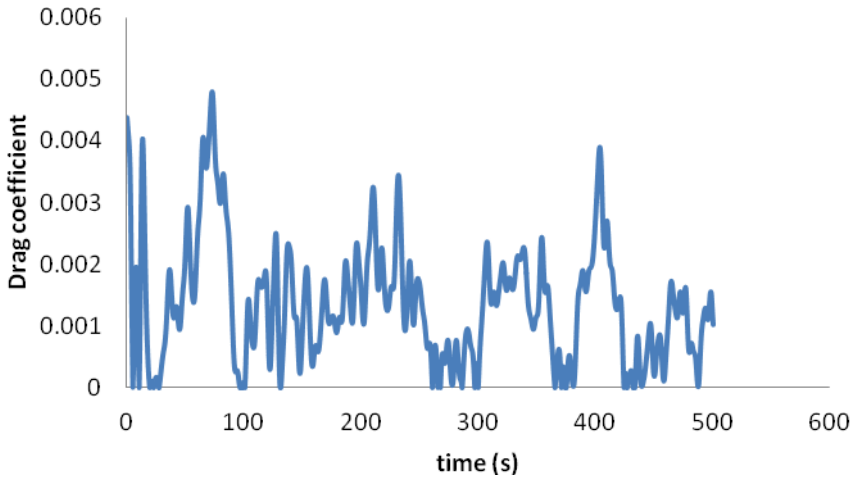

Figure 5.86: 1187th velocity profile drag coefficient history

The mean drag coefficient for the case simulated with the 1187th velocity has a value of 0.0014. This profile has the largest velocity magnitude but produces the lowest drag coefficient values. This is because the drag coefficient is inversely proportional to the square of the velocity magnitude. The simulation results can also be explained from the view point of the Reynolds number drag relationship: For fluid systems with the same fluid viscosity and size of domain, a lower velocity value will result to a lower Reynolds consequently, a higher drag coefficient. The velocity profiles with the largest magnitudes thus appear to generate more turbulence.

From the simulation results, it can be stated that the seabed drag coefficient at the Forth estuary during the 23 day experiment period, ranged between 0.0013 and 0.0075. The result agrees with some measured seabed drag coefficient at various locations presented in Table 5.2 above. Although comparing seabed drag coefficient results with experimental values from

different location around the world, it should be noted that the velocity profiles for those sites differs.

5.4 Chapter summary and conclusion.

Large scale turbulence in tidal current channel is a potential threat to the installation and operations of tidal current devices and /or its support structures. The submerged energy system is exposed to fluctuating currents in magnitude and direction that generate fluctuating dynamic forces. This has implication for design and optimisation for engineering practical application.

Due to the difficulties encountered in simulating large scale ambient turbulence in the laboratory, a novel method of using a turbulent velocity profile sampled with ADCP from a real tidal current site has been demonstrated. The idea is on the premise that velocity profile sampled from a tidal current flow is affected by waves, channel walls, seabed roughness and other physical and natural processes. These effects were evident as fluctuations on the measured experimental velocity profile and contributed to generating visible turbulent structures in a LES of an empty channel. On the other hand, the physical, natural and biological processes affecting velocity profiles of real flow have been averaged out in theoretical velocity profiles.

Based on the simulation results of the flow fields, it can be stated that; the uniform flow velocity profile is an idealised profile that can allow spatial and temporal changes in a LES when a velocity fluctuating algorithm and no slip wall boundary conditions are specified. However, the general behaviour of the flow field can better be described as a pulsation of the mean flow containing fine turbulence. The examinations of the vorticity at different instantaneous times were relatively low and mostly confined to the walls where turbulent dissipation also occurs. The associated velocity vectors and flowline plots were relatively well pattern, organised and one directional and does not fully fit the description of a real turbulent flow field.

The flow field behaviour evolving from the $1/7^{th}$ power law simulation case is similar to the uniform flow case. The $1/7^{th}$ power law is popular because it is an appropriate mean flow approximation of a wall bounded channel flow. From the foregoing, it can be stated that although, the $1/7^{th}$ power law velocity profile has been an approximate but successful modelling strategy that describes the mean turbulent velocity profiles, it cannot adequately aid generating ambient coherent structures suitable for numerical testing of a tidal current energy device.

The simulation results based on the ADCP data shows significant presence of ambient turbulent structures. The turbulent structures were found everywhere in the flow field because they were generated by the influenced by ADCP measured velocity profile specified at the inlet and not just by the walls and the fluctuating velocity algorithm specified in LES.

The ability to generate large scale turbulent structures in a small numerical domain demonstrates the possibility of representing a large scale prototype in a small scale numerical model for credible simulation of devices in an ambient turbulent environment.

The effect of ambient turbulent structures on the channel bed drag coefficient show that, they can affect the value of the drag coefficient significantly by reducing it and this has implications for estimating the amount of energy available for extraction.

A paper published from the outcome of this study is appended as appendix C. Following from this work, simulation of the classical monopile structure commonly used as support structure in offshore processes is investigated. The monopile has known values of drag coefficient published in literatures. The study aims to investigate the effect of ambient turbulent structures on a monopile drag coefficient.

Chapter 6.0

Effect of Large Scale Turbulent Structures on Dynamic Loading of a Turbine Support Structure.

6.1 Introduction

It has been demonstrated in the preceding chapter that large scale turbulent structures can be generated with the aid of experimental velocity profile acquired from a real tidal current site and integrated in a LES of an empty open channel flow. It was apparent that a turbulent velocity profile sampled within a small time resolution contain fluctuation that allows the generation of significant turbulent structures in an open channel flow compared with simulation carried out by specifying the classical $1/7^{th}$ power law and uniform flow velocity profiles at inlet. This chapter presents the effect of large scale structures on dynamic loading of a monopile commonly used as a support structure.

Natural flow within tidal currents contains coherent structures or vortices. The presence of the vortices in relation to the amount of energy available for extraction was mentioned by (97) by stating that regions of random vortex activity will not provide viable power at least with the current technology. In design and optimisation of tidal current energy devices also, large scale structures may have an undesirable effect during hydrodynamic loading of a submerged device. In the present study it is anticipated that there will be significant difference in hydrodynamic forces when an energy device is simulated using the theoretical velocity profiles and experimental velocity profile resulting from the presence of coherent vortices in the latter. Following the enormous level of numerical modelling tidal current energy devices currently undergo, it is important to account or discount for the effect of large scale structure to add credibility to simulation results.

There are a variety of tidal current turbines and support structures being proposed for energy extraction. A few examples are included in the general

introductory chapter. A monopile is chosen as a generic support structure because of its simplicity and common use in the offshore energy industry. The monopile is modelled as a vertical cylindrical object rigidly fixed to the bed of an open channel. The monopile as a fixed cylinder has been extensively studied in wind tunnel experiments with data published in literatures (63-65; 98-99).

Numerical simulation studies have also been carried out by numerous authors which includes Wang (100) on predictions of high Reynolds number flow with assumption of a periodic flow boundary condition. Wang aim was to evaluate the viability and the accuracy of LES for wall bounded complex flows. His key conclusion was that overall drag coefficient was predicted reasonable well when results were compared with wind tunnel test results. Tutar (68) carried out comparative studies to investigate the performance of various turbulence model including LES with the assumption of a uniform flow at the inlet boundary and Gao (101) investigated turbulent flow around a vertical cylinder in a steady current. In almost all CFD calculations theoretical velocity profiles, which appear as organised flow lines on the incident flow are normally employed as input boundary conditions although turbulent flow lines are chaotic in nature appearing as tangled flow lines as evident in the simulation results presented in chapter 5. The upstream flow commonly simulated does not contain ambient flow structures that resemble those in natural flows.

Furthermore, the use of RANS turbulence models has known limitations: The RANS methodology does not distinguish the large scale structures from the small scale structures. The averaging procedure dampens out the contributions of the large scale structures on the flow behaviour thereby rendering it unsuitable for explicit investigation of the effect of large scale turbulent structures. This study uses the novel application of a turbulent velocity profile affected by natural processes in tidal currents to investigate drag coefficient on a monopile using LES. Simulation results were benchmarked with those based on theoretical velocity profiles.

6.1.1 Forces on submerged offshore structures

Forces acting on fully submerged structures in marine environment arise from currents and waves, seabed roughness, other physical and natural processes. These processes induce a steady and unsteady load component on structures. The oil and gas industry has been involved in calculating hydrodynamic loading on structures for design and optimisation purposes. Forces due to wind and current are usually calculated using a similar approach for practical applications in the offshore industry although, wind and water have different physical properties and exhibits different character of turbulent fluctuations.

Morrison (102) was the first to propose an equation to solve hydrodynamic forces acting on an offshore structure based on the assumption that force acting on a section of a pile due to wave motion is made up of two components: a steady flow of a real fluid and an inertia force, analogous to that of a body subjected to a uniformly accelerated flow of an ideal fluid. The wave flow past a pipe is strongly similar to a two dimensional sinusoidal flow past a circular section. The Morrison's equation for a circular section is expressed in equation 6.1 below as;

$$F = 0.5\rho D_m C_D u|u| + 0.25\rho\pi {D_m}^2 C_m \frac{du}{dt} \qquad (6.1)$$

Where F total force per unit length acting on the structure. D_m is the circular section diameter, u is the incident wave velocity, C_D and C_m are the drag and inertia coefficient respectively and $\frac{du}{dt}$ is the fluid acceleration. The Morrison equation implicitly implies that the flow pattern in the vicinity of the structures is uniform due to the relatively small size of the structure to the wavelength of the incident flow (102). This suggests its unsuitability to

investigate effect of large scale turbulent structures on hydrodynamic loading because the shape of a turbulent velocity profile in a tidal current channel is not uniform. The wake method (103) presents an alternative method to the Morrison's equation that takes into account the structure interaction with the wake when the velocity reverses and considers the time dependent force coefficients. The wake II method is a continuation of the wake I model based on solving the linearized Navier-Stokes equation for oscillatory flows.

Analogy is currently drawn between the tidal current energy technology and the wind energy technology with respect to modelling and design of structures, although it is generally agreed that the boundary condition may result in important differences in design and strength of materials. For example tidal current turbines operate in a confined space limited by the free surface compared with wind turbines that have sufficient space above the boundary layer that gives possibilities to avoid or reduce the turbulent effect due to the bottom topography. Also Fraenkel (15) observed differences in load cases between tidal stream rotors and wind rotors because higher forces are generated by water and this necessitated the use of carbon fibre for the construction of SeaGen (Figure 1.2). Typically forces that could act on a 3D structure submerged in a stream of current are illustrated in Figure 6.1.

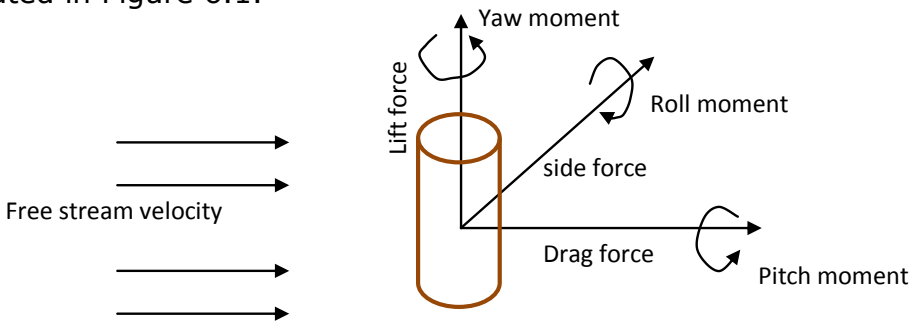

Figure 6.1: Illustration of forces acting on a structure submerged in a fluid.

The forces and moment arising from the device interacting with the environment are presented in three coordinates system. The drag force has

an associated rolling moment about its axis. Perpendicular to the drag force is the lift associated with the yaw moment and the side force linked with the pitching moment. The forces occur in terms of wall shear stress due to viscous effect and pressure forces distributed along the surface of the object in varying magnitude and direction.

The drag force for a cylindrical device is made up of two components; the pressure drag arising from the pressure distribution on the surface of the device due to flow separation, and the friction drag contributed from the friction generated due to fluid flow. Although boundary layer theory can gives a qualitative illumination of viscous fluid flow, it however cannot produce satisfactory quantitative result for real flow over tidal current energy structures due to occurrence of flow separation or turbulent eddies or vortices. Therefore CFD and physical experiment are the keys for investigating such flows.

6.1.2 Classifications of flow regimes around a cylindrical structure.

The flow around a cylindrical structure illustrated in Figure 6.2 shows the complex flow regime relating to the formation of a boundary layer, flow separation and the formation of a wake boundary which may involve vortex shedding depending on the Reynolds number (104).

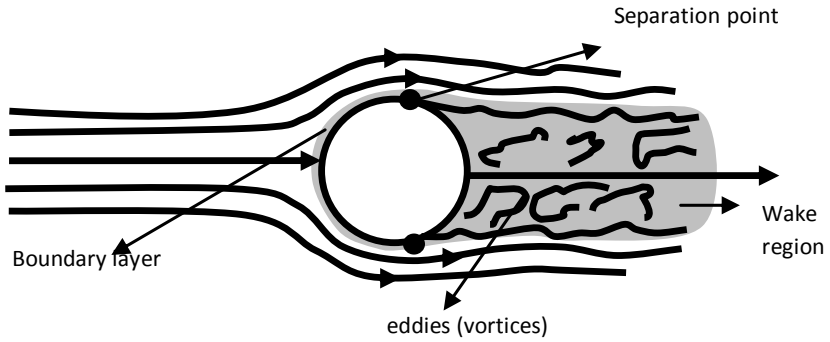

Figure 6.2: Illustration of terms association with the complex flow around a cylinder.

The flow around a cylinder is therefore characterized by its Reynolds number and the drag coefficient. Table 6.1 is a description of the flow behaviour around a smooth cylinder in a steady flow as the Reynolds number increases as accounted in (63).

Table 6.1: Description of flow character around a circular cylinder

Reynolds number, Re	Boundary layer behaviour	Flow separation and wake behaviour	Flow regime classification	C_D
Less then 5	Laminar	Symmetric flow around the cylinder with no separation	Creeping flow	
5 < Re < 40	Laminar	Laminar boundary layer separation first occurs and a fixed pair of symmetric vortices formed in the wake.		
40 < Re < 200	Laminar	2 – Dimensional vortex shedding with wake filled with vortices. Laminar vortex street.		
200 < Re < 300	Laminar	Transition to turbulence in the wake region. 3-Dimensional vortex shedding.		
300 < Re < 3×10^5	Laminar	A completely turbulent wake and a laminar boundary layer separation.	Sub critical flow	1.2
3×10^5 < Re < 3.5×10^5	Laminar at one side Turbulent boundary (B.L) layer at only at separation point.	Boundary layer separation is laminar on one side and turbulent on the other side.	Critical *Or* Lower transition	
3.5×10^5 < Re < 1.5×10^6	Incomplete transition to turbulence in the B.L. The B.L on one side is fully turbulent at 1.5×10^6	Turbulent boundary layer separation on both sides of cylinder.	Supercritical flow	0.25
1.5×10^6 < Re < 4×10^6	The boundary layer is completely turbulent at one side	At 1.5×10^6, the boundary layer is completely turbulent at one side and partly turbulent and laminar on the other side.	Upper transition	
Re > 4×10^6	Completely turbulent	Boundary layer completely turbulent at two sides.	Trans-critical	0.5

The terms used to describe the flow and associated Reynolds number in which they occur are not in strict agreement with the work of others. An account given in (105), suggests that laminar boundary separation with the formation of a fixed pair of vortices in the wake, occur between $2 < Re < 30$ and that the approximate critical Reynolds number for boundary layer transition from laminar to turbulent before separation is 2×10^5 depending on the free stream turbulent intensity. The flow regimes described in Table 6.1 based on the account given by Summer (63) suggests that, flow separation first occur at a Reynolds number of 5 with formation of a fixed pair of vortices between $5 < Re < 40$ and that, the boundary layer developed around the cylinder remains laminar up to the sub-critical flow regime which covers a wide range: $300<Re < 3 \times 10^5$.

Scale models normally used to represent large scale prototype would likely fall within the subcritical flow regime while scale of engineering interest usually would fall into the transcritical flow category. Figure 6.3 illustrates Reynolds number – drag coefficient relationship (96) of flow over cylinders. It shows that the drag coefficient generally decreases as the scale increases (Reynolds number).

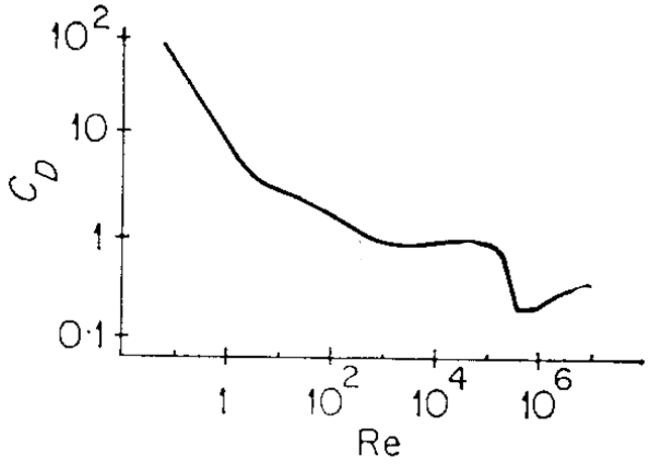

Figure 6.3 : Illustration of the Reynolds number-drag coefficient relationship (96).

6.1.3 Experimental studies on drag coefficient of a cylinder

Schewe (65) carried out force measurements on a cylinder, in a pressurized wind tunnel on Reynolds number range $2.3\,x\,10^4 \le Re \le 7.1\,x\,10^7$. This value encompasses the sub-critical to trans-critical Reynolds number. Trans-critical flows are of practical engineering interest as already mentioned. The results presented in Table 6.2 show two discontinuities drop of drag coefficient, C_D in the lower transitional range from the 1.2 value for the sub-critical flow regime.

Table 6.2:Drag coefficients, C_D results of Schewe and Roshko from wind tunnel test carried out on flow around a cylinder

	Sub-critical	Critical	Super-critical	Upper Transition	Trans-critical
Schewe	1.2	-	0.22	-	0.52
Roshko	-	-	-	-	0.7

Further down to the super-critical flow regime, which begins at a Reynolds number of 3.5 x 10^5, the value of C_D remains fairly constant at 0.22 up to a Reynolds number of approximately 10^6. In the upper transition range which has Reynolds number of approximately 10^6 to 5 x 10^6 inclusive, the C_D increases up to a value of about 0.52 and remains nearly constant in the trans-critical range with Reynolds number greater than approximately 5 x 10^6. Roshko's (99) experimental result also presented in Table 6.2 was based on Reynolds number range of 10^6 to 10^7. The C_D value increased from a low value of 0.3 to 0.7 in the upper transition flow regime. Roshko's (99) noted that the Reynolds number value of 3.5 x 10^6 marks the end of the upper transition range. Roshko's higher C_D value of 0.7 in the trans-critical range was attributed to possible surface roughness effect. The drop and rise of C_D values is caused by transition to turbulence in the boundary layer with increase in Reynolds number resulting to the drag crises phenomenon. The reported experimental data in Table 6.2 has been used to compare with the numerical simulation results from the present study in accordance with the

recommended practice in the DNV code (106) for CFD analysis of wind turbines.

6.2 Methodology

The finite volume technique was used to discretisize the filtered continuity and momemtum equations (presented in section 2.3) governing the flow using the LES commercial code provided by ANSYS. LES explicitly resolves the large scale motions while the small scale motions were modelled using the Smagorinsky's-Lily dynamic stress model. The filtered equations were solved for an open channel flow domain with dimensions 10m x 5m x 2m with a monopile of diameter 0.4m and length 3m fixed to the channel bed as shown in Figure 6.4.

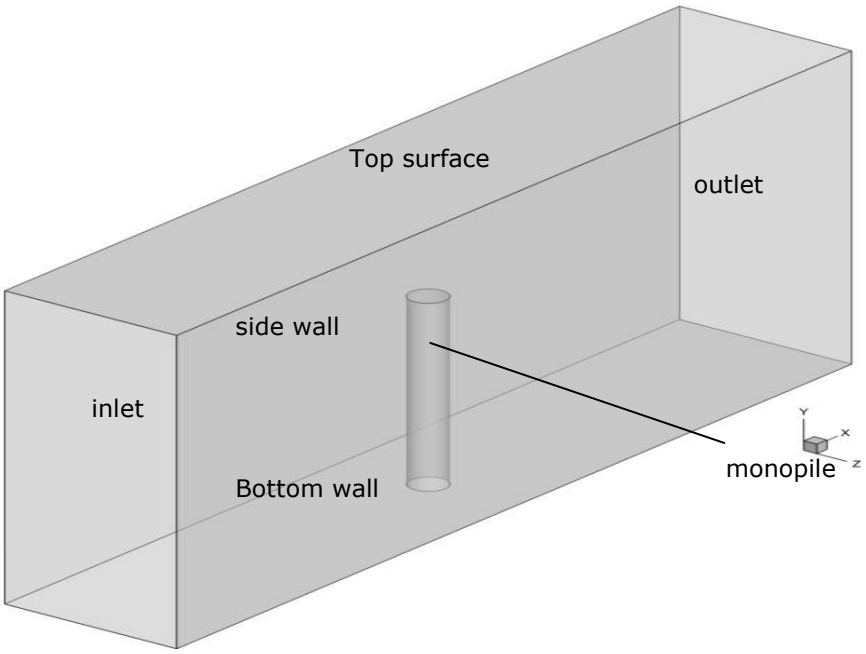

Figure 6.4: Simulation domain with a fixed monopile structure

6.2.1 Boundary specifications

The following boundary conditions were applied;

Wall boundaries: No slip boundary was applied at the side walls, the channel bottom, and the monopile wall.

Inlet boundary: The inlet velocity was varied according to three simulation cases namely;

1. the uniform inflow profile,
2. the $1/7^{th}$ power law inlet profile
3. Experimental velocity inlet profile sampled with ADCP at the Forth estuary specified in two horizontal directions.

The uniform and the $1/7^{th}$ power law simulation results were used to benchmark the simulation results from experimental velocity profile case. The 309^{th} experimental velocity profile (presented in chapter 4), was arbitrarily chosen for the simulation. The mean and the average velocity based on the 309^{th} turbulent velocity profile were determined and used to obtain values for the uniform flow and a $1/7^{th}$ power law profile using equation 4.9 for the later. The data for the theoretical profiles were based on a 50 data point assuming 50 experimental depth cell in the channel, while the raw experimental data was specified as 44 data points to remove the effect of the velocity inflection observed towards the water surface. The spectral synthesizer algorithm for velocity fluctuation was specified at the inlet for all simulation cases with a turbulence level of 10% and a length scale of 0.4m based on the monopile diameter. A zero shear and a zero gauge pressure outlet were specified at the water surface and outflow respectively. The average time step for the simulation was 0.03s.

6.2.2 Meshing strategy:

The simulations were carried out on a three dimensional mesh shown in Figure 6.5 with the side walls, surface, inlet and outlet removed. The mesh consists of 183063 nodes. A meshing scheme with quad elements was used for the side walls, the inlet and the outlet faces of the domain. The monopile mesh consists of the tri element with a pave mapping. A tri element is good for cylindrical surfaces. The bottom area around the fixed monopile consists of an attached boundary layer having with a first row of

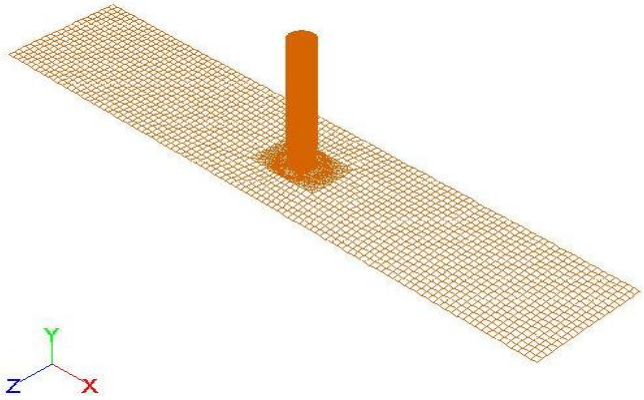

Figure 6.5: A wire mesh display of the monopile structure

0.01 and a growth rate of 1.2 over 4 rows. The presence of the boundary layer at the base of the monopile resulted to meshing the seabed with quad element with a pave type setting. The fluid domain was meshed with the Hex/Wedge, cooper meshing scheme in Gambit using the top of the domain as source.

6.3 Simulation Result and Discussion.

Following from the simulation procedures, the following result and discussion is based on results extracted from the LES result database. Firstly, a discussion on the evolution of the flow field resulting from the uniform flow and the $1/7^{th}$ power law flows were compared with the experimental velocity profile simulation case. The theoretical velocity profiles were used as comparison components to benchmark the experimental result because of their popular use in CFD analysis of tidal current energy devices.

The development of the flow field for each simulation case was scrutinized at different instantaneous times. The modifications of water particle path occurring in the flow field surrounding the monopile structure plots were examined using streamtraces plots. Velocity magnitude vector plots are used to probe and observe for evidences and extent of fluid rotation associated with turbulence. Furthermore, vorticity magnitude contour plots

were used to visualise the evolution of large vortex structures in the flow fields resulting from each simulation case.

The drag coefficient is a critical parameter for design purposes and is investigated. The drag history was monitored for each simulation case to observe the variation of the drag coefficient with time. The mean values of the simulated monopile drag coefficient resulting from each simulation case were compared with each other and also with the experimental results from Schewe (65) and Roshko (99) presented in Table 6.2. Comparing drag coefficient results from the experimental velocity simulation case with drag coefficient from the theoretical velocity profile simulation case, ascertain the implication of using the theoretical velocity profiles for numerical simulation of tidal current energy devices for practical applications.

6.3.1 Evolution of the flow field with a uniform flow Inlet.

A streamtrace plot for the uniform flow simulation case at time = 2s is shown in Figures 6.6. The flow lines are nearly uniformly organised, one

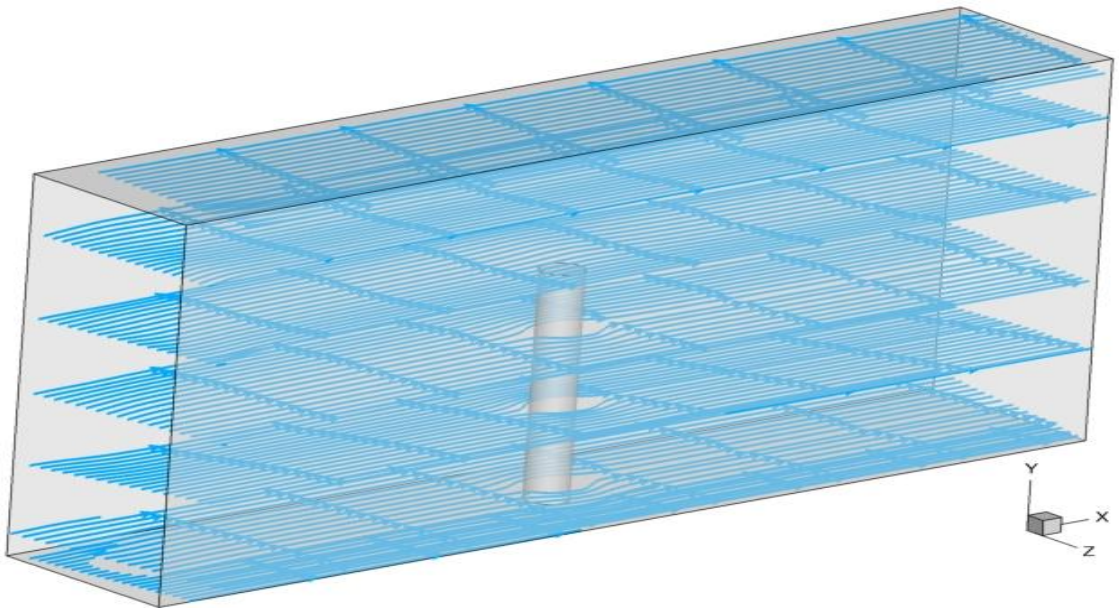

Figure 6.6: streamtraces for uniform flow condition at t = 2s

directional and appear undisturbed upstream and downstream of the monopile except very close to the pile where the flow lines separates laminarly and re-joins downstream. The ability of the flow to re-join smoothly after separation at t = 2s is because of the early stage of the simulation. As the simulation time increases, the flow should develop with noticeable changes.

The vorticity contour plot corresponding to the streamtrace plot at t =2s is shown in Figure 6.7. Perceptibly, there are no turbulent flow structures or vortices upstream and downstream of the monopile in the flooded plot. The greatest vorticity is concentrated near the monopile wall due to flow separation associated with turbulence generated by the presence of the pile. The maximum attained vorticity magnitude near the monopile wall was $16s^{-1}$. Vorticity relates to the amount of circulation around the vortex core or the vortex line and begins from a boundary. Vorticity is transmitted around in the presence of a viscous fluid.

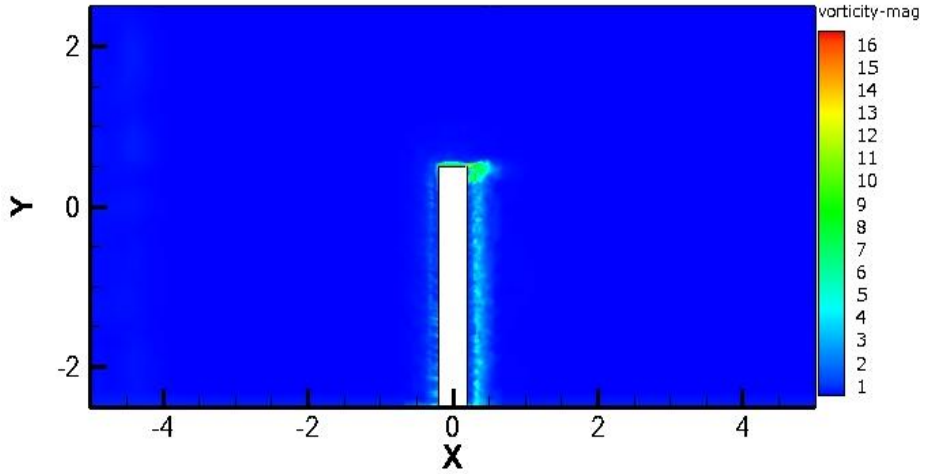

Figure 6.7: Instantaneous vorticity plot for uniform flow condition at t = 2s

Vortex structures are associated with fluid rotation and are easily decipherable in a velocity vector plot as regions of rotational motion. The length of a velocity vector indicates its magnitude and the orientation of the velocity vector indicates its direction. Figure 6.8 is an x-y vertical plane slice

of the vector field at the middle of the channel where z = 0. The flow upstream of the structure show smooth organised and well patterned

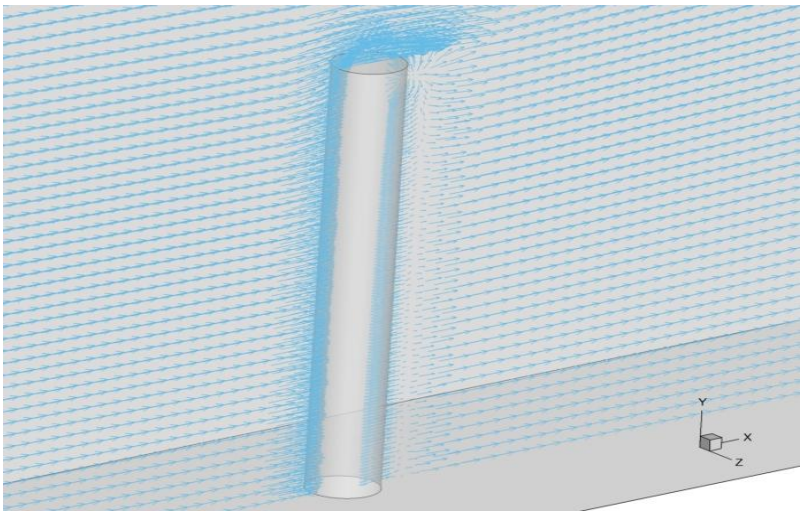

Figure 6.8: Velocity magnitude vector for uniform flow at t = 2s.

vectors. Absence of fluid rotation is obvious in the ambient flow. However, near the top of the pile there is evidence of some rotation where vorticity (Figure 6.7) has the greatest magnitude. A further investigation of the streamtrace plot at instantaneous time t = 38s in Figure 6.9 shows evidence of changes in the path of the fluid particles with time.

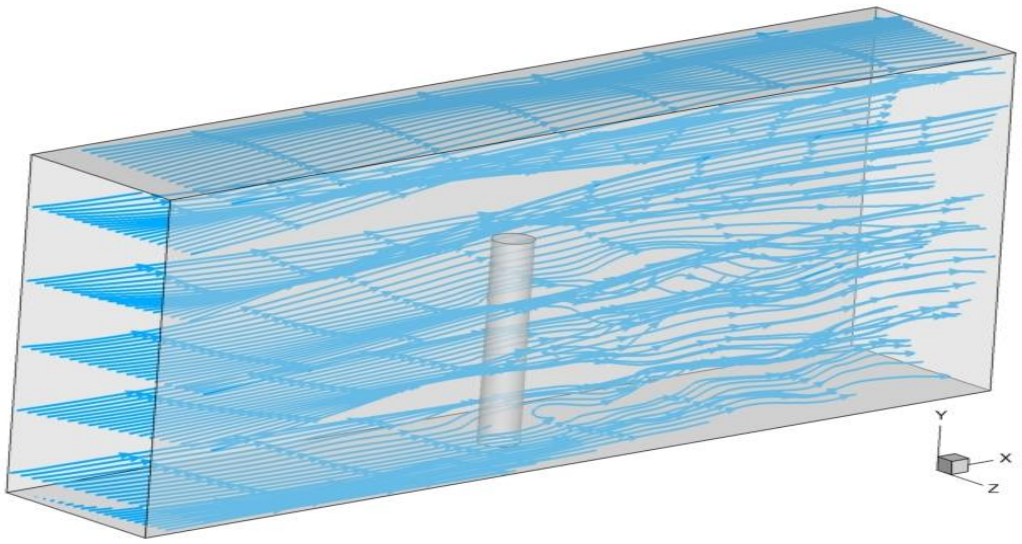

Figure 6.9: streamtraces for uniform flow condition at t = 38s

The changes occurring upstream and downstream of the monopile are apparent. What appears as a pulsating or rhythmic motion flow can be noticed in the upstream ambient flow field. It has the appearance of a smooth wave-like or undulating motion. A pulsating flow has been observed as a large scale vortical motion in natural flows by Matthes (81) where it was described as a lower frequency flow containing fine turbulence. The flow downstream of the monopile display irregular flow lines resulting from turbulence generated by the presence of the monopile. The flow in the wake is complex, involving flow separation with the consequence of a high drag force resulting from the pressure differential created in the flow field. A further investigation of the flow field at t =80s as streamtraces plot in Figure 6.10 also reflect turbulence in the wake as tangled flow lines downstream of the monopile. The pulsating flow behaviour upstream of the monopile is also apparent like an undulating wave motion.

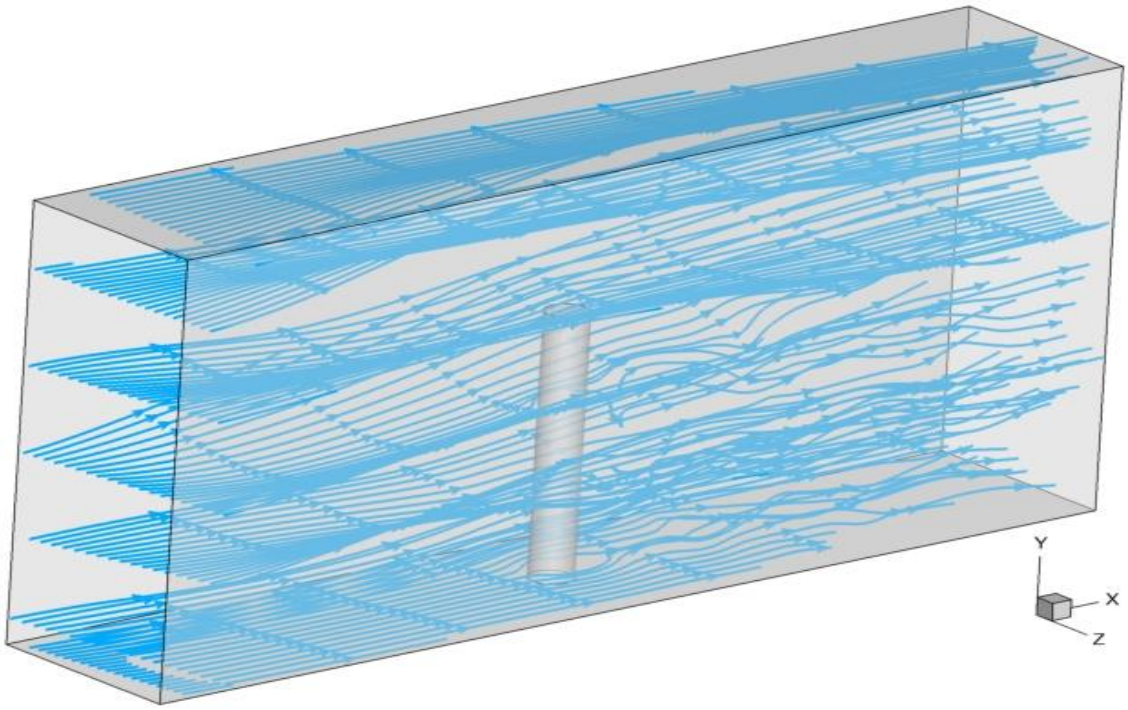

Figure 6.10: streamtraces for uniform flow condition at t = 80s

The turbulence generated by the presence of the monopile in terms of vorticity is better appreciated by observing the plot at t =80s in Figure 6.11.

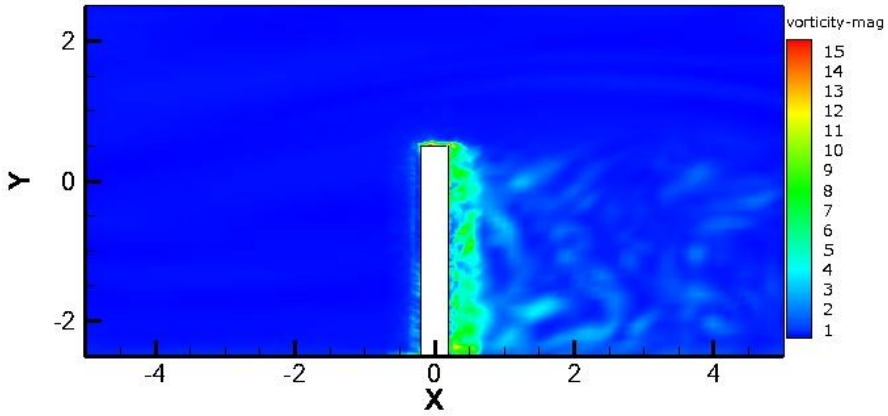

Figure 6.11: Instantaneous vorticity plot for uniform flow at t = 80s

Comparing the plots in Figures 6.7 and 6.11 show that the region of significant vortex activity has widened further downstream. Although the maximum vorticity value near the monopile in each plots do not significantly differ having a maximum vorticity magnitude value of $16s^{-1}$ at 2s and $15s^{-1}$ at 80s of simulation time. Evidence of diminishing vorticity with distance from the monopile is observed in Figure 6.11 due to turbulent dissipation associated with a viscous fluid. A corresponding velocity magnitude instantaneous vector plot in Figure 6.12 below shows the associated fluid

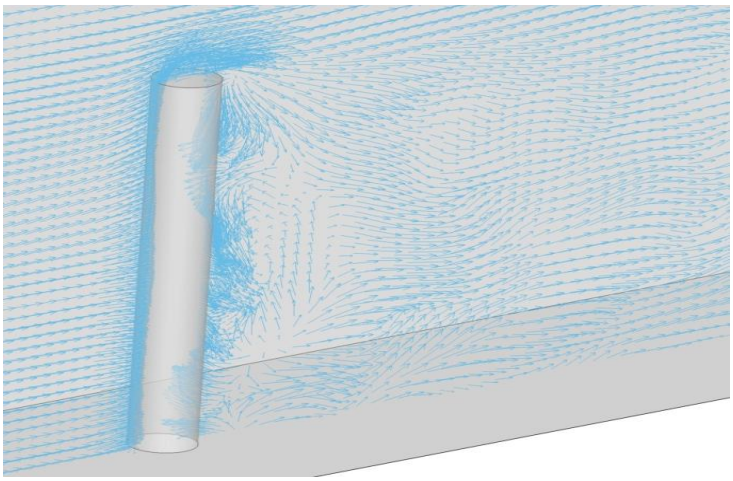

Figure 6.12: Velocity magnitude vector for uniform flow at t = 80s.

rotation with turbulence downstream of the monopile. The orientation of the vector gives a clue to the rotational tendency within the fluid.Comparing

Figures 6.11 and 6.12 shows how of the velocity vectors and the equivalent vortex structures relate. It is clear that a chaotic vector field results to the formation of significant turbulent structures. The flow upstream flow of the monopile is relatively uniform. The flow fields investigated at t= 108.6s and 120s using the streamtraces plots in Figures 6.13 and 6.14 underpins the

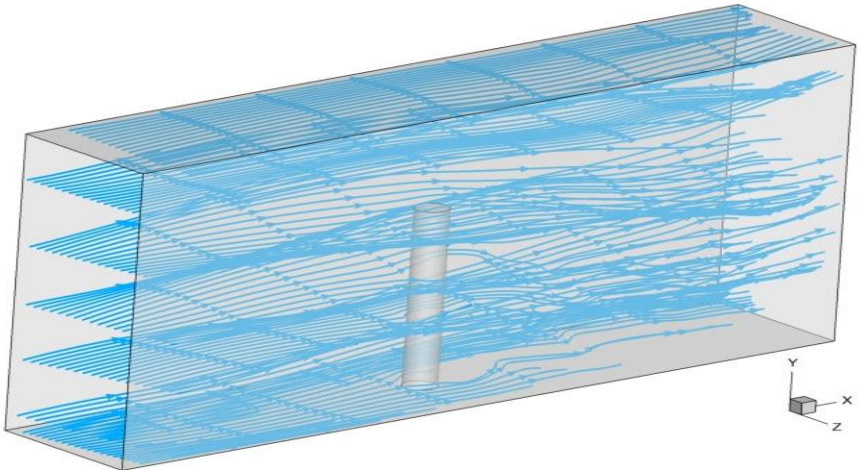

Figure 6.13: Instantaneous streamtraces for uniform flow at t =108.6s

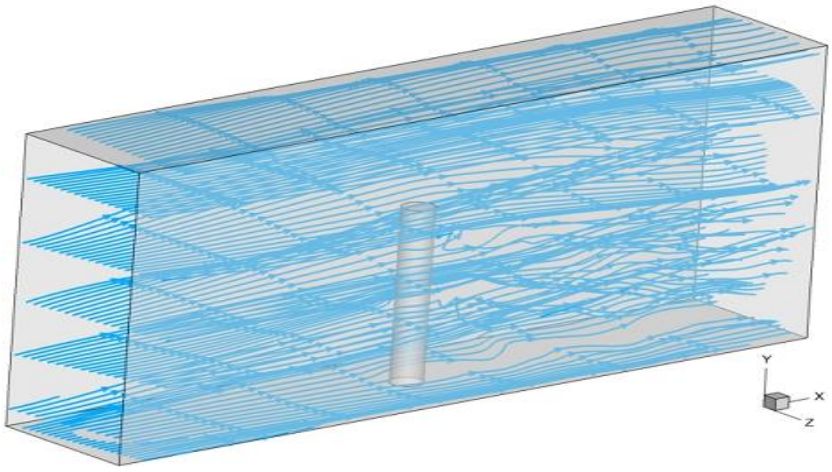

Figure 6.14: Instantaneous streamtraces for uniform flow at t =120.6s

nature of the flow already just previously described. As the flow progresses, modification to the flow field are also observed because it is an unsteady process with temporal and spatial changes. The pulsation of the ambient mean flow upstream was still evident in both plots**.**

The turbulence generated in the uniform flow simulated case is influenced by the fluctuating velocity algorithm integrated into the LES technique, the no slip conditions applied at the channel walls and the monopile structure. Turbulence generated at the wall is mostly dissipated near the walls. The best, LES could produce with a uniform velocity inlet condition is a flow field resembling a pulsation of the mean flow in the ambient upstream region which contains fine turbulence but lacks ability to reproduce significant ambient coherent structures resembling real flow. From the simulation results of the uniform flow inlet condition case, it can be stated that it is unsuitable for use with LES when effect of ambient turbulent structures are of importance. The simulation results thus demonstrate the importance of specifying a realistic velocity profile at the inlet boundary of a LES results if turbulent structures are of interest.

6.3.2 Evolution of the flow field with a 1/7th power law velocity profile inlet condition.

The $1/7^{th}$ power law velocity profile is characterised by a sheared velocity depth profile. Shear acts on turbulent eddies and causes it to deviate from the assumed isotropic to anisotropic flow behaviour. Isotropic behaviour of a turbulent flow implies that the flow is identical in all directions in disparity to the behaviour of flow encountered in the natural environment. The $1/7^{th}$ power law velocity profile approximates more closely the shape of a velocity profile in a wall bounded flow such as encountered in tidal current channels. The ADCP data analysed and presented in chapter 4 evidently show the evidence of velocity shear from the shape of the plot few meters above sea bottom.

Steamtraces, vorticity contours and velocity magnitude vectors plots are used to give a visual impression of the flow behaviour and associated flow structures evolving from the flow fields with the use of the $1/7^{th}$ power law velocity profile as inlet condition. Figure 6.15 show the streamtraces plot at instantaneous time t = 1.6 s. The flow lines generally look organised with a definite line patterns because the simulation is still at an early stage.

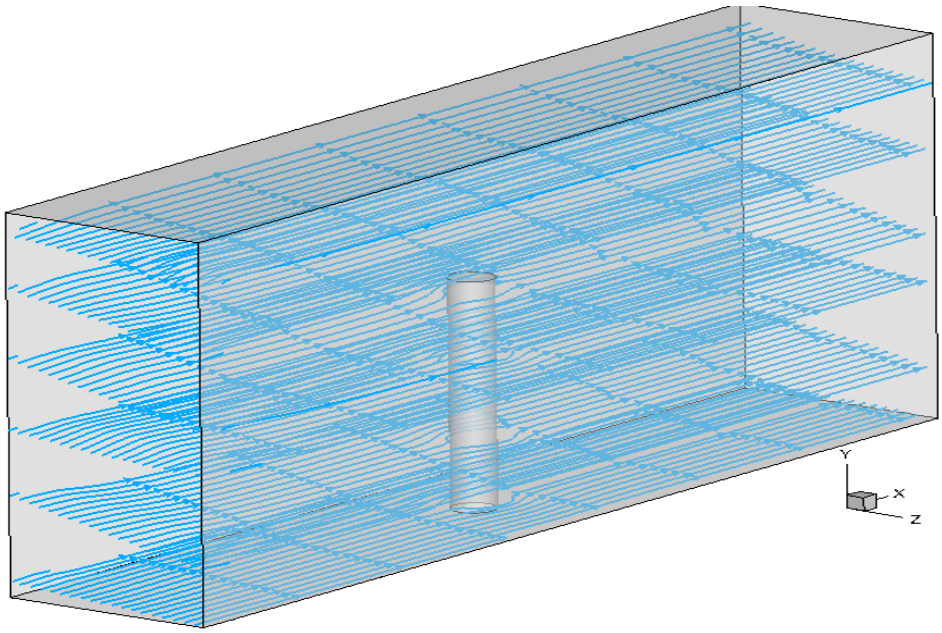

Figure 6.15: Streamtrace plot for 1/7th power law condition at t = 1.6s

Noticeable changes in the streamtrace plots can be visualised in Figures 6.16, 6.17, 6.18 and 6.19 extracted from the simulation result database at instantaneous times t = 32s, 58s, 112s and 130s respectively.

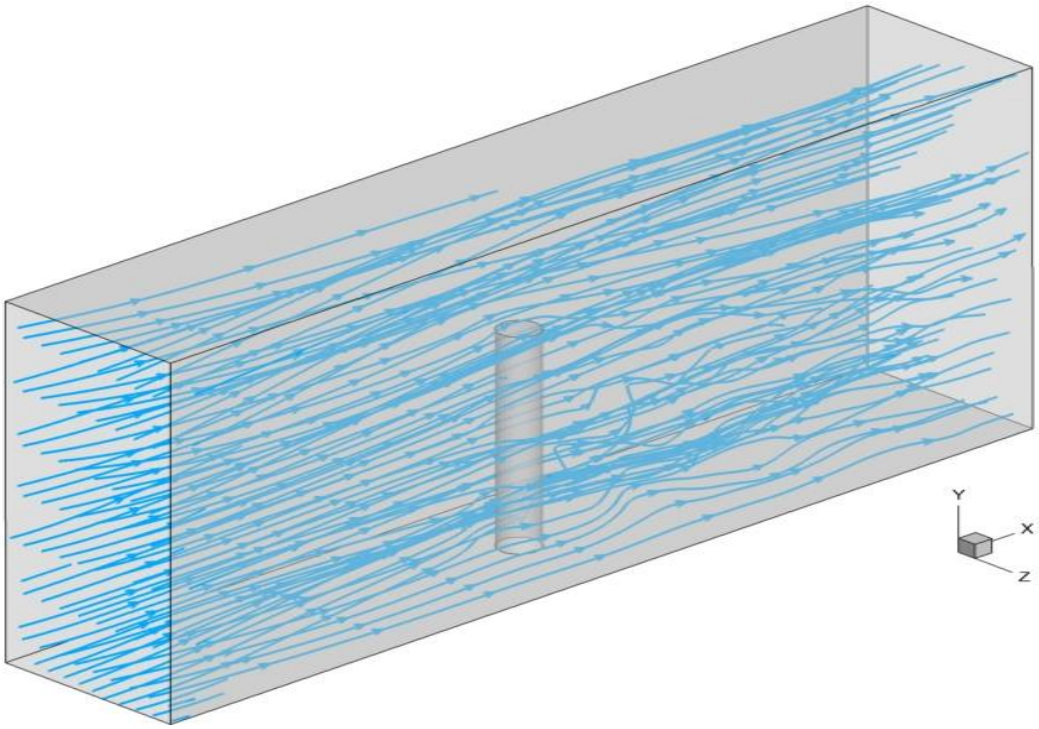

Figure 6.16: Streamtrace plot for 1/7th power law condition at t = 32s

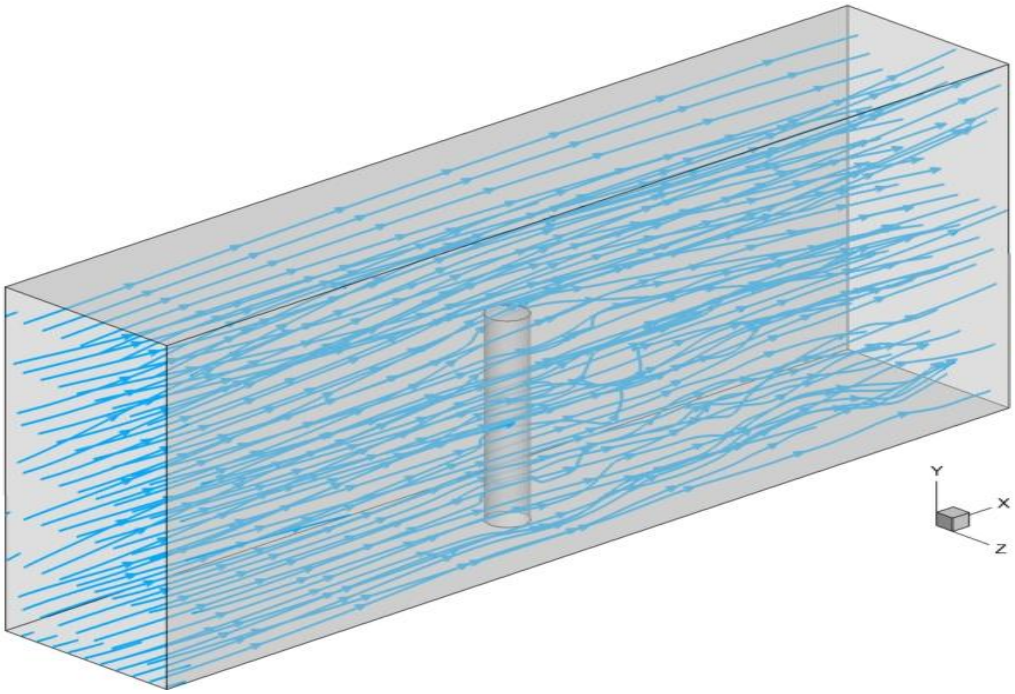

Figure 6.17: Streamtrace plot for 1/7th power law condition at t = 58s

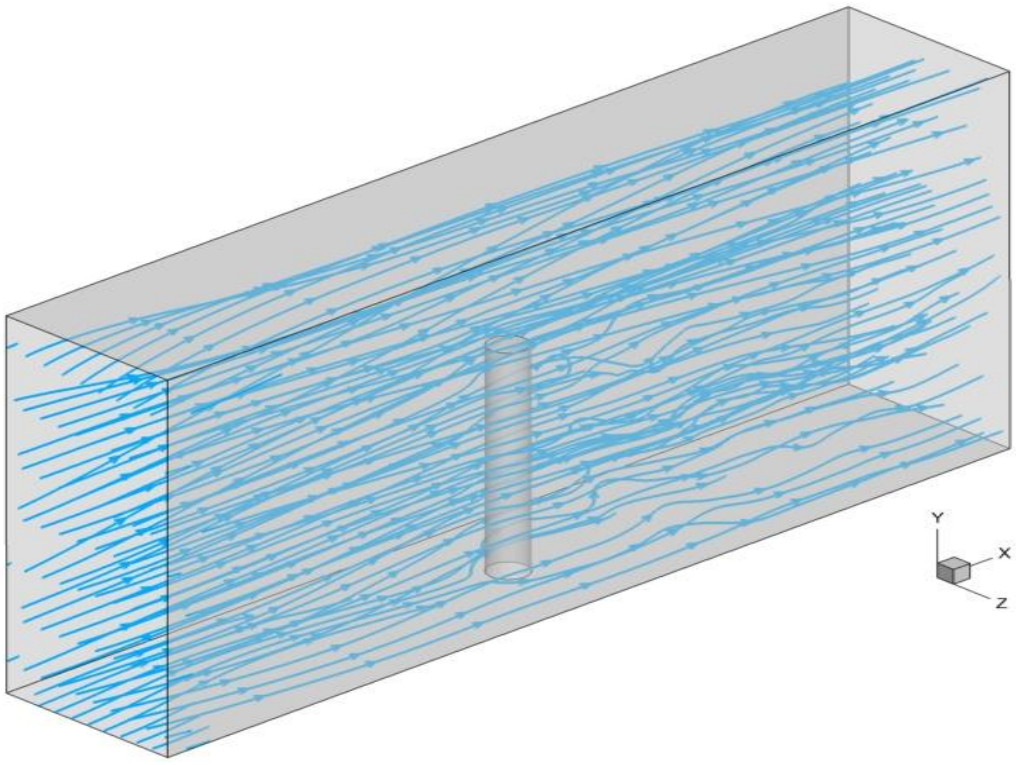

Figure 6.18: Streamtrace plot for 1/7th power law condition at t = 112s

The 1/7th power law streamtraces behaves similarly to the uniform flow streamtraces presented in the previous sections. The streamtraces are marked by a rhythmic flow pattern upstream and a more turbulent flow (chaotic flow lines) downstream.

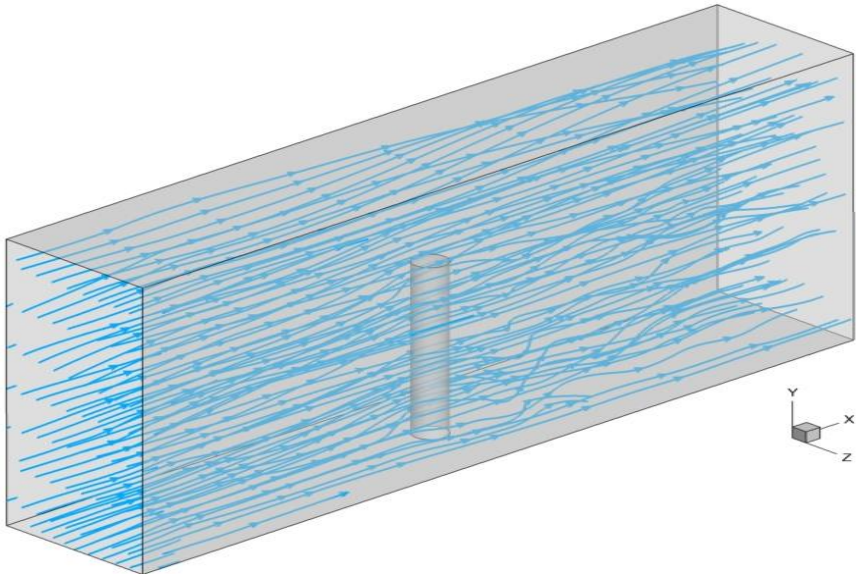

Figure 6.19: Streamtrace plot for 1/7th power law condition at t = 130s

Associated with the stream trace plot at t = 130 are the vorticity contour plot and the velocity magnitude vector plots in Figures 6.20 and 6.21 respectively.

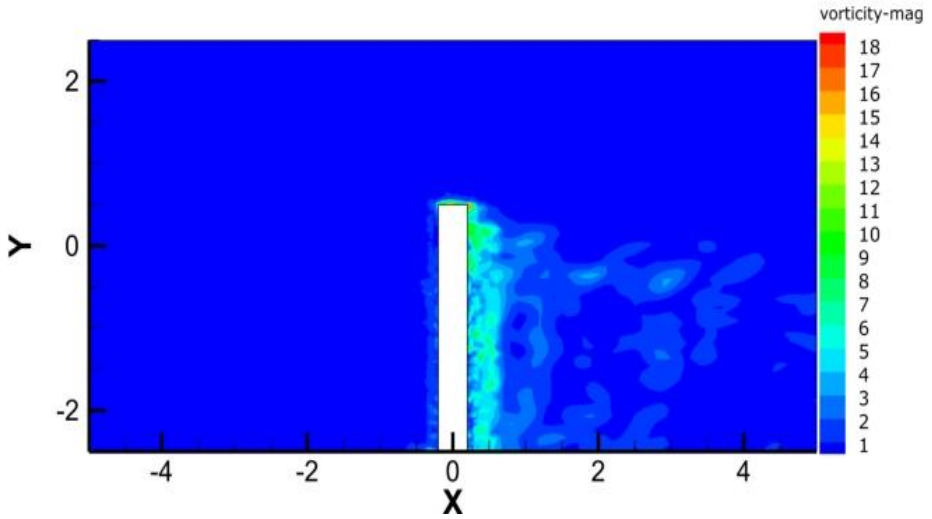

Figure 6.20: Vorticity contour plot of 1/7th power law condition at t = 130s

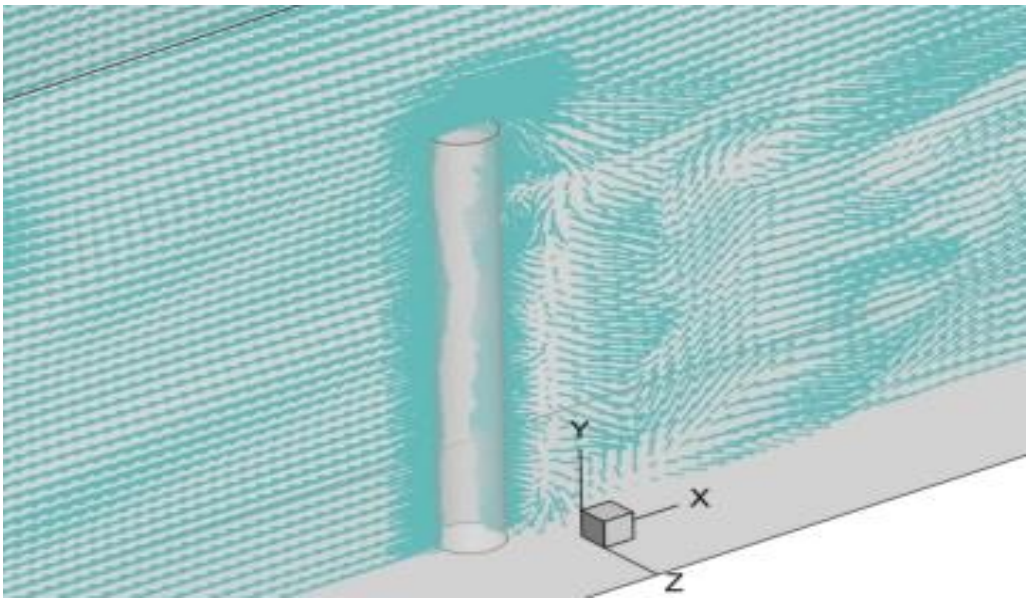

Figure 6.21: Velocity magnitude vector plot for 1/7th power inlet condition at t = 130s

The vector and vorticity plot in Figures 6.20 and 6.21 aid the visualisation of the vector field and the tendency of the fluid to rotate. The turbulence is quantified in terms of vorticity magnitude and had a maximum of $18s^{-1}$ close to the top of the monopile. As expected, there are significant structures downstream of the monopile than upstream.

The differences in shape of the uniform flow and the $1/7^{th}$ power law profile do not have significant effect on the evolution of the flow field. The flow fields in both cases can generally be described as consisting of organised flows line upstream of the monopile and more chaotic flow behaviour downstream of the monopile due to turbulence generated by the monopile structure. This important resemblance in the flow field generated by the uniform flow and the $1/7^{th}$ power law boundary conditions is attributed to the 1 dimensionality of the mean flow velocity profiles. In what follows, the flow field generated with the experimental velocity profile sampled by an ADCP is explored.

6.3.3 Evolution of the flow field with experimental velocity profile inlet condition.

The velocity profile sampled from the Firth of Forth and specified at the inlet of a LES has been used to carry out this investigation. The velocity data is recorded in three coordinate. Plots of single realisation of turbulent velocity profiles from the ADCP experiment have different shapes but are similar in the sense that, they contain visible fluctuations that causes their shapes to deviate from the classical $1/7^{th}$ power law velocity profile. The fluctuations inherent in the experimental velocity profile are due to sea waves, seabed roughness, side walls bounding the estuary, variable weather conditions and other processes that affect real flows and its use in a LES implies that the effects of these processes are implicitly captured in the numerical simulation. The effect of the experimental velocity profile on the evolution of the flow field is discussed using streamtraces, velocity vector plots and vorticity contour plots in what follows. Figure 6.22 is a streamtrace plot showing the path traced by massless particles placed at an arbitrary

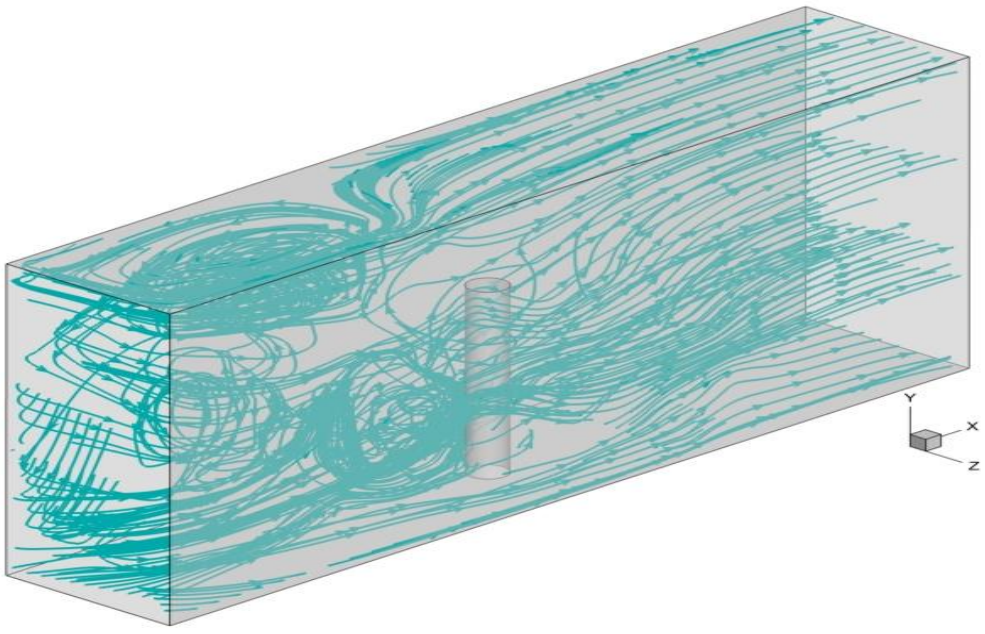

Figure 6.22: Streamtrace plot for experimental velocity profile inlet condition at t = 18.46s

location in a vector field at instantaneous time, t = 18.46s. The flow lines appear as twisted and tangled with some swirl having irregular shape or form. It is obvious that the turbulent velocity profile have made a significant impact on the ambient flow.

For clearer visualisation, not all flow lines are shown. The chaotic manifestation are absent in the theoretical profiles simulation cases. The effect of the disorganized flow field on force acting on the monopile structure will be elucidated from the analysis of the drag coefficient in later sections.

The streamtraces downstream of the monopile, appears relatively more organised (Figure 6.22) than the flowlines upstream because the simulation is at an early stage because the effect of the inlet condition is yet to be felt downstream of the monopile. The next series of plots demonstrates the extent of fluid deformation and evolution of flow structures with simulation time. Corresponding to the streamtrace plot of Figure 6.22 are the vorticity and the velocity magnitude vector plot presented in Figures 6.23 and 6.24 respectively. The vorticity plot is a slice of the flow field from the channel centre where the z cordinate is zero.

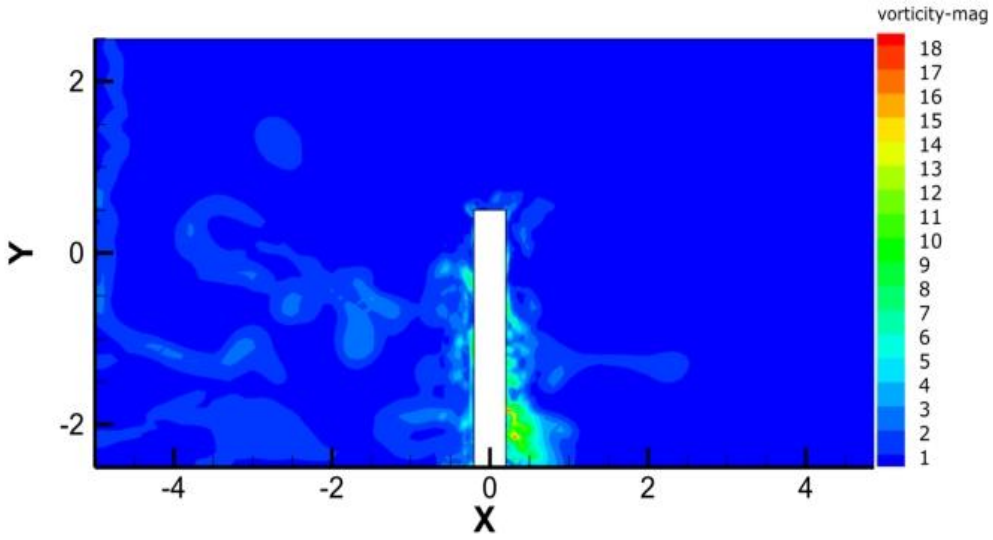

Figure 6.23: vorticity contour plot for experimental velocity profile simulation case at t = 18.46s

Clearly visible in Figure 6.23 are the upstream turbulent structures reflecting the tangled flows lines previously shown in Figure 6.22 in form of coherent upstream of the monopile. These strutures play a major role in the dynamics of turbulent flow. The relatively fewer structures noticeable downstream of the monopile reflects that the simulation is at an early stage and further demonstrates that, well pattern idealised flow lines are not associated with turbulence structures in ambient natural flow.

Since many of the significant structure in a turbulent flow are vortices, the vorticity contour plot thus provides a suitable measure of turbulence in the flow field. From Figure 6.23, the vorticity have a maximum magnitude of about 18 s^{-1} occuring downstream near the monopile walls close to the channel bed. The flow field also show regions of high and low vorticity. However, vorticity plots for the theoretical profile simulation cases in Figures 6.7, 6.11 and 6.20, shows nearly constant and very little vorticity upstream of the monopile. While the vorticity contour plot gives an indication of the existense of turbulent vortices, the vector plot in Figure 6.24 indicates the presence or absence of fluid rotation or eddying.

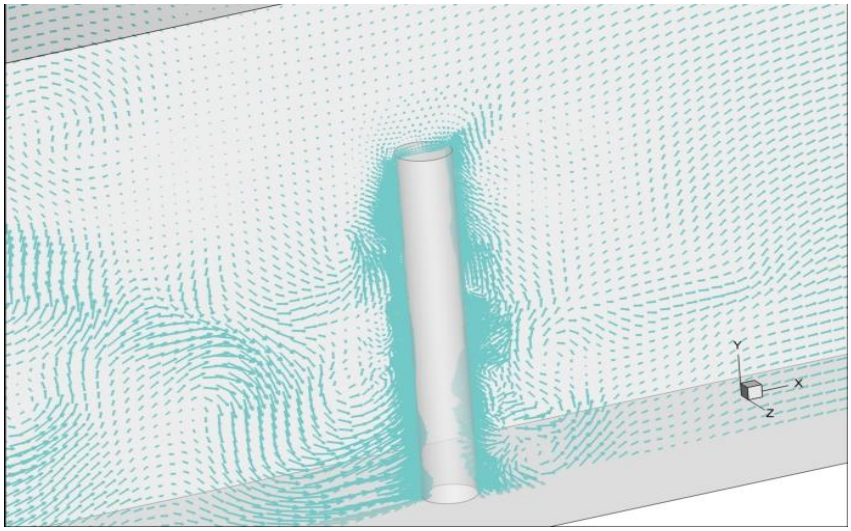

Figure 6.24: velocity magnitude vector plot for ADCP data at t = 18.46s.

The orientation and magnitude of each vector in the plot relates to its direction and magnitude. Notice the apparent relatively organised vector

field downstream of the monopile compared with the vectors upstream also resulting from the early simulation stage. Further investigation of the flow field at t = 90.46s in Figure 6.25 shows how the flowlines downstream has evolved with time.

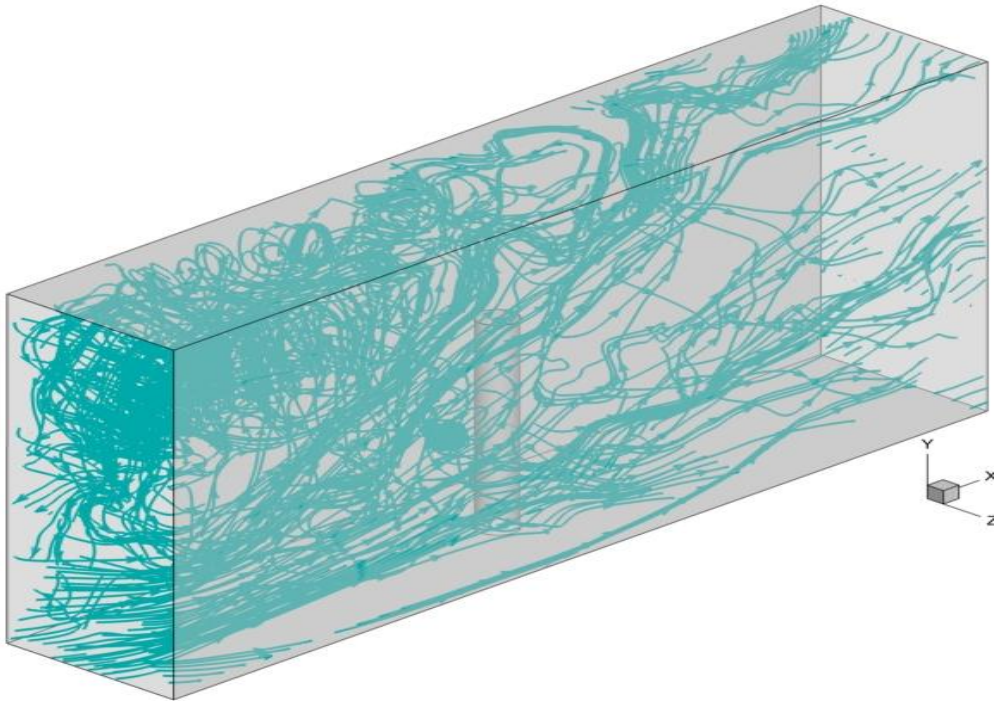

Figure 6.25: Streamtrace plot for the experimental velocity profile simulation case at t = 90.46s.

There is evidence of a completely chaotic flow lines everywhere in the flow field. This behaviour is expected of a turbulent flow in natural environment. With this simulation result, it appears that the turbulence will continue to be sustained in the ambient flow. The flow structure downstream is also modified by the presence of the monopile in addition to the effect of the inlet flow velocity. If this is the case, then it is anticipated that there will be a change in the pressure and velocity distribution downstream of the monopile which will produce a drag force equivalent to the effect of the inlet velocity profile.

The flow structures upstream and downstream of the monopile are visibly more chaotic than those observed with the uniform flow and the $1/7^{th}$ power

law simulation cases. The behaviour of the velocity vector field at t =90.46s can be appreciated by observing Figure 6.26. Of particular interest in this plot, is presence of sustained rotation of fluid parcels. The location, size and eddies orientation changes from time to time. This replicates the phenomenon of vortex dynamics in a turbulent flow.

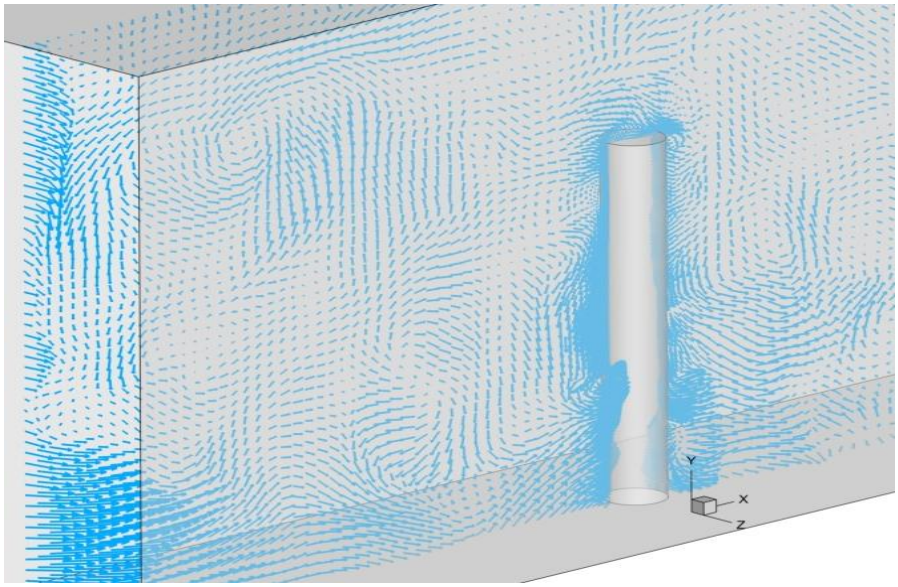

Figure 6.26: velocity magnitude vector plot for experimental velocity profile simulation case at t = 90.46s.

A close examination of the vortices or eddies at t = 18.46s in Figure 6.24 and those in Figure 6.26 at t = 90.46s show that eddies occupy different regions of the flow domain at different times. Their random behaviour makes it difficult to follow the path they trace so that it is more easily studied and investigated by flow visualisation techniques developed in CFD and in physical experiment.

The vorticity field plot in Figure 6.27 below associated with the vector plot Figure 6.26 above show that regions of highest vorticity is closest to the monopile wall however, vortex structures are distributed over the entire flow field. Regions of lower vorticity are sandwiched between regions of higher vorticity. The regions of low vorticity could be explained to

correspond to regions of turbulent mixing due to intense strain by definition of the mechanism of turbulence.

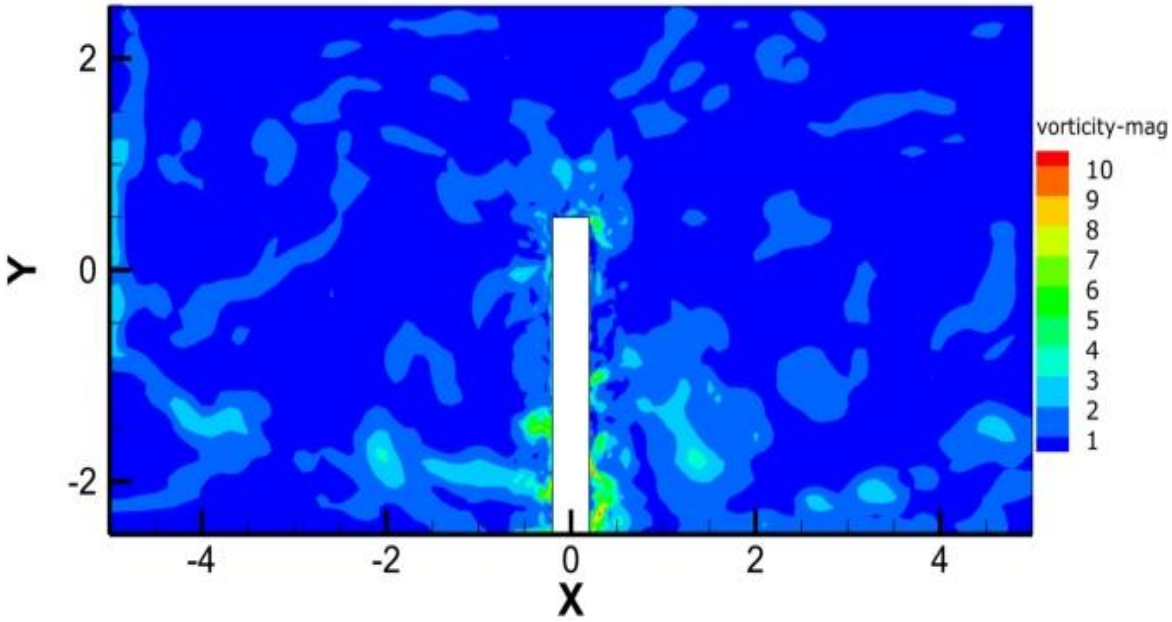

Figure 6.27: vorticity contour plot for experimental velocity profile simulation case at t = 90.46s.

It is also observed that the vorticity magnitude is not constant but fluctuates with time. The fluctuation of the vorticity field can be comprehended by observing the maximum vorticity values at different instantaneous times shown in Table 6.3 below.

Table 6.3: Fluctuating vorticity magnitude table

Instantaneous time (s)	Maximum Vorticity magnitude in s^{-1}
18.46	18
90.46	10.3
154.5	11.4
239.4	26.6
305.3	17.9

The fluctuation of vorticity magnitude is an integral part of turbulence that is expected and it is of significance in the design of marine structures.

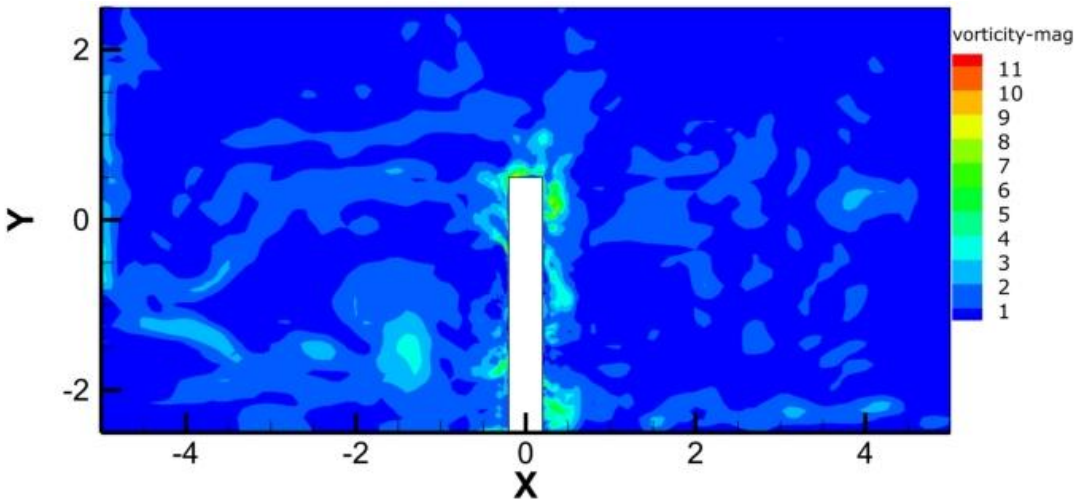

Figure 6.28: vorticity contour plot for experimental velocity profile simulation case at t = 154.5s

Vorticity fluctuation is reflected in the changes in the flow topological features from time to time. A bounded plot is chosen to visualise the vorticity contour plots to make the flow structure outline clearer. A continuous plot would show the links between the structures thereby reducing the contrast.

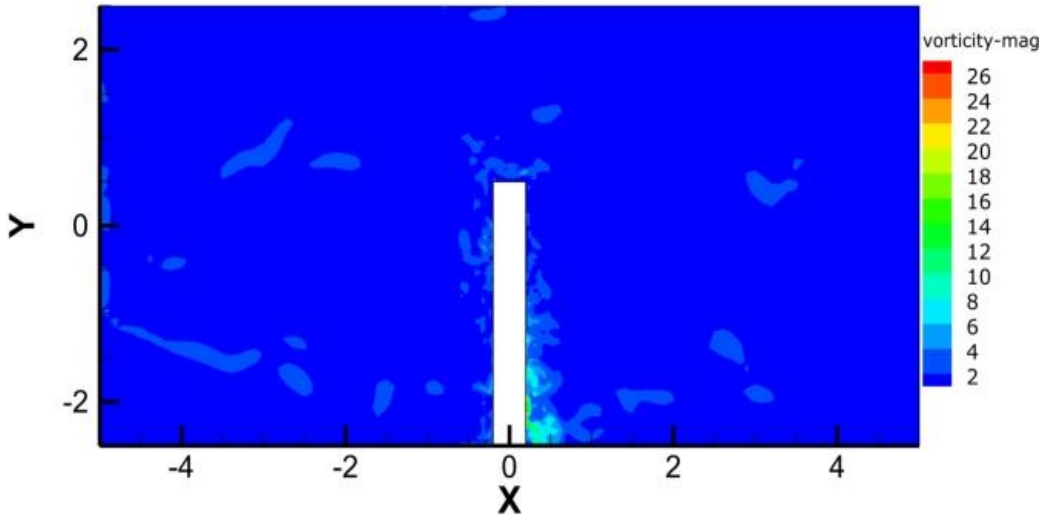

Figure 6.29: vorticity contour plot for ADCP data case at t = 239.4s

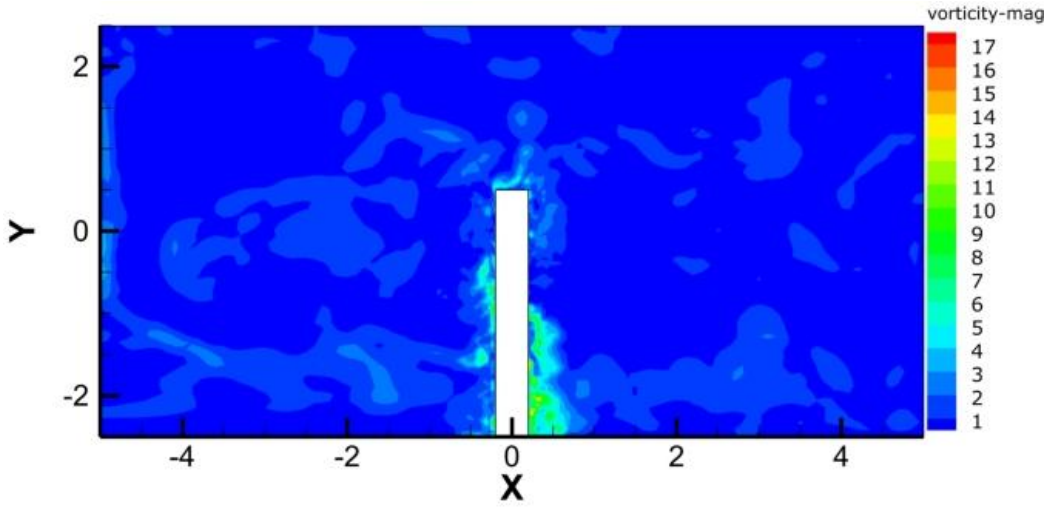

Figure 6.30: vorticity contour plot for experimental velocity profile simulation case at t = 305.3s

It is not surprising that the maximum vorticity value is found closest to monopile wall because turbulence is produced at the immediate vicinity of an impermeable wall. The turbulence generated by the presence wall in terms of vorticity is redistributed, diffused or destroyed. For example in Figure 6.30, the maximum vorticity magnitude value of 17.9s^{-1} near the monopile wall is visibly reduced further downstream as you move away from the monopile wall. The intensity or the strength of the vorticity in the wake of a tidal current turbine is an essential parameter when considering the design of turbine in an array for large scale energy extraction. Past experimental studies on vortex measurement in the wake of a cylinder using hot wire anemometers by Bloor (107) suggest that vorticity produced at separation point can drop to about 70% in about 4D downstream of the cylinder.

A very interesting point to note in this present study is that vorticity magnitude upstream and downstream region of the monopile are comparable as observed from the contour plots. A careful observation of Figures 6.27 - 6.30 gives a visual impression of vorticity strength upstream and downstream of the monopile. The implication of this observation hangs

on the ability of the flow to revert to the ambient conditions in the some distance downstream of the monopile.

6.3.4 Hydrodynamic loading on a monopile support structure

A discussion on the ambient flow structures generated in all three simulation cases in the previous section of this chapter was necessary to understand the behaviour of the ambient flow field in the presence of a monopile. In this section, the effect of the vortex field generated on the monopile drag coefficient is investigated. The results are compared with those simulated with the uniform flow and the $1/7^{th}$ power law velocity profiles and also with experimental studies results presented in Table 6.2. Recall that there were little or no vortex structures visualised in the ambient flow upstream of the monopile with the uniform and the $1/7^{th}$ power law velocity profiles simulation cases but high vorticity was found near the monopile wall.

Forces of certain magnitude are produced when fluid interact with structures obstructing its flow paths. Typically, the forces are in terms of drag force and lift forces. The drag is the component of the hydrodynamic force that coincides with the direction of the flow against the monopile. The drag force is a function of drag coefficient. The lift force acts perpendicular to the drag force. The drag coefficients associated with each force component are used to quantify the forces. The force coefficient of a structure is expressed as a ratio of the force to its surface area, the square of fluid velocity in which it is submerged and the fluid density.

The fluctuations of forces are key considerations in the design of offshore energy structures for survivability and fatigue analysis. Drag coefficient values vary according to the surface area involved. However, in this present study, the surface area of the monopile has been kept constant for each simulation case in order to focus the analysis on the effect of upstream ambient turbulent flow on the monopile drag coefficient.

Theoretical drag coefficient for rounded structures like a cylinder in a steady has been extensively studied in wind tunnel experiment and is generally accepted to be around 1.2 in the subcritical flow regime. The Reynolds number for the present study has a value of 1.5×10^5 which falls within the subcritical flow regime. The Reynolds number was calculated based on the monopile diameter and the mean velocity of the flow of tidal current at the Firth of Forth.

Several other investigations have been carried out in wind tunnel testing of flow around cylindrical surfaces by different authors within the subcritical flow found in (64) and (63), they report values of drag coefficient scattered around 1.2. A review paper on fluctuating load on circular cylinders by Farell (98) reveals that the values of drag coefficient is subject to variation because of differences in experimental condition for example, ambient turbulence, near wall effect, cylinder surface roughness effect, etc.

In practical offshore applications, a drag coefficient between 1.1 – 1.3 is usually applied for most bluff body structures exposed to wind in an open space although higher values can be used for structures whose length to diameter ratio is more than 5 to incorporate a safety factor and lower values of around 0.7 have also been used for cylinders greater than 0.3 m or for short structures according to Minoo (104).

In this present numerical study, drag coefficient history for the uniform flow, the $1/7^{th}$ power law and experimental velocity profile has been monitored and presented in Figures 6.31, 6.32 and 6.33 respectively.

Instantaneous drag coefficient for the uniform flow simulation case fluctuates between a minimum value of 1.1 and a maximum value of 1.8 with an average value of approximately 1.5.

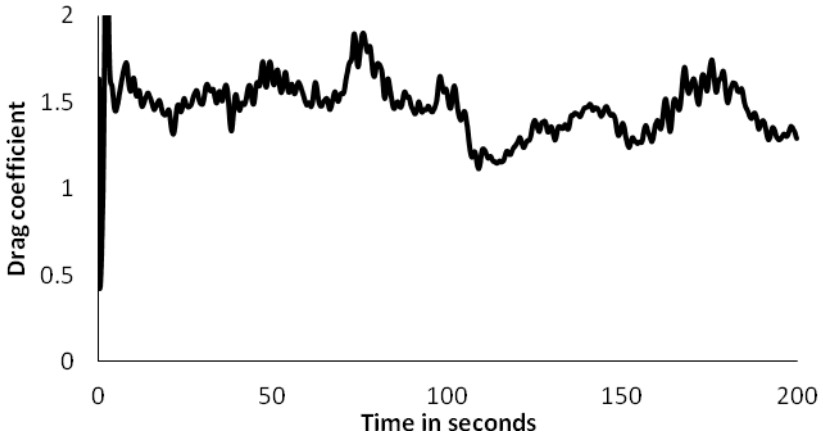

Figure 6.31: drag history for the uniform flow simulation case.

Similarly, drag coefficient values for the 1/7th power law simulating case in Figure 6.32 below, fluctuates between a minimum of 1.0 and a maximum of 1.6 with a mean value of 1.3.

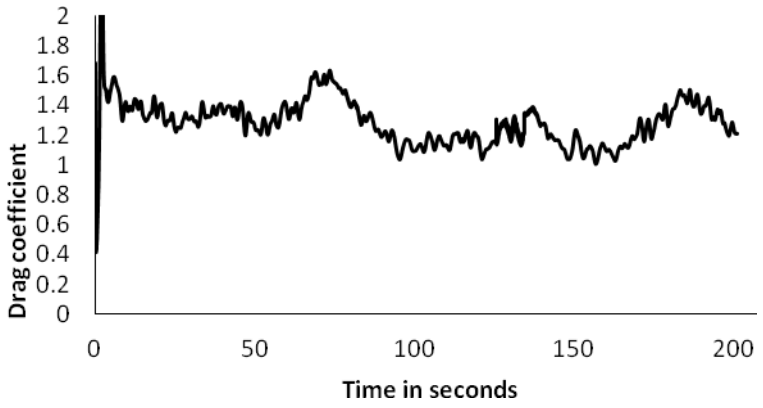

Figure 6.32: drag history for the 1/7th power law simulation case.

The resulting drag coefficient for the uniform flow simulation case is comparable to the 1/7th power law simulation case result. The closeness in the drag coefficient values is attributed to the similarity in behaviour of the upstream incident flow on the monopile structure. Both plots generally have irregular waveforms of time dependent drag coefficient with some fluctuations on the wavy shape.

It has been observed from analysis results based on simulating an empty channel flow in chapter 5 that, flow fields generated by specifying the uniform flow and the $1/7^{th}$ power law as boundary conditions have insignificant ambient turbulent structures compared with those generated by specifying experimental velocity profile. It is therefore not surprising that the values of the drag coefficient were relatively the same. Both flow patterns are predominantly one directional and appear nearly organised upstream on the monopile.

The drag coefficient history based on the experimental velocity profile is presented in the Figure 6.33 below;

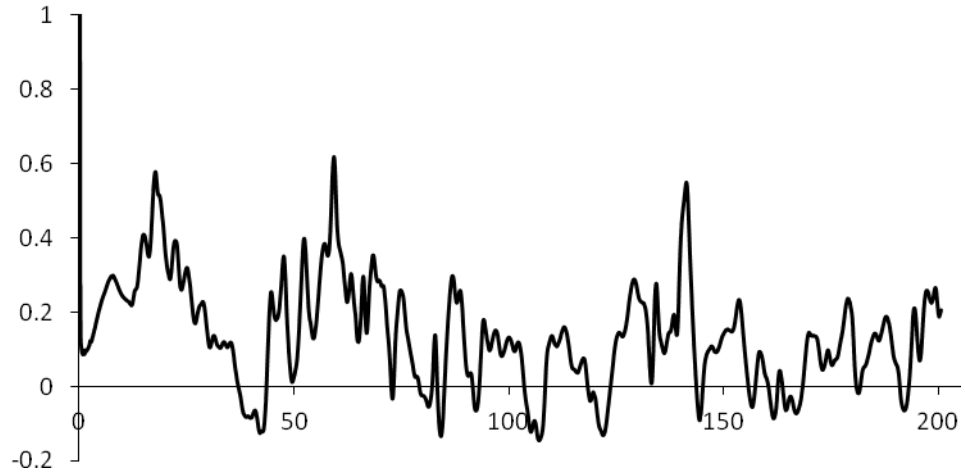

Figure 6.33: drag coefficient history for the experimental velocity data simulation case.

The drag coefficient fluctuations experienced by the monopile are clearly distinct from those experienced when theoretical velocity profiles were specified as inlet velocity profiles. Significantly lower instantaneous values of drag coefficient ranging from less than -0.2 to about 0.6 with a mean of approximate 0.2 was observed. The appearance of the negative signs on the drag coefficient values gives evidence of reverse flow processes due to turbulence. The reason for the lower drag coefficient values can be explained theoretically from the way drag force is usually calculated: The drag force component lies parallel and in the same direction as the

streamwise flow. On the occasion of flow reversal, the force vectors in opposing direction will act to detract from the positive drag force vectors acting in the streamwise direction with a consequence of drag reduction.

For flow systems simulated with theoretical velocity profiles which cannot produce evidence of ambient turbulence upstream of the structures, it be can be argued that force predictions using such profiles will lead to over prediction of hydrodynamic forces. The mean values of the simulated and experimental drag coefficient are presented in Table 6.4 below;

Table 6.4: Comparing simulated drag coefficient with experimental results

	Sub-critical	Critical	Super-critical	Upper Transition	Trans-critical
Schewe	1.2	-	0.22	-	0.52
Uniform flow velocity profile	1.5	-	-	-	-
$1/7^{th}$ power law velocity profile	1.3	-	-	-	-
Experimental ADCP data.	0.2	-	-	-	-

The mean drag coefficients evaluated from the theoretical velocity profiles simulation cases were quantitatively comparable to the experimental measurement results of Schewe (65) for steady flow in the Subcritical flow regime.

The mean drag coefficient evaluated from the experimental velocity profile simulation case was significantly lower when compared with theoretical profile simulation case results. The generally low value of drag coefficient is attributed to the simulated ambient turbulence in the flow field using the experimental velocity profile. The reduction in drag coefficient agrees with Reynolds number-drag coefficient relationship of flow over cylinders. The more turbulent a flow becomes in terms of its Reynolds number, the smaller the drag coefficient.

6.4 Chapter summary and conclusion

The effect of ambient turbulence resembling those in real tidal current channel on a monopile support structure fixed to the channel bed has been investigated. Based on the simulation results, the following conclusions were made;

- Ambient turbulence lead to a reduction of monopile drag coefficient compared to simulation done by specifying theoretical velocity profiles.
- The reduction of drag coefficient can be theoretically explained as due to the reverse flow associated with turbulent flow and the way drag forces are usually calculated. Force vectors opposing the conventional drag force direction (streamwise direction) will act to detract from the positive values of drag coefficient due to reverse signs.
- The use of uniform flow and the classical $1/7^{th}$ power law velocity profile to predict hydrodynamic forces will lead to over estimation for practical engineering applications and subsequently over design of structures.

Chapter 7.0

Overall Summary, Conclusion and Further Work.

7.1 Summary and Conclusion

Climate change and sustainable energy concerns has led to interest in developing tidal current energy technology. Based on this motivation, numerous energy devices has been undergoing laboratory testing, sea trails and numerical simulations but turbulence within tidal currents present a challenge to small scale model testing. It is important to account for turbulence before scale model results can be extrapolated and applied to prototypes. Based on this, dimensional and turbulence scale effect in tidal current energy device testing have been investigated using CFD. The dimensional scale effect is concerned with geometric size of a physical device. Turbulence scale effect involves the dynamic behaviour of the large scale turbulent eddies in tidal currents and its effect on dynamic loading of a device.

Dimensional scale effect

Dimensional scale effects have been investigated on four Froude scale virtual physical models using the RANS methodology. A key conclusion from the investigating dimensional scale effect is that, in numerical testing of tidal current energy devices, the smaller the geometric scale of a device, the better the simulation results agrees with experimental results. The disparity between experimental force coefficient and simulated force coefficients increases as the scale increases. Empirical equations that estimate the drag coefficient scale effects e_{C_D} and the drag force scale effect e_D within the subcritical flow regime have been derived. The

equations are expressed in terms of a dimensionless length scale K_L and velocity scale K_V represented below as;

$$e_{C_D} = 0.1662 In K_L + 0.779 \quad (7.1)$$

$$e_D = 819.2 K_L^2 - 13.68 K_L + 0.058 \quad (7.2)$$

$$e_{C_D} = 0.393 K_V + 0.092 \quad (7.3)$$

$$e_D = 18.55 {K_V}^{2.416} \quad (7.4)$$

$$e_D = 27.20 {K_V}^2 - 7.307 K_V + 0.548 \quad (7.5)$$

The dimensionless length and velocity scale are normalised by a virtual prototype length and velocity scale respectively.

The discrepancies between the numerical and the experimental results suggest that the sensitivity of the k-epsilon turbulence model to boundary layer separation and wake behaviour needs further investigation.

Turbulence scale effect

Turbulence in tidal current occupies a wide range of length and time scales ranging from the largest scale of turbulence to the kolmogorov dissipative scale of turbulence. Turbulence is described as random as well as containing coherent structures. Turbulence scale effect investigation is focused on the large scale structures which occupy the energy containing scale of turbulence kinetic energy spectrum. It is anticipated that the large scale

structures in turbulent flow will have structural implications when they interact with a submerged energy structure.

Preceding the investigation of turbulence scale effect, it was necessary to deploy an ADCP experiment in a real tidal current site to acquire turbulent velocity profiles with the aim to integrate the data in a small scale numerical model. The intuition behind the simulation of large scale turbulent structures site data is based on the fact that a depth-velocity profile sampled within a small time resolution contains turbulence fluctuation due to the effect of wind, waves, sea bottom roughness, biologically, physical and other natural processes occurring within tidal currents and that, the effect of these natural and physical processes are implicitly accounted for in a the numerical simulation results at least qualitatively.

The ADCP instrument was successfully deployed at the Firth of Forth to acquire real current data for 23 days period and was successfully retrieved afterwards. Essential analysis of the ADCP data has been carried out and the resulting velocity profiles have been compared with theoretical velocity profiles.

Significant ambient turbulent structures resembling those in natural environment have been successfully simulated in an empty open channel. The effects of large scale structures on a generic tidal turbine support structure have also been investigated using LES. Results were compared with qualitative description of turbulent flow structures in a natural environment observed by Matthes (81). Simulation results were also benchmarked with those simulated with theoretical velocity profiles due to their popular use in simulating performance and hydrodynamic loading on tidal current energy structures.

Based on the investigations, it has been demonstrated that;

1. The use of ADCP data as input to a CFD numerical model aided the generation of significant ambient turbulent structures comparable to those in real flows.

2. A turbulent velocity sampled with a small time resolution contains turbulent fluctuations due to waves, currents, shape of the coastline, seabed roughness, and other physical and natural processes while these turbulent fluctuations have been averaged out in the uniform and the $1/7^{th}$ power law velocity profiles.

3. Theoretical velocity profiles are specified as flow in one direction and as such, not suitable to investigate the effect of turbulent structures during device modelling. Turbulence is three dimensional but could be satisfactorily approximated as two dimensional.

4. Results from investigating seabed drag coefficient shows that, ambient turbulent structures results to significant reduction in seabed drag coefficient when simulation results were compared with those based on theoretical velocity profiles as boundary conditions. The simulated seabed drag coefficient using the experimental velocity profile is comparable to measured seabed drag coefficient at various tidal current locations. This implies that the use of theoretical profiles to estimate amount of energy available for extraction in a tidal current will lead to an under estimation of available resources because some of the energy available in tidal currents is required to overcome seabed friction.

5. Results from investigating the hydrodynamic force on a monopile support structures also show that ambient turbulent structures causes a significant reduction in the monopile drag coefficient. Consequently, it can be stated that the quantification of hydrodynamic forces based on theoretical velocity profile would result to overestimation of forces acting on structures in real flow conditions.

6. Ambient turbulent structures cause fluctuations in critical parameter which has implications for the strength of materials in design of structures for engineering practical applications.

7.2 Application and recommendation for further work.

The amount of energy extracted for electricity production is a key interest in tidal current energy tidal technology. The energy extracted is a function of the cube of the velocity. The rotational effect of a turbine also implies that local turbulence will be generated. Results of testing a turbine are usually outputs as power and torque. These two parameters vary as a function of fluid velocity. It is therefore anticipated that a fluctuating velocity profile will have a significant effect on energy extraction and device performance.

As part of further work, it is recommended that the methodology be applied to investigate the effect of ambient turbulent structures on hydrodynamic loading and device performance of a turbine undergoing sea trials.

Due the significant vortices generated with the site data, this study further demonstrate the possibility of representing large scale prototype in a small scale numerical simulation domain.

The methodology is also suitable for investigating effect of turbulent flow on any structure submerged in the sea and is therefore applicable to oil and gas subsea applications.

References

(1) United Nations Framework Convention on Climate Change. *Kyoto Protocol Reference Manual on Accounting of Emmision and Assigned Amount.* UNFCCC; November 2008.

(2) DTI. *Renewable Energy.* London: Department of Trade and Industry; 2007.

(3) Metoc. *The World Offshore Renewable Energy Report. 2004-2008.* Department of Trade and Industry's Renewables 2010 Target Team; 2010.

(4) Energy Technology Support Unit. *Tidal Streams Energy Review:* ETSU; 1993.

(5) European Commision. *The Exploitation of Tidal and Marine Currents: Technical Report EUR 166683.* Directorate General for Science, Research and Development.; 1996.

(6) Black and Veatch. *Tidal Stream Energy Resource and Technology Summary Report.* United Kingdom.: Carbon Trust; 2004.

(7) Department of Trade and Industry. *The World Offshore Renewable Energy Report - 2004-2008.* Department of Trade and Industry's Renewables Target Team; 2010.

(8) Carbon Trust. *The Renewables Obligation.* [homepage on the Internet]. Copyright 2011 Carbon Trust; Available from: http://www.carbontrust.co.uk/policy-legislation/energy-supply/renewable-energy/pages/renewables-obligation.aspx.

(9) Department of Trade and Industry.
Meeting the Energy Challenge - A White Paper on Energy. May 2007; .

(10) Wright J, Colling A, Park D, Open University S330/Course readers. *Waves, tides and shallow-water processes.* 2nd ed. Oxford: Butterworth-Heinemann in association with the Open University; 1999.

(11) Charlier RH. Renewable and Sustainable Energy Reviews. 2003; 7(6):515-529.

(12) Tidal Energy UK. *The Seagen Turbine.* [homepage on the Internet]. UK: 2011 cited 2011 August]. Available from: http://www.tidalenergy.eu/sea_gen_turbine.html.

(13) Volker Q. *Understanding Renewable Energy Systems.* First Edition ed. Bath, UK: Bath Press; 2005.

(14) U.S Department of Energy. *Energy Efficiency and Renewable Energy.* [homepage on the Internet]. U.S.A.: 2011 [updated 17/06/2010; cited 2011 17/06/2011]. Available from: http://www1.eere.energy.gov/windandhydro/hydrokinetic/default.aspx.

(15) Fraenkel PL. Development and Testing of Marine Current Turbine's SeaGen 1.2MW Tidal Stream Turbine. Development and Testing of Marine Current Turbine's SeaGen 1.2MW Tidal Stream Turbine. *International Conference of Ocean Energy; 6th - 8th October;* Bilbao, Spain.; 2010.

(16) BWEA. *The TidEl Turbine.* [homepage on the Internet]. 2010 cited 2011 August]. Available from: http://www.bwea.com/marine/devices.html.

(17) GCK Technology. *Gorlov Helical Turbine.* [homepage on the Internet]. 2011 cited 2011 Available from: http://www.gcktechnology.com/GCK/pg2.html.

(18) BWEA. *The Reciprocating Hydrofoil.* [homepage on the Internet]. 2010 cited 2011 Available from: http://www.bwea.com/marine/devices.html.

(19) Rourke FO, Boyle F, Reynolds A. Tidal Energy Update. *Applied Energy.* 2010; 87:398-409.

(20) Lunar Energy. *Rotech Tidal Turbine.* [homepage on the Internet]. 2011 cited 2011 Available from: http://www.lunarenergy.co.uk/technology.htm.

(21) Owen A, Bryden IG. Prototype Support Structure for Seabed Mounted Tidal Current Turbines. *Proceedings of the Institution of the Mechanical Engineers, Part M: Journal of Engineering for the Maritime Environment.* 2005; 219:173-183.

(22) Bryden IG, Couch SJ. MEI - Marine Energy Extraction: Tidal Resource Analysis. *Renewable Energy.* 2006; 31:133-139.

(23) Germain G. Marine Current Energy Converter Tank Testing Practices. Marine Current Energy Converter Tank Testing Practices. *2nd International Conference on Ocean Energy; 15-17 October;* France: ICOE; 2008.

(24) Myers L and Bahaj B. Scale Reproduction of the Flow Field for Tidal Energy Converters. Scale Reproduction of the Flow Field for Tidal Energy Converters. *Proceedings World Renewable Energy Congress (WREC X); 19-25 July;* Glasgow, UK; 2008.

(25) Smyth WD, Moum JN. *3D Turbulence.* [homepage on the Internet]. Academic Press; 2001 cited 2009 02/11]. Available from: http://mixing.coas.oregonstate.edu/papers/turbulence_physics.pdf.

(26) SuperGen Marine. *A Monograph on SuperGen Marine Energy Research.* [monograph on the Internet]. UK: The University of Edinburgh; 2007 .

(27) Doherty T, Mason-Jones A, Doherty DM, Byrne CB, Owen I and Wang YX. Experimental and Computational Analysis of a Model Horizontal Axis Tidal Turbine. *Proceedings of the 8th European Wave and Tidal Energy Conference; 7th -10th September;* Uppsala Sweden.: EWTEC; 2009. p. 833-841.

(28) Maganga F, Germain G, King J, Pinon G and Rivoalen E. Experimental Studies to determine Flow Charateristic Effects on Marine Current Turbine Behaviour. Experimental Studies to determine Flow Charateristic Effects on Marine Current Turbine Behaviour. *Proceedings of the 8th European Wave and Tidal Energy Conference.; 7-10 September;* Uppsala Sweden: EWTEC; 2009. p. 661-667.

(29) Bahaj AS, Batten WMJ, McCann G. Exprimental Verification of Numerical Predictions for the Hydrodynamic Performance of Horizontal Axis Marine Current Turbines. *Renewable Energy.* 2007; 32:2479-2490.

(30) Myers L, Bahaj AS. Experimental Analysis of the flow field around Horizontal Axis Tidal Turbines by use of Scale Mesh Disk Rotor Simulators. *Ocean Engineering.* 2010; 37:218 - 227.

(31) Myers L, Bahaj AS. Wake Studies of a 1/30th Scale Horizontal Axis Marine Current Turbine. *Ocean Engineering.* 2006; 34:758-762.

(32) Versteeg HK, Malalasekera W. *An introduction to computational fluid dynamics : the finite volume method.* 2nd ed. Harlow: Pearson/Prentice Hall; 2007.

(33) Gant S and Stallard T. Modelling a Tidal Turbine in Unsteady Flow. *International Offshore and Polar Engineering Conference (ISOPE); 6th to 11th July;* Vancouver; 2008. p. 473-479.

(34) Luolin B, Spence RRG and Dudziak G. Investigating the Influence of Array Arrangement and Spacing on Tidal Energy Converter (TEC) Performance using a 3-Dimensional CFD Model. *Proceedings of the 8th European Wave and Tidal Energy Conference; 7-10 September;* Sweden; 2009. p. 654-660.

(35) De Chant LJ. The Venerable 1/7th Power Law Turbulent Velocity Profile: A Classical Nonlinear Boundary Value Problem and Its Relationship to Stochastic Processes. *Applied Mathematics and Computation.* 2005; 161:463-474.

(36) McCann G, Thomson M and Hitchcock S. Implications of Site-Specific Conditions on the Prediction of Loading and Power Performance of a Tidal Stream Device.*; 15th - 17th, October; ;* 2008.

(37) Williams AJ, Croft TN, Masters I, Willis MR and Cross M. Combined BEM-CFD Modelling of Tidal Stream Turbines Using Site Data. *International Conference on Renewable Energies and Power Quality; 23rd -25th March;* Granada, Spain: ICREPQ; 2010.

(38) Novak P. Scaling Factors and Scale Effects in Modelling Hydraulic Strutures. In: Kobus H, editor. *Symposium on Scale Effects in Modelling Hydraulic Structures.* Second ed. Stuttgart, Germany.: Sprint Druck; 1989. 0 p. 0.3-1-0.3-2, 0.3-3, 0.3-4, 0.3-5.

(39) Harrison R, Hau E, Snel H. *Large wind turbines : design and economics.* Chichester: Wiley; 2000.

(40) Morfiadakis EE, Glinou GL, Koulouvari MJ.
The Suitability of the Von Karman Spectrum for the Structure of Turbulence in a Complex Terrain Wind Farm. *Journal of Wind Engineering and Industrial Aerodynamics.* 1996; 62:237-257.

(41) Burton T. *Wind energy handbook.* Chichester: Wiley; 2001.

(42) Bearman PW, Morel T. Effect of free stream turbulence on the flow around bluff bodies. *Progress in Aerospace Science.* 1983; 20:97-123.

(43) Couch SJ, Jeffery HF and Bryden IG. Tidal Current Energy: Development of a Device Performance Protocol. Tidal Current Energy: *International Conference on Clean Electrical Power (ICCEP); 21-23 May;* : IEEE; 2007. p. 720 - 722.

(44) Bates PD, Lane SN, Ferguson RI. *Computational fluid dynamics : applications in environmental hydraulics.* Chichester: John Wiley & Sons; 2005.

(45) Sangsan Lee. Unsteady Aerodynamic Force Prediction on a Square Cylinder using k - epsilon Turbulence Models. *Journal of Wind Engineering and Industrial Aerodynamics.* 1997; 67-68:79-80-90.

(46) Rodi W. Comparison of LES and RANS calculations of the flow around bluff bodies. *Journal of Wind Engineering and Industrial Aerodynamics.* 1997; 69-71:55-56-75.

(47) Nezu I, International Association for Hydraulic Research. *Turbulence in open-channel flows.* Rotterdam: Balkema; 1993.

(48) Hinze JO. *Turbulence : An Introduction to its Mechanism and Theory.* New York: McGraw-Hill; 1959.

(49) Biswas G, Eswaran V. *Turbulent flows : fundamentals, experiments and modeling.* Pangbourne: Alpha Science; 2002.

(50) Rodi W. *Turbulence models and their application in hydraulics : a state-of-the-art review.* 3rd ed. Rotterdam: Balkema; 1993.

(51) Launder BE, Spalding DB. *Lectures in mathematical models of turbulence.* London: Academic Press; 1972.

(52) Wilcox DC. *Turbulence modeling for CFD.* Third ed. La Canada, California: DCW Industries; 2006.

(53) Shih TH, Liou WW, Shabbir A, Yang Z, Zhu J. A new K-Epsilon Eddy Viscosity Model for high Reynolds Number Flows: Model Development and Validation. *Computer an d Fluids.* 1994; 24(3):227-238.

(54) Ansys Inc. Turbulence. *Ansys Fluent Theory guide.* Release 13 ed. U.S.A; November, 2010. Chapter 4 p. 41-131.

(55) Hughes SA. *Physical models and laboratory techniques in coastal engineering.* Singapore; River Edge, NJ: World Scientific; 1993.

(56) Smagorinsky J. General Circulation Experiments with the Primiive Equations. I. The Basic Experiment. *American Meteorological Society- Monthly Weather Review.* 1963; 91(3):99-164.

(57) Davidson PA. *Turbulence an introduction for scientists and engineers.* Oxford [England: Oxford University Press; 2007.

(58) Germano M, Piomelli U, Moin P, Cabot WH. A Dynamic Subgrid-Scale Eddy Viscosity Model. *Physics of Fluids A.* 1991; 3(7):1760-1765.

(59) Lily DK. A Proposed Modification of the Germano Subgrid-Scale Closure Model. *Physics of Fluids A.* 1991; 4(3):633-635.

(60) Kobus H. *Symposium on Scale Effects in Modelling Hydraulic Structures.* Second ed. Stuttgart, Germany: Sprint Druck; 1984.

(61) Young Min Park and Byeong-Hee Chang. Numerical Simulation of Wind Turbine Scale Effects By Using CFD. *45th AIAA Aerospace Sciences Meeting and Exhibit; 8-11, January;* Reno, Nevada.: American Institute of Aeronautics and Astronautics; 2007.

(62) Starke B. The prediction of scale effects on ship wave systems using a steady iterative RANS method. *7th Numerical Towing Tank Symposium, Hamburg Germany.* 2004; .

(63) Sumer BM. *Hydrodynamics around cylindrical strucures.* Revised ed. Singapore ; London: World Scientific Publishing; 2006.

(64) Zdravkovich MM. *Flow around circular cylinders : a comprehensive guide through flow phenomena, experiments, applications, mathematical models and computer simulations. Vol.1.* Oxford: Oxford University Press; 1997.

(65) Gunter S. On the force fluctuations acting on a circular cylinder in a crossflow from subcritical up to transcritical Reynolds numbers. *Journal of Fluid Mechanics.* 1983; 133:265-285.

(66) Tu J, Yeoh GH, Liu C. *Computational fluid dynamics : a practical approach.* Burlington, MA ; Oxford: Butterworth-Heinemann; 2008.

(67) Kim SE, Choudhury D. A Near-Wall Treatment Using Wall Functions Sensitized to Pressure Gradient. *ASME FED.* 1995; 217:273-279.

(68) Tutar M, Holdo AE. Computational modelling of flow around a circular cylinder in the sub-critical flow regime with various turbulence models. *International Journal for Numerical Methods in Fluids.* 2001; 35:763-784.

(69) Helmut Z. B, John S, Jurgen S. *Marine Turbulence Theory, Observations and Models.* First ed. United Kingdom: Cambridge University Press; 2005.

(70) Mark TS, Stephen GM Jon RB. Observation of Turbulence in a Partially Stratified Estuary. *Journal of Physical Oceanography.* [serial on the Internet] 1999 29(8):Available from: http://ams.allenpress.com/perlserv/?request=get-abstract&doi=10.1175%2F1520-0485(1999)029%3C1950%3AOOTIAP%3E2.0.CO%3B2&ct=1.

(71) Mark TS, Stephen GM, Jon RB. Measurements of Reynolds stress profiles in unstratified tidal flow. 1999; 104(C5):10933-10949.

(72) Osalusi E, Side J, Robert H. Structure of Turbulent Flow in EMEC's Tidal Energy Site. *International Communication of Heat and Mass transfer.* 2009; 36(5):422-423-431.

(73) Elizabeth AN, Chris RR, M.ASCE, Kevin AO. Evaluation of Mean Velocity and Turbulence Measurements with ADCPs. *Journal of Hydraulic Engineering.* 2007; 133(12):1310-1318.

(74) Rippeth TP, Eirwen W, Simpson JH. Reynolds Stress and Turbulent Energy Production in a Tidal Current. *Journal of Physical Oceanography.* 2001; 32:1242-1243-1251.

(75) Youyu LuRolf G. Lueck. Using a Broadband ADCP in a Tidal channel Part 1: Mean Flow and Shear. *Journal of Atmospheric and Oceanic Technology.* [serial on the Internet] 1998 16.

(76) Youyu Lu, Rolf G. Lueck, Daiyan Huang. Turbulence Characteristics in a Tidal Channel. *Journal of Physical Oceanography.* 2000; 30(5):855-856-867.

(77) Youyu L, Rolf GL. Using a Broadband ADCP in a Tidal Channel. Part II: Turbulence. *Journal of Atmospheric and Oceanic Technology.* 1999; 16(11):1568-1569-1579.

(78) Fan X, Wei H, Yuan Y, Zhao L. Vertical Structure of Tidal Currents in a Typical Coastal Raft-Culture Area. *Continental Shelf Research.* 2009; 29:2345-2357.

(79) Schlichting H, Gersten K. *Boundary-layer theory.* 8th rev and enl ed. Berlin: Springer; 2000.

(80) Okorie OP and Owen A. Turbulence: Charateristics and Its Implication in Tidal Current Energy Device Testing. *OCEAN'S 08 MTS/IEEE; 15th -18th September;* Quebec, Canada.; 2008.

(81) Matthes GH. Macroturbulence in Natural Stream Flow. *Trans,. Amer. Geophy. Union.* 1947; 28:255-265.

(82) Richardson LF. *Weather Prediction by Numerical Process.* Cambridge: University Press; 1922.

(83) Kolmogorov AN. The Local Structure of Turbulence in Incompressible Viscous Fluid for very Large Reynolds Numbers. *Royal Society (London), Proceedings, Series A - Mathemetical and Physical Sciences.* 1991 (first Published in 1941).; 434(1890):9-13.

(84) Deardoff JW. A Numerical Study of Three Dimensional Turbulent Channel Fow at Large Reynolds Number. *Journal of Fluid Mechanics.* 1970; 41(2):453-480.

(85) Moin P, Kim K. Numerical Investigation of Turbulent Channel Flow. *Journal of Fluid Mechanics.* 1982; 118:341-377.

(86) Nakagawa H, Nezu I. Prediction of the contributions to the Reynolds stress from bursting events in open channel flows. *Journal of Fluid Mechanics.* 1977; 80(Part 1):99-128.

(87) Lesieur M. *Large-eddy simulations of turbulence.* Cambridge: Cambridge University Press; 2005.

(88) Helgeland A, Reif AP, Andreassen O, Wasberg CE. Visualisation of Vorticity and Vortices in Wall Bounded Turbulent Flows. *IEEE Transactions on Visualisation and Computer Graphics.* 2007; 13(5):1055-1066.

(89) Smirnov S, Shi S, Celik I. Random Flow Generation Technique for Large Eddy Simulations and Particle - Dynamics Modelling. *Journal of Fluid Mechanics.* 2001; 123:359-371.

(90) Isern-Fontanet J, Garcia-Ladona E, Font J. Identification of Marine Eddies from Altimetric Maps. *Journal of Atmospheric and Oceanic Technology.* 2003; 20:772-778.

(91) Salter SH. Correcting Under-estimation of the Tidal Stream Resource of the Pentland Firth. *Proceedings of the 8th European Wave and Tidal Energy Conference; 7th -10th September;* Uppsala Sweden: EWTEC; 2009.

(92) Green MO, McCave IN. Seabed Drag Coefficient under Tidal Currents in the Eastern Irish Sea. *Journal of Geophysical research.* 2001; 100:16057-16069.

(93) Bricker JD, Inagaki S, Monismith SG. Bed Drag Coefficient Variability under Wind Waves in a Tidal Estuary. *Journal of Hydraulic Engineering.* 2005; 131(6):497-508.

(94) Campbell AR, Simpson JH, Allen GL. The Dynamic Balance of Flow in the Menai Strait. *Estuarine Coastal and Shelf Science.* 1998; 46:449-455.

(95) White FM. *Fluid mechanics.* 5th ed. Boston, MA: McGraw-Hill; 2003.

(96) Reynolds AJ. *Turbulent flows in engineering.* London: Wiley-Interscience; 1974.

(97) Owen A and Bryden IG. Energy Extraction Implications of Structurally Significant Velocity Variation in Tidal Currents. *OCEANS 2007 - Europe; 18-21 June;* : IEEE; 2007.

(98) Farell C. Flow Around Fixed Circular Cylinders: Fluctuating Loads. *ASCE Journal of Engineering Mechanics.* 1981; 107:565-588.

(99) Roshko A. Experiments on the flow past a circular cylinder at very high Reynolds number. *Journal of Fluid Mechanics.* 1961; 10(3):345-356.

(100) Wang M, Catalano P and Iaccarino G. *Prediction of High Reynolds Number Flow Over a Circular Cylinder using LES with Wall Modeling.* Italy: Centre for Turbulence Reserach; 2001.

(101) Gao F, McGovern D, Mingham CG, Ilic S and Causon DM. Numerical and Experimental Investigation of Turbulent Flow around a Vertical Circular Cylinder. *Proceedings of the International Offshore and Polar Engineering Conference (20th); June 20-25;* Beijing China: ISOPE; 2010. p. 639-643.

(102) Sarpkaya T, Isaacson M. *Mechanics of Wave Forces on Offshore Structures.* Copyright ed. U.S.A.: Van Nostrand Reinhold Ltd.; 1981.

(103) Sabag SR, Edge BL, Soedigdo I. Wake II Model for Hydrodynamic Forces on Marine Pipelines including Waves and Currents. *Ocean Engineering.* 2000; 27:1295 - 1319.

(104) Minoo HP. *Dynamics of Offshore Strutures.* First ed. Great Britain: Butterworths; 1989.

(105) Douglas JF. *Fluid mechanics.* 5th ed. Harlow, England ; New York: Pearson/Prentice Hall; 2005.

(106) DET NORSKE VERITAS. *Recommended Practice DNV-RP-C205.* DNV; 2007.

(107) Bloor MS, Gerrard JH. Measurement of Turbulent Vortices in a Cylinder Wake. *Proceedings of Royal Society of London. Series A. Mathematics and Physical Sciences (1934 - 1990).* 1966; 294:319 - 342.

Appendix A

Turbulence: Characteristics and its Implications in Tidal Current Energy Device Testing.

P.O.Okorie
B.Eng (Hons), M.Eng, Ph.D Student,
School of Engineering, Robert Gordon University, Aberdeen, AB 10 1FR, Scotland, United Kingdom
Alan Owen
B.Eng (Hons), PhD, C.Eng, MEI, Chartered Energy Engineer
Robert Gordon University, Aberdeen, AB 10 1FR, Scotland, United Kingdom.

Abstract
The need for a tidal energy conversion system is enumerated in addition to the possible challenges in its installation and operations, stemming from the interactions of the energy device with its surrounding. The highly idealised case of isotropic, homogenous and stationary turbulence is discussed and its deviation from real flows, as observed in a tidal estuary is presented. Also, the principle of dimensional analysis and the concept of similarity are introduced, as tools to access the effect of scaling in a tidal current energy device testing. A better understanding of the structure of turbulence in any tidal site allows for the right choice of dimensionless numbers that are relevant to the system. Turbulence characteristic differ from site to site and, introducing an energy device into the environment modifies the velocity and pressure distribution of the site. The dimensionless numbers essential for the tidal current energy conversion process are clearly defined.

I. INTRODUCTION

Global drive for renewable energy research and development arose from the need to: reduce green house effect, combat the inevitable declining, in traditional energy provision by fossils and to reduce the level of environmental pollution due to energy production and consumption. Recently, the high cost of crude oil, which has been predicted to have come to stay, has led to a more radical interest in the research and development of alternative sources of energy.

This group of energy sources is not based on the burning of fossil fuels or the splitting of atoms as in nuclear energy. Among this class of energy are; wind power, solar, hydrogen, electric, geothermal, biomass and marine energy. Marine energy can be further categorized into hydroelectric, wave energy, and tidal energy. Tidal energy is a form of hydropower which converts the energy in the tide into electricity. Tidal energy systems can be further classified into two groups. Tidal barrages which make use of the potential energy in the difference in height between the high and low tides and tidal current systems which make use of the kinetic energy in the ebb and flood flow to drive the turbines.

Tidal current energy conversion system has been noted as one of the viable technology for its inherent predictability, reliability and minimal or no negative environmental impact. In addition, the natural resource is cheap and continuous. Unlike wind and solar energy, it is not weather dependent. The World Offshore Renewable Energy Report 2002 - 2007, released by the Department of Trade and Industry, suggests that 3000GW of tidal energy is estimated to be available. The Scottish enterprise has estimated that, about 34% of UK electricity demand can be produced from tidal currents; this signifies a huge untapped resource. Alternative energy sources hold the key towards the future, without them, energy crises is inevitable.

A typical tidal current energy system is a simple system comprising of a tidal turbine supported on a structure positioned to extract the kinetic energy of the ebb and flood flow of the tides. An electrical grid connected system, allows for the supply of electricity to consumers. The aspect of interest is the tidal turbine and its support structure, fully submerged in high density flow sea water.

A typical site for a tidal current energy device is a challenging environment; exhibiting large scales of turbulent motion. A better understanding of the nature of turbulence in tidal channels is therefore, a key goal in the successful installation and operation of tidal energy devices. Understanding the structure turbulence; will make it possible to be able to predict its appearance and possibly manage or control it. Large scale motion has been observed from previous work carried out on real flows and theses may take the form of volumes of random motion or more organised vortices and shear flows. Rapid velocity changes within large scale turbulence coupled with the relatively high density of sea water implies that significant fluctuation loading may be applied to a submerged tidal current energy device by such flow behaviour.

978-1-4244-2620-1/08/$25.00 ©2008 IEEE

II. DESCRIPTION OF TURBULENCE

Turbulence in simple terms is the random velocity fluctuations of fluid flow superimposed on the mean fluid flow. A time history plot of turbulent velocities will clearly show these random velocity fluctuations about a mean flow velocity value. Two main processes in turbulence are momentum transport and scalar mixing. In general, turbulence is characterised by a large range of scales of length and time and a number of length scales of varied physical significance have been identified.

The idea of energy cascade was introduced by Richardson in 1922 as in [1], where he visualised that kinetic energy enters turbulence at the largest scales of motion in form of eddies. Due to the instability of this large scale eddies, they break up and their energy is transferred to smaller eddies. The break up process continues creating even smaller eddies and their energy is transferred to yet smaller eddies. This process continues until such that, the Reynolds number reaches a range that makes the eddy motion to become stable and the kinetic energy is dissipated through viscous effect.

The largest scales of motion are estimated to be as large as the flow width and are strongly influenced by the flow geometry and boundary conditions. The interactions between the different range of scales of motion makes the analytical solution of a three dimensional turbulent flow very difficult. Turbulence is therefore, more easily understood in statistical terms. In the mathematical analysis of turbulent flows, the assumptions of isotropy (statistical properties are independent of direction), homogeneity (statistical properties are independent of position), and stationary (the statistical properties are independent of time), are made in order to simplify the problem. Results are often presented in the form of the energy spectrum, which is the Fourier transformation of the autocorrelation. The energy spectrum show clearly the breakdown of the measured function, into waves of different frequency or wavelengths and in addition, gives us an understanding of how turbulence receives energy at large scales and dissipates it at small scales.

In the 1940's, Kolmogorov, added to and quantifies the energy cascade picture where, he hypothesized that at sufficiently high Reynolds number, the small scale turbulence are statistically isotropic. He quantitatively defined that, at small scales turbulence, the inertial and dissipation ranges depends on the energy dissipation rate (ε), viscosity (ν) and the wavenumber (k) . That is $E = f(k, \varepsilon, \nu)$, where E is the energy spectrum. He further hypothesized that in the inertial subrange, where the spectrum is independent of viscosity, $E = f(k, \varepsilon)$ from [2]. The implications of theses hypotheses are that: inertia effect are significant in the inertial subrange, the viscous effect dominate the dissipation range and are responsible for all the energy dissipation and that, the statistics of the small scales of motion are universal within the inertial subrange and the dissipation range. The two ranges combined to form the universal equilibrium range where, the rate of energy transfer is also the rate of energy dissipated. See fig.1. Thus, the picture of turbulence as painted by Kolmogorov is that, turbulent energy is created in the energy containing eddies and transferred through a process of energy cascade. Recent finding have made it evident that the process of energy cascade is not entirely one way. Energy is also transferred from the small scales to large scales however; this is regarded as a secondary process, as in [3].

Turbulence in the ocean and tidal estuaries occurs on a scale much larger than the energy containing scales of turbulence. While Kolmogorov's theory of turbulence has offered invaluable conceptual frame work, recent research work since around the 1960's has been to examine the shortcomings of Kolmogorov hypothesis and consequently improve on them.

Fluid motion like those occurring in ocean and tidal channels deviates from the above mentioned assumptions of stationary, isotropy and homogenous turbulence. Interactions of turbulence, stratification and shear has been the focus of numerous laboratory, numerical, and observational studies by Rohr et al. (1988), Holt et al. (1992), and Gregg (1987) respectively from [4].

Shear modifies the homogeneity and isotropy by deforming the turbulent eddies. These turbulent eddies exchange energy with the background shear through the mechanism of Reynolds stresses. The Reynolds stresses represent the transport of momentum by turbulence. They arise from the non-linear advection term when the Navier-Stokes equations are Reynolds decomposed and Reynolds averaged. The shear denoted by $S = dU/dz$, is the vertical gradient of the ambient horizontal current. Its effect on turbulence causes it to be anisotropic. The spectrum must therefore be anisotropic in some wavenumber range. Motions on scales larger than the Corrsin scale $L_c = \sqrt{\varepsilon/S^3}$ are deformed by shear.

Stratification is another important phenomenon that could possibly affects the evolution of turbulence with the mean flow in a tidal channel. Stratification occurs when water of high and low salinity as well as water of high and low temperature forms layers that inhibit water mixing. A column of water can either be stably or unstably stratified. Unstable stratification occurs when a fluid layer of a higher density overlies that of a lower one and could often leads to a vigorous turbulence as convective turbulence

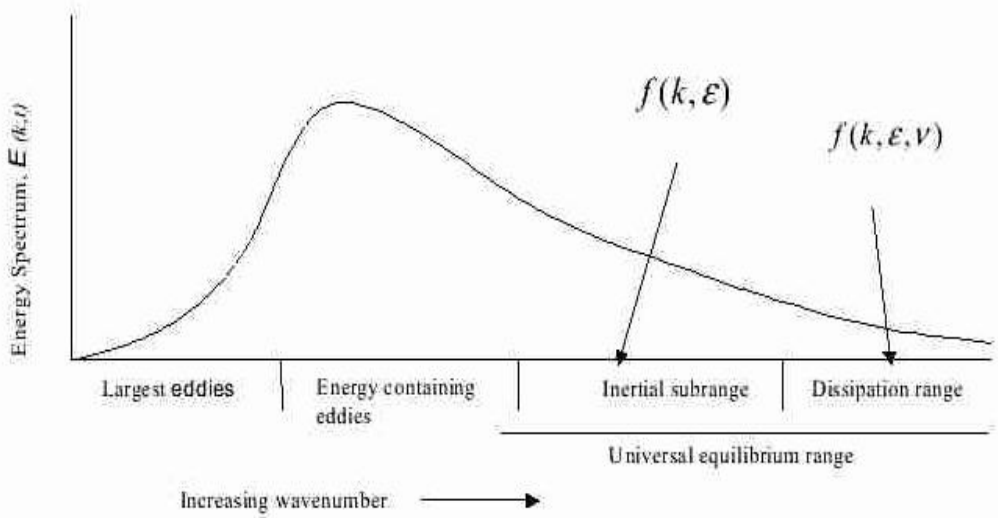

Fig. 1: A typical Energy spectrum showing the essential features.

restores the fluid to a stable state. Stable stratification is when water of a lower density overlies that of a higher one. As in [2], a stable stratification can further be classified into strongly, moderately or weakly stable stratification. In a stable stratification, the fluid particle displaced from equilibrium, oscillate with a frequency $N = \sqrt{(-g\rho^{-1}\, d\rho/dz)}$, where, N is the Brunt-Vaisala or the buoyancy frequency, $\rho(z)$ is the ambient mass density and g is the acceleration due to gravity.

Another important phenomenon worthy of note in a stable stratification is the presence of internal gravity wave. They occur at interfaces between high and low density fluid, it is distinct from the water surface waves that occur between the water surface and the air above it. Internal gravity waves propagate along the boundaries and are commonly found in the continental shelf regions of the world, where brackish water overlie salt water and at the outlet of large rivers. In a strongly stable stratification, fluid motion may be visualised as two- dimensional turbulence and this is referred to as the vortical mode.

Buoyancy modifies the structure of turbulence in a moderately stable stratification and hence gives rise to a three dimensional turbulence. Buoyancy forces acts on the largest scales of the vertical motion and tends to suppress the large scale turbulent eddies. While viscous forces acts on the smallest scales of motion and determines the size of the smallest eddies. Therefore, an important scale in the presence of buoyancy is the Ozmidov scale, $L_0 = \sqrt{\varepsilon/N^3}$. L_0 is the largest overturning scale in a stratified flow. Buoyancy dominated flow, is within scales larger than L_0 and therefore, cannot overturn. Buoyancy can either force or damp turbulence therefore, it plays a significant role in turbulence intensity. In analysing any turbulent flow it is important to know if shear effect or buoyancy effect is more important. It is also worthy of mention that, there are other intermediate scales of motion which are not discussed or mentioned in this write up for example, the Ellison scale. Turbulent Reynolds and Froude numbers can be derived from a combination of these length scales and can be used to diagnose the state of the turbulence as in [4].

III. OBSERVATION OF TURBULENCE IN A TIDAL SITE

The characteristic of a typical tidal site is of extreme intense turbulence forced by the interactions between tidal currents and three- dimensional topography. Turbulent length scales in the bottom boundary layer are limited below by the solid boundary and above by stratification. The interaction of Reynolds stresses with shear and stratification is normally characterised by the gradient Richardson number $R_g = N^2/S^2$. When gradient Richardson number is above 2.5, turbulent mixing is retarded by stratification. Below 2.5, the shear effect is actively responsible for the generation of turbulence as in [4].

In recent years, the use of Acoustic Doppler Current Profilers (ADCP) to measure tidal current has become the current practice. The main turbulence parameters measured are the Reynolds stresses, Turbulent Kinetic Energy, Eddy viscosity and the Kinetic Energy Dissipation rate. Stacey et al. (1998) as in [4], carried out turbulent studies in a partially stratified estuary, see Fig 2. It

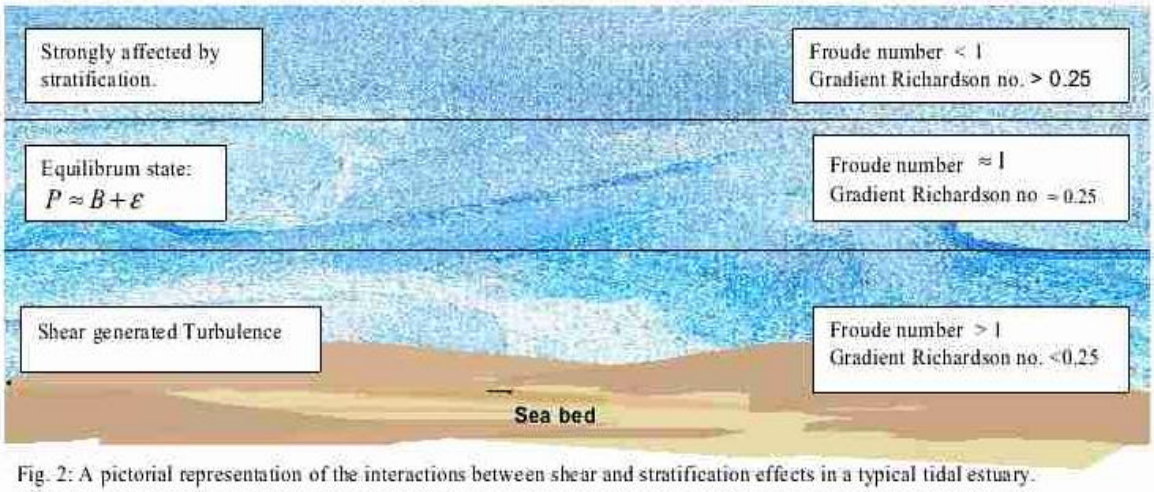

Fig. 2: A pictorial representation of the interactions between shear and stratification effects in a typical tidal estuary.

was evident from their work that near the bed, high energetic turbulence is actively produced by shear and therefore not largely affected by stratification effects. In the balance region of the fluid layer, the turbulent Froude number is ≈ 1. The turbulent energy produced in this region, is transported to the stratified region above, through turbulence self transport. As stratification effect increases away from the bed, it reaches a region where the shear effect balances the stratification effect. In this region called the transition region, local turbulence production, P and destruction ($B + \varepsilon$), where B is the buoyancy term, is in balance.

Approximation of homogenous indicates that the turbulence will decay but, it does not because, turbulence kinetic energy is supplied to the highly stratified region thereby, turbulence is maintained. The value of the turbulent Froude number, is an indication of the nature of turbulence. For Froude number > 1, turbulence is stronger than stratification. For Froude number < 1, stratification has stronger effect on turbulence.

IV. EFFECTS OF TURBULENCE LOADING ON A TIDAL DEVICE.

A tidal device is subject to a resultant force due to the interaction between the fluid and the device. This force can be described in terms of walls shear stresses due to the viscous effects of the fluid and acts tangential to the wall of the device and pressure forces which acts in the normal direction. These normal and tangential forces are distributed over the body of the device and they vary in both magnitude and direction as in [5].

A typical flow over a marine device is turbulent (a multi scale, random 3- dimensional motion) with significantly high Reynolds number, with generation and shedding of large coherent vortex structures. These motions have a profound impact on the fluid loading on the device. Flow separations, viscous effect of water, leading to boundary layers and vortex shedding frequency due to stratification are important phenomenon that affect loading on tidal devices.

For any flow past a solid body, the relative velocity between the flow field and the body is governed by the no-slip boundary condition as in [6]. i.e the relative velocity of the thin layer of fluid adjacent to the body is zero. However, the velocity increases rapidly, from zero to the free stream velocity, a certain distance away from object's body with a velocity gradient proportional to the shear stress or friction developed due to fluid flow over the body. The sheared layer of fluid is referred to as the boundary layer.

A. Boundary Layer Flow Separation

With increase in Reynolds number, boundary layer thickness gets thinner at the leading edge of the object and also, a turbulent wake is generated that extends far downstream. When the device is not sufficiently streamlined, for example a cylinder, it could lead to flow separation.

Boundary layer separation occurs when the no-slip condition is satisfied and vorticity is generated. As fluid flow past a submerged body, an accelerated flow with pressure drop occurs at the leading edge. This pressure drop is transformed into kinetic

energy. As the flow progresses, towards the rear of the object, and as long as the boundary layer remains thin, the kinetic energy is transformed into pressure leading to a pressure increase. Because of the presence of strong frictional forces in the boundary layer, it becomes difficult for the fluid to climb the pressure mountain. It stops momentarily, and is pushed backward into motion due to the adverse pressure gradient that the flow imposes on the boundary layer. This process forms vortices that soon separates from the body and moves on downstream as in [6]. Thus, a strong negative pressure is developed in the region filled with vortices and this is the origin of the large form drag of the body. Thus the flow in the wake consists of highly turbulent large scale eddies.

Boundary layer separation may occur either due to sharp edges or from a continuous surface or where the velocity at the edge of a bluff body boundary layer is higher than the free stream velocity. Also, roughness of the body of marine structures, caused by the growth of marine organisms on the body, may give rise to boundary layer flow separation.

B. Vortex Shedding

Within a range of Reynolds number, a periodic flow develops downstream of any fixed marine structure, due to regular patterns of vortices shed from the body (karman vortex trail) and this creates an oscillating flow at a discrete frequency. When the frequency of vortex shedding matches the resonance frequency of the body, the structure will begin to resonate and this can have an undesirable effect on the structure. A high rate of vortex shedding leads to a high drag.

C. Dimensional Analysis

Scale modelling is a critical step in the design process of a tidal current energy device. The techniques of dimensional analysis employed should be both reliable and affordable. In model testing, the drag resulting from the effect of the pressure and velocity distributions on the body is often modelled. Relevant dimensional numbers includes:

1) Reynolds number, $\mathrm{Re} = Ud/\nu$, where ν is the kinematic viscosity, U is the approach stream velocity and d is a representative length. The Reynolds number is a dimensionless ratio of the inertia force to the viscous force. It plays an important role in the hydrodynamic stability and turbulence.

2) Froude number, $Fr = U/Nd$, where N is the Brunt-Vaisala or the buoyancy frequency, U the approach stream velocity and d is a representative length, is the non-dimensional parameter that characterized the extent of stratification.

3) Strouhal number, $St = fd/U$ is the dimensionless number of consequence due to vortex shedding. where f is the vortex shedding frequency, d is a representative length and U is the approach stream velocity. Further work on this project will seek to determine the interplay between these three dimensionless numbers and evaluate their effects on model testing, while ensuring geometric, dynamic and kinematic similarity as much as possible.

CONCLUSIONS

The nature of turbulence will have a profound impact on the design, installation and operation of a tidal current energy device. A clear understanding of the problem is a gate way to an adequate and successful model testing. It is evident from the discussions above that; turbulence in a tidal site can be affected by stratification above, by shear below and the topography of the coastline. Therefore, the flow nature can be described as a stratified sheared flow. Furthermore, the introduction of a tidal energy device in such a flow field modifies the pressure and velocity gradient. Thus, an addition concept of boundary layer comes into effect.

A typical tidal energy device comprise of a turbine (whose blades is designed to minimise drag) and a support structure (whose shape may classify it as a bluff body). In general, when a fixed body (bluff or streamline), is immersed in a fluid and is in relative motion with respect to it, the fluid will exert a resultant force on the body. The drag is the component of the resultant force acting on the body, in the direction of the relative motion while the lift is the force component perpendicular to the drag force. For an aerofoil section, the lift to drag ratio, could be as high as 40 whereas for a bluff body, the mean lift force is zero and the drag is high as in [7].

ACKNOWLEDGMENT

The writers acknowledge the financial assistance of the Sustainable Power Generation and Supply Initiative (SUPERGEN), sponsored by the Engineering and Physical Sciences Research Council (EPSRC), United Kingdom.

REFERENCES.

[1] Stephen B. Pope, Turbulent Flows (2000), pp. 182- 263.
[2] W.D. Smyth and J.N.Moum, "3D Turbulence" Copyright 2001, Academic Press
[3] G.Biswas and V. Eswaran, "Turbulent flows, Fundamental, Experimental and Modelling".Alpha Science International. pp. 52-53.
[4] Mark T. Stacey et al. Journal of Physical Oceanography. Volume 29 pp. 1950-1970
[5] Bruce R. Munson, Donald F. Young, Theodore H. Okiishi, "Fundamental of Fluid Mechanics. Copyright 2002, John Wiley and Sons International. pp 535-544.
[6] H.Schlichting, K.Gersten, "Boundary Layer Theory". 8th Revised and Enlarged Edition (1999).pp.39-43.
[7] Minno H. Patel. 1989. Dynamics of Offshore Structures. Butterworth and Co. Publishers, pp 174-214.

Appendix B

3rd International Conference on Ocean Energy, 6 October, 2010 Bilbao

Implications of Froude Scaling in the Numerical Testing of a Generic Support Structure.

P. Okorie[1], A. Owen[2] and M. Hossain[3]

[1]School of Engineering
Robert Gordon University,
Aberdeen, AB10 1FR, United Kingdom
E-mail: o.p.okorie@rgu.ac.uk

[2] School of Engineering
Robert Gordon University,
Aberdeen, AB10 1FR, United Kingdom
E-mail: a.owen@rgu.ac.uk

[3] School of Engineering
Robert Gordon University,
Aberdeen, AB10 1FR, United Kingdom
E-mail: m.hossain@rgu.ac.uk

Abstract

The study aims to investigate the scale effects arising from the use of a two equation turbulence model to simulate Froude scaled models.

In physical modeling of hydraulic structures, scale effects arise from the use of the Froude scaling criterion to establish similarity between the scale model and its prototype. In numerical modeling, scale effects may arise due to the assumptions made while formulating the model. It is imperative to estimate the scale effects associated with numerical testing of Froude scaled models using the k-epsilon ($k-\varepsilon$) realisable turbulence because of its frequent use in engineering applications in this era of 'hybrid' modeling.

Force coefficients and non-dimensional vortex shedding frequency have been calculated on four Froude scaled models. From comparison with physical experimental results, it is seen that the forces acting on the device can be simulated with reasonable accuracy depending on the choice of length and velocity scale associated with the model. Equations that estimate the errors resulting from the use of the turbulence model are presented.

Keywords: Froude scaled models, numerical turbulence modelling, scale errors.

1. Introduction

Tidal Current Energy (TCE) technology is developing with some evidences of sea trials [1-2] but large scale commercial schemes are not yet in operation. Accurate scaling of devices is required to move forward.

Three complementary methods are known for dealing with a complex flow regime such as flow around any device submerged in a stream of tidal currents. They include small scale laboratory testing and observation, field testing and observations and numerical modeling.

Although field measurements provide the best data, the costs and natural turbulence conditions makes data interpretation more difficult. On the other hand, small scale laboratory testing and numerical modeling are relatively cheap because the input conditions are more easily controlled and can be varied systematically to study their effects. Physical modeling in turn, is more expensive than numerical modeling. According to [3] the investment cost of Computational Fluid Dynamics (CFD) is high although the total expense is not normally as great as the cost of high quality experimental facility. Furthermore, the cost associated with new designs and parametric studies are avoided in numerical modeling.

The advantages of numerical modeling have not prevented the use of physical models indeed, progress has been made with them because the results from a physical model can be used as input conditions to a numerical model and vice–versa. Also, physical models provide calibration and verification data for numerical data.

The exact Navier-Stokes (N-S) equations govern the turbulent flow around a device in a stream of current. Small scale details of turbulence are not required for engineering applications [4] therefore, the time averaged N-S equations were rather exploited. This process of averaging the N-S equations resulted to the

appearance of Reynolds stresses that requires turbulence modelling.

There is a natural progression in the complexity of turbulence models in this order: the algebraic turbulent viscosity (zero equation), the one equation and two equation turbulence models. These models are based on the Boussinesq hypothesis which suggests that the Reynolds stresses can be replaced by a product of the turbulent viscosity and the mean velocity gradient. A comprehensive account of turbulence and its modeling can be found in [4-6].

It is known that in predicting the behaviour of any engineering prototype using physical modelling techniques, similarity between model and prototype is established when certain scale laws and conditions are met. These scale laws are derived by non-dimensionalising the continuity and the averaged N-S equations. The procedure for non- dimensionalising the N-S equations with associated assumption is explained in [7]. Results from non- dimensionalising the equations suggest that complete similarity is established when the Froude, Reynolds, Euler and the Struohal numbers have the same value in both model and prototype.

In practical terms it is difficult to maintain similarity of the Reynolds number in free surface flow. Therefore, it is a well established practice in TCE research that the Froude number is the most important parameter. Scaling based on this assumption introduces the Reynolds scale effect although, viscosity becomes important near the wall of any device. Understanding scale effect (scaling errors) and quantifying them where possible are very important in developing new TCE devices. Norvak [8] states that "…*If we cannot quantify the error, at least we must be aware in which direction it acts and be able to answer the question - does it contribute to safety or does it diminish the safety factor? Only then can we modify the saying "models are to be used but not believed into models are to be used, sometimes believed but always understood*". According to Kamphius in [7], scale effects in physical models are analogous to decreased accuracy in numerical models when complex physical processes are represented by a simplified mathematical formulation.

This study investigates the scale errors resulting from solving a flow around a generic cylindrical support structure submerged in a stream of current using realisable $k-\varepsilon$ turbulence model.

Flow around cylindrical structures has been extensively studied mainly in wind tunnel experiments with low stream turbulence level for force measurements with results published in literatures. In particular, the study carried out by Schewe [9] is used in the present study to compare with the numerical simulation results. This present study exploits the fact that the force coefficients which are well known should be the same for all flow in the sub-critical flow regime independent of the Reynolds numbers. Deviations from the physical experimental results are treated as scaling errors and are quantified. In what follows, the turbulence model equation and the procedures used in investigating the scale errors are described followed by the discussion of results and concluding remarks.

2. Governing equations for $k-\varepsilon$ turbulence model

The Reynolds stresses which appears as a result of the averaging procedures of the N-S equation is related to the mean velocity gradient according to the Boussinesq hypothesis as:

$$-\rho\overline{u_i' u_j'} = \mu_t\left(\frac{\partial u_i}{\partial x_j}+\frac{\partial u_j}{\partial x_i}\right)-\frac{2}{3}\left(\rho k+\mu_t\frac{\partial u_k}{\partial x_k}\right)\delta_{ij} \quad (1)$$

ρ is the fluid density , $u_i' u_j'$ are the Reynolds stresses.

$\frac{\partial u_i}{\partial x_j}+\frac{\partial u_j}{\partial x_i}$ is the mean velocity gradient.

δ_{ij} is the kronecker delta defined as:

$\delta_{ij}=1$ if $i=j$ and $\delta_{ij}=0$ if $i\neq j$

i and j takes the value 1, 2 or 3.

The turbulent viscosity μ_t is calculated from

$$\mu_t = \rho C_\mu \frac{k^2}{\varepsilon}. \quad (2)$$

k is the turbulent kinetic energy while ε is the turbulent dissipation rate. C_μ is a variable and methods for computing it can be found in [10].

The transport equation for the realizable $k-\varepsilon$ turbulence model which solves for the Reynolds stresses are given by turbulent kinetic energy, k and the turbulent dissipation, ε as:

$$\frac{\partial}{\partial t}(\rho k)+\frac{\partial}{\partial x_j}(\rho k u_j)=\frac{\partial}{\partial x_j}\left[\left(\mu+\frac{\mu_t}{\sigma_k}\right)\frac{\partial k}{\partial x_j}\right] + G_k + G_b - \rho\varepsilon + S_k \quad (3)$$

and

$$\frac{\partial}{\partial t}(\rho \varepsilon)+\frac{\partial}{\partial x_j}(\rho \varepsilon u_j)=\frac{\partial}{\partial x_j}\left[\left(\mu+\frac{\mu_t}{\sigma_\varepsilon}\right)\frac{\partial \varepsilon}{\partial x_j}\right]+ \rho C_1 S\varepsilon - \rho C_2\frac{\varepsilon^2}{k+\sqrt{\nu\varepsilon}}+C_{1\varepsilon}\frac{\varepsilon}{k}C_{3\varepsilon}G_b + S_\varepsilon \quad (4)$$

respectively.

$$C_1 = max\left[0.43,\frac{\eta}{\eta+5}\right], \quad \eta = S\frac{k}{\varepsilon}, \quad S=\sqrt{2S_{ij}S_{ij}}$$

G_k is turbulence kinetic energy generation term, G_b is the generation of turbulence due to buoyancy S_k and S_ε are source terms. S is a scalar measure of deformation and S_{ij} is the mean strain rate tensor. The model constants: $C_{1\varepsilon}$, C_2, σ_k and σ_ε are 1.44, 1.9,

1.0 and 1.2 respectively. The constant have been established to perform well for certain canonical flows according to [10]. The present flow simulation is assumed to be incompressible with negligible buoyancy effects.

The model transport equation for k and ε are derived from the exact equation and the dynamic equation of the mean square vorticity respectively.

More information on the realizable $k-\varepsilon$ turbulence model can be found in [10] and [11].

3. Solution domain and numerical approach

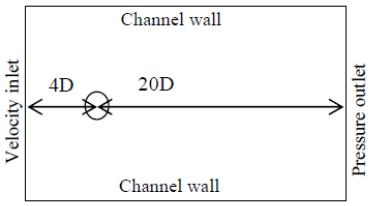

Figure 1: Computational domain

The simulation was carried out on four Froude scaled models with different dimensions. The velocity scale and length scale of the four scale models was calculated using the Froude transfer relation given in equation 5.

$$\frac{V_P}{V_m} = \sqrt{\frac{L_P}{L_m}} \qquad (5)$$

The Froude transfer relation states that the velocity ratio of prototype to model equals the square root of their length scale ratio. The length and velocity scale of each scale model is based on a virtual prototype with a free stream velocity of 1m/s and device diameter of 5m.

Using equation 5, the scale models free stream velocity domain dimensions and associated Froude and Reynolds number are calculated and shown in **Table 1.**

The flow is assumed to be two dimensional across the horizontal plane of a channel with flowing current. The pressure outlet is located 20 cylinder diameters downstream of the centre of the device and the velocity inlet is located 4 cylinder diameters upstream of the centre of the device. The channel walls are located 8 cylinder diameters from the middle of the channel.

The velocity scale was further varied for the 1:50 scale model in order to investigate the effect of change in velocity scale on the drag force and its coefficient within the sub-critical flow regime.

The cylinder walls were meshed with the same size function specifications to ensure similarity of the boundary layer behaviour. Thus the number of nodes on each cylinder increases as the diameter of the device.

The solution method employed is the second order implicit transient formulation for better accuracy with the pressure-velocity coupling scheme.

4. Boundary conditions and near wall treatments.

No slip boundary conditions are applied at the device as well as channel walls. i.e the velocity is zero.

$$u_x = u_y = 0$$

At the inlet, a turbulent intensity of 0.01 % (a value lower than the acceptable value in wind tunnel testing) as recommended in [12] is specified for all four scale models.

The turbulent Kinetic energy and dissipation rate at the boundaries are calculated using;

$$k_{inlet} = \frac{3}{2}(u_{inlet} I)^2 \qquad (6)$$

and

$$\varepsilon_{inlet} = C_{\mu}^{\frac{3}{4}} \frac{k^{\frac{3}{2}}}{\ell} \qquad (7)$$

respectively.

ℓ is the specified characteristic length scale of turbulence.

A two layer non-equilibrium wall function is used in conjunction with the turbulence model. This wall function approach is recommended for flow with pressure gradients involving flow separation and it is able to calculate the cell averaged turbulence kinetic energy production and dissipation in wall neighbouring cells in the flow. Thus it is suitable for flows that depart from the local equilibrium theory of turbulence.

5. Results and Discussion

The results of the present study are based on a numerical simulation of forces acting on a fixed cylinder submerged in a current flow. Extensive physical experimental research has been carried out on flow around cylindrical structures with data published in literatures. The different length scale and velocity scales used in the simulation as well as the associated Froude and Reynolds number are presented in **Table 1.**

Length scale ratio	**1:1**	**1:30**	**1:50**	**1:70**	**1:90**
Velocity scale (m/s)	1	0.18	0.14	0.12	0.11
Device diameter (m)	5	0.17	0.10	0.07	0.056
Froude number	0.14	0.14	0.14	0.14	0.14
Reynolds Number	5E06	3E04	1.4E4	8.4E3	6E3

Table 1: Froude scaled models dimensions

The four Froude scaled models falls within the sub critical flow regime which has a Reynolds number range of $300 < Re < 3 \times 10^5$ according to (13). Flow in this regime is characterized by a completely turbulent wake and a laminar boundary layer separation. Several studies carried out in this flow regime include the work of Schewe (9) who performed an experiment in a

pressurized wind tunnel that could reach up to a maximum velocity of 38m/s and on a cylinder of diameter 0.06m. The minimum Reynolds number obtained for Schewe's experiment was 10^4. The calculated mean drag coefficient, $\mathbf{C_d}$ has an approximate value of 1.2; the root mean square of the lift coefficient, $\mathbf{C_l}$ has a maximum value of 0.38 in the sub-critical regime. The Strouhal number, $\mathbf{S_t}$ was around 0.2 with very minimal scatter.

According to (14) two parameters: the Strouhal number and the drag coefficient are of practical importance. The results of the force coefficients and the Strouhal number, S_t computed from the realizable $k-\varepsilon$ turbulence, for the different Froude scaled models is compared with the results of Schewe's and shown in **Table 2**.

Parameters	Schewe's results	Length scale ratio			
		1:30	1:50	1:70	1:90
C_d	1.2	0.99	1.06	1.12	1.18
r.m.s C_l	0.38	0.25	0.37	0.47	0.48
S_t	0.2	0.25	0.25	0.23	0.20

Table 2: Results comparison

The mean drag and the r.m.s lift coefficient are calculated from the steady state values of the drag and lift convergence monitors. The results show that the smaller the scale model, the closer the $\mathbf{C_d}$ compares with experimental results. The Strouhal number show some variation from the experimental values except for the 1:90 scale which is in better agreement with experimental value. The analytical drag force, F_d is calculated using;

$$F_d = \tfrac{1}{2} C_d \rho D U^2 \qquad (8)$$

D is the diameter of the device, U is the inlet velocity specified at the boundary and ρ is the density of water.

The difference between the simulated drag force and the analytical drag force calculations are shown in **Table 3**. The deviation of the simulated mean drag coefficient from the experimental value of Schewe's is also shown in **Table 3.** The differences are treated as the scale errors resulting from the use of the k-epsilon realizable turbulence model.

Errors	Scale ratios			
	1:30	1:50	1:70	1:90
e_{cd}	0.21	0.14	0.08	0.02
e_{fd}	0.54	0.14	0.02	0.01

Table 3: Scale error estimates: effect of length scale

Where e_{cd} and e_{fd} are the errors estimates for the coefficient of drag coefficient and the drag force respectively.

A plot of the drag coefficient errors, e_{cd} versus a normalized length scale K_D is shown in Fig. 2.

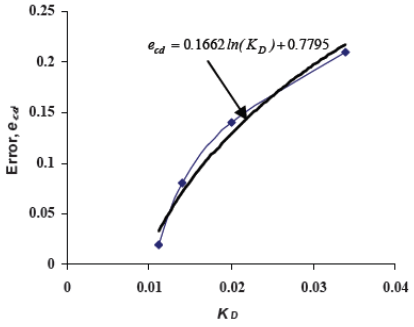

Figure 2: Error, e_{cd} versus normalized length scale

$$K_D = \frac{D_m}{D_p} \qquad (9)$$

D_m is the diameter of the model and D_p is the diameter of the prototype.

It is seen that e_{cd} varies according to a logarithmic relation described by the equation;

$$e_{cd} = 0.1662\ln(K_D) + 0.7795 \qquad (10)$$

determined from curve fitting the graph.

Similarly, a plot of the drag force error, e_{fd} is shown in Fig. 3.

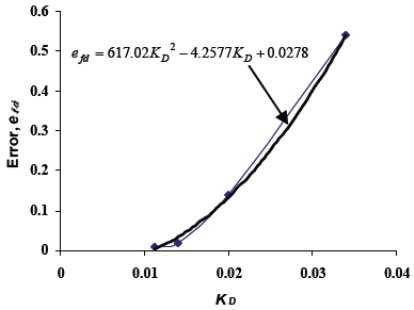

Figure 3: Error, e_{fd} versus normalized length scale.

The drag force error can be approximated by a polynomial function described by the equation;

$$e_{fd} = 617.02K_D^{\,2} - 4.2577K_D + 0.0278 \qquad (11)$$

It is seen that the drag force error increase as the scale of the device increases. The smaller the size of the model, the better it approximates the experimental values of Schewe's results. The simulated drag force is calculated per unit length in Newton (N).

To further investigate the effect of change in the velocity scale for a particular scale model, the 1:50 scale model was used as a case study. The inlet velocity was varied from 0.05m/s to 0.7m/s.

The complete result would need fifteen columns therefore, some have been omitted for space reasons.

The domain size of the 1:50 scale model is 2.4m x1.6m, with a device diameter of 0.10m.

The e_{cd} and e_{fd} have also been calculated and shown in **Table 4**.

	0.10m/s	**0.3m/s**	**0.4m/s**	**0.5m/s**	**0.6m/s**
e_{cd}	0.13	0.21	0.25	0.29	0.33
e_{fd}	0.0989	0.79	2.182	3.5	5.46

Table 4: Scale error estimates: effect of velocity scale

It is seen that a change in the velocity scale affect the accuracy of the mean drag coefficient. The deviations from the experimental value of drag coefficient increases as the velocity is increased. Fig. 4 is a plot of the drag coefficient error versus a normalized velocity scale.

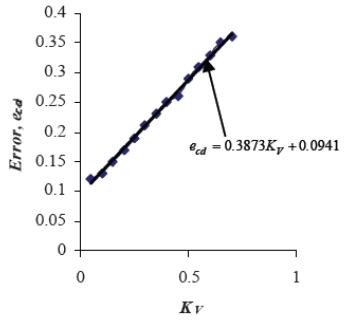

Figure 4: Error, e_{cd} versus normalized velocity plot

The relation between the error and the velocity scale can be described by a linear function represented by;

$$e_{cd} = 0.3873K_V + 0.0941 \qquad (12)$$

$K_V = \frac{V_m}{V_p}$ is a dimensionless velocity scale where V_m is the velocity of the model and V_p is the velocity of the prototype.

The drag force deviation also increases as the velocity scale increases. Fig. 5 is a plot of the drag force error versus a normalized velocity scale.

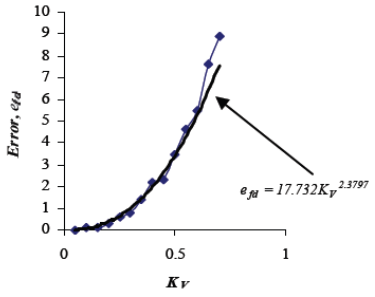

Figure 5: Variation of drag force with deviations

The drag force error can be approximated by a power function represented by;

$$e_{fd} = 17.732\mathrm{K_V}^{2.3797} \qquad (13)$$

The error (deviation) associated with the drag force increases significantly with scale. This suggests that, the higher the specified inlet velocity, for a numerical simulation the greater the deviation from the analytical drag force calculation for flows within the sub-critical flow regime.

Mean pressure coefficient

The pressure coefficient, C_p is Reynolds number dependent and it is related to the drag force.

C_p can be evaluated using the formula;

$$c_p = \frac{p - p_0}{0.5\rho U_i^2} \qquad (14)$$

p is the mean pressure, p_0 is the ambient pressure, U_i is the incident flow velocity on the cylinder.

It is known in the sub-critical flow regime that, the flow separates at an angle of about 78^0. This angle increases to 140^0 when the flow develops to the supercritical regime. The mean pressure coefficient for the various velocities on the 1:50 scale model is plotted in Fig 6.

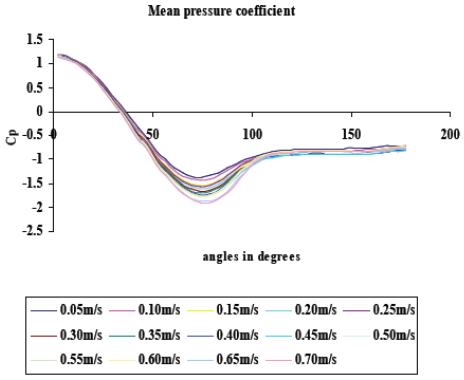

Figure 6: Graph of mean pressure coefficient

From the graph although the separation angles for all numerical simulation is consistent at 74.24^0, they however, have different base pressure coefficients values that decreases from a value of -1.37 to a value of -1.9 with velocity increase.

Flow separation is due to adverse pressure gradient created due to the geometry of the cylinder resulting to a stream of vortices behind the cylinder. The pressure remains fairly constant at the lee end of the side as in Fig.6. The shed vortices can be visualized in the contour plot in Figures 5a-d.

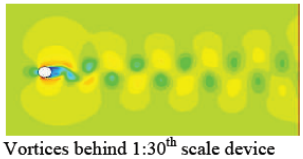

Figure 5a: Vortices behind 1:30th scale device

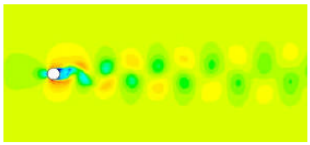

Figure 5b: Vortices behind 1:50th scale device

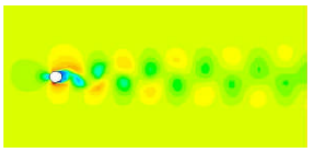

Figure 5c: Vortices behind 1:70th scale device

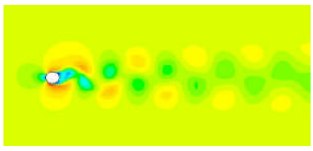

Figure 5d: Vortices behind 1:70th scale device.

It is seen that the turbulence model is able to capture the vortex shedding phenomenon reasonably.

6. Conclusion

The flow around a cylindrical device is a classical problem of fluid mechanics that has potential application to tidal current energy technology.

It is evident from the simulation results that the drag force and its coefficient are not in quantitative agreement with the experimental values/analytical values although, the deviations decreases as the scale decreases.

The drag coefficient is constant in the sub-critical flow regime from physical experimental result but numerical results shows a variation. The computed drag force deviates significantly from the analytical drag force result as the velocity scale is increased for the 1:50 scale model. This behaviour shows that the choice of a velocity scale is an important consideration in numerical modeling for engineering applications.

Equations for quantifying these variations have been determined.

Further work will extend to the investigation of a 1:1 scale Froude model and intermediate scales with more complex boundary conditions. It is likely that the effect of the drag crises with increased Reynolds number would need more complex error estimation techniques should numerical analysis be required.

Acknowledgements

Thanks to EPSRC who is the sponsor of this project through SuperGen.

References

[1] Marine Current Turbine Ltd. (2009): SeaGen.. Marine Current Turbine; cited 2009 09/26]. Available from: http://www.marineturbines.com/.

[2]Open Hydro. (2009): Open Hydro Turbine.]cited 2009 09/26]Availablefrom: http://www.openhydro.com/home.html.

[3] H.K. Versteeg, W. Malalasekera. (2007): An introduction to computational fluid dynamics : the finite volume method. 2nd ed. Harlow: Pearson/Prentice Hall.

[4] B.E. Launder, D.B Spalding. (1972): Lectures in mathematical models of turbulence. London: Academic Press.

[5] D.C Wilcox. (2006): Turbulence modelling for CFD. Third ed. La Canada, California: DCW Industries;.

[6] S.B Pope. (2000) Turbulent flows. Cambridge: Cambridge University Press.

[7] S. A Hughes.(1993) Physical models and laboratory techniques in coastal engineering. Singapore; River Edge, NJ: World Scientific;.

[8] P. Novak. (1989): Scaling Factors and Scale Effects in Modelling Hydraulic Structures: H. Kobus, editor. Symposium on Scale Effects in Modelling Hydraulic Structures. Second ed. Stuttgart, Germany.: Sprint Druck; 1989.

[9] S. Gunter. (1983): On the force fluctuations acting on a circular cylinder in a crossflow from subcritical up to transcritical Reynolds numbers. Journal of Fluid Mechanics.; 133: 265-285.

[10] Ansys Fluent Inc. Turbulence. (2009): k-epsilon model. Ansys Fluent - Theory guide. Release 12 ed. Chapter 4 p. 4-13.

[11] J. Tu, G.H. Yeoh, C. Liu. (2008): *Computational fluid* dynamics : a practical approach. Burlington, MA; Oxford: Butterworth-Heinemann;.

[12] G. Biswas, V. Eswaran (2002): Turbulent flows: fundamentals, experiments and modelling. Pangbourne: Alpha Science;.

[13] B.M. Sumer. (2006): Hydrodynamics around cylindrical structures. Revised ed. Singapore ; London: World Scientific Publishing.

[14] M.M Zdravkovich. (1997): Flow around circular cylinders: a comprehensive guide through flow phenomena, experiments, applications, mathematical models and computer simulations. *Vol.1*. Oxford: Oxford University Press.

Appendix C

Study of Coherent Structures Suitable for Numerical Testing of Tidal Current Energy Devices.

Patricia O. Okorie[1], Alan Owen[2], Pat Pollard[3], Mamdud Hossain[4]

[1-4]*School of Engineering,*

Robert Gordon University

Schoolhill, Aberdeen, AB10 1FR

United Kingdom.

[1]o.p.okorie@rgu.ac.uk [2]a.owen@rgu.ac.uk

[3]p.pollard@rgu.ac.uk [4]m.hossain@rgu.ac.uk

Abstract— **Flow within tidal current is random and contains coherent structures. Much progress has been made in research and development of Tidal Current Energy (TCE) technology but the understanding of the effect of coherent structures on TCE device performance and loading is unclear. The study aim to simulate and study coherent structures in an empty channel suitable for numerical testing of a TCE device using experimental velocity profile.**

The Acoustic Doppler Current Profiler (ADCP) is the standard instrument for measuring the velocity of tidal currents despite known limitations. With the aid of a single realisation of the ADCP experimental velocity profile, acquired in a tidal estuary and specified at the inlet boundary of a Large Eddy Simulation (LES), a significant increase in turbulence in terms of maximum vorticity magnitude, by a factor more than 4 was achieved as well as a substantial amount of visible vortex structures, when results were compared with simulations done by specifying the uniform flow and the 1/7th power law velocity profiles at inlet boundary of a LES.

A discussion on the effect of the coherent structures on channel bed drag coefficient is included.

Keywords— **Tidal Currents, ADCP Data, Coherent Structures, LES, TCE Device Testing.**

I. Introduction

In response to the growing need for sustainable energy and climate change demands, the tidal current energy technology has been identified as a viable option among the energy mix portfolio. The energy resource in tidal currents in the UK has been estimated by several sources [1] that includes [2] – [3] but with differing estimates resulting from the analysis method. Also, the World Offshore Renewable Energy Report (2004 – 2008), released by the Department of Trade and Industry, suggests that 3000GW of tidal energy is estimated to be available.

Several devices / technology for harnessing the available resource are currently being developed and tested. The progress made so far is significant with some commercial test prototype currently connected to the grid. An example is the Marine Current Turbine [4]. A database of some known technologies can be found in [5].

Despite the progress made so far in developing tidal current energy devices, the technology faces a challenge due to the turbulent flow environment they operate: The effect of turbulence on device dynamic loading and performance is unclear. The need to understand the effect of turbulence during model testing was highlighted by Bearman, [6] in wind tunnel experiments. He emphasised that turbulence should be accounted for before satisfactory scale model results are extrapolated and applied to prototypes.

The testing of small scale tidal current energy devices are usually carried out in water circulating channels or tow tanks although, differences occur between measured forces when device are towed in water and when fixed in flowing water from studies by [7]. It is known that, turbulence generated in these test facilities does not fully represent those inherent in natural flows. It becomes a challenging task to account for turbulence during experimental testing of tidal current energy devices. During the development of tidal current energy device performance protocol by [8], the effect of turbulence on device performance and survivability was highlighted as a knowledge gap that could become a major issue.

Turbulence within tidal current is a random process and appears in form of coherent structures ranging from small scale to large scales eddies. The interaction between the small and large scale structures is described by the energy cascade process [9]. Large scale coherent structures contain most of the turbulent kinetic energy. The turbulence phenomenon is mathematically explained by the Kolmogorov spectrum [10] in the high frequency range while the large scale structures occupy the lower frequency range of the energy spectrum.

A qualitative description of the large scale structures observed in natural flows is contained in [11] and [12]. The large scale structures are anisotropic and have been categorised into the bursting phenomenon and large scale vortical motion. The bursting phenomenon is a quasi-cyclic process of sweeps and ejections motion that generates Reynolds stresses and produces the turbulent energy that acts

to maintain turbulence in shear flows. The ejection process consists of a lifting away of a low speed parcel of fluid from the wall region into the outer region of the flow. The sweeping process consists of a higher speed parcel of fluid rushing into the wall region to sweep away the left over low speed fluid parcel from the wall region. These appear as streaky structures and appear randomly in space and time. The bursting phenomenon has been observed in previous studies to occur both in rough and smooth bed according to [13].

Large scale vortical motion that constitutes turbulence consists of a strong upward vortex called kolk [11]. The kolk vortices are generated intermittently near the channel bed. Kolk vortices with high enough turbulence have the potential to ascend to the water surface to become a boil. Other types of large scale vortical motion that has been observed in natural flows are regarded as a pulsation of the mean flow because it is a much lower frequency motion containing fine turbulence.

In numerical simulation of turbulent flow, coherent vortices are recognised as regions of high concentration of vorticity. It is anticipated that the large scale coherent structures may cause potential hazard during its interactions with the device. An illustration of a vortex structure interacting with a generic tidal current energy device is shown in fig.1. In wind energy generation, significant departures from steady operating loads conditions can occur in gusty conditions according to [14]. Correspondingly, testing of tidal current devices in a field of coherent structures is necessary to validate and optimise prototype before full scale deployment.

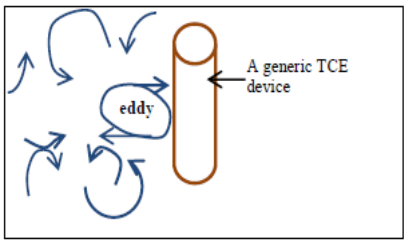

Fig.1 An eddy interacting with a generic structure

The primary aim of this study is to demonstrate the possibility of simulating a flow field of ambient coherent structures suitable for numerical testing of a tidal current energy device, with the aid of experimental velocity ADCP data.

It is a common practice to specify the $1/7^{th}$ power law and the uniform flow boundary conditions in Computational Fluid Dynamics (CFD) calculations of marine devices. However, these profiles assume a smooth and organised incident flow upstream of the device. The upstream flow structure exhibited by the theoretical velocity profiles thus deviates from real flow structure observed in natural flows. The popular use of these profiles to investigate turbulence effects may largely be attributed to the scarcity of real turbulent velocity profile from a tidal current site or perhaps the logistics and the associated cost of acquiring real current profiles. This study thus presents a preliminary step for accounting for large scale turbulent structures during tidal current energy device numerical testing.

The study is carried out based on two research components: Firstly to acquire experimental velocity data using the ADCP and then to simulate coherent structures using the ADCP data and the theoretical velocity profiles in a LES of an empty channel.

The flow field generated with the aid of the ADCP data are compared with those generated using the theoretical velocity profiles and also qualitatively compared with the description of coherent structures in [11] and [12].

A. *ADCP Instrument and Its Uses.*

The ADCP has become the standard instrument for estimating the mean flow and turbulence quantities in a tidal current channel. It is a sonar instrument that measures water current velocities across an entire water column by sending pings of sounds or beams through the water column from its transducers head. The ADCP is limited in the sense that, it cannot be used to observe the smallest scale of turbulence and there are zones in the water column where measurements are not possible, because of the inaccessibility of the acoustic beams, nevertheless, ADCP data is still popularly used for example by [15-22] to estimate mean flow and turbulent quantities in tidal currents channels, It is also used for tidal current resource characterisation [23], environment monitoring and harmonic analysis of the tidal constituents etc. The ADCP data is used here to simulate vortices in an open channel flow resembling those inherent in natural flows in a LES.

B. *ADCP Deployment Site*

The Forth estuary is 93km long and extends from Stirling up to join the North Sea, with the Isles of May lying at its entrance. See fig. 2. It is reported that the bathymetry of the upper Forth varies and changes with time. These changes occur naturally and are continuous, indicating a high degree of sedimentation processes. Further downstream, the estuary increases in width and the bathymetry is more stable.

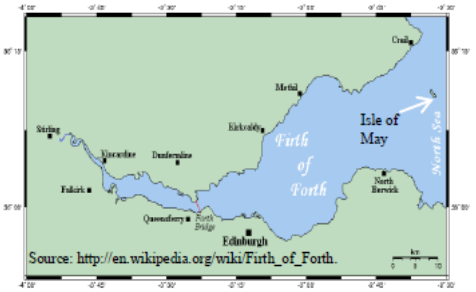

Fig.2 Map of the Firth of Forth.

C. *Large Eddy Simulation*

The basic concept of the LES techniques began in early 1960 with the work of Smagorinsky. It dealt with the energetic structures of the flow with a characteristic scale larger than a given cut-off scale. LES and its variants are becoming more popular as increasing computational power makes it more accessible. The behaviour of large scale

structures suggests that the LES is suitable for predicting their evolution. Detailed information on the LES techniques can be found in [24].

II. METHOD AND APPROACH

The approach requires sampling tidal current velocity data using the ADCP instrument and the numerical simulation of the flow field using the ADCP data as input. The method exploits the three dimensionality effect and depth variation of the fluctuating velocity profile of tidal current based on a single realisation of the ADCP experiment in conjunction with the LES technique available in ANSYS software package.

A. *Experimental Method*

A SonTek/YSI three beam ADCP shown in fig. 3 was deployed at location 56^0 10.642' and 2^0 32.359' in 53m depth of water at the Firth of Forth, near the Isles of May, North East of Scotland. The ADCP basically comprise of a transducer and an external battery mounted on the supporting frame.

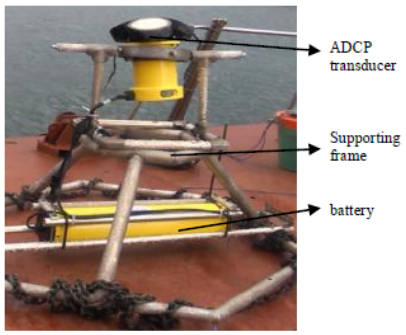

Fig. 3 ADCP on a supporting frame

The ADCP was deployed to sample tidal current velocity for 23 days, beginning midday on the 20th of July 2010 and was retrieved on the 11th of August, 2010. An autonomous sampling strategy of 60 seconds and recorded every 10 minutes was set. A total of 3185 velocity profiles with a spatial resolution of one meter were acquired. The vertical water column was divided into 50 bins.

The ADCP measured the along beam current velocity which was then converted into the ENU coordinates system. The acronym ENU stands for East, North and Up respectively. The east-west velocity components is the along channel velocity which flows along the x-axis. The north-south component is the across channel component which flows along the y-axis (see fig. 4). Both are known as the horizontal velocity components of tidal current. The up component is the vertical velocity component.

The ENU coordinate system illustrated in fig. 4 allows the ADCP to always report the true water velocity. This is because of updated compass/tilt information available during the averaging of the velocity vectors for each profile. Therefore, data reported in the ENU coordinate system are not affected by the orientation of the ADCP.

The east–west, north-south and the up-down velocity refers to the u, v and w components respectively and they are orthogonal to each other. The u velocity component is parallel

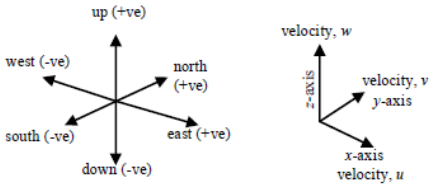

Fig. 4: ENU Coordinate system illustrated

to the net flow of tidal current. Using vector arithmetic, the time averaged current velocity magnitude, $\bar{u}$ in the net flow is calculated using equation 1 below:

$$\bar{u} = \sqrt{u^2 + v^2 + w^2} \qquad (1)$$

The angle the averaged current velocity makes with the three directions is evaluated from equations 2 - 4 below:

$$\cos(\propto) = \frac{u}{\bar{u}} \qquad (2)$$

$$\cos(\beta) = \frac{v}{\bar{u}} \qquad (3)$$

$$\cos(\gamma) = \frac{w}{\bar{w}} \qquad (4)$$

Where $\propto$, β and γ are the angles the current vector makes with the positive directions of x, y and z axis respectively.

The results from the ADCP experiment are reported in section III - A.

B. *Numerical Method*

1) Governing Equations: The Large Eddy Simulation method solved the 3D Navier - Stokes equation based on the dynamic stress, Smagorinsky-Lily subgrid scale model. The LES consists of a filtering operation analogous to superimposing the turbulence fluctuation on the mean flow.

Applying the filtering procedure to the Navier-Stokes equation and the continuity equations yields;

$$\frac{\partial \bar{u}_i}{\partial x_i} = 0 \qquad (5)$$

$$\frac{\partial \bar{u}_i}{\partial t} + \frac{\partial (\bar{u}_i \bar{u}_j)}{\partial x_j} = -\frac{1}{\rho}\frac{\partial \bar{p}}{\partial x_i} + \frac{1}{\rho}\frac{\partial \tau_{ij}}{\partial x_j} + \nu \frac{\partial^2 \bar{u}_i}{\partial x_i \partial x_j} \qquad (6)$$

The operation filters out the eddies that has scales smaller than the filter width. The resulting filtered equations governs the dynamics of the large eddies. The effect of the small scale is represented by the subgrid scale tensor τ_{ij} ,

$$\tau_{ij} = \overline{u_i u_j} - \bar{u}_i \bar{u}_j \quad (7)$$

The behaviour of turbulent flow makes the use of velocity magnitude vectors and vorticity plots a convenient method to characterise the flow structure based on the premise that the kinematic and dynamic evolution of an incompressible fluid can equivalently be expressed in terms of velocity and vorticity [25] so that no information about the numerical simulated flow field is lost by considering the vorticity as a measure of turbulence. Vorticity ω, is formally defined as the curl of the velocity vector expressed in equation 8 below:

$$\omega = \nabla x \hat{u} = \left(\frac{\partial w}{\partial y} - \frac{\partial v}{\partial z}, \frac{\partial u}{\partial z} - \frac{\partial w}{\partial x}, \frac{\partial v}{\partial x} - \frac{\partial u}{\partial y}\right) \quad (8)$$

where u, v and w are the velocity components in the x, y and z directions respectively. The vorticity magnitude is calculated using equation 9 below:

$$|\omega| = \sqrt{\omega_x^2 + \omega_y^2 + \omega_z^2} \quad (9)$$

2) Meshing: The computational domain is a structured coarse mesh consisting of 150000 hexahedron prisms with 1500 inlet faces. Fig. 5a is a three dimensional mesh showing the sides and the bottom walls and fig. 5b is a 2D vertical plane view (not to scale) of the mesh. The domain is sized 10m x 5m x 3m. Note that the vertical velocity represents the y component in the numerical model.

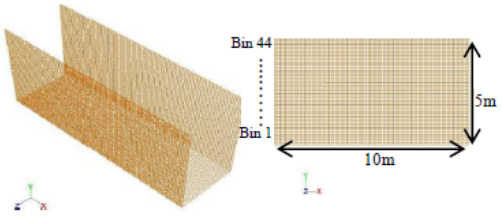

Fig.5 A three dimensional mesh Fig 5b An x-y vertical plane mesh.

3) Boundary Conditions:
Wall boundaries: A no slip wall condition is specified for the sides and bottom walls.
Outlet: Pressure outlet.
Top Surface: A zero shear was specified at the channel surface
Inlet: Three different conditions were applied at the inlet;

- Uniform flow
- 1/7th power law velocity profile
- ADCP experimental velocity data.

The ADCP data for bin 1 to 44 was used for the simulation. The top 6 bin data were not used because the shape of the profile deviate significantly from a velocity-depth profile possibly due to effect of surface waves, winds or other processes. The uniform and the 1/7th power law velocity profiles are used as base case studies because of their popular use and therefore serves as a comparison component in this study.

All velocity data were specified as point profiles files at the inlet. The profiles were extrapolated using the zeroth order extrapolation technique. A turbulent scale of one meter length, a 10% turbulent intensity and the spectrum synthesizer techniques based on the work of [26], was specified at the inlet of all simulation cases. The resulting flow fields from the three simulation cases are reported in section III - B.

III. ADCP DATA ANALYSIS AND LES RESULTS AND DISCUSSION.

The standard error associated with each velocity data gives a direct measure of the quality of the velocity data. A good velocity profile has approximately constant standard error for each velocity data. A rapid increase in the standard error indicates a beam may have reached the end of a profiling range. The comprehensive results of the quality checks are not reported here however, it is sufficient here to state that the overall data quality is good except the acquired data for the top six bins at the water surface which showed some rapid increase in standard error values, thus underpinning why those data were eliminated from the LES model of ADCP data simulation case.

Several types of plots are used to visualise the nature of the velocity field/profile: They include the horizontal velocity scatter plot, a plot comparing the theoretical velocity profiles with a one minute and a 23 days averaged experimental velocity profiles with emphasis on the effect of averaging the turbulent velocity profiles. Also included are plots showing the velocity profiles for three single realisations of the ADCP experiment: a turbulent velocity profile sampled during a high tide designated as the 309th profile, a velocity profile sampled during another high tide designated as the 441st and a third profile - the 1187th, sampled during a low tide in the spring. The single realisations samples have been chosen arbitrarily to represent all other profiles in the sense that, there are fluctuations inherent in the profiles however, they vary in velocity magnitude values.

The LES results includes visualisations plots showing differences in the behaviour of the flow fields between using theoretical velocity profiles and a single realisation of the turbulent velocity profile in a LES. The results are visualised in the form of pathlines, velocity vectors and the vorticity contour plots

A. *ADCP Data Analysis*

1) UV Scatter Plot: The scatter plot in Fig. 6 is a representation of the east-west and the north-south velocity vector. Velocity samples used for the plot are a 14 days data acquired during a spring and neap tides at bin 10, representing 10m depth of water.

The plot gives a strong visual clue of the tendency of the current vectors to align along a particular directional axis (marked in blue colour), where the flood and the ebb direction are 229.9 and 49.9 degrees respectively along the axis. The

plot also indicates that the velocity vectors do not necessarily align strictly along the predominant east-west direction.

2) *Comparison Plot:* Fig. 7 show distinguished differences in the shape of velocity profiles plotted with a one

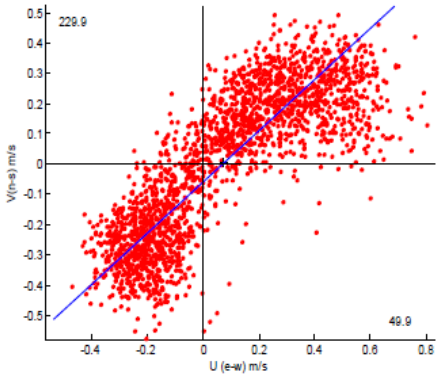

Fig. 6 UV scatter plot for a neap and spring tide

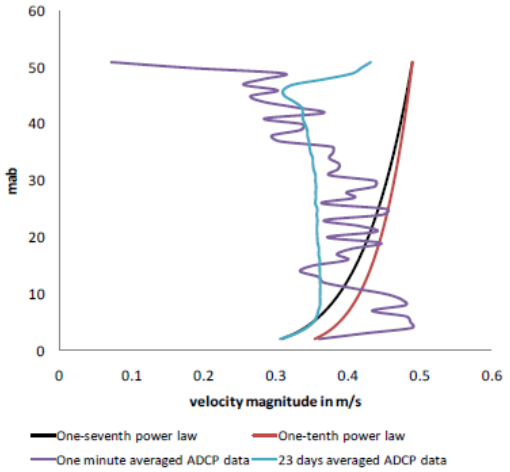

Fig. 7 A comparison plot showing ADCP averaged depth profile with theoretical velocity profiles.

minute averaged ADCP data, 23 days averaged ADCP data, the $1/7^{th}$ and the $1/10^{th}$ power law velocity profiles. The entire 50 bins data was used for the plots to visualise the possible effect of processes going on at the water surface. Data sampling was possible from 2 meters above bottom (mab) up to the water surface. This represents one of the limitations of the use of the ADCP instrument.

The uncharacteristic shape of the profile occurring towards the water surface is attributed to the effect of the end of a profiling range and/or the influence of surface waves and wind on current velocity.

The slight 'double drag' effect noticed near the top of the 23 days ADCP averaged profile, just before the graph inverted, is attributed to other processes other than tides near the water surface. A more pronounced 'double drag' effect on a vertical structure of tidal current had been observed by [27] from ADCP data sampled from a coastal raft-culture area.

The one minute averaged profile is far from being smooth and organised, reflecting a significant influence of the fluctuations associated with the turbulent velocity within the limit of the averaging.

It is interesting to note the clean overlay existing between the $1/7^{th}$ power law and the 23 days averaged velocity data in the first few bins from the seabed and that, for the most part, the middle section of the 23 days averaged data produces a relatively uniform flow. Theoretically, it is known that the $1/7^{th}$ power law approximation is valid for flow with Reynolds number of 10^5. The exponent value falls below $\frac{1}{7}$ for higher Reynolds number flow having values of $\frac{1}{8}, \frac{1}{9}$ *and* $\frac{1}{10}$ at extreme values.

2) Plots Showing a Single Realisation of Turbulent Velocity for Profiles 309, 441 and 1187: Figs. 8a, 8b and 8c, show velocity profiles for the ADCP data sampled and recorded in one minute and at different times. Note that the three profiles have been chosen randomly and all other velocity profiles are comparable to these three. The plots represent velocity samples acquired during profiles 309, 441 and 1187 respectively and presented in 1-dimension, 2-dimensions and 3-dimensions plots. Data used to generate the plots were computed using equations 10-12 below:

$$\sqrt{u^2} \qquad (10)$$

$$\sqrt{u^2 + v^2} \qquad (11)$$

$$\sqrt{u^2 + v^2 + w^2} \qquad (12)$$

Generally, the shapes of velocity profiles taken at different times in a turbulent flow are different from each other. Common to them all, is the lack of smoothness exhibited in all the profiles. The shapes also differ based on the number of velocity components used to generate the plots. These differences confirm the spatial and temporal variability of velocity in a turbulent channel flow. Also, the vertical velocity component has minimal effect on the profile shapes, this suggest a reason why turbulence may be assumed as 2 dimensional especially in geophysical flows.

The dimensional effects are much more pronounced in profiles 309 and 441 plots. All three profiles plots correspond to the same vertical water column under which the ADCP was located at the Forth estuary. The 309^{th} velocity profile had a peak velocity magnitude of about 0.49m/s and a mean velocity of 0.37m/s. Profile 441 had a peak velocity magnitude of 0.46m/s and a mean of 0.17m/s and profile 1187 had a peak velocity of 1m/s and a mean of 0.56m/s. Any of the profiles

is capable of aiding the generation of coherent structures in conjunction with a LES of an empty tidal current chan

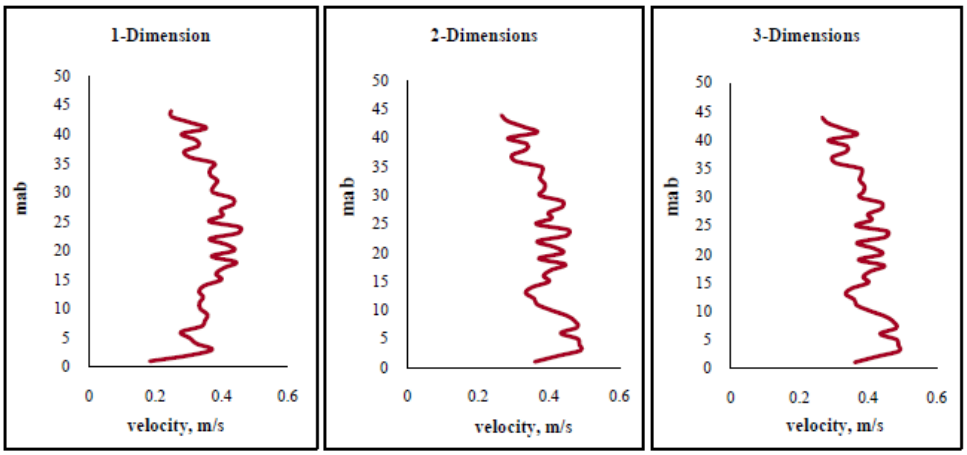

Fig. 8a: One minute averaged ADCP data plot using the 309th profile data.

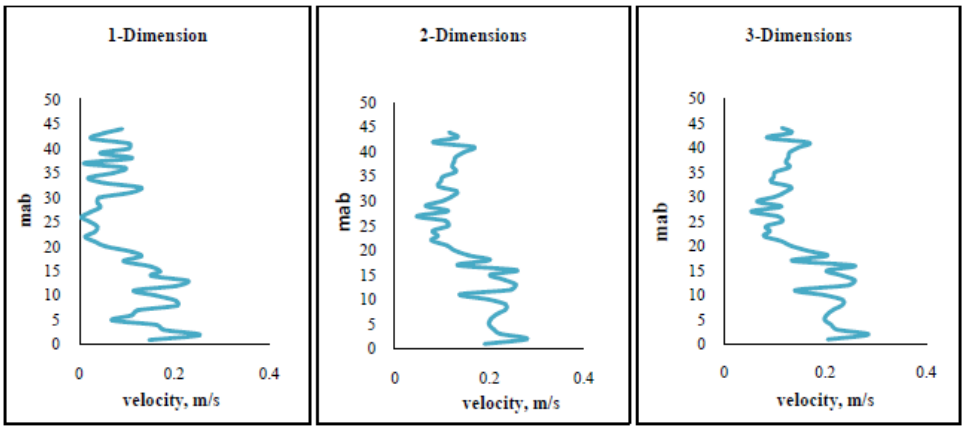

Fig. 8b: One minute averaged ADCP data plot using the 441st profile data.

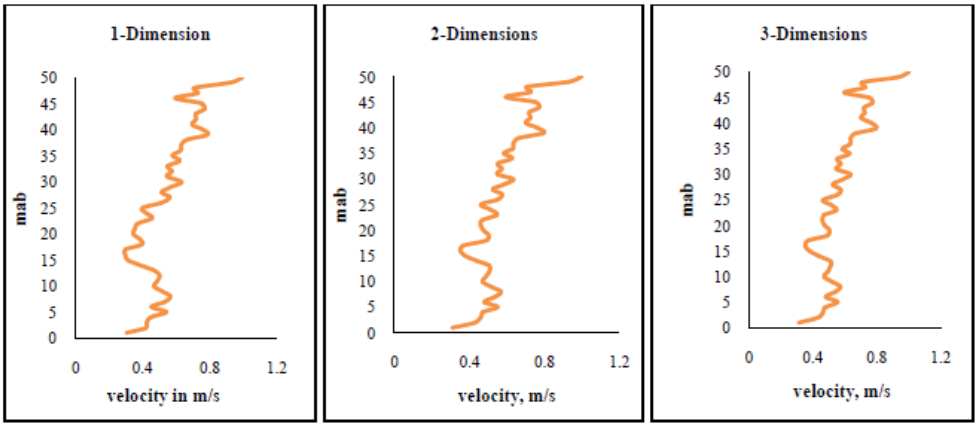

Fig. 8c: One minute averaged ADCP data plot using the 1187th profile data.

B. *LES Simulation Results and Discussion*

A mesh sensitivity test was carried out on a domain with 6000 inlet faces and 1200000 hexahedron prisms for the ADCP simulation case. The finer mesh produced higher amount of vorticity, 4 times larger than the vorticity produced with the coarser mesh used for this study. However, due to computational requirement to simulate the theoretical velocity profiles case studies, the coarser mesh was chosen. Also, since the interest is on comparing flow fields containing coherent structures, it is considered sufficient to show the relative magnitude of vorticity rather than absolute values.

To visualise the translational and the rotational effect of the of the flow field, instantaneous plots showing velocity magnitude pathlines, vectors and vorticity magnitude contour plots for the three simulation cases are presented in what follows. Based on the maximum velocity of 0.49m/s reached and the mean velocity of 0.37m/s of the current at the Forth estuary during acquisition of the of the 309th velocity profile, depth profile data were generated for the uniform flow simulation case (Fig. 9a) and also for the 1/7th power law simulation case (Fig. 9b) using equation 13 below:

$$\frac{u_x}{u_{max}} = \left(\frac{y}{z}\right)^{\frac{1}{7}} \qquad (13)$$

where y is any distance measure from the seabed. z is the channel depth. u_x is the mean velocity and u_{max} is the max velocity close to the channel surface. The mean velocity acts to average out the turbulent fluctuations in the x direction measured at any particular value of y. The uniform flow and the 1/7th power law velocity profiles data generated were specified at the inlet of the simulation domain figs. 9a and 9b. The one minute averaged velocity data acquired during profile 309 was specified at the inlet of the third simulation case (Fig. 9c).

1) Instantaneous Pathlines: A plot showing the trajectories that the individual fluid particles follow in velocity magnitude is shown in figs. 9a, 9b and 9c. The pathlines should generally be changing as the flow progresses for transient flow calculations.

The uniform and the 1/7th power law profile produced a relatively organised flow lines. Pathlines for the ADCP data simulation case (Fig. 9c) can be described as chaotic with no definite pattern. The irregular behaviour of the pathlines in fig.9c describes flowlines associated with turbulent flow because they are usually difficult to follow and also to create in a physical experiment.

However, comparable in all three simulation cases are the values of the simulated maximum velocity magnitude attained at some point in the flow field, to the maximum acquired velocity magnitude of 0.49 m/s during sampling the 309th profile ADCP data. The simulated maximum velocity values for the uniform, the 1/7th power law and the ADCP simulation cases are 0.58m/s, 0.53m/s and 0.59m/s respectively.

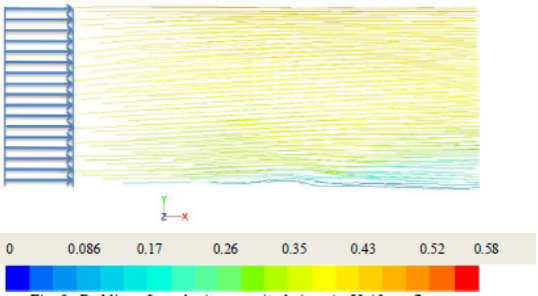

Fig. 9a Pathlines for velocity magnitude in m/s- Uniform flow.

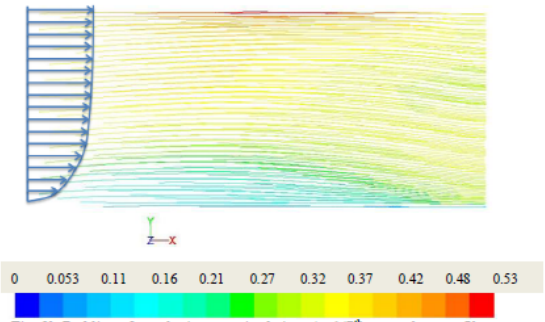

Fig. 9b:Pathlines for velocity magnitude in m/s- 1/7th power law profile.

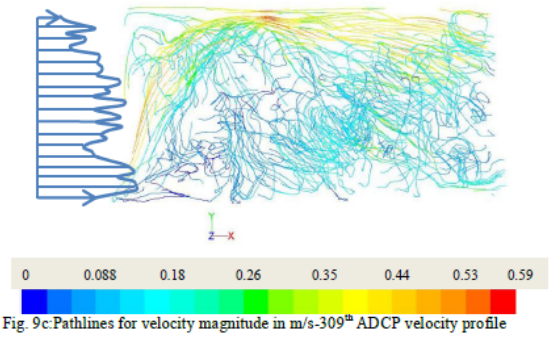

Fig. 9c:Pathlines for velocity magnitude in m/s-309th ADCP velocity profile

2) Vorticity plots: Vorticity is an important quantity for characterising turbulence. It is a feature of turbulent flow that measures the degree of local rotation in the fluid with units in per second. Coherent vortices are defined in (24) as regions of flow satisfying a high concentration of vorticity, enough to enable a local roll up of the surrounding fluid. Figs. 10a, 10b and 10c show the vertical plane of instantaneous vorticity plots at mid section of the channel. A qualitative comparison based on the description of flow structures by (11) in natural flow is made.

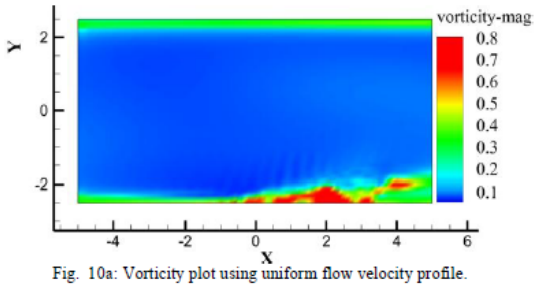

Fig. 10a: Vorticity plot using uniform flow velocity profile.

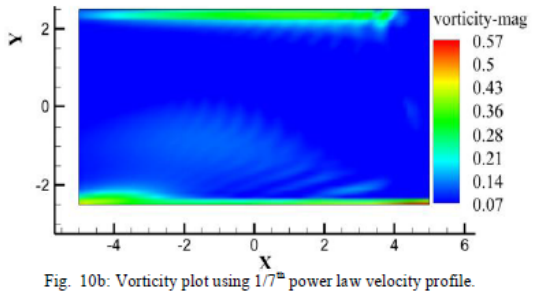

Fig. 10b: Vorticity plot using 1/7th power law velocity profile.

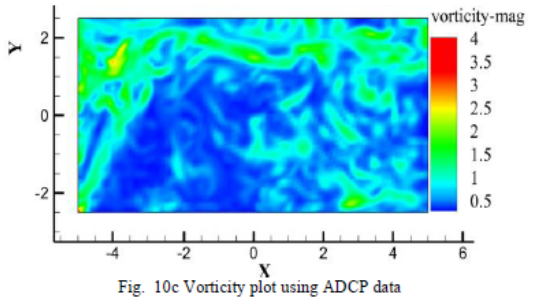

Fig. 10c Vorticity plot using ADCP data

Maximum vorticity is observed near the bottom walls in all three simulation cases. Coherent structures generated by the bottom walls are faintly noticeable in figs. 10a and 10b as streaks of fluid parcels especially in fig. 10b. This is in agreement with the explanation offered by the bursting phenomenon that describes a lifting away of low speed streaks of fluid parcels from the wall region during the ejection phase of a turbulent flow process. However, the vorticity generated near the channel bed region is observed to diffuse with distance away from the walls in figs. 10a and 10b. The vorticity magnitudes for the uniform and the 1/7th power law simulation cases are not significantly different from each other, with maximum values of around $0.8s^{-1}$ and $0.6s^{-1}$ respectively.

Coherent structures observed in fig. 10c are higher by a factor of more than 4 in terms of maximum vorticity magnitude. The coherent structures field also gives a better representation of flow structures observed in natural flows. Since the mesh sizing is the same for all simulation cases, the increase in the vorticity magnitude in the ADCP simulation case, is a direct outcome of the experimental velocity ADCP data used at the inlet boundary. Based on the premise that the velocity profile used to calculate the vorticity field represents a single realisation of the flow at the Forth estuary, the vorticity plot in fig. 10c, thus provides a reasonable representation of the turbulence in terms of vorticity magnitude at the estuary. There is evidence of sustained turbulence in fig. 10c due to a strong vortex generated near the wall region in form of a kolk reaching up to the water surface in form of a boil as described by [11].

The effect of the sustained turbulence made possible the presence of coherent structure in the outer region of the channel thus providing a suitable environment to investigate the effect of coherent structures on any device submerged in such flow conditions. The turbulence generated using the theoretical velocity profiles resemble a pulsation of the mean flow as visualised from the time animation of the flow lines of the velocity magnitude

3) Velocity vector plots: Corresponding vector plots for velocity magnitude are shown for the uniform flow, 1/7th power law and the ADCP data simulation cases in figs. 11a, 11b, and 11c respectively. The vector plot shows the magnitude and direction of each vector signified by its length and orientation in the vector field. A section of the flow domain in two dimensions is shown for better visualisation. The theoretical velocity profiles show relatively regular patterns of a vector field as in figs. 11a and 11b.

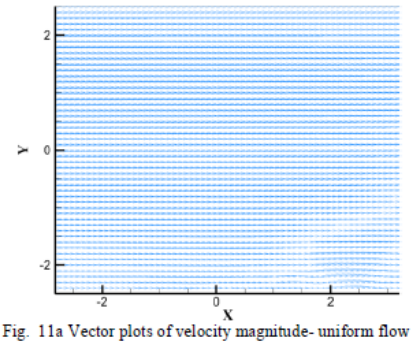

Fig. 11a Vector plots of velocity magnitude- uniform flow

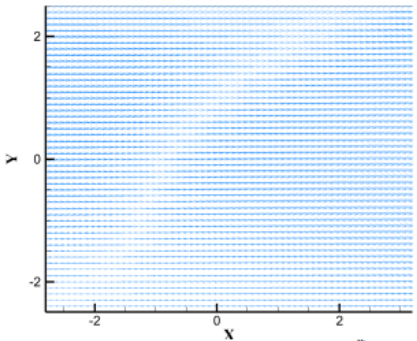

Fig. 11b Vector plots of velocity magnitude- 1/7th law

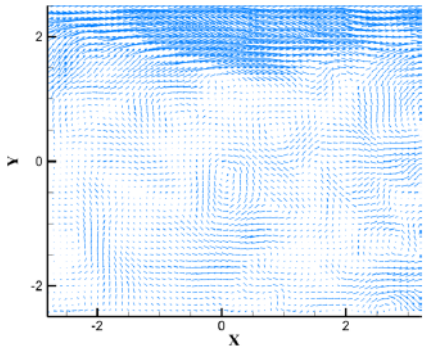

Fig. 11c Vector plots of velocity magnitude- ADCP data

However, rotation of parcels of fluid is clearly observed in plots 11c. Vortices are associated with rolled up fluid parcel. The roll up effects is clearly absent in the uniform and the 1/7th power law profile simulation cases as a consequence of a one dimensional flow.

The effect of the structure of the flow fields in all three simulation cases on the seabed drag are investigated in what follows.

C. *Effect of Flow Field on Seabed Drag.*

The effect of a no slip condition implies that there will be a sea bed drag. The drag acting of the channel seabed was monitored throughout the simulation duration. Plots 12a, 12b and 12c show the drag coefficient time history for the three simulation cases.

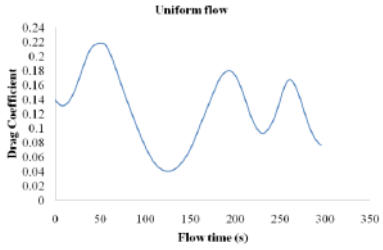

The drag resulting from uniform flow and the 1/7th power law profile are comparable fluctuating within 0.02 - 0.22. Drag coefficient resulting from the ADCP data simulation case, have much lower values up to a maximum of 0.008 and could have negative values sometimes.

One apparent effect of the turbulent flow field is a reduction in the channel bed drag coefficient. This behaviour is in agreement with the known Reynolds number – drag behaviour which shows decrease in drag coefficient as the flow becomes more turbulent based on the Reynolds number. The reduce drag coefficient in the ADCP simulation case is attributed to the effect of flow vectors in opposing direction to the streamwise flow and to the way drag force is normally calculated.

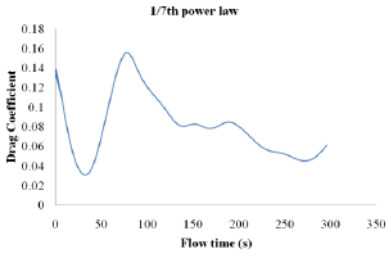

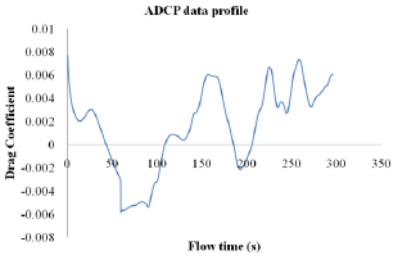

Drag force is customarily known to be positive downstream, acting parallel to the axis of the free stream (28). In the event that velocity vectors reverses direction, the drag in the opposite direction becomes negative thus detract from the positive values and causing an overall reduction in the value of the drag coefficient.

Equivalently, it is anticipated that any device submerged in a stream of coherent vortices, would experience a significant decrease in its drag coefficient when compared with its drag coefficient value simulated using the theoretical velocity profiles.

The implication for energy extraction may mean that, less energy is required to overcome the resistance offered by the seabed making more energy available for extraction by a turbine.

IV. Conclusions and Further Work

This study has demonstrated the possibility of generating significant ambient coherent structures with the aid of experimental velocity data. It offers a methodology suitable for investigating the effect of coherent structures during numerical testing of a tidal current energy device. It makes use of a single realisation of a turbulent velocity profile a LES.

An in-depth analysis of experimental turbulent velocity profiles sampled with the ADCP instrument has been carried. The shapes of the turbulent velocity profiles based on a single realisation of the experiment and a 23 days averaged velocity profile are compared with known theoretical velocity profiles commonly used in CFD calculations.

The overall conclusion is that a single realisation of a turbulent velocity profile specified at the inlet boundary condition of a LES, results to an increase in turbulence in terms of the maximum vorticity magnitude by more than a factor of 4 as well as offering an adequate environment of ambient coherent structures for device numerical testing.

The results from ADCP data analysis and LES of the three simulation scenarios allow the following specific conclusion to be drawn.

1. The ADCP data analysis plots represent the flow nature at the Forth estuary. It is a slow flowing current with an overall mean speed of about 0.36m/s.
2. A single realisation of the experimental velocity ADCP data contain turbulent fluctuations while the uniform and the $1/7^{th}$ power law assumes a one directional smooth and organised velocity profiles.
3. The evolution of the flow field in a LES is very sensitive to the specified inlet profile: The ADCP data produce significant turbulent structures that are visible everywhere in the flow field making it a preferred flow field to investigate the effect of large scale turbulent structures on energy device/support structure performance and fluid loading.
4. The values of the simulated seabed drag coefficient using the ADCP data is significantly lower than those generated with the theoretical velocity profiles. Consequently, it is anticipated that hydrodynamic loading on a device using the theoretical velocity profiles in CFD calculation of tidal current devices are over estimated. Also, it appears the reduced drag coefficient associated with the use of the ADCP data will have flow similarity implications between a small scale numerical model and a large scale prototype.

Following the results from this study, simulation of forces acting a monopile support structure with a known drag is ongoing. It is also suggested that the work be extended to simulating the performance and loading on a tidal turbine submerged in a stream of coherent structures. More studies are also required on the similarity implications of a small scale numerical representation of a physical prototype. In this way, there are possibilities to use a small scale numerical model to investigate the performance of a large scale prototype operating in real sea conditions of upstream coherent structures based on the similarity of drag coefficient.

ACKNOWLEDGMENT

Many thanks to EPSRC and SuperGen Marine.

REFERENCES

[1] Metoc. *The World Offshore Renewable Energy Report. 2004-2008.* Department of Trade and Industry's Renewables 2010 Target Team; 2010.
[2]Energy Technology Support Unit. *Tidal Streams Energy Review:* ETSU; 1993.
[3] Black and Veatch. *Tidal Stream Energy Resource and Technology Summary Report.* United Kingdom.: Carbon Trust; 2004.
[4)]Peter Fraenkel. *Marine current Turbine: feedback on experience so far.* [homepage on the Internet]. France: Ocean Energy Conference; 2004 [updated 20/10/2004; cited 2009 02/11]. Available from: http://www.ifremer.fr/dtmsi/colloques/seatech04/mp/proceedings_presentations/4.%20courants_marins/MCT.pdf.
[5] U.S Department of Energy. *Energy Efficiency and Renewable Energy.* [homepage on the Internet]. U.S.A.: 2011 [updated 17/06/2010; cited 2011 17/06/2011]. Available from: http://www1.eere.energy.gov/windandhydro/hydrokinetic/default.aspx.
[6] Bearman PW, Morel T. Effect of free stream turbulence on the flow around bluff bodies. *Progress in Aerospace Science.* 1983; 20:97-123.
[7] SuperGen Marine. *A Monograph on SuperGen Marine Energy Research.* [monograph on the Internet]. UK: The University of Edinburgh; 2007 .
[8] Couch SJ, Jeffery HF and Bryden IG. Tidal Current Energy: Development of a Device Performance Protocol. Tidal Current Energy: Development of a Device Performance Protocol. *International Conference on Clean Electrical Power (ICCEP); 21-23 May;* : IEEE; 2007. p. 720 - 722.
[9] Richardson LF. *Weather Prediction by Numerical Process.* Cambridge: University Press; 1922.
[10] Kolmogorov AN. The Local Structure of Turbulence in Incompressible Viscous Fluid for very Large Reynolds Numbers. *Royal Society (London), Proceedings, Series A - Mathemetical and Physical Sciences.* 1991 (first Published in 1941).; 434(1890):9-13.
[11] Matthes GH. Macroturbulence in Natural Stream Flow. *Trans,. Amer. Geophy. Union.* 1947; 28:255-265.
[12] Nezu I, International Association for Hydraulic Research. *Turbulence in open-channel flows.* Rotterdam: Balkema; 1993.
[13] Nakagawa H, Nezu I. Prediction of the contributions to the Reynolds stress from bursting events in open channel flows. *Journal of Fluid Mechanics.* 1977; 80(Part 1):99-128.
[14] Harrison R, Hau E, Snel H. *Large wind turbines : design and economics.* Chichester: Wiley; 2000.
[15] Mark TS, Stephen GM Jon RB. Observation of Turbulence in a Partially Stratified Estuary. *Journal of Physical Oceanography.* [serial on the Internet] 1999 29(8):Available from: http://ams.allenpress.com/perlserv/?request=get-abstract&doi=10.1175%2F1520-0485(1999)029%3C1950%3AOOTIAP%3E2.0.CO%3B2&ct=1.
[16] Mark TS, Stephen GM, Jon RB. Measurements of Reynolds stress profiles in unstratified tidal flow. 1999; 104(C5):10933-10949.
[17]Osalusi E, Side J, Robert H. Structure of Turbulent Flow in EMEC's Tidal Energy Site. *International Communication of Heat and Mass transfer.* 2009; 36(5):422-423-431.
[18] Elizabeth AN, Chris RR, M.ASCE, Kevin AO. Evaluation of Mean Velocity and Turbulence Measurements with ADCPs. *Journal of Hydraulic Engineering.* 2007; 133(12):1310-1318.
[19] Rippeth TP, Eirwen W, Simpson JH. Reynolds Stress and Turbulent Energy Production in a Tidal Current. *Journal of Physical Oceanography.* 2001; 32:1242-1243-1251.
[20]Youyu LuRolf G. Lueck. Using a Broadband ADCP in a Tidal channel Part 1: Mean Flow and Shear. *Journal of Atmospheric and Oceanic Technology.* [serial on the Internet] 1998 16.
[21] Youyu Lu, Rolf G. Lueck, Daiyan Huang. Turbulence Characteristics in a Tidal Channel. *Journal of Physical Oceanography.* 2000; 30(5):855-856-867.
[22] Youyu L, Rolf GL. Using a Broadband ADCP in a Tidal Channel. Part II: Turbulence. *Journal of Atmospheric and Oceanic Technology.* 1999; 16(11):1568-1569-1579.
[23] Carballo R, Iglesias G, Castro A. Numerical Model Evaluation of Tidal Stream Energy Reources in Ria de Muros (NW Spain). *Renewable Energy.* 2009; 34:1517-1524.
[24] Lesieur M. *Large-eddy simulations of turbulence.* Cambridge: Cambridge University Press; 2005.
[25] Helgeland A, Reif AP, Andreassen O, Wasberg CE. Visualisation of Vorticity and Vortices in Wall Bounded Turbulent Flows. *IEEE Transactions on Visualization and Computer Graphics.* 2007; 13(5):1055-1066.
[26] Smirnov S, Shi S, Celik I. Random Flow Generation Technique for Large Eddy Simulations and Particle - Dynamics Modelling. *Journal of Fluid Mechanics.* 2001; 123:359-371.
[27] Fan X, Wei H, Yuan Y, Zhao L. Vertical Structure of Tidal Currents in a Typical Coastal Raft-Culture Area. *Continental Shelf Research.* 2009; 29:2345-2357.
[28] White FM. *Fluid mechanics.* 5th ed. Boston, MA: McGraw-Hill; 2003.

Appendix D

Effect of Large Scale Turbulent Structures on a Generic Tidal Current Turbine Support Structure.

P.O . Okorie , A. Owen, M. Hossain, P. Pollard
Work stream 1:Numerical and Physical Convergence.

Introduction

Turbulence in a tidal channel is composed of eddies ranging from small scale to large scale. The smaller scale eddies characterise the fine structures of turbulence and are nearly isotropic. The large scale turbulent structures contains most of the turbulent kinetic energy. Thus structural loading on any device exposed to such flow conditions may have an adverse effect during device installation and operation. Thus it is important to account and /or discount for the effects of these large structures on the loading on the device.

The Acoustic Doppler Current Profiler (ADCP) is currently the standard instrument for measuring tidal current velocities and associated higher moments in a tidal current channel, irrespective of known limitations. The velocity structure in a tidal current channel is site specific however, a well conducted ADCP experiment will produce a reasonable velocity profile for a typical tidal current channel.

Approach and Method.

The small scale eddies are random in natures they can be described by the Gaussian probability density function since they behave randomly. The large scale eddies which are produced due to their interactions with the mean flow are coherent in nature and their behaviour suggest that Large Eddy Simulation (LES) and Direct Numerical Simulation (DNS) are appropriate to reproduce an evolutionary relation of the coherent structure of turbulence [1].

ADCP Experimental velocity profile data from the Firth of Forth, has been used as input boundary condition into numerical simulation using LES.

The vertical water column above the ADP was divided into 50 bins each 1m apart. The deployment period was for about 23 days.

Samples were collected with an autonomous sampling setting averaging one velocity sample over 1 minute every 10 minutes.

Results

The effect of upstream turbulent eddies on loading force is investigated by comparing results with uniform flow and assumed velocity profile of the 1/7th power law at the inlet boundary conditions. The figures below illustrate the flow structures and corresponding drag coefficient , Cd.

Flows structures and corresponding drag coefficients from uniform flow velocity profile

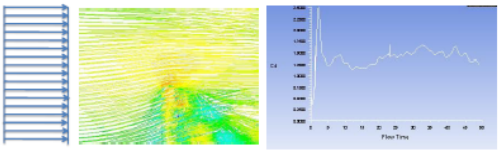

Flow structures and resulting Cd history from 1/7th law velocity profile.

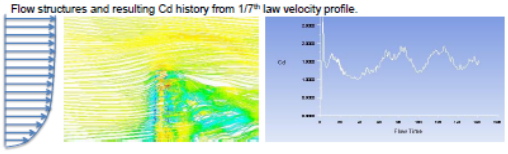

Flow structures and resulting Cd history from experimental ADCP velocity profile- Firth of Forth.

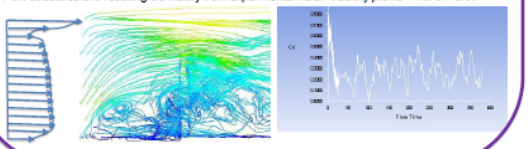

Discussion/Conclusion

Drag coefficient has been calculated on a steady flow around cylindrical structures with results published [2]. Generally, the effect of turbulent flow results in a decrease in drag coefficient. The drag coefficient resulting from input uniform flow varies from a minimum of about 1.1 to a maximum of about 1.6. Similarly, the Cd from the 1/7th power law profile fluctuates between 1.0 and 1.8.

A real velocity profile from the ADCP produced much lower Cd values fluctuating between 0.1 and 0.5. This may be explained from the point of view of the reverse flow associated with the movement of the eddies therefore detracting from the effective drag coefficient of the device.

References

[1]. Nezu I, International Association for Hydraulic Research. *Turbulence in open-channel flows*. Rotterdam: Balkema; 1993.

[2]. Gunter S. On the force fluctuations acting on a circular cylinder in a crossflow from subcritical up to transcritical Reynolds numbers. *Journal of Fluid Mechanics*. 1983; 133:265-285.

ROBERT GORDON UNIVERSITY•ABERDEEN

EPSRC
Engineering and Physical Sciences Research Council